

# Effect of Bridge Geometry on Seam Weld Microstructures in AA6xxx Aluminum Porthole Die Extrusions

by

Yu Wang

A thesis

presented to the University of Waterloo

in fulfilment of the

thesis requirement for the degree of

Doctor of Philosophy

in

Mechanical and Mechatronics Engineering

Waterloo, Ontario, Canada, 2020

© Yu Wang 2020

## Examining Committee Membership

The following served on the Examining Committee for this thesis. The decision of the Examining Committee is by majority vote.

External Examiner	Name	Hatem Zurob
	Title	Professor
Supervisor(s)	Name	Mary Wells
	Title	Professor
Internal Member	Name	Shahrzad Esmaeili
	Title	Professor
Internal Member	Name	Kaan Inal
	Title	Professor
Internal-external Member	Name	Scott Walbridge
	Title	Associate Professor

## **Author's declaration**

I hereby declare that I am the sole author of this thesis. This is a true copy of the thesis, including any required final revisions, as accepted by my examiners.

I understand that my thesis may be made electronically available to the public.

## **Abstract**

A series of porthole die extrusion trials were conducted with AA6xxx aluminum alloys to understand the influence of die geometry (bridge shape and welding chamber height), extrusion process parameters (ram speed) on the weld seam formation of the extrudate and its tensile properties in the natural aged (T4) and artificially aged (T5 and T6) conditions. In addition, a mathematical model was developed of the porthole die extrusion process to complement the experimental trials and provide quantitative information on the thermal mechanical history experienced by the material as a way to help understand the linkages between the extrusion process history, the microstructure formed and the final mechanical properties.

The extrusion trials were conducted at Rio Tinto's facility in Jonquiere, Quebec using their instrumented extrusion press to produce an extruded strip that had a weld seam along its length. In these trials, different die geometries were used to vary the shape of the bridge (flat versus streamlined) and the weld chamber height. In addition, a range of ram speeds was used to more fully understand the effect that extrusion speed has on the formation of the weld seam. These trials were conducted for three different compositions of AA6xxx aluminum alloys where the amount of Mn and Cr additions were altered (0Mn, 0.5Mn and 0.5Mn0.15Cr) to increase the number of dispersoids in the matrix and inhibit the recrystallize process.

The mathematical model of the porthole die extrusion process was developed using the commercial Finite Element Method (FEM) package DEFORM 3D. The results from the model predictions were verified by comparing them to the measured extrusion breakthrough load and comparing model-predictions of material flow to a slice of the material part way in the extrusion process to show the presence of dead metal zones.

The experimental results indicate that the microstructure and texture that formed along the weld seam was different than the matrix in cases where the final microstructure in the matrix was unrecrystallized or fibrous. The weld seam microstructure was strongly dependent on the shape of the bridge used and the weld chamber height. The extrusion simulation results, indicated the weld seams produced using a flat bridge experienced higher strains and temperatures during extrusion relative to a streamlined bridge. The simulation results also showed that the final weld seam

experienced much higher cumulative strain and higher temperatures than the surrounding matrix material and these effects extended out a few millimetres on either side of the weld seam.

The influence of ram speed on porthole die extrusion showed that as the ram speed increased several types of defects, such as edge cracking and a groove along the weld seam appeared on the surface of the extrudate. However, the final mechanical properties of the extruded profiles and the microstructure along the weld line did not appear to be significantly affected by ram speed.

The effect of material composition on the weld seam properties was significant and for cases where the matrix material did not recrystallize and had a fibrous microstructure, tensile tests aided by Digital Image Correlation (DIC) revealed that the strain concentrated at the weld seam region at a very early stage of plastic deformation. Analysis revealed that this was related to the softer texture at the weld seam compared to the matrix. This led to a significantly lower elongation to failure compared to extruded samples without a weld seam. In contrast, for cases where the matrix material did recrystallize (0Mn), the microstructure and texture at the weld seam were similar to the microstructure and texture in the matrix. For these cases, the strain to failure was similar to samples extruded without a weld seam and failure did not occur at the weld seam. This research clearly showed that the extrudate weld seam tensile properties were related to the texture both at the weld seam and in the matrix of the extrudate and that the weld seam microstructure can be influenced by the die geometry during porthole die extrusion.

## **Acknowledgements**

As an international student, studying in an unfamiliar country of completely different cultures and languages can not be an easy task. I still clearly remember the first day when I arrived in Canada with two large suitcases and got on the bus to Waterloo at dusk. At that time, I had no idea what lied ahead in my future. Very fortunately, I received so many people's help to overcome difficulties during the four and half years' Phd study. Without their sincere help, I can not finish my Phd study completely on myself.

First, I would like to thank my supervisor Prof. Mary Wells for giving me such a precious opportunity to study in University of Waterloo. Without her insightful guidance and suggestions, it is impossible to complete my PhD study. I also appreciate her to let me attend several high level international academic conferences, which really opened my eyes. I am also grateful for her huge efforts put into the revisions of this thesis.

Second, I am thankful for Prof. Warren Poole from University of British Columbia. I received many useful suggestions from him at the weekly meeting with his research group. He also allows me to use equipment at UBC to finish my experiment work.

Third, I also express my gratitude to Nick Parson from Rio Tinto and Mei Li from Ford Motor. We have regularly meeting to report our work's progress twice in one year. My extrusion trials were conducted in Rio Tinto under Nick Parson's help.

Furthermore, many thanks to Yahya Mahmoodkhani, Massimo Di Ciano, Mark Whitney, Michael Benoit, Paresh Prakash, Xiaoying Wang, Amir Zhumagulov, Jiangqi Chen, Chenglu Liu, Andrew Zang and Ali Khajezade. They offered me a lot of help on experiment and simulation work.

Finally, I am deeply grateful to my family for their understanding, encouragement and unconditional support. Thanks for them to give me the strength to overcome hardships during the long PhD study period.

# Table of Contents

Author's declaration .....	iii
Abstract .....	iv
Acknowledgements .....	vi
List of Figures .....	xi
List of Tables .....	xx
Chapter 1 Introduction .....	1
Chapter 2 Literature review .....	4
2.1 6xxx aluminum alloys .....	4
2.2 Porthole die extrusion .....	4
2.3 Longitudinal seam in porthole die extrusion .....	6
2.3.1 Mechanical properties of longitudinal seam .....	6
2.3.2 Longitudinal weld formation .....	8
2.3.3 Weld quality prediction.....	10
2.4 Microstructure evolution during porthole die extrusion .....	11
2.4.1 Recrystallization in extrusion .....	11
2.4.2 Microstructure.....	13
2.4.3 Texture evolution .....	14
2.5 Effect of minor alloying elements.....	17
2.6 Die design optimization .....	18
2.6.1 Welding chamber height .....	19
2.6.2 Bridge geometry.....	20
2.7 Extrusion parameters effects on welding quality .....	21
2.7.1 Extrusion temperature .....	21
2.7.2 Ram speed .....	22
2.7.3 Extrusion ratio.....	23
2.8 Front/back end defect.....	24
2.8.1 Front end defect formation.....	24
2.8.2 Estimation of charge seam length .....	25
2.8.3 Back end defect.....	26

Chapter 3 Scope and objective.....	28
Chapter 4 Methodology .....	29
4.1 Extrusion material.....	29
4.2 Extrusion trials .....	31
4.2.1 Die configurations.....	31
4.2.2 Extrusion parameters .....	34
4.3 Finite element method (FEM) simulation.....	35
4.3.1 Lagrangian and ALE simulation methods .....	35
4.3.2 Material model .....	36
4.3.3 DEFORM 3D simulation .....	37
4.3.4 Lagrangian simulation .....	38
4.3.5 ALE simulation .....	39
4.3.6 Mesh sensitivity .....	40
4.3.7 Flow path calculation based on ALE simulation .....	43
4.4 Material characterization .....	44
4.4.1 Metallography .....	44
4.4.2 Electron backscattered diffraction (EBSD) .....	45
4.4.3 Tensile test .....	45
Chapter 5 Results and discussion.....	47
5.1 Extrusion trials .....	47
5.1.1 Typical microstructure .....	47
5.1.2 As-deformed microstructure (low temperature extrusion) .....	48
5.1.2.1 Absence of PCG at the weld seam .....	48
5.1.2.2 Microstructure away from the seam .....	49
5.1.3 Typical texture .....	50
5.1.3.1 Texture at the weld seam .....	50
5.1.3.2 Quarter width texture .....	51
5.1.4 Mechanical properties of profiles .....	53
5.1.4.1 Stress-strain curves .....	53
5.1.4.2 Tensile test using DIC.....	57
5.1.4.3 PCG influence.....	59

5.2 Effect of bridge geometry .....	60
5.2.1 Microstructure at the weld seam .....	61
5.2.2 Texture analysis .....	62
5.2.2.1 Weld seam and adjacent area .....	62
5.2.2.2 Matrix .....	65
5.2.2.3 Welding chamber height .....	68
5.2.2.4 Porthole layout .....	71
5.2.3 Mechanical properties .....	73
5.2.3.1 Heat treatment .....	78
5.3 Model .....	80
5.3.1 Model verification .....	80
5.3.2 Simulation of the porthole die extrusion trials .....	83
5.3.2.1 Velocity distribution .....	83
5.3.2.2 Thermal mechanical history .....	85
5.3.2.3 Strain distribution .....	89
5.3.2.4 Welding quality prediction .....	91
5.4 Effect of ram speed .....	92
5.4.1 Breakthrough load .....	92
5.4.2 Surface quality .....	93
5.4.3 Microstructure .....	97
5.4.4 Texture analysis .....	100
5.4.5 Mechanical properties .....	101
5.4.6 Model predictions .....	102
5.5 Effect of composition .....	103
5.5.1 Microstructure .....	103
5.5.2 EBSD .....	105
5.5.2.1 0Mn sample texture .....	105
5.5.2.2 0.5Mn samples .....	107
5.5.3 Mechanical properties .....	109
5.5.3.1 0Mn samples .....	109
5.5.4 Texture influence on mechanical properties .....	112

5.5.4.1 0.5Mn0.15Cr sample.....	112
5.5.4.2 0Mn sample.....	115
5.5.4.3 0.5Mn samples .....	117
Chapter 6 Application of the extrusion model.....	119
6.1.1 Bridge angle.....	119
6.1.2 Upper part of bridge.....	123
6.2 Charge seam.....	126
6.2.1 Charge seam simulation - effect of die geometry .....	126
6.2.2 Model configuration.....	127
6.2.3 Charge seam formation.....	128
6.2.3.1 Bridge angle .....	129
6.2.3.2 Welding chamber height.....	130
6.2.4 Charge seam length calculation .....	132
6.3 Back end defect.....	133
6.3.1 The model setup of billet skin tracking.....	133
6.3.2 Billet skin flow behaviour.....	134
6.3.3 Die geometry influence.....	135
6.3.3.1 Bridge angle .....	135
6.3.3.2 Welding chamber height.....	135
Chapter 7 Summary, conclusions and future work.....	137
7.1 Summary .....	137
7.2 Conclusions.....	138
7.3 Future work.....	140
References.....	141

## List of Figures

Fig. 1-1 Typical 6xxx alloys for automotive applications [6].	2
Fig. 1-2 Aluminum extruded components used in light vehicles [14].	2
Fig. 2-1 Aluminum components in F-150 pick-ups: (a) main body structure, (b) internal webbing, (c) roof head and (d) roof bow [17].	5
Fig. 2-2 Porthole die configurations (1/2 section) [18].	6
Fig. 2-3 Porthole die extrusion stages: (a) dividing stage, (b) welding chamber fulfilling stage and (c) forming stage [19].	6
Fig. 2-4 Burst test for multi-cavity aluminum extrusion profile: (a) experimental methodology, (b) the final result [22].	7
Fig. 2-5 Tensile strength and elongation of porthole samples from different die dimensions: (a) tensile strength and (b) elongation [23].	8
Fig. 2-6 Mechanism of longitudinal seam formation [22].	8
Fig. 2-7 Two types of bonding surface under TEM observation: (a) Bridge field TEM image of type I bonding surface, (b) Bridge field TEM image of type II bonding surface, (c) HRTEM image of the selected area marked in (a), (d) HRTEM image of the selected area marked in (b) [25].	9
Fig. 2-8 The mechanism of GDRX in extrusion (thick lines stand for grain boundaries and the hexagons are subgrains): (a) grains are elongated in the extrusion direction, (b) grains are serrated during the further deformation and (c) grains are finally pinched off [37].	12
Fig. 2-9 The micrographs of Al-4.5Zn-1Mg rods extruded at different temperature: (a) 460 °C (no PCGs) and (b) 500°C [39].	13
Fig. 2-10 Microstructure of porthole die extruded AA6082 samples [40].	13
Fig. 2-11 Microstructure evolution from welding chamber to extruded profile: (a) welding chamber, (b) bearing length and (c) extruded profile [41]. (White dash line indicates the seam.)	14
Fig. 2-12 Texture evolution during porthole die extrusion: (a) flow path in porthole die extrusion, (b), (c), (d),(e) and (f) $\varphi_2 = 45^\circ$ ODF sections of different points on flow plath [42].	15
Fig. 2-13 Locations of interesting textures in $\varphi_2 = 45^\circ$ ODF section [42].	16
Fig. 2-14 Flow paths for the texture analysis and prediction of the porthole die extrusion of a multi-port tube [46].	16

Fig. 2-15 Comparison between the model-predicted (Sim.) and experimentally measured (Exp.) texture along the flowpath C [46]. .....	17
Fig. 2-16 Microstructures of extruded profile's cross-section: (a) Mn / Cr free aluminum alloy and (b) Mn / Cr rich aluminum alloy [57]. .....	18
Fig. 2-17 Metal flow through welding chamber of different heights: (a) very small welding chamber, (b) small welding chamber and (b) large welding chamber [28]. .....	19
Fig. 2-18 Hydrostatic pressure distribution in welding chamber of EN AW-6060 porthole die extrusion: (a) 2 mm, (b) 10mm and (c) 15 mm welding chamber [60]. .....	20
Fig. 2-19 Common bridges used in porthole die extrusion [63]. .....	21
Fig. 2-20 Microstructure of the welding zone of AA6063 samples extruded at different temperatures: (a) 460 °C, (b) 490 °C and (c) 520 °C [69]. .....	22
Fig. 2-21 Surface quality of extruded bars of different ram speeds at 500 °C: (a) 12 mm/s, (b) 22 m/s [72]. .....	23
Fig. 2-22 The cross section of the extruded profile [73]. .....	24
Fig. 2-23 Schematic showing the charge seam formation during porthole die extrusion [80]. ....	25
Fig. 2-24 Formation of back end defect [88]. .....	27
Fig. 4-1 Metallography of the as-cast samples of: (a) 0Mn, (b) 0.5Mn and (c) 0.5Mn0.15Cr [90]. .....	30
Fig. 4-2 SEM image (backscatter mode) of as homogenized (550 °C for 2 hrs) microstructure of different compositions: (a) 0Mn, (b) 0.5Mn and (c) 0.5Mn0.15Cr [90]. .....	31
Fig. 4-3 CAD drawing showing the split porthole die assembly for the welding chamber with the streamlined die. ....	32
Fig. 4-4 Cross-section of the porthole die showing the two bridge geometries used in this research: (a) Die C (streamlined die) and (b) Die E (flat die). .....	33
Fig. 4-5 Cross-section of the porthole die showing the two welding chamber heights used in this research: (a) h = 12.7 mm and (b) h = 25.4 mm. ....	33
Fig. 4-6 Top view of the die mandrel showing the two types of porthole die layout: (a) asymmetric and (b) symmetric. Note the green rectangle is the final die exit and reflective of the final extrudate profile. ....	33
Fig. 4-7 Different methods used to describe the material's motion: (a) Lagrangian, (b) Eulerian and (c) Arbitrary Lagrangian-Eulerian (ALE) [91]. .....	35

Fig. 4-8 Comparison between the true stress – strain curves in the DEFORM database and those calculated using the Sellars-Tegart (Eq. 4-1) model with constants given Table 4-3: (a) 450 °C and (b) 500 °C.....	37
Fig. 4-9 Lagrangian model of porthole die extrusion: (a) the top view of die mandrel and (b) half FEM model. ....	39
Fig. 4-10 ALE simulation model of asymmetric porthole die extrusion .....	40
Fig. 4-11 ALE simulation model of symmetric porthole die extrusion.....	40
Fig. 4-12 Element size in the Lagrangian simulation (three subfigures in the second row are the blow up of the mesh in the red square). ....	41
Fig. 4-13 Element size in ALE simulation (four subfigures in the second row are the blow up of the mesh in the red square). ....	41
Fig. 4-14 Model-predicted strain rate distribution along line 1 mm above the die corner (red line in the inset figure) calculated by different element sizes: (a) Lagrangian and (b) ALE.....	42
Fig. 4-15 Schematic drawing of point tracking based on ALE simulation.....	44
Fig. 4-16 Tensile test samples.....	46
Fig. 5-1 Metallography of extruded profile cross section for samples (T5) taken from six consecutive billets during Trial 1: (a) first billet, (b) second billet, (c) third billet, (d) forth billet, (e) fifth billet and (f) sixth billet. ....	47
Fig. 5-2 Metallography of the seam (T4) extruded at 400 °C using (a) Die C / 12.7 mm / Sym (Trial 16) and (b) Die E / 12.7 mm / Sym (Trial 17). ....	49
Fig. 5-3 Microstructure variation from the seam to the edge (T4): (a) Die C / 25.4 mm / Sym (480 °C) (Trial 14), (b) Die E / 25.4 mm / Sym (480 °C) (Trial 15), (c) Die C / 12.7 mm / Sym (400 °C) (Trial 16) and (d) Die E / 12.7 mm / Sym (400 °C) (Trial 17).....	50
Fig. 5-4 Regions studied by EBSD: Weld (seam) region and quarter width region.....	50
Fig. 5-5 EBSD image (inverse polar figure) and pole figure of weld seam region of samples (T5) extruded by Die C / 12.7 mm / Asym at 5 mm/s and 480 °C (Trial 1). ....	51
Fig. 5-6 EBSD images (inverse polar figure) of quarter width region of strips (T5) extruded by Die C / 12.7 mm / Asym (Trial 1). ....	52
Fig. 5-7 Pole figures of quarter width region of strips (T5) extruded using Die C / 12.7 mm /Asym (Trial 1). ....	52

Fig. 5-8 Measured stress-strain curve showing the repeatability of the tensile tests (T5 treated Trial 1 extruded samples). .....	54
Fig. 5-9 Tensile properties of T5 treated porthole die extruded samples. ....	55
Fig. 5-10 Fracture surface of tensile samples (T5): (a) Die C / 12.7 mm / Asym (Trial 1), (d) seamless (Trial 11) and (e) front view of fractured porthole die extruded specimen. ....	56
Fig. 5-11 Fractography of porthole die extruded samples (T5) in Trial 1. ....	57
Fig. 5-12 The strain distribution along the white line in the gauge length of T5 heat treated samples (Trial 1): (a) elongation of 1%, (b) elongation of 5% and (c) elongation of 7%. ....	58
Fig. 5-13 The removal of PCG layer. ....	59
Fig. 5-14 The strain distribution along the gauge length of the T5 heat treated sample (Trial 1) with PCG removed (a) with PCG layer and (b) without PCG layer when the elongation is 2.5%. ....	60
Fig. 5-15 Metallography at the weld seam of samples (T4) extruded using different die configurations: (a) Die C / 12.7 mm / Sym (Trial 12), (b) Die E / 12.7 mm / Sym (Trial 13), (c) Die C / 25.4 mm / Sym (Trial 14) and (d) Die E / 25.4 mm / Sym (Trial 15). ....	62
Fig. 5-16 The examined area by EBSD close to the seam. ....	62
Fig. 5-17 (a) EBSD image (inverse pole figure) of a region close to the weld seam for the sample (T4) extruded using Die C / 12.7 mm / Sym (Trial 12), (b) associated pole figure for the weld seam, (c) 1.5 mm away from the weld line and (d) 3 mm away from the weld line. ....	64
Fig. 5-18 (a) EBSD image (inverse pole figure) of the region close to the seam in the sample (T4) extruded by Die E / 12.7 mm / Sym (Trial 13), and the pole figure of region at (b) the weld line, (c) 1.5 mm away from the weld line and (d) 3 mm away from the weld line. ....	65
Fig. 5-19 The regions examined by EBSD at the quarter width: quarter width centre (QC) and quarter width edge (QE). ....	66
Fig. 5-20 Inverse pole figure of the symmetric dies extruded samples (T4) at the quarter width location: (a) Die C / 12.7 mm / Sym (Trial 12) – QC, (b) Die E / 12.7 mm / Sym (Trial 12) – QC, (c) Die C / 12.7 mm / Sym (Trial 13) – QE, and (d) Die E / 12.7 mm / Sym (Trial 13) – QE. ....	67
Fig. 5-21 The polar figures of the symmetric dies extruded samples at the quarter width location: (a) Die C / 12.7 mm / Sym (Trial 12) – QC, (b) Die E / 12.7 mm / Sym (Trial 12) – QC, (c) Die C / 12.7 mm / Sym (Trial 13) – QE, and (d) Die E / 12.7 mm / Sym (Trial 13) – QE. ....	68
Fig. 5-22 A schematic of the area characterized via EBSD to determine the welding chamber height's effects on texture at the seam region. ....	68

Fig. 5-23 Measured EBSD images (inverse pole figure) of the weld seam region in profiles (T5) extruded for different extrusion trials: (a) Die C / 12.7 mm / Asym (Trial 1), (b) Die C / 25.4 mm / Asym (Trial 2), (c) Die E / 12.7 mm / Asym (Trial 4) and (d) Die E / 25.4 mm / Asym (Trial 5). ..... 71

Fig. 5-24 (a) EBSD image (inverse pole figure) and (b) the polar figure of the seam region in the sample (T5) extruded by Die C / 12.7 mm / Asym (Trial 1). ..... 72

Fig. 5-25 (a) EBSD image (inverse polar figure) and (b) the polar figure of the seam region in the sample (T5) extruded by Die E / 12.7 mm / Asym (Trial 2). ..... 73

Fig. 5-26 Repeatability of tensile tests of T4 porthole die extruded samples (Trial 12). ..... 74

Fig. 5-27 Measured stress–strain curves of T4 samples extruded using different die geometries at ram speed of 5 mm/s: (a) 12.7 mm welding chamber and (b) 25.4 mm welding chamber height. .... 75

Fig. 5-28 Strain distribution along the white line in the gauge length during tensile test, when (a) elongation is 1% and welding chamber is 12.7 mm, (b) elongation is 1% and welding chamber height is 25.4 mm, (c) elongation is 8% and welding chamber is 12.7 mm, (d) elongation is 8% and welding chamber is 25.4 mm, (e) elongation is 12% and welding chamber is 12.7 mm and (d) elongation is 12% and welding chamber is 25.4 mm. .... 77

Fig. 5-29 Heat treatment’s effect on porthole die extruded samples’ mechanical property: (a) T4 and (b) T6..... 79

Fig. 5-30 Measured strain distribution along the white line of the gauge length for the extruded samples, when (a) the elongation is 1% and T4 heat treated, (b) the elongation is 1% and T6 heat treated, (c) the elongation is 3% and T4 heat treated and (d) the elongation is 3% and T6 heat treated..... 80

Fig. 5-31 Comparison between model-predicted and measured load-stroke behaviour during extrusion using Die C (trial 1) and Die E (Trial 2) as well as a no-bridge die (Trial 11)..... 81

Fig. 5-32 Comparison between the experimental and model-predicted DMZ a slice plane shown in (a): (b) experimental result and (c) model-prediction..... 83

Fig. 5-33 Model-predicted velocity distribution during porthole die extrusions for different bridge geometries and welding chambers: (a) Die C / 12.7 mm / Sym (Trial 12), (b) Die E / 12.7 mm / Sym (Trial 13), (c) Die C / 25.4 mm / Sym (Trial 14) and (d) Die E / 25.4 mm / Sym (Trial 15). .... 84

Fig. 5-34 Model-predicted flowlines in porthole die extrusions: (a) Die C / 25.4 mm / Sym (Trial 14) and (b) Die E / 25.4 mm / Sym (Trial 15). .....	85
Fig. 5-35 Temperature distribution at the die exit. ....	86
Fig. 5-36 The two selected points for thermal mechanical history calculation. ....	86
Fig. 5-37 Model-predicted flow paths in different porthole die extrusion dies of different bridges and welding chambers: (a) Die C / 12.7 mm / Sym (Trial 12), (b) Die E / 12.7 mm / Sym (Trial 13), (c) Die C / 25.4 mm / Sym (Trial 14) and (d) Die E / 25.4 mm / Sym (Trial 15). ....	87
Fig. 5-38 Model-predicted temperature history of tracked points during porthole die extrusion: (a) centre point and (b) quarter width point. ....	89
Fig. 5-39 Strain distribution through the cross section of the extruded profile: (a) Die C / 12.7 mm / Sym (Trial 12), (b) Die E / 12.7 mm / Sym (Trial 13), (c) Die C / 25.4 mm / Sym (Trial 14) and (d) Die E / 25.4 mm / Sym (Trial 15). ....	89
Fig. 5-40 Model-predicted strain history at the centre of the weld seam for different dies and different weld chamber heights.....	90
Fig. 5-41 (a) EBSD image (inverse polar figure) of Die C / 12.7 mm / Sym, (b) model-calculated strain of Die C / 12.7 mm / Sym, (c) EBSD image (inverse polar figure) of Die E / 12.7 mm / Sym and (d) model-calculated strain of Die E / 12.7 mm / Sym. ....	91
Fig. 5-42 Breakthrough load at different ram speeds: (a) Die C / 12.7 mm / Sym (Trial 12), (b) Die E / 12.7 mm / Sym (Trial 13), (c) Die C / 25.4 mm / Sym (Trial 14) and (d) Die E / 25.4 mm / Sym (Trial 15). ....	93
Fig. 5-43 Outer appearance of the extruded samples at different ram speeds through different die configurations: (a) Die C / 12.7 mm / Sym (Trial 12), (b) Die E / 12.7 mm / Sym (Trial 13), (c) Die C / 25.4 mm / Sym (Trial 14) and (d) Die E / 25.4 mm / Sym (Trial 15). ....	95
Fig. 5-44 (a) The front and (b) back part of the extruded profile by Die C / 25.4 mm / Sym (Trial 14) at 7 mm/s. ....	95
Fig. 5-45 The surface quality at the seam: (a) Die C / 12.7 mm / Sym (Trial 12), (b) Die E / 12.7 mm / Sym (Trial 13), (c) Die C / 25.4 mm / Sym (Trial 14) and (d) Die E / 25.4 mm / Sym (Trial 15). ....	97
Fig. 5-46 Optical metallography of samples (T4) extruded using Die C / 25.4 mm / Sym (Trial 14) at different ram speeds: (a) 4 mm/s, (b) 5 mm/s, (c) 6 mm/s, (e) 7 mm/s and (e) 8 mm/s. ....	98
Fig. 5-47 The relationship between the PCG thickness and ram speed.....	99

Fig. 5-48 abnormal grain growth in high ram speed extruded samples (T4): (a) Die C / 12.7 mm at 8 mm/s (Trial 12), (b) Die E / 25.4 mm at 7 mm/s (Trial 15) and (c) Die E / 12.7 mm at 8 mm/s (Trial 13). .....	100
Fig. 5-49 EBSD iamge (inverse polar figure) of welding region of samples (T5) extruded by Die C / 12.7 mm at ramspeed of (a) 5 mm/s (Trial 1) and (b) 7 mm/s (Trial 3). .....	101
Fig. 5-50 Stress – strain curve of samples extruded at different ram speed (T4): (a) Die C / 12.7 mm / Sym (Trial 12), (b) Die E / 12.7 mm / Sym (Trial 13), (c) Die C / 25.4 mm / Sym (Trial 14) and (d) Die E / 25.4 mm / Sym (Trial 15).....	102
Fig. 5-51 The temperature distribution throughout the cross section of the profile extruded by Die C / 25.4 mm (Trial 14) at the die exit: (a) 4 mm/s, (b) 5 mm/s and (c) 7 mm/s. ....	103
Fig. 5-52 Optical metallography of welding region in the extrudates of different compositions (T4): (a) 0Mn (Trial 9), (b) 0.5Mn (Trial 7) and (c) 0.5Mn0.15Cr (Trial 2). ....	104
Fig. 5-53 Optical metallography of the 0Mn profiles' cross section extruded by different die configurations (T4): (a) Die C (Trial 8) and (b) Die E (trail 9). ....	104
Fig. 5-54 Optical metallography of the profiles' cross section of different compositions extruded using no bridge die (T4): (a) 0Mn (Trial 10) and (b) 0.5Mn0.15Cr (Trial 11).....	105
Fig. 5-55 Measured EBSD image (inverse pole figure) of 0Mn sample extruded by Die C / 12.7 mm (Trial 8, T4) at (a) centre and (b) quarter width. ....	106
Fig. 5-56 Polar figure of 0Mn sample extruded by Die C /12.7 mm (Trial 8, T4) at (a) centre and (b) quarter width. ....	107
Fig. 5-57 EBSD image (inverse pole figure) and polar figures at the seam of the 0.5Mn sample (Trial 6, T4).....	108
Fig. 5-58 EBSD image (inverse pole figure) and polar figures at the seam of the 0.5Mn sample after solution treatment: (a) the centre region and (b) the quarter width. ....	109
Fig. 5-59 Measured stress–strain curve of 0Mn sample in the T6 condition.....	110
Fig. 5-60 Fracture position of T6 treated 0Mn samples extruded by different dies: (a) Die C / 12.7 mm (Trial 8), (b) Die E / 12.7 mm (Trial 9) and (c) no bridge (Trial 10). ....	111
Fig. 5-61 Strain distribution along the white line during the tensile test of the 0Mn samples when the elongation is (T6): (a) 0.025 and (b) 0.05. ....	112

Fig. 5-62 VPSC model-predicted true stress–true strain curves in the TD direction for the weld seam (centre) and matrix (quarter width) textures for material extruded using Die C / 12.7 mm/ Asym (Trial 1).....	113
Fig. 5-63 Schematic showing how the simulation of the tensile test for the porthole die extruded sample. ....	115
Fig. 5-64 Comparison between the measured and simulated strain distribution in the tensile specimen extruded using Die C / 12.7 mm / Asym (Trial 1) when the elongation is 2.5%: (a) model-predicted strain distribution map and (b) model-predicted and measured strain distribution profile along the white line.....	115
Fig. 5-65 VPSC simulation results of the center and quarter texture in 0Mn samples.....	116
Fig. 5-66 Comparison between the measured and simulated strain distribution in the tensile specimen extruded using Die C / 12.7 mm / Asym (Trial 8) when the elongation is 5%: (a) model-predicted strain distribution map and (b) (b) model-predicted and measured strain distribution profile along the black line. ....	116
Fig. 5-67 Measured stress – strain curves of 0.5Mn0.15Cr and 0.5Mn samples in T4 state.....	117
Fig. 5-68 Stress – strain curve of 0.5Mn samples extruded by Die C / 12.7 mm (Trial 6): (a) T4 and (b) T6.....	118
Fig. 5-69 Fracture location of 0.5Mn samples extruded by Die C / 12.7 mm (Trial 6): (a) T4 and (b) T6. ....	118
Fig. 6-1 Bridges of varying angles.....	119
Fig. 6-2 Model-predicted velocity distribution in the welding chamber for different bridge angles: (a) 15°, (b) 30°, (c) 45°, (d) 60°, (e) 75° and (f) 90°. ....	120
Fig. 6-3 Bridge angle’s influence on temperature distribution at the die corner. ....	121
Fig. 6-4 Bridge angle’s effects on the strain distribution: (a) die 15°, (b) die 30°, (c) die 45°, (d) die 60°. (e) die 75° and (f) die 90°.....	122
Fig. 6-5 Strain distribution from the seam edge in the middle thickness (the red line) of the profiles extruded using bridges of different angles.....	122
Fig. 6-6 Bridge geometries proposed to examine the upper part of bridge’s effects on porthole die extrusion.....	123
Fig. 6-7 Model-predicted temperature distribution along the mid-width of the strip for a range of die geometries which include changes to the upper part of the die. ....	124

Fig. 6-8 Strain distribution from the seam edge in the middle thickness (the red line) of the profiles extruded using bridges of different angles.....	125
Fig. 6-9 Model-predicted strain distribution from the weld seam in the middle thickness (the red line) of the profiles extruded using bridges with different upper geometries.....	125
Fig. 6-10 Schematic showing the different geometries used to examine the bridge geometry's effects on the charge seam formation in porthole die extrusion: (a) bridge 90° (Die E), (b) bridge 60°, (c) bridge 30° (Die C) and (d) bridge 15° .....	126
Fig. 6-11 Schematic showing the four different welding chamber heights used to examine the welding chamber height's effects on the charge seam formation in porthole die extrusion.....	127
Fig. 6-12 Mesh generation scheme for the simulation of charge seam. ....	128
Fig. 6-13 X-section view of the extrusion process showing the model-predicted flow behaviour of new material (red) into the die cavity: (a) t = 0 s, (b) t = 1.5 s, (c) t = 1.8 s and (d) t = 32 s. ....	129
Fig. 6-14 Front view of the extruded strip showing model predictions of the charge seam evolution for two different dies with different bridge angles: (a) 15° / 12.7 mm and (b) 90° / 12.7 mm. ..	130
Fig. 6-15 Front view of the extruded strip showing model predictions of the charge seam evolution for different welding chamber heights: (a) 90° / 6.35 mm and (b) 90° / 38.1 mm.....	131
Fig. 6-16 Model-prediction of the new material fraction in the profile's cross section versus extrude length.....	132
Fig. 6-17 Mesh generation scheme for the billet skin tracking.....	133
Fig. 6-18 X-sectional view of the extrusion process showing the model-predicted flow behaviour of the billet skin in red: (a) t = 0 s, (b) t = 16.1 s, (c) t = 27.5 s and (d) t = 28.3 s. ....	134
Fig. 6-19 Model predictions of the length of profile containing a back end defects as a function of the bridge angle.....	135
Fig. 6-20 Model predictions of the length of profile containing a back end defect as a function of the welding chamber height.....	136

## List of Tables

Table 4-1 Composition of alloys used in the extrusion trials (wt.%) .....	29
Table 4-2 Extrusion parameters used during extrusion trials .....	34
Table 4-3 Material constants used in the Sellars-Tegart constitutive equation for AA6082.....	37
Table 4-4 Simulation parameters and boundary conditions used in the DEFORM model. ....	39
Table 5-1 Identified area fraction of texture components at the quarter width region of samples extruded using Die C / 12.7 mm / Asym (Trial 1). .....	52
Table 5-2 Tensile properties of each tensile specimen taken from T5 treated Trial 1 extruded profile. ....	54
Table 5-3 Area reduction of tensile specimens.....	56
Table 5-4 Tensile properties of porthole die extruded samples using different die configurations. ....	76
Table 5-5 Measured and model predicted load at the breakthrough.....	82
Table 5-6 Welding quality prediction of porthole die extrusions of different bridges and welding chambers. ....	92
Table 5-7 Summary of the surface quality at different ram speeds. ....	97

## Chapter 1 Introduction

As we think of ways to combat climate change and green house gas emissions, lightweight design in the transportation industry is becoming more important. It is estimated that a 10% reduction in a vehicle's weight can result in 5 to 8% less energy consumption [1]. By 2025, North American automakers must deliver vehicles with fleet fuel economy of 54.5 mpg to avoid government penalties. This target was established and adopted in 2012 to curtail US energy consumption and limit carbon dioxide and other greenhouse gases [2]. Automakers have challenged their engineering teams to rethink vehicle architecture and pursue new technologies to achieve this goal. Among other strategies, aluminum extrusion is a growing part of the lightweighting solution automakers are adopting to meet this goal [3, 4].

The Ford F-Series has been an icon in the pickup truck market for more than 60 years. In 2015, Ford introduced a model of the F150 that was up to 315 kg lighter than its predecessor model, increasing available payload without sacrificing strength due to the significant use of aluminum in the form of both sheet and extruded components [5]. Below the surface of the F150 is a wide range of extruded aluminum components. In fact, the Aluminum Extruders Council (AEC) estimates over 18 kg of extrusion per truck, much of it in body structure applications [6].

Extrusion is a common technology in modern industry to produce long sections of constant cross-section such as rods, tubes, and more complicated profiles. During the extrusion process, the billet is pressed through a die orifice to form a profile with a smaller cross section than the original billet. The coarse microstructure of the cast and homogenized billet is refined and small casting pores are healed after extrusion. Extrusion is an effective and low cost way to get a semi-finished component with good mechanical properties [7, 8].

Among the different aluminum alloys used for extrusions, 6xxx aluminum alloys (with Mg and Si as the main alloy additions) are some of the most common. These alloys are heat treatable alloys and have both excellent formability and relatively high strength [9-11]. 6xxx aluminum alloys can be extruded at high speed without severe deterioration of the surface quality, and also can be extruded into profiles of complex cross section due to their relative good weldability at high temperature [12]. Fig. 1-1 shows some of the typical AA6xxx alloys used in automotive applications.

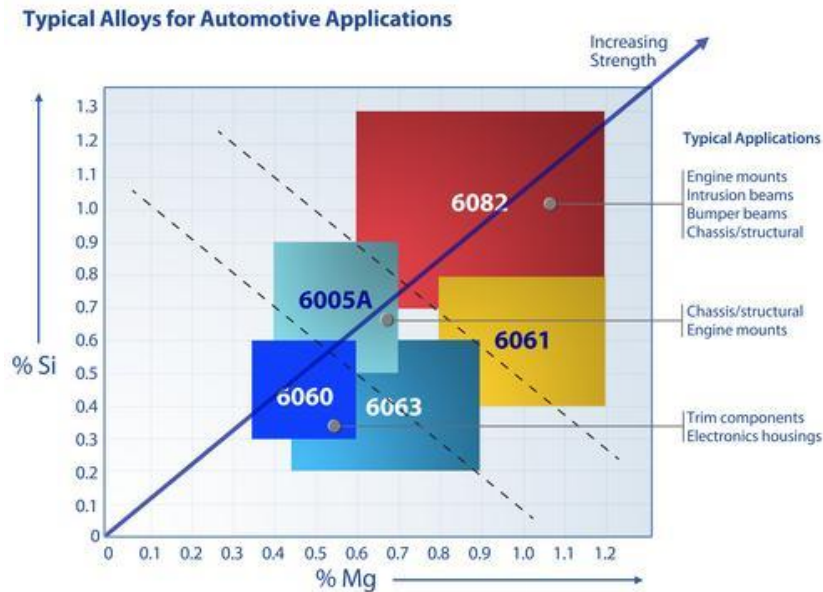


Fig. 1-1 Typical 6xxx alloys for automotive applications [6].

As shown in Fig. 1-2, there are many components in the automobile that can be made by extrusion and most of them are made from 6xxx aluminum alloys. Usually hollow profiles are made by conventional conical extrusion or porthole die extrusion. Conventional conical extrusion is only able to fabricate simple shaped hollow profiles, but porthole die extrusion is much more versatile and theoretically able to produce any complex hollow profiles. Actually, 90% of aluminum hollow profiles are produced by the latter technology [13].

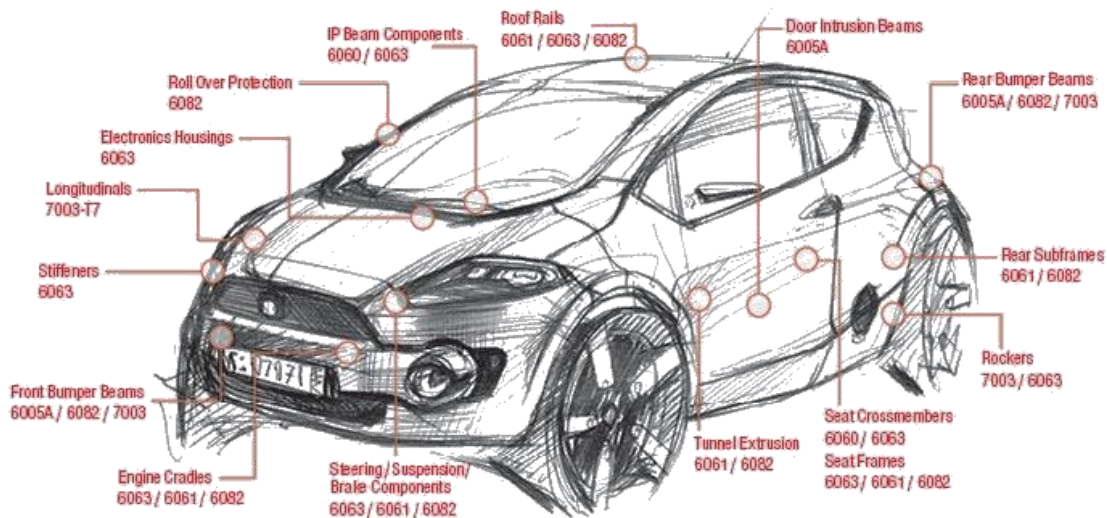


Fig. 1-2 Aluminum extruded components used in light vehicles [14]

However, porthole die extrusion always leaves one or more welding seams in the extruded profile. The welding seams in the extruded profiles are usually the crack initiation sites and can severely decrease the component strength and ductility. In most cases, profiles made using porthole die extrusion have lower mechanical properties compared to material extruded without any welds. Therefore, increasing the welding quality by optimizing die design and extrusion parameters is an important research focus for extrusion engineers. Many researchers have pointed out the extrusion die geometry can have a significant effect on weld quality in the final extruded product. However, how the die geometry affects the texture and microstructure evolution during extrusion is still not well understood from a scientific perspective.

This project is a collaborative research and development project between the University of British Columbia, Rio Tinto Aluminum and Ford, to understand the weld seam formation during porthole die extrusion of AA6xxx aluminum alloys. Within this overall project, this research focusses on the effect of die design, extrusion parameters and alloy compositions on the formation of the microstructure, and resulting mechanical properties of the weld or seam line after extrusion. The research method used in this project is a combination of experiments and state of the art modelling techniques. The experimental work starts with industrially produced as-cast alloys and then encompasses the following aspects of the process: extrusion, quenching and the subsequent heat treatment which is used to increase strength. The modelling work in this project is conducted to quantify the unmeasurable temporal and spatial state variables such as temperature, strain and strain rate experienced by the material during the experiments. This combination of experiments and modelling will lead to a better scientific understanding of the formation of different microstructures in samples extruded using different die configurations. This research will also assist producers and users of extruded aluminum alloys, providing them with a tool which can be used to optimize die configurations and processing routes for aluminum alloys being extruded.

## **Chapter 2 Literature review**

### **2.1 6xxx aluminum alloys**

Mg and Si are the two major alloying elements in 6xxx alloys, and the concentrations of Mg and Si are usually within the range of 0.2 to 1.5 wt.%. 6xxx alloys are medium strength aluminum alloys of good extrudability. It is estimated that 60% of extruded products are made by 6xxx alloys [15].

6xxx aluminum alloys are heat treatable alloys, and their mechanical properties can be modified by deformation and subsequent heat treatment [9-11]. The pronounced hardening phenomena of 6xxx aluminum alloys during age process is related to the precipitation at the aging temperature. Needle shaped  $\beta''$  phase is considered to be the major hardening phase in 6xxx aluminum alloys at the peak aging. However, the coarsening of  $\beta''$  phases results into the hardness decrease during over aging [10]. Through deliberate design of heat treat after processing, 6xxx aluminum alloys of variable mechanical properties can be obtained [16].

### **2.2 Porthole die extrusion**

Porthole die extrusion is used to produce aluminum hollow complex profiles, and is becoming more popular due to its relatively low cost, high efficiency and that there is no need for subsequent processing. As shown in Fig. 2-1, the main body structure of the F-150 pick-up is made by aluminum, and some components of complex cross section are manufactured using porthole die extrusion. Traditional methods for manufacturing hollow profiles includes welding procedures after forming, while the porthole die extrusion can produce hollow profiles with a near net shape [17].

Porthole die extrusion's strong ability to produce complex profile compared by normal extrusion lies in its unique die configurations. As shown in Fig. 2-2, there exists two dies instead of one in porthole die extrusion, namely a die mandrel and die cup. The die mandrel has complex structures such as portholes, bridges and mandrels. The bridges are used to keep the mandrel stable rather than floating in the extrusion. While the die cup's structure is relatively simple with the die orifice in the middle. The welding chamber is the cavity between the die mandrel and die cup and is an important part in porthole extrusion die configuration [18].

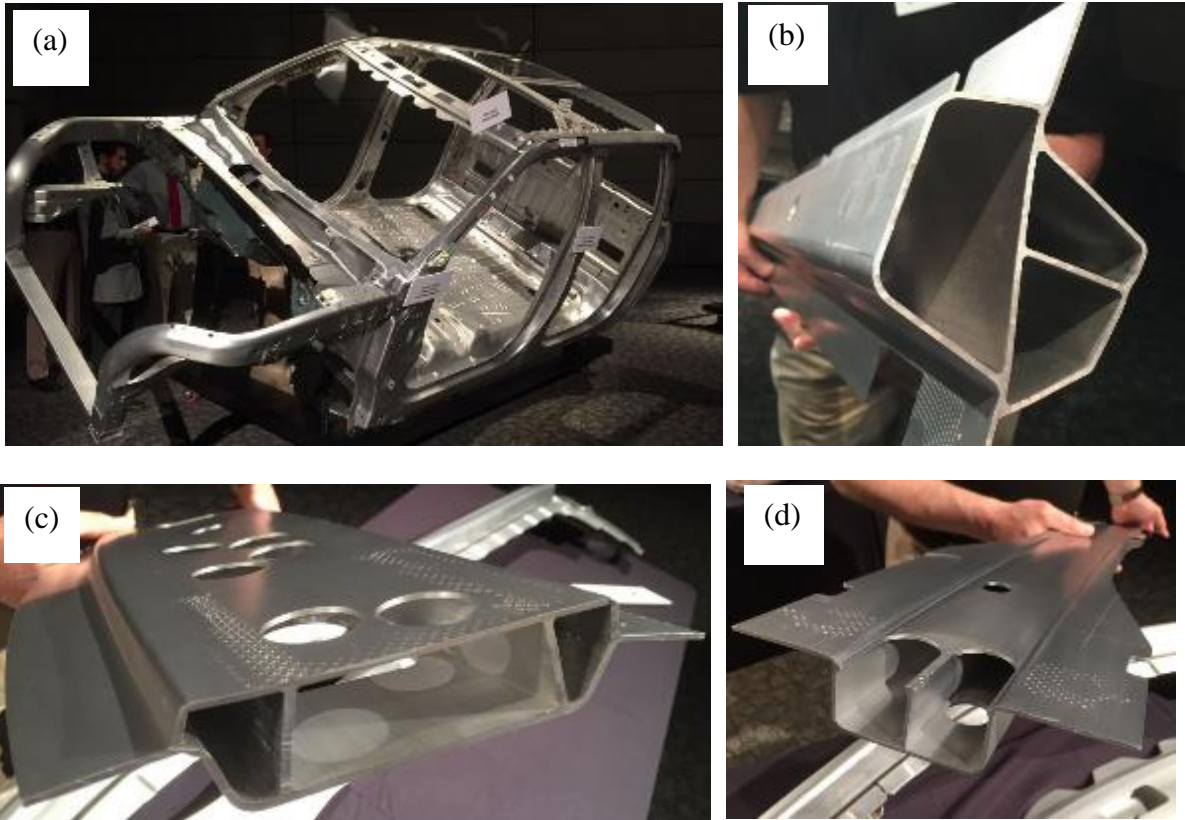


Fig. 2-1 Aluminum components in F-150 pick-ups: (a) main body structure, (b) internal webbing, (c) roof head and (d) roof bow [17].

At the start of porthole die extrusion, the billet is pressed through the die mandrel, and the billet is divided into several streams around the bridges. Then the separated metal streams gradually fill the welding chamber and subsequently contact each other to form the welding seam as shown in Fig. 2-3. The welding seam which forms in the welding chamber is usually referred to as a longitudinal seam and is usually the weakest part of the profile. Finally, the material is squeezed into the gap between the die bearing and mandrel to get the final desired profile shape [19].

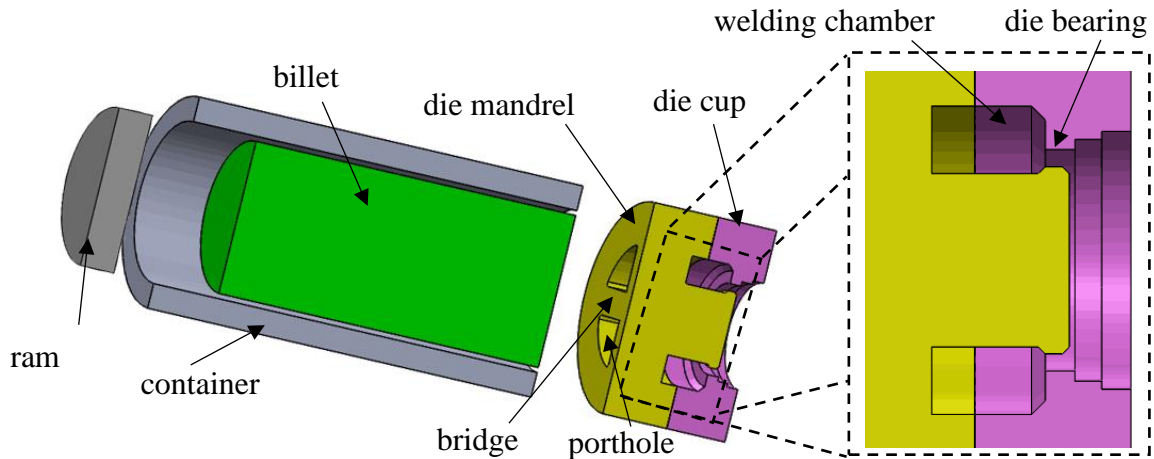


Fig. 2-2 Porthole die configurations (1/2 section) [18].

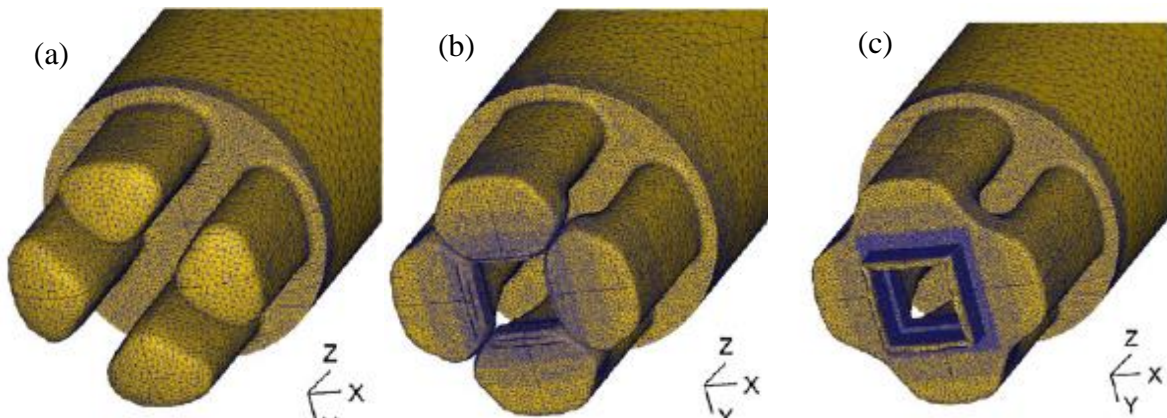


Fig. 2-3 Porthole die extrusion stages: (a) dividing stage, (b) welding chamber fulfilling stage and (c) forming stage [19].

## 2.3 Longitudinal seam in porthole die extrusion

### 2.3.1 Mechanical properties of longitudinal seam

The formation of a longitudinal weld seam is a phenomenon in porthole die extrusion, which is generated from rejoining of the different metal streams. The longitudinal seam can be the initial site for crack formation [20, 21]. As shown in Fig. 2-4, in a burst test of a multi-cavity aluminum profile, it fractured at the welding seam due to its relatively lower strength [22].

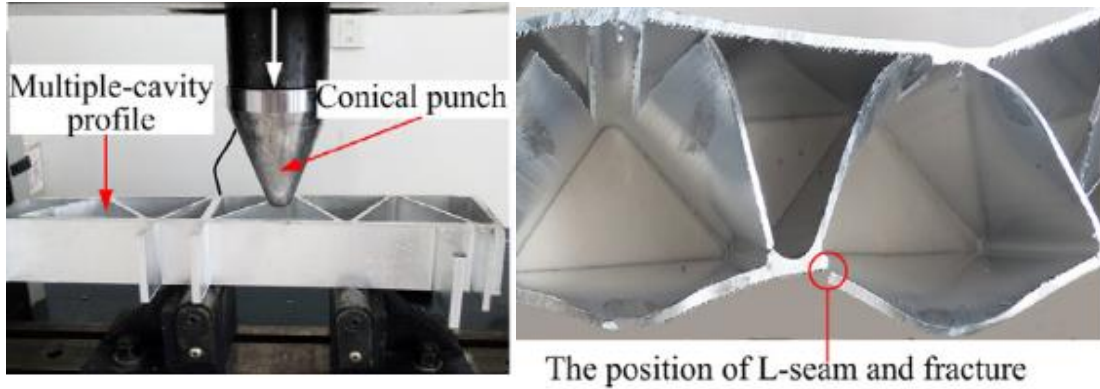


Fig. 2-4 Burst test for multi-cavity aluminum extrusion profile: (a) experimental methodology, (b) the final result [22].

As shown in Fig. 2-5, in most cases, the profile made using porthole die extrusion has lower mechanical properties compared to material extruded without any welds. However, through careful die design and extrusion parameter optimization, the porthole die extruded profile's mechanical properties could be comparable to a seamless profile [23].

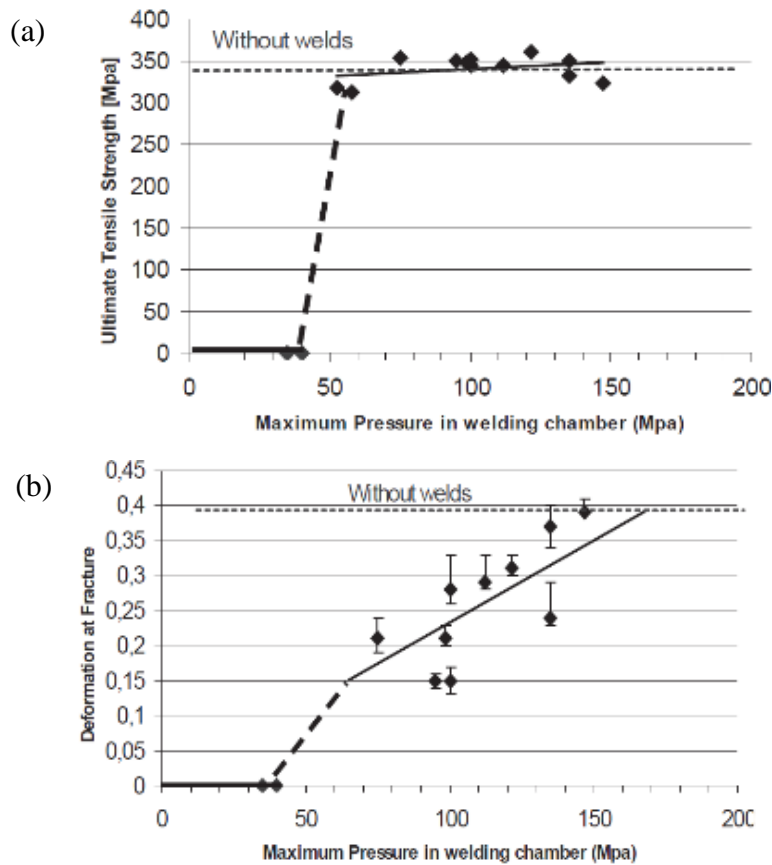


Fig. 2-5 Tensile strength and elongation of porthole samples from different die dimensions: (a) tensile strength and (b) elongation [23].

### 2.3.2 Longitudinal weld formation

Fig. 2-6 shows the longitudinal weld seam formation proposed by Yu et al. based on their research on porthole die extrusion [22]. At the initial contact, the surface of the separated metal streams generated by the bridges is not even and as the two streams come together filled with microvoids and asperities. After these two streams meet, they are under significant pressure and the microvoids are gradually flattened and can even close such that there is intimate contact between the two originally separated streams of metal. Along this interface, when the distance ( $d$ ) between the contact atoms is lower than 10 atoms, a very strong inter-atomic force can be generated between the contact atoms and a sound weld joint can form [24]. After the intimate contact is initiated, the diffusion of atoms through the interface can further strengthen the bonding and even promote grain growth across the interface.

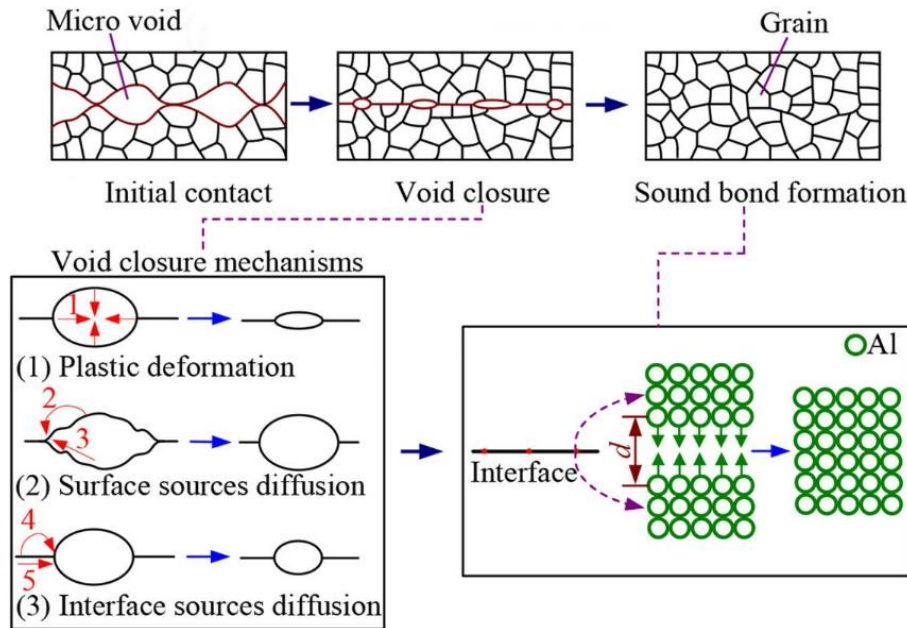


Fig. 2-6 Mechanism of longitudinal seam formation [22].

TEM observation on the longitudinal weld seam conducted by Yu et al. verified their hypothesis about the mechanism of longitudinal seam formation [25], as shown in Fig. 2-7. In their research, two types of bonding structures were identified: Type I where no grains cross the interface and type II where gain can grow across the interface. On type I bonding surface, there

exists discontinuous micro voids whose length can be as long as 2  $\mu\text{m}$  (Fig. 2-7a). Closer observation of the selected region on the type I bonding surface revealed different grain orientations on the two side of the interface (Fig. 2-7c). On the other hand, the microvoids on type II bonding face are much smaller and the maximum length of the observed microvoids is only about 50 nm (Fig. 2-7b). What's more, the HRTEM image of the type II bonding surface does not show a noticeable grain orientation differences across the bonding surface (Fig. 2-7d), which indicates grain growth across the bonding surface is prominent. In their research, type I bonding surface was generated by a short welding chamber and short contact time. However, type II bonding surface was generated using a deep welding chamber and when longer contact time was experienced. As a result, it is reasonable to assume that the microvoids can gradually shrink under pressure and grains can grow across the interface due to diffusion when the contact time is increased. This experimental result agrees with the aforementioned mechanism of longitudinal weld seam formation and also provides an insight into the bonding structure across the longitudinal weld seam.

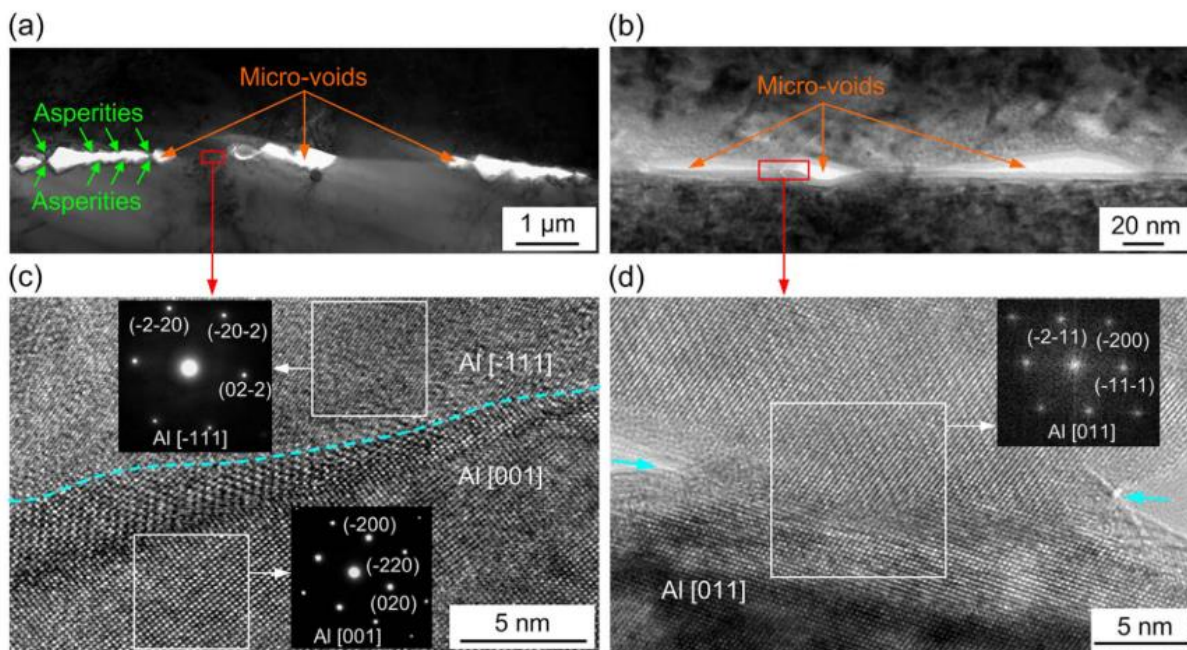


Fig. 2-7 Two types of bonding surface under TEM observation: (a) Bridge field TEM image of type I bonding surface, (b) Bridge field TEM image of type II bonding surface, (c) HRTEM image of the selected area marked in (a), (d) HRTEM image of the selected area marked in (b) [25].

### 2.3.3 Weld quality prediction

In order to predict welding quality of the longitudinal seam without wasting too much time and effort on trial and error experiments, several welding quality criteria have been proposed based on state variables calculated by commercial finite element software packages [22, 23, 26, 27].

The first extrusion weld quality prediction criteria, pressure criteria, was proposed by Akeret [28] in the 1970s. Akeret believed that only when the welding pressure exceeds a critical value, as shown in Eq. 2-1, that a strong weld bond could be obtained. As shown in Fig. 2-5, the deformation fracture of porthole die extruded specimens is comparable to specimens without seam, when the welding pressure exceeds 140 MPa.

$$P > P_{cr} \quad 2-1$$

where  $P$  is the welding pressure (MPa), and  $P_{cr}$  is the critical value (MPa) to get good welding quality.

Plata and Piwnik [26] proposed pressure time criteria based on the assumption that a strong bond is formed once the deformation energy is above a critical value, as shown in Eq. 2-2.

$$Q = \int_0^t \frac{P}{\sigma} dt > W \quad 2-2$$

where  $P$  is the welding pressure (MPa),  $\sigma$  is the effective stress (MPa),  $t$  is the contact time (s) and  $W$  is the critical value (s) to get a permanent bonding.

The problem with pressure time criteria is that when the material flows through the dead zone, the material is stuck in the dead zone for a long period of time and Eq. 2-2 gives an unreasonably high value. In order to solve this flaw in the pressure time criteria, Donati and Tomesani [23, 29] suggested that the velocity should also be taken into consideration and Eq. 2-2 modified as shown below:

$$K = \int_0^t \frac{P}{\sigma} dt \cdot v = \int_0^l \frac{P}{\sigma} dl > K \quad 2-3$$

where  $P$  is the welding pressure (MPa),  $\sigma$  is the effective stress (MPa),  $t$  is the time (s)  $v$  is the velocity (mm/s) and  $K$  is the critical value (mm) to get a strong bond.

Yu et al proposed and testified a so-called J-criterion in recent years, as shown in Eq. 2-5 [22, 30]. Different from the previous three criteria, J-criterion does not only take the stress into consideration, but also strain and temperature. The solid bonding formation mechanism involves the deformation of the microvoids on the bonding surface and also the diffusion of atoms through the interface. In order to flatten and closure the microvoids on the seam, a sufficient strain is necessary. What's more, the temperature and contact time determine the atom diffusion behaviour through the interface, which should also be included into the criterion.

$$J = \int_0^t k_0 \frac{\sigma_m}{\bar{\sigma}} \dot{\epsilon} \exp\left(\frac{RT}{Q_D}\right) dt \quad 2-4$$

where  $k_0$  is the coefficient related to the material and surface condition for bonding (assumed to be 1 in this thesis),  $\sigma_m$  is the mean stress normal stress (MPa),  $\bar{\sigma}$  is the effective stress (MPa),  $\dot{\epsilon}$  is the effective strain rate ( $s^{-1}$ ),  $R$  is the universal gas constant ( $8.314 \text{ J}\cdot\text{mol}^{-1}\cdot\text{K}^{-1}$ ),  $T$  is the absolute temperature (K),  $Q_d$  is the diffusion activation energy (which is  $1.42 \times 10^5 \text{ J}\cdot\text{mol}^{-1}$  from 450 to 650 °C [30]),  $t$  is the time (s).

## 2.4 Microstructure evolution during porthole die extrusion

### 2.4.1 Recrystallization in extrusion

The most obvious microstructure feature in extruded aluminum samples is the elongated fibrous grains aligned with the material flow direction, which form under an intensive shear stress when squeezed through the die orifice. Besides fibrous microstructure, recrystallized grains close to the surface (Peripheral Coarse Grains or PCG) are also very common in aluminum extruded samples [31, 32].

Dynamic recrystallization (DRX) is usually classified into two categories in aluminum extrusion: continuous dynamic recrystallization (CDRX) and geometric dynamic recrystallization (GDRX) [33]. In aluminum alloys, dislocations accumulate along the low angle boundaries ( $\theta < 15^\circ$ ) of subgrains during extrusion, which can transform from low angle boundaries to high angle boundaries ( $\theta > 15^\circ$ ) during further deformation. In this case, subgrains (low angle boundary) can transform into new grains (high angle boundary) progressively within the original deformed grain. This process is known as CDRX [34].

When the deformation is very severe in extrusion, the elongated grains are severely serrated and grain boundaries get very close to each other, as shown in Fig. 2-8b. On the other hand, subgrains keep their equiaxed configuration and the subgrain size is almost unchanged. When the grain thickness is further reduced to the size of the subgrain, the grain boundaries contact each other and one elongated grain is pinched off into several grains of similar orientation, known as GDRX [35, 36].

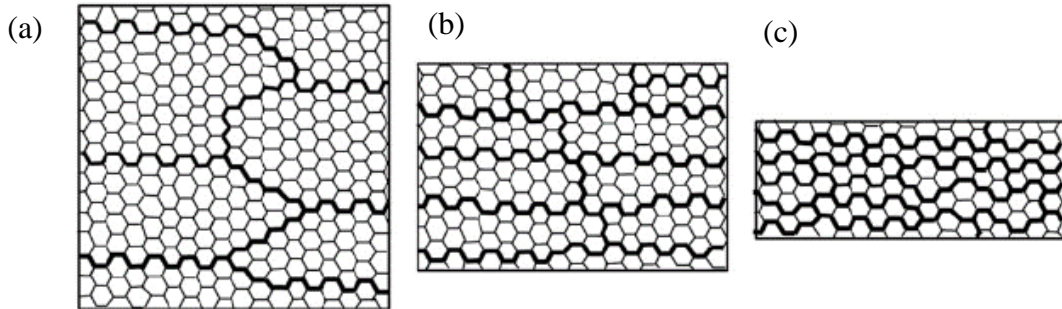


Fig. 2-8 The mechanism of GDRX in extrusion (thick lines stand for grain boundaries and the hexagons are subgrains): (a) grains are elongated in the extrusion direction, (b) grains are serrated during the further deformation and (c) grains are finally pinched off [37].

The surface of extrudates always experiences the highest temperatures, strain and strain rate. Sometimes the high stored energy on the surface causes abnormal grain growth, and make the peripheral grains (along the surface) very coarse compared to the other grains, as shown in Fig. 2-9b. The PCG usually are the initiation site of cracks and reduce the strength, which should always be avoided [38].

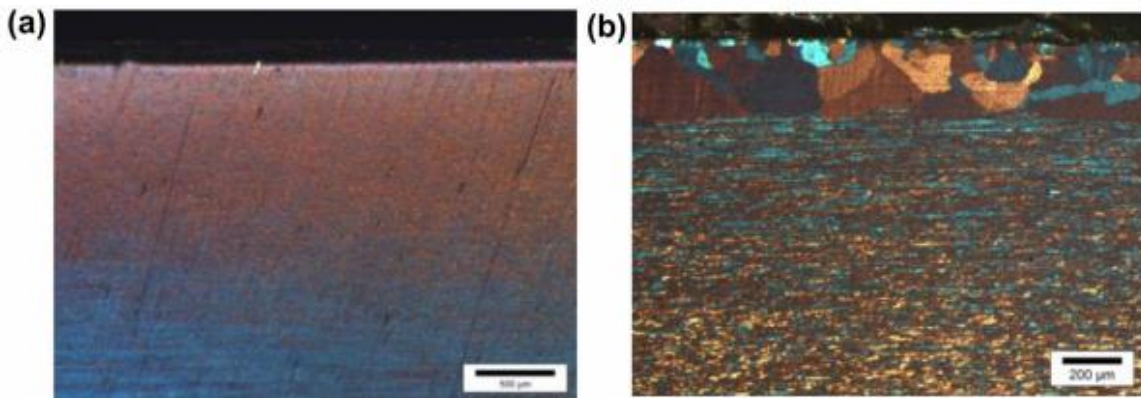


Fig. 2-9 The micrographs of Al-4.5Zn-1Mg rods extruded at different temperature: (a) 460 °C (no PCGs) and (b) 500°C [39].

### 2.4.2 Microstructure

The porthole die extruded samples do not only have the common as-extruded microstructure features as described above, but have a unique microstructure along and close to the longitudinal weld seam. As shown in Fig. 2-10, the PCG layer becomes thicker when it gets closer to the longitudinal weld seam, and piles up like a cone in the welding zone. The weld seam experiences very severe deformation when the separated metal streams are squeezed back together in the welding chamber, and high stored energy encourages growth of the PCG layer into the welding zone [21, 40].

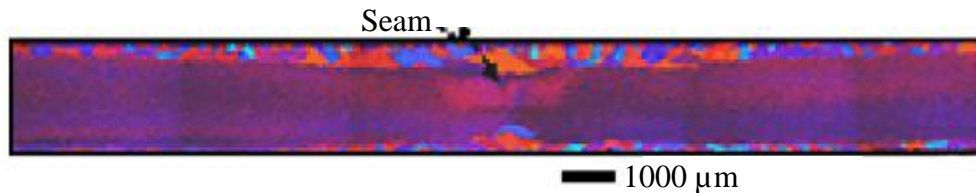


Fig. 2-10 Microstructure of porthole die extruded AA6082 samples [40].

Another interesting aspect during porthole die extrusion is the unique grain morphology evolution. Yu et al. [41] studied the microstructure evolution during the porthole die extrusion of AA6063, and their results showed the grains were still equiaxed when the material just entered the welding chamber. Then, the grains along the weld seam deformed into fibrous grains and the ratio between the grains' length and thickness continued to increase under the effect of high shear, as shown in Fig. 2-11a. While just before the breakthrough, the deformation was so severe that the serrated grains along the welding seam were pinched off and broke into several small equiaxed grains (Fig. 2-11c).

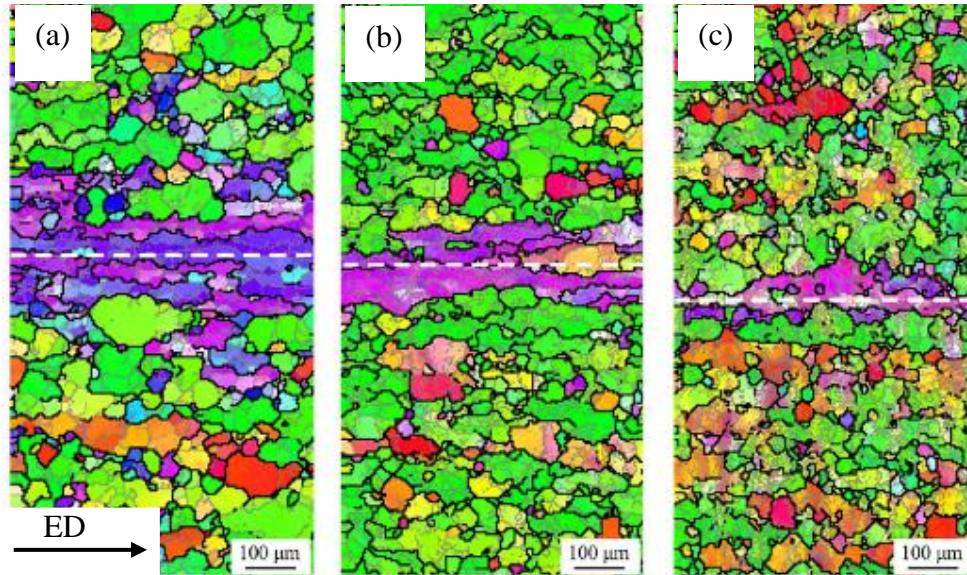


Fig. 2-11 Microstructure evolution from welding chamber to extruded profile: (a) welding chamber, (b) bearing length and (c) extruded profile [41]. (White dash line indicates the seam.)

### 2.4.3 Texture evolution

In porthole die extrusion, the existence of the longitudinal weld seam makes the texture formation more complex. Fan et al. [42] carefully examined the texture evolution during porthole die extrusion of AA1100. As shown in Fig. 2-12b and Fig. 2-13 (used to index texture type), fiber texture of the A component first formed when the metal streams flowed along the mandrel. Then, shear texture consisting of  $A^*_1$  and  $A^*_2$  components also appeared as well as A component, as shown in Fig. 2-12c. However, Fig. 2-12d indicates that the shear texture began to disappear, when the material just entered the welding chamber. In the welding chamber, Cube and brass textures appeared, as shown in Fig. 2-12e. Finally, the recrystallization texture as cube and deformation texture as brass remained along the welding seam after die exit. Yu et al. [41] showed similar results after they studied AA6063 porthole die extrusion. After the formation of shear texture along the bridge surface, strong goss and copper components appeared in the welding chamber. Finally, due to CDRX and GDRX of the welding seam microstructure, a cube texture gradually replaced goss and copper texture.

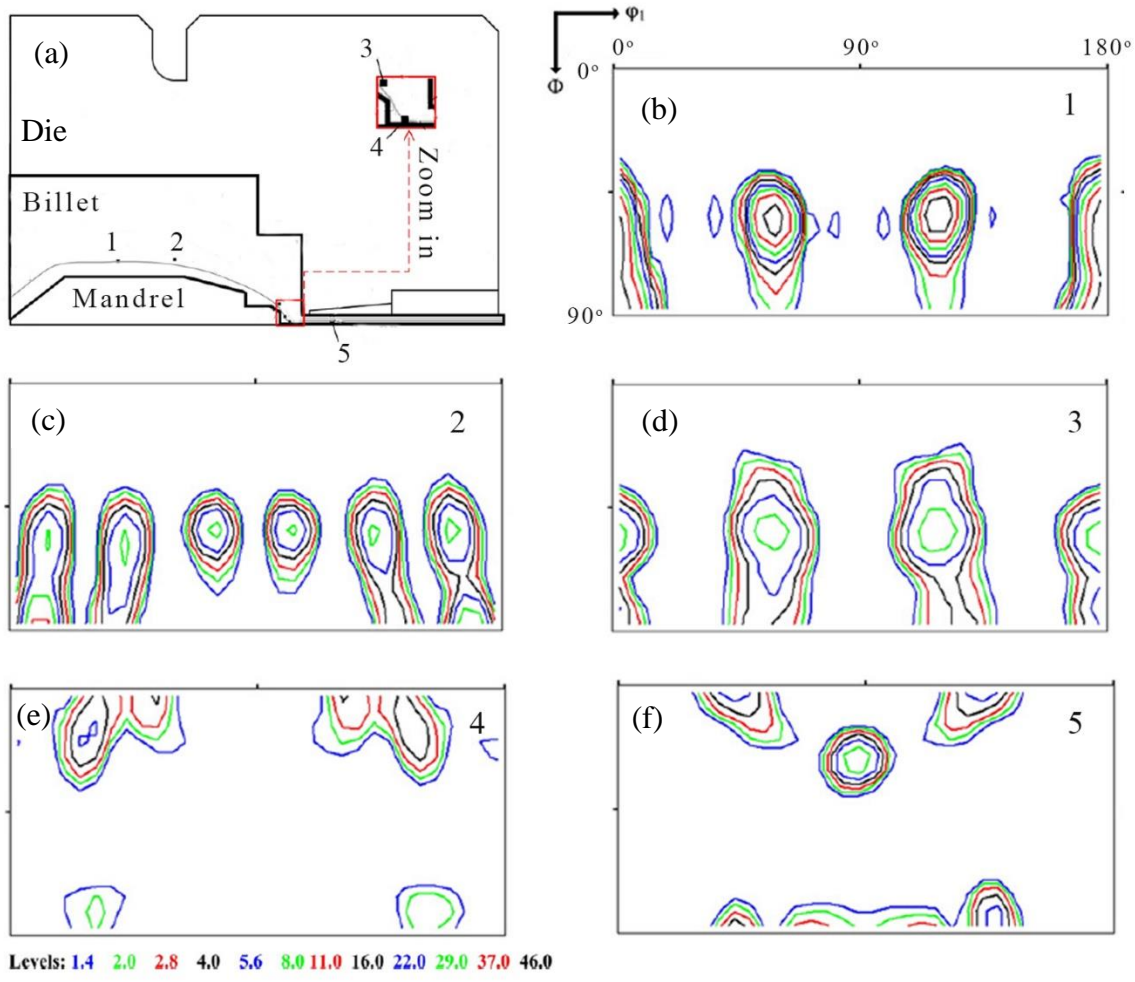


Fig. 2-12 Texture evolution during porthole die extrusion: (a) flow path in porthole die extrusion, (b), (c), (d),(e) and (f)  $\varphi_2 = 45^\circ$  ODF sections of different points on flow plath [42].

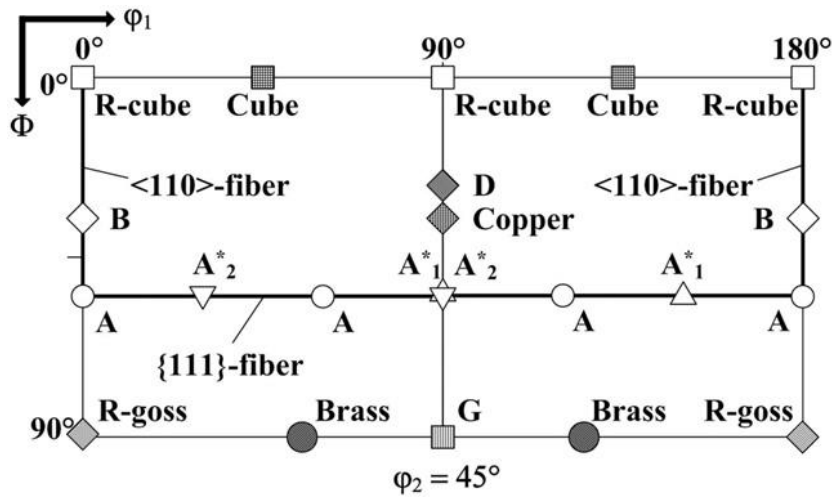


Fig. 2-13 Locations of interesting textures in  $\phi_2 = 45^\circ$  ODF section [42].

Considering the texture's prominent effects on the aluminum alloys' mechanical properties and subsequent processing, an understanding of how the final texture in the extrudate forms is practically important for industry [43, 44]. Although there are a substantial number of research papers on the texture prediction of some simple extrusion without bridges, texture prediction in much more complex during porthole die extrusion and both the understanding and the ability to predict the texture after porthole die extrusion is limited [45, 46]. One success in this regard was by Tang et al who successfully predicted the texture evolution during porthole die extrusion using a coupled FEM and viscoplastic self-consistent (VPSC) modeling. In their research, three particles' (A, B and C) flow paths and their deformation history were calculated using the Lagrangian method in DEFORM 3D (Fig. 2-14). By substitution of the tracked particle' deformation history into the VPSC model, the texture evolution of the each particle was simulated. Fig. 2-15 shows the experimental and model predicted texture evolution history of the C particle close to the seam. The method combining both the flow path calculation and VPSC precisely predicted the texture evolution from the C1 to the C6 position, which is in high agreement with the measured experimental results. However, at C7 position, which is inside the welding chamber, the VPSC model failed to predict the emergence of cube texture under the extremely high hydrostatic pressure.

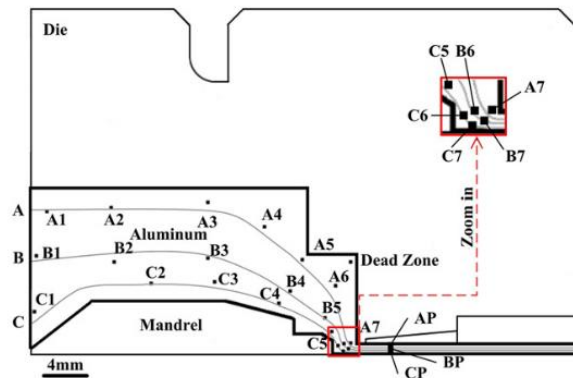


Fig. 2-14 Flow paths for the texture analysis and prediction of the porthole die extrusion of a multi-port tube [46].

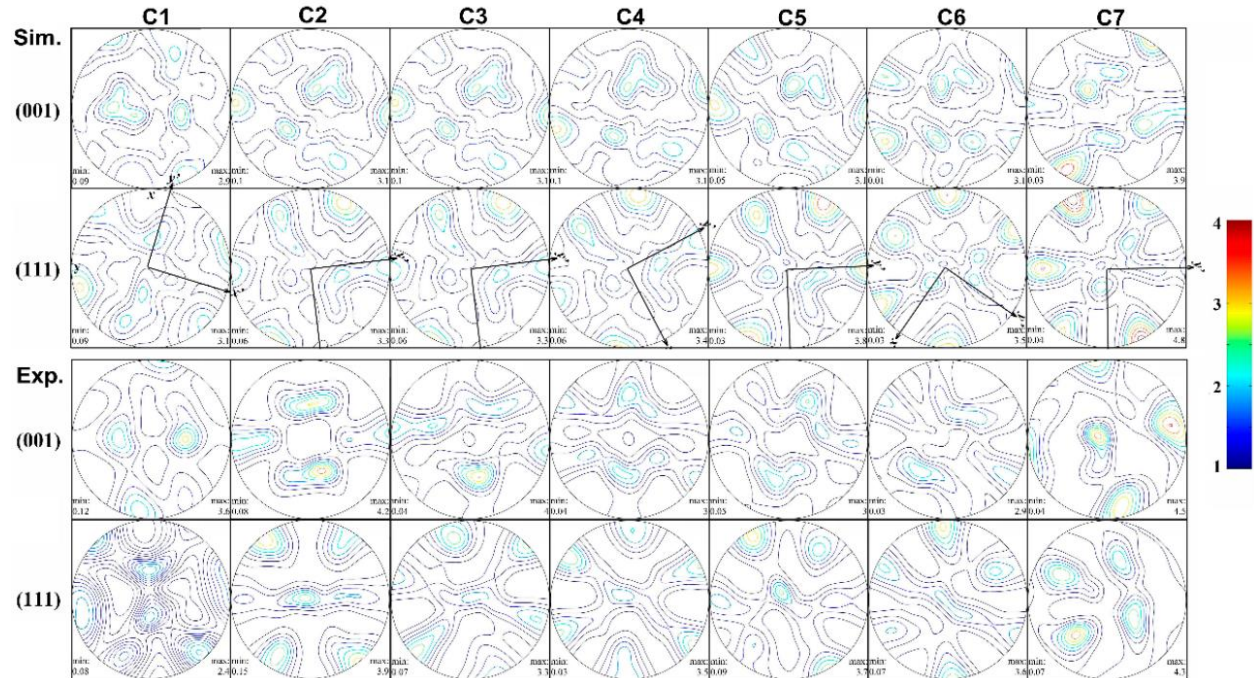


Fig. 2-15 Comparison between the model-predicted (Sim.) and experimentally measured (Exp.) texture along the flowpath C [46].

## 2.5 Effect of minor alloying elements

The minor alloying elements Mn and Cr play an important role in the 6xxx aluminum alloys' mechanical properties and recrystallization behaviour [47]. It is well known that 6xxx aluminum alloys are mainly strengthened by  $\beta''$  and  $\beta'$  precipitates after artificial aging [48-50]. However,  $\beta''$  and  $\beta'$  precipitates are not stable at high temperature, and are dissolved into the matrix during the heating to the homogenization temperature [51, 52]. On the other hand, the addition of Mn and Cr into 6xxx aluminum alloys promotes the formation of  $\alpha$ -Al(Mn-CrFe)Si dispersoids during homogenization. According to the research by Lodgaard and Ryum [53, 54], a rod shaped intermediate phase called the u-phase begins to nucleate on the boundary of  $\beta'$  at 350 °C, and  $\beta'$  will be gradually dissolved as the temperature continues to rise. The  $\alpha$ -Al(Mn-CrFe)Si uses the u-phase as nucleation sites, and can remain stable even when for temperature up to 550 °C. The high density of small dispersoids at high temperature give rise to a more homogeneous distributed dislocations during and after deformation, which reduces the potential nucleation sites for recrystallization. What's more, small dispersoids also pin the movement of grain boundaries and

increase the difficulty of subgrain rearrangement [47]. Consequently, the presence of Mn and Cr in the 6xxx aluminum alloys makes recrystallization much more difficult.

Even though additions of Mn and Cr can have a huge effect on the microstructures and textures that form during porthole die extrusion of AA6xxx alloys, relatively little research has been done [55, 56]. Den Bakker et al [57] extruded hollow profiles using both Mn / Cr free and Mn / Cr rich 6xxx aluminum alloys, and they found that the microstructure of different compositions were very different. As shown in Fig. 2-16, the cross-section of Mn/Cr free AA6xxx aluminum alloy profile was fully recrystallized (including the weldline), while the extruded samples of Mn/Cr rich AA6xxx aluminum alloy were unrecrystallized and still retained a severely deformed microstructure. Referring to Fig. 2-16, for the Mn / Cr free profiles, the welding zone is not distinguishable from the other parts of the extrudate, and the weld line is not obvious. In contrast, the microstructure of the welding zone is clearly different from the matrix in the AA6xxx alloys with Mn / Cr.

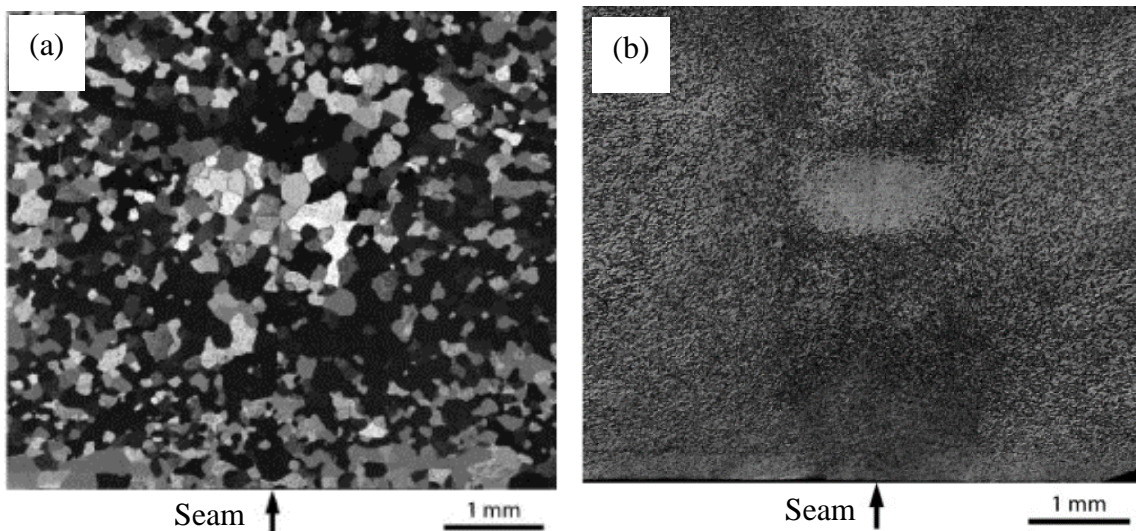


Fig. 2-16 Microstructures of extruded profile's cross-section: (a) Mn / Cr free aluminum alloy and (b) Mn / Cr rich aluminum alloy [57].

## 2.6 Die design optimization

Die design optimization can be used to ensure a uniform velocity distribution and better weld quality in the final extrudate. For example, the velocity distribution can be modified by changing

the bearing length and resizing and relocating portholes. In addition, the weld seam quality can be influenced by the welding chamber height and bridge geometry.

### 2.6.1 Welding chamber height

Welding chamber height significantly affects the material flow in the welding chamber. As shown in Fig. 2-17a, when the welding chamber is too short, the two metal streams do not rejoin each other completely, which can leave a cavity in the extruded profile. In Fig. 2-17b, the welding chamber height is taller such that the metal streams mutually contact each other but leaves a void in front of the bridge. The oxygen in the void oxidizes the metal surface and can severely deteriorate the weld seam quality [58]. When the welding chamber height is tall enough to ensure the welding chamber is completely filled by the metal (Fig. 2-17c), a strong bond can be generated between the metal streams [28].

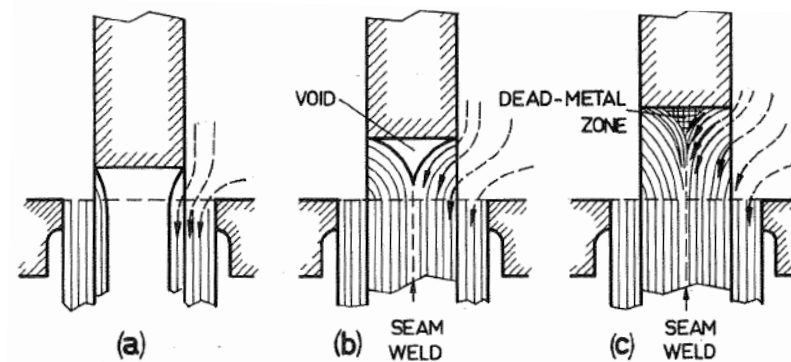


Fig. 2-17 Metal flow through welding chamber of different heights: (a) very small welding chamber, (b) small welding chamber and (b) large welding chamber [28].

The pressure in the welding chamber increases with increasing welding chamber height [59, 60]. As shown in Fig. 2-18, when the welding chamber height increased from 2 mm to 15 mm, the hydrostatic pressure increased from less than 45 MPa to 135 MPa. The experimental results show that the ductility of the extruded samples made using a welding chamber with a height of 15 mm is close to that of extruded samples without a seam [60].

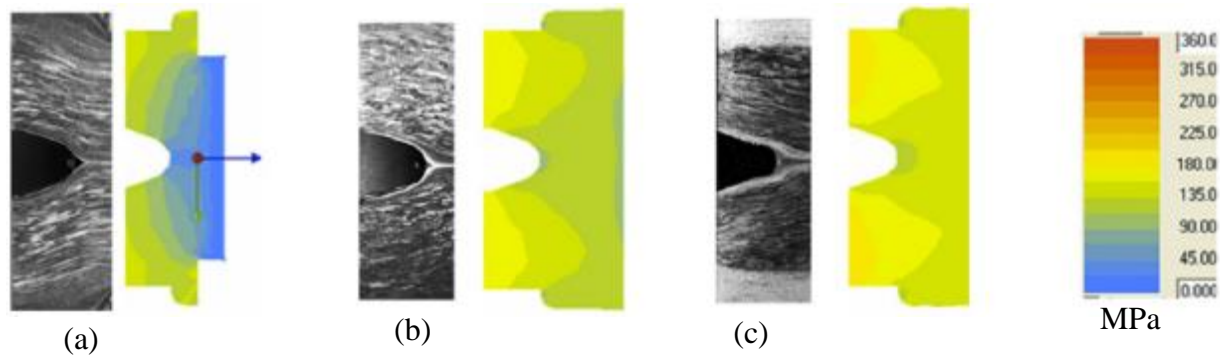


Fig. 2-18 Hydrostatic pressure distribution in welding chamber of EN AW-6060 porthole die extrusion: (a) 2 mm, (b) 10mm and (c) 15 mm welding chamber [60].

Donati et al. [61] conducted a series of extrusion trials with different welding chamber heights. When the welding chamber height increased from 10 mm to 36 mm, the ultimate tensile strength of the extruded specimens did not change considerably but the reduction of area increased from 16% to 28%, which was comparable to the ductility of the seamless samples.

Larger welding chambers also allow a higher productivity and a higher extrusion temperature at high extrusion speed. In extrusion trials by Donati and Tomesani [62], the production rate rose from 18 mt/min to 24 mt/min without showing any tearing defects on the surface, when a short welding chamber was replaced by a taller one. Also the extrusion temperature could be increased from 510 to 540 °C by using a taller welding chamber.

Generally, increasing welding chamber height results in a better weld quality, but the die abrasion and extrusion load can also increase.

### 2.6.2 Bridge geometry

A bridge is used to support and fix the mandrel during porthole die extrusion, while the existence of bridges splits the billet into several streams. The metal streams flow around the bridges and converge under the pressure of bridges, so bridge geometry greatly affects metal flow and pressure distribution in the welding chamber [21, 63, 64].

Gagliardi et al. [63] compared mechanical properties of AA6084 samples extruded using different die geometries, as shown in Fig. 2-19. He found that extruded samples through hexagon and rhombus bridge geometries had a higher fracture elongation than those made using a flat bridge.

At the same time, with a proper design of bridge, fracture elongation could be enhanced to the same level as those samples extruded without bridges.

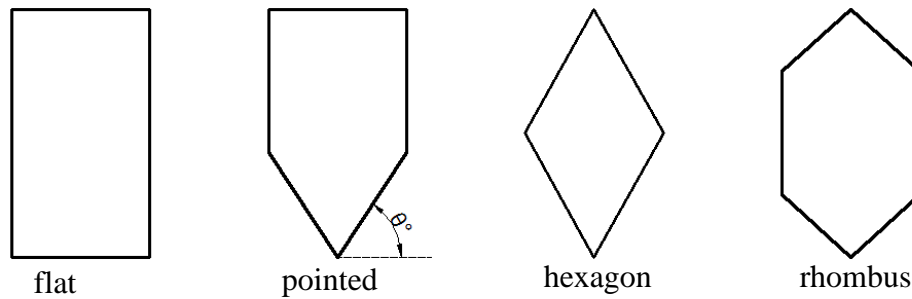


Fig. 2-19 Common bridges used in porthole die extrusion [63].

Gagliardi et al. [65] simulated the extrusion load and pressure distribution of eight different porthole die extrusions for different bridge geometries based on the ALE method in DEFORM 3D. Their results showed that the extrusion load is not dependent on bridge geometry but increases with the bridge volume. On the other hand, the bottom part of the bridge determines the pressure level in the welding chamber, and a pointed shape of bridge bottom creates smoother metal flow and enhanced weld quality.

The gas pocket behind the bridge, as shown in Fig. 2-17b, is detrimental for the weld quality and should be avoided in porthole die extrusion. It is found that when the welding chamber height is the same, a pointed bridge is much easier for the welding chamber to be completely filled due to more homogeneous metal flow under a pointed bridge compared to a flat bridge [21, 66]. Besides the bridge shape, the width of the bridge is also an important factor and can influence the gas pocket size. Valberg et al. [58] pointed out that a wider bridge makes the complete filling of the welding chamber more difficult.

## 2.7 Extrusion parameters effects on welding quality

### 2.7.1 Extrusion temperature

Aluminum porthole die extrusion is a hot working manufacturing process, and the extrusion temperature usually ranges from 400 to 500 °C [8]. The study on extrusion temperature's effects on weld quality is quite limited, but most researchers believe that a higher extrusion temperature is beneficial to welding quality [67-69]. Bingöl and Keskin's research on the porthole die extrusion of AA6063 at varying temperature shows that a high extrusion temperature promotes

recrystallization and grain growth, which results in coarse grains at the weld seam region and decreases the distinction between the matrix and the welding region [70]. Their research results were also confirmed by Yu et al., as shown in Fig. 2-20, the welding zone became less clear and grains grow across the welding line as the extrusion temperature increases. The ultimate strength and fracture elongation also increase at a higher extrusion temperature, which indicates a better weld quality [69]. The reason behind the increase of weld quality at a high temperature lies in the higher diffusion rate across the weld line and also the change of pressure in the welding chamber. A DEFORM simulation of porthole die extrusion of AA7003 tubes by Jo et al. shows that the ratio of welding pressure ( $p$ ) versus effective stress ( $\sigma$ ) (namely  $p/\sigma$ ) increases at a high temperature [71]. According to Eq. 2-2, the increase of  $p/\sigma$  implies a better weld quality.

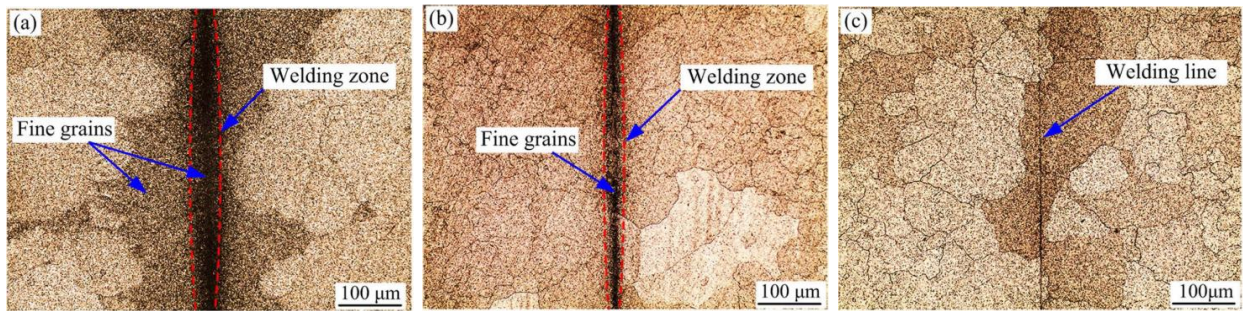


Fig. 2-20 Microstructure of the welding zone of AA6063 samples extruded at different temperatures: (a) 460 °C, (b) 490 °C and (c) 520 °C [69].

### 2.7.2 Ram speed

Ram speed is one of principle extrusion parameters, and has a prominent effect on the extrudate's surface quality, microstructure and mechanical properties. One major defect resulting from high ram speed can be “speed cracking”, as shown in Fig. 2-21 [72]. Secondary phases in aluminum alloys usually have a relatively low melting point relative to the matrix. Hence, high exit temperature's resulting from high extrusion speed might exceed the solidus of the secondary phases and degrade the surface quality [12]. High ram speed can also coarsen the microstructure and decrease the extrudate's strength. Francesco et al. [73] compared the microstructure of aluminum samples extruded at different ram speed ranging from 1 mm/s to 10 mm/s. The average grain size was less than 10  $\mu\text{m}$  at the ram speed of 1 mm/s. However, due to the rising exit temperature in the extrudate introduced by the increase in ram speed resulted in the grain size gradually increased to more than 50  $\mu\text{m}$  at the ram speed of 10 mm/s.

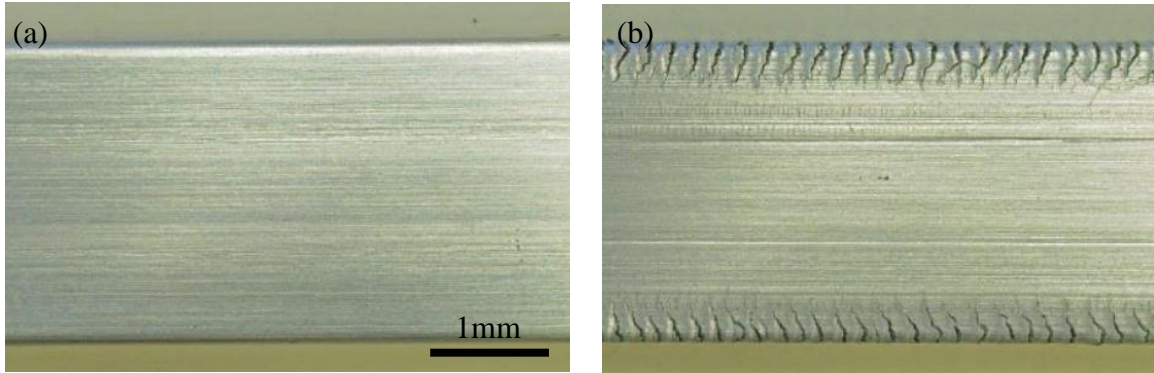


Fig. 2-21 Surface quality of extruded bars of different ram speeds at 500 °C: (a) 12 mm/s, (b) 22 m/s [72].

Another big concern about high ram speed is the deterioration of weld quality. Bingöl and Bozacı [74] studied the effect of ram speed on the stress distribution in the welding chamber using DEFORM 2D. According to their simulation results, the ratio between the normal stress and effective stress dropped at high ram speed, which indicates the welding quality would deteriorate. Tensile tests of weld seams gave the same result as the simulation predicted. The yield stress of extruded specimens dropped from 120 to 110 MPa, and the elongation dropped from 16 to 9 %, when the ram speed increased from 4 mm/s to 15 mm/s.

### 2.7.3 Extrusion ratio

Extrusion ratio, given in Eq. 2-5, directly determines the effective strain experienced by the extrudate. Generally, the extrusion ratio is within 20 to 80 in typical industry practice [8, 75].

$$ER = \frac{A_c}{nA_e} \quad 2-5$$

where  $A_c$  is the area of the container,  $n$  is the number of die openings, and  $A_e$  is the cross-section area of the profile.

Valberg et al. [58] studied the metal flow behavior in the welding chamber, when the thickness of the profile varied from 3 mm to 11 mm. When the profile thickness decreased, which corresponded to a higher extrusion ratio, it became more difficult for the welding chamber to be completely filled. The gas pocket behind the bridge became bigger with an increasing extrusion ratio. Partially filling of the welding chamber could result in improper welding seam and lower strength.

In research by Gagliardi et al. [73], the dimensions of extruded profile as shown in Fig. 2-22, had a direct impact on the welding quality; the welding quality became better when the profile thickness reduced from 2 to 1 mm. This occurred because the welding pressure doubled from 70 to 150 MPa in the die configurations with a higher extrusion ratio. On the other hand, when the thickness was further reduced to 0.5 mm (namely the extrusion ratio is increased to 13.8), more stored deform energy was induced into the extruded profile. The high stored deformation energy introduced by the high extrusion ratio promoted recrystallization and grain growth, and reduced the strength due to the coarser microstructure.

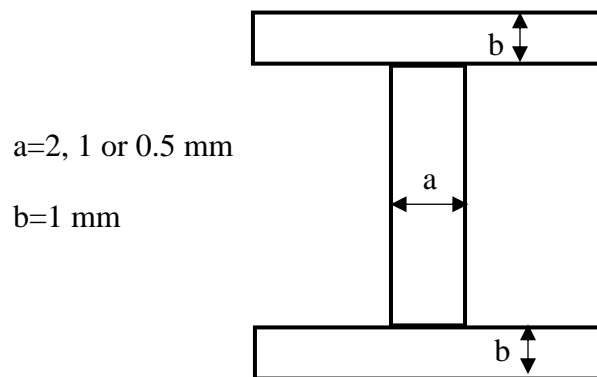


Fig. 2-22 The cross section of the extruded profile [73].

## 2.8 Front/back end defect

In addition to the longitudinal weld, porthole die extruded profiles also contain front and back end defects similar to more traditional extrusion processes which do not include a porthole. As its name implies, the front end defect exists at the front part of the extruded profile, and its formation is related to the charge seam that forms between the old and new billet. The back end defect appears at the back part of the extruded profile, and it forms when the billet skin material flows into the extruded profile. The length of extruded profile containing front/back end defects and which have inferior mechanical properties compared by the other parts of profile and typically scrapped to ensure the quality of the extrudate is consistent [76, 77].

### 2.8.1 Front end defect formation

Due to the difficulty in removing residual material left in the die cavity after one cycle of extrusion, billet on billet extrusion is the most used method to manufacture continuous aluminum profile's in industry. At the start of each extrusion cycle, a new billet is loaded into the container

and is in contact with the remaining material in the die cavity from the previous extrusion. Under the extremely high hydrostatic pressure in extrusion, the new billet is welded onto the old billet material, and a weld seam will be created at the interface between the new billet and the old billet material. This seam is called a charge seam or transverse seam in the literature [78, 79]. Since charge seams only exist at the front end of the profile, it is also referred to as the “front end defect” in industry. As shown in Fig. 2-23, the charge seam is extended into a “tongue” shape in the extruded profile, and the length of profile containing a charge seam is typically discarded due to poor mechanical properties.

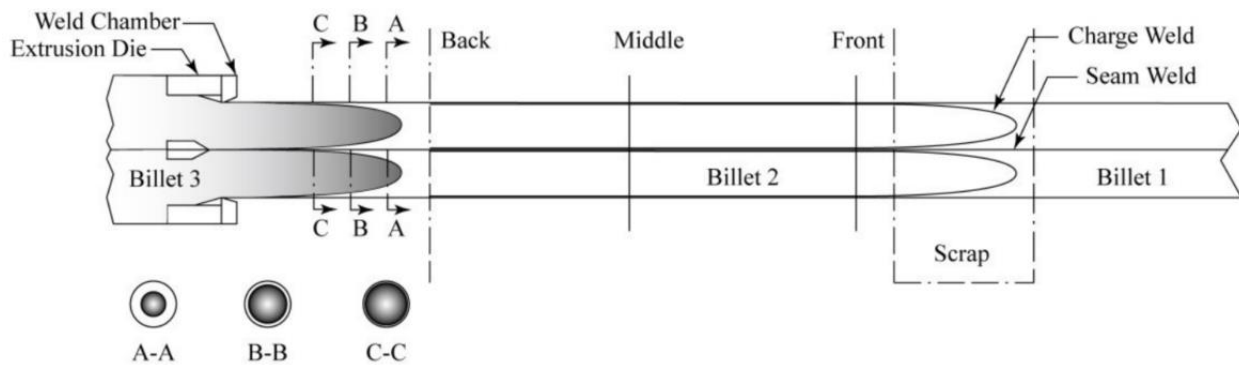


Fig. 2-23 Schematic showing the charge seam formation during porthole die extrusion [80].

### 2.8.2 Estimation of charge seam length

As discussed above, the charge seam is an unavoidable part in the extruded profile during billet on billet extrusion, and is typically discarded in industry. However, before the wide usage of finite element simulation software, the length of the charge seam was estimated using trial and error experiments and some empirical rules. One frequently used industry practice to assess the length of the charge seam is simply based on the extrusion ratio ( $R$ ). As a guideline, a 3 m profile should be scrapped when  $R > 40$ , 2 m for  $30 < R < 40$ , and 1 m for  $R < 30$  [81]. In the last decade, the rapid development of finite element simulation software makes it possible to compute the length of charge seam precisely. Reggiani et al. simulated the charge seam formation in a complex aluminum profile using HyperXtrude and the result can be used to increase the product’s quality and process efficiency [82]. Mahmoodkhani et al. calculated the length and thickness of the charge seam based on velocity field given by DEFORM 2D simulation, and their results showed that the feeder geometry can affect the length of the charge seam [83]. Liang et al. studied the ram speed’s effects on the length of the charge seam, and they found that a longer profile should be scrapped

at a higher ram speed [84]. The length of the charge seam is also significantly affected by the velocity distribution along the cross-section of the extruded profile. Zhang et al. found out that the length of the charge seam can be shortened by 10%, when the flow velocity became more uniform after die design optimization [85].

### **2.8.3 Back end defect**

The billet skin has an exceptionally high concentration of impurities, such as oxide and contaminants, compared to the interior billet material. The billet skin is oxidized during casting, homogenization and reheating, and the lubricant, if used, during extrusion can also contaminate the billet surface. Due to inverse segregation in casting, the billet skin for AA6xxx alloys has a high concentration of Mg and Si and coarse iron rich intermetallics [8, 86]. During the extrusion process, the high friction between the billet and container causes inhomogeneous material flow between the billet skin and billet core. The billet skin is almost stuck on the container wall, while the core material flows towards the die opening at a relatively higher speed. The velocity discrepancy between the billet skin and the interior billet material causes the billet skin to flow along the ram surface inwards towards the interior of the billet to compensate for the material lost in the billet core due to its high flow velocity as shown in Fig. 2-24. The billet skin gradually accumulates in front of the ram, and the billet skin may flow into the extrudate profile and form an internal oxide ring. The internal oxide can severely reduce the extrudate's strength and promote crack propagation under high stress [86]. In research by Yu et al., extruded material that contained billet skin or the back end defect can have significantly poorer mechanical properties and corrosion resistance [76]. In order to prevent the billet skin from entering into the extrudate, a certain thickness of billet butt is typically removed at the end of each extrusion cycle. The billet skin can also be dragged to form the profile's surface by the strong shear force along the boundary of the dead metal zone (DMZ), which is called "forward skin flow" and shown in Fig. 2-24. This type of defect can impair the integrity and surface finish of the final extrudate [86, 87].

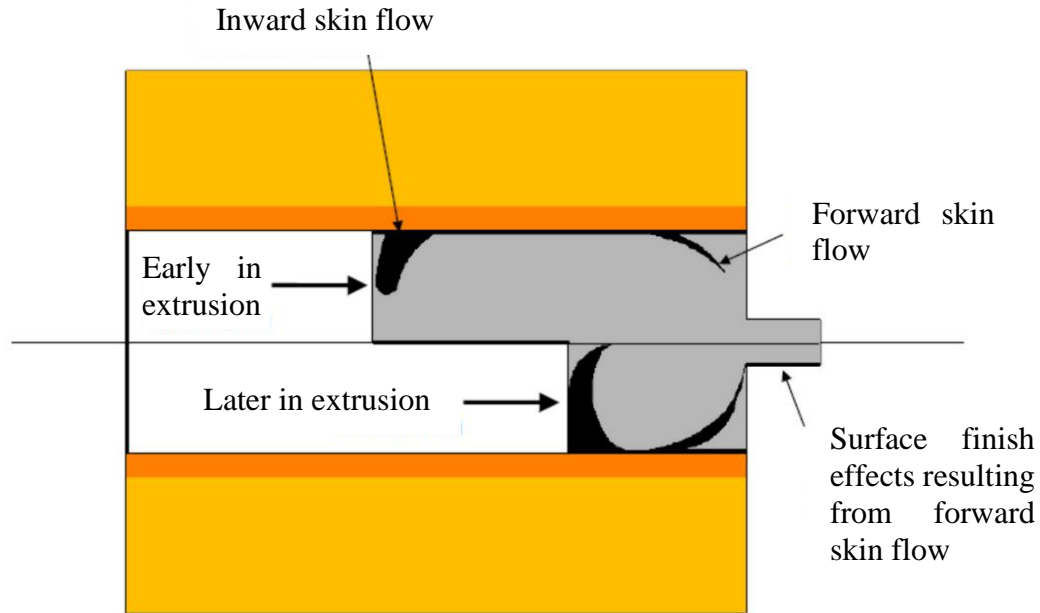


Fig. 2-24 Formation of back end defect [88].

To date, the majority of the research on porthole die extrusion has focussed on the weld quality of the longitudinal seam in the extruded profile. Through optimization of the die design and extrusion parameters, the mechanical properties of the porthole die extruded samples can be comparable to a seamless extruded sample [23, 60]. With the wide usage of commercial finite element (FE) software, welding quality criteria based on FE simulation results were proposed in the last few years [22, 29]. However, most of research only investigates the final profile's mechanical properties and microstructure, but has not examined how the microstructure and texture evolves during porthole die extrusion. Moreover, the relationship between microstructure and texture evolution and thermal mechanical history has never been studied. In this research, the evolution of the microstructure and texture extrusion during porthole die extrusion and the effect of a number of parameters including composition, bridge geometry and extrusion parameters on the weld seam on the final microstructure and mechanical properties will be carefully studied utilizing both experimental and simulation methods.

## Chapter 3 Scope and objective

A scientific understanding of the influence of the porthole die or weld chamber geometry in conjunction with extrusion parameters such as ram speed and temperature on the evolution of the microstructure including texture and final mechanical properties, especially along the weld seam is still quite limited for aluminum extrusion [41, 42]. Commercial finite element (FE) simulation software packages such as DEFORM and HyperXtrude have been widely used to determine the state variables and material flow behavior during porthole die extrusion. The quantitative information related to the thermomechanical history and flow behaviour of specific locations in the extrudate provided by commercial finite element (FE) models such as DEFORM and HyperXtrude enables researchers to understand the microstructure evolution and, and in some cases predict, the extrudate quality [82, 89]. The main purpose of this research is to understand how the microstructure and mechanical properties of AA6082 aluminum porthole die extruded profiles are affected by die geometry, extrusion parameters and alloy composition. In order to achieve this goal, several specific sub-objectives were identified:

- Develop and validate a Finite Element model of the AA6082 porthole die extrusion process for a range of extrusion die configurations and process parameters.
- Characterize the microstructure, texture and mechanical properties of porthole die extruded profiles obtained using different dies and extrusion parameters.
- Examine the effect of die design and extrusion parameters on the extrudate's microstructure and mechanical properties after porthole die extrusion.
- Study the effects of Mn and Cr in AA6082 on the recrystallization behaviour and final mechanical properties after porthole die extrusion.

# Chapter 4 Methodology

## 4.1 Extrusion material

The material used in this research were three model alloys based on aluminum alloy AA6082 with different Mn and Cr concentrations, as shown in Table 4-1. As part of the research, the Mn and Cr levels were varied in order to promote (no Mn or Cr) recrystallization during extrusion or inhibit (increasing Mn and Cr) recrystallization during extrusion through the formation of dispersoids. The extrusion billets used in Trial 1 to 3 had the dimension of  $\Phi 101.6 \times 400$  mm, and the extrusion billets used in Trial 4 to 17 had the dimension of  $\Phi 101.6 \times 200$  mm.

Table 4-1 Composition of alloys used in the extrusion trials (wt.%)

Alloy	Si	Fe	Mn	Mg	Cr	Al
0Mn	0.9	0.2	-	0.7	-	Balanced
0.5Mn	1.03	0.2	0.5	0.7	-	Balanced
0.5Mn0.15Cr	1.04	0.2	0.5	0.7	0.15	Balanced

The billets were cast, homogenized and extruded at Rio Tinto Aluminum's Arvida Research and Development Centre (ARDC) in Jonquiere, Quebec. Homogenization is essential to reduce segregation, break down coarse constituents and generate fine dispersoids, resulting in a higher workability of the metal and a better surface finish. In this research, all of these billets were homogenized at 550 °C for 2 hours prior to extrusion.

In this research, the microstructure of the starting samples were examined by optical microscopy and Scanning Electron Microscopy (SEM) at the University of British Columbia (UBC) [90]. Fig. 4-1 shows the metallography of the as cast samples of different compositions under polarized light. Referring to Fig. 4-1, all of the cast samples were made up by equiaxed grains with dendrites inside the grains. Further analysis shows that the average grain size and secondary dendrite arm spacing are 100-120  $\mu\text{m}$  and 17-20  $\mu\text{m}$  respectively regardless of the alloy composition.

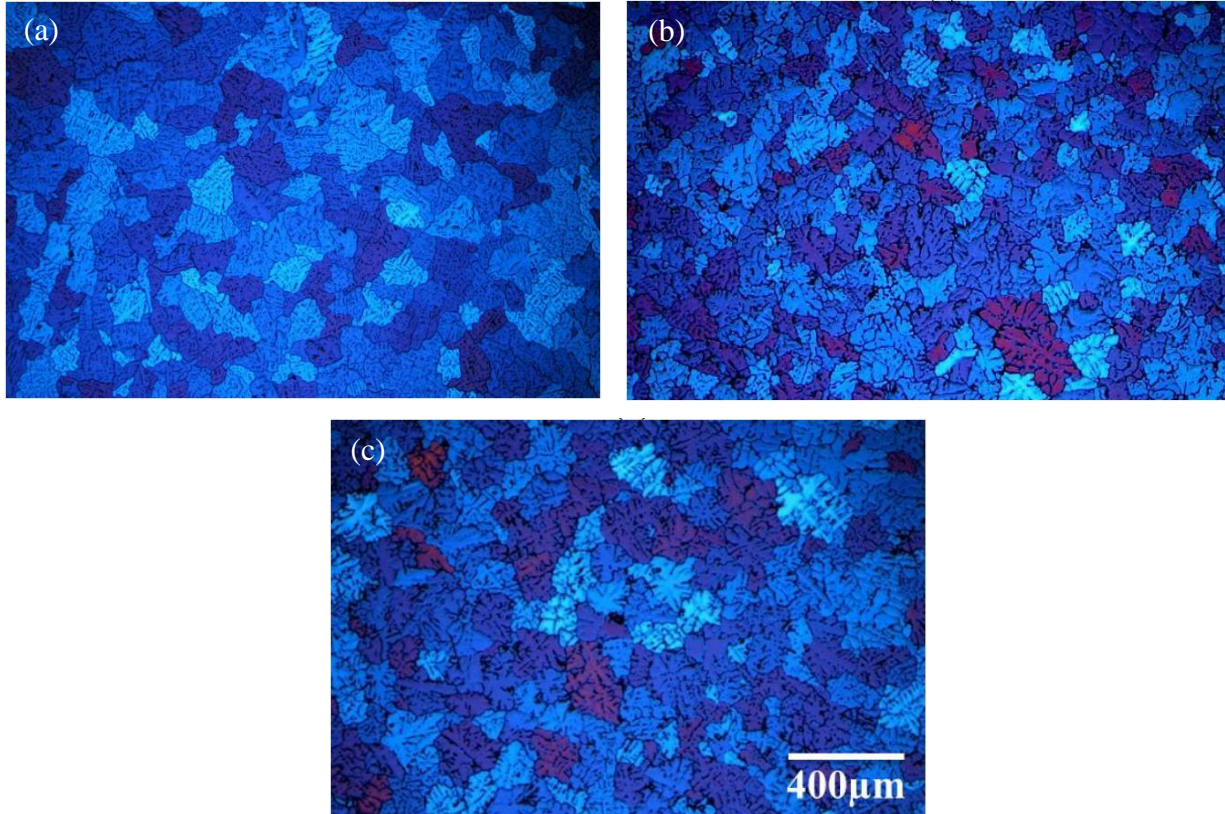
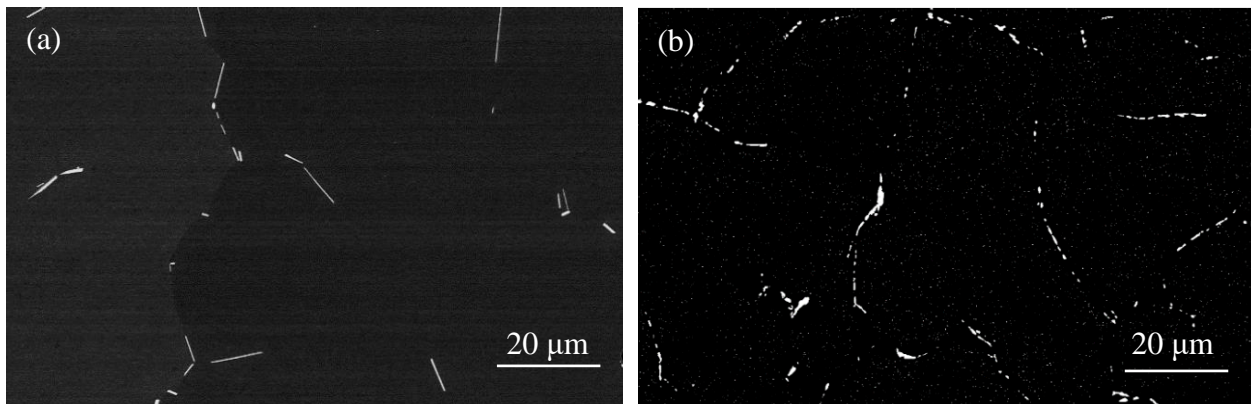


Fig. 4-1 Metallography of the as-cast samples of: (a) 0Mn, (b) 0.5Mn and (c) 0.5Mn0.15Cr [90].

Fig. 4-2 shows the dispersoid distribution in as-cast and homogenized samples of different compositions under SEM observation. Due to a lack of Mn/Cr, the 0Mn sample had virtually no dispersoids after homogenization (Fig. 4-2a). Some dispersoids appeared in the 0.5Mn sample, and as expected the 0.5Mn0.15Cr samples had the highest density of dispersoids among the three alloys due to the highest content of Mn and Cr. The different densities of high temperature stable Mn/Cr containing dispersoids will have a significant effect on the final extrudate's microstructure and mechanical properties.



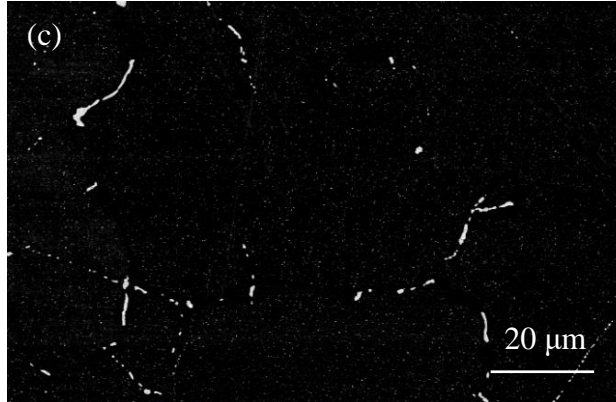


Fig. 4-2 SEM image (backscatter mode) of as homogenized (550 °C for 2 hrs) microstructure of different compositions: (a) 0Mn, (b) 0.5Mn and (c) 0.5Mn0.15Cr [90].

## 4.2 Extrusion trials

### 4.2.1 Die configurations

After homogenization, the billets were extruded using the fully instrumented industrial extrusion press at the Rio Tinto ARDC using a range of porthole die geometries. This extrusion press can record ram position and ram press during extrusion, which can be used to verify the accuracy of the extrusion simulation predictions. The extruded profile was a strip with a rectangular cross-section of  $50 \times 2.5$  mm. After extrusion, the profiles were quenched using a standing wave water tank to room temperature. For each extrusion trial, six billets were extruded consecutively.

After extrusion, the extruded samples were heat treated to study the effect of subsequent heat treatment on the mechanical properties. In this research, the extruded sample was heat treated in three different ways: T4 (natural aging after extrusion), T5 (natural aging after extrusion plus artificial aging at 175°C for 8 hr) and T6 (natural aging after extrusion plus solution heat treatment at 550°C for 10 min followed by aging at 175°C for 8 hrs).

As shown in Fig. 4-3, the porthole die extrusion die used in this project consisted of two parts — a die mandrel and a die cup. The bridge in the die mandrel divides the billet into two streams, which will pass through the two portholes. The space enclosed by the die mandrel and die cup is called the welding chamber. In this chamber, the separated metal streams rejoin each other to form

a weld seam. The long and thin rectangular slot in the die cup is the die orifice, which gives the extruded profile's final shape.

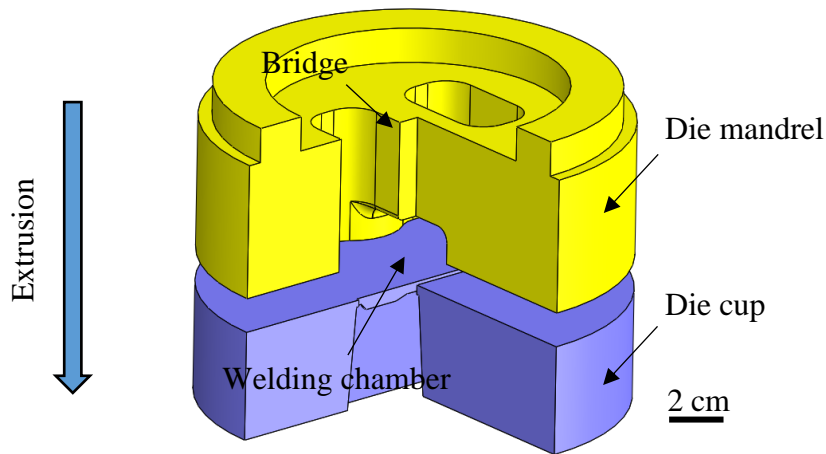


Fig. 4-3 CAD drawing showing the split porthole die assembly for the welding chamber with the streamlined die.

In this research, three parameters of the die geometry were changed in order to study the effect of the die geometry on the porthole die extrusion. Firstly, two different bridge shapes were used a streamlined die (Die C) and a flat die (Die E), as shown in Fig. 4-4. Die C, the streamlined bridge, creates relatively smooth material flow during extrusion in the die. In contrast, Die E is flat and will create dead zones during porthole die extrusion. Secondly, two welding chamber heights (12.7mm and 25.4 mm) were also studied. The die cup used for the 12.7 mm welding chamber is flat, but the die cup used for the 25.4 mm welding chamber has a 12.7 mm deep pocket. Thirdly, two types of the porthole die layouts were used (an asymmetric die and a symmetric die). For the asymmetric die, the centre of the two portholes was slightly offset from the mid-thickness or centre plane of the strip, as shown in Fig. 4-6a. For the symmetric porthole die layout, the centre of the two portholes coincides with the mid-thickness plane, as shown in Fig. 4-6b. Considering each of the three parameters studied had two values, a total of eight die configurations were studied in this research. Every die configuration is denoted by the combination of the three parameters. For instance, the die configuration, which has a streamlined bridge shape (Die C), 12.7 mm welding chamber and symmetric porthole layout, is denoted by Die C / 12.7 mm / sym.

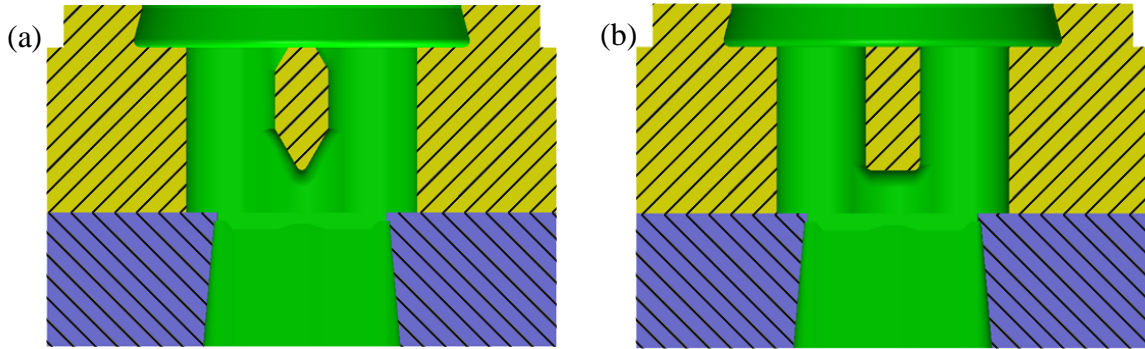


Fig. 4-4 Cross-section of the porthole die showing the two bridge geometries used in this research: (a) Die C (streamlined die) and (b) Die E (flat die).

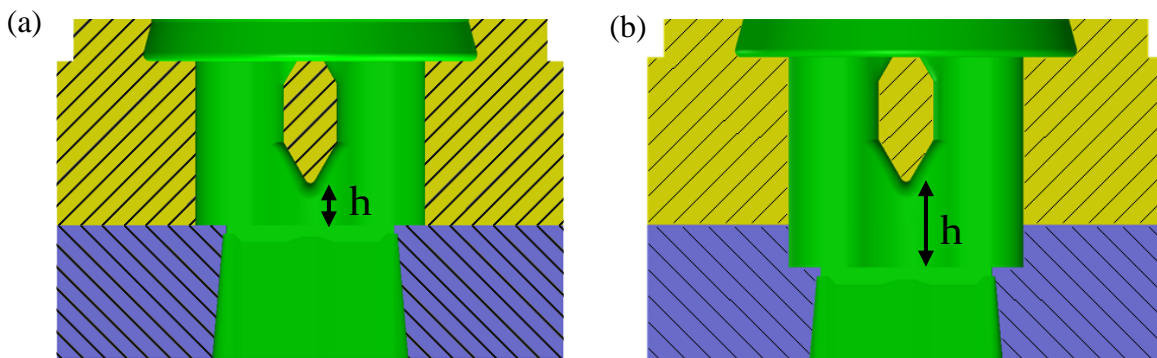


Fig. 4-5 Cross-section of the porthole die showing the two welding chamber heights used in this research: (a)  $h = 12.7$  mm and (b)  $h = 25.4$  mm.

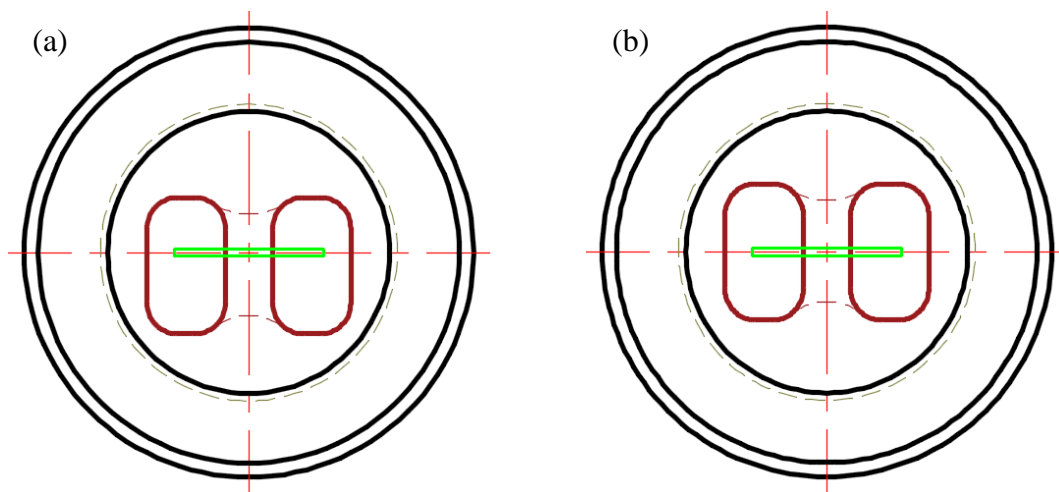


Fig. 4-6 Top view of the die mandrel showing the two types of porthole die layout: (a) asymmetric and (b) symmetric. Note the green rectangle is the final die exit and reflective of the final extrudate profile.

#### 4.2.2 Extrusion parameters

Table 4-2 shows the alloy's composition, die configurations and extrusion parameters used during the extrusion trials. As shown in Table 4-2, a total of 17 extrusion trials were run and the most common alloy used for the extrusion trials was 0.5Mn0.15Cr, due to its strong ability to inhibit recrystallization at high temperature. AA6xxx alloys with 0.5Mn and 0Mn (no Cr) were also extruded to study the effect of composition on the extrudate microstructure and mechanical properties. In addition, a no bridge die was used which created an extruded strip with no weld seam for comparison purposes. Table 4-2 provides the experimental details for each of the extrusion trials run. Referring to Table 4-2, for most of the extrusion trails, the ram speed was set to 5 mm/s. However, in Trial 12 to 15, a range of ram speeds were used to study this effect. In Trial 18 and 19, a very low extrusion temperature was used in order to try and maintain a deformation structure (with no recrystallization) in the extruded samples especially along the weld seam.

Table 4-2 Extrusion parameters used during extrusion trials

Trial No.	Alloy	Die Configuration	Ram speed (mm/s)	Die temperature (°C)	Billet temperature (°C)
1	0.5Mn0.15Cr	Die C / 12.7 mm / asym	5	450	480
2	0.5Mn0.15Cr	Die E / 12.7 mm / asym	5	450	480
3	0.5Mn0.15Cr	Die C / 12.7 mm / asym	7	430	440
4	0.5Mn0.15Cr	Die C / 25.4 mm / asym	4	480	480
5	0.5Mn0.15Cr	Die E / 25.4 mm / asym	4	480	480
6	0.5Mn	Die C / 12.7 mm / asym	5	480	480
7	0.5Mn	Die E / 12.7 mm / asym	5	480	480
8	0Mn	Die C / 12.7 mm / asym	5	480	480
9	0Mn	Die E / 12.7 mm / asym	5	480	480
10	0Mn	No bridge	5	480	480
11	0.5Mn0.15Cr	No bridge	5	480	480
12	0.5Mn0.15Cr	Die C / 12.7 mm / sym	4, 5, 6, 8, 9	480	480
13	0.5Mn0.15Cr	Die E / 12.7 mm / sym	4, 5, 6, 7, 8	480	480

Trial No.	Alloy	Die Configuration	Ram speed (mm/s)	Die temperature (°C)	Billet temperature (°C)
14	0.5Mn0.15Cr	Die C / 25.4 mm / sym	4, 5, 6, 7, 8	480	480
15	0.5Mn0.15Cr	Die E / 25.4 mm / sym	4, 5, 6, 7, 8	480	480
16	0.5Mn0.15Cr	Die C / 12.7 mm / sym	5	400	400
17	0.5Mn0.15Cr	Die E / 12.7 mm / sym	5	400	400

## 4.3 Finite element method (FEM) simulation

### 4.3.1 Lagrangian and ALE simulation methods

During FEM simulation of large plastic deformation, there are three different ways to describe the material's motion, as shown in Fig. 4-7.

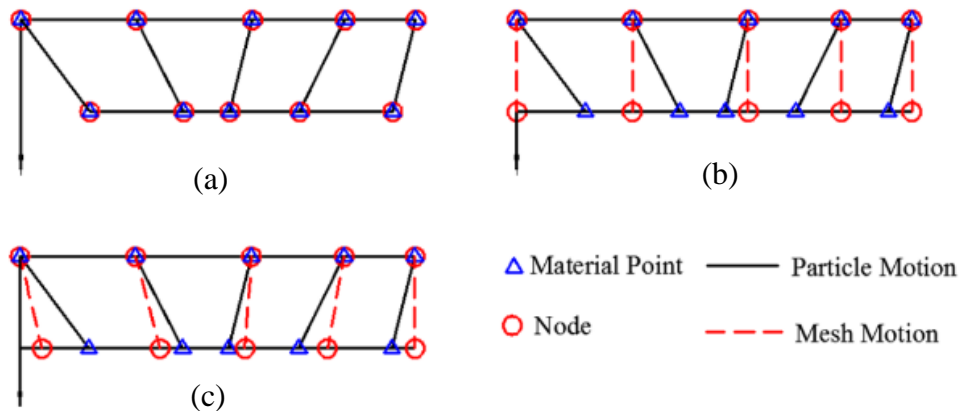


Fig. 4-7 Different methods used to describe the material's motion: (a) Lagrangian, (b) Eulerian and (c) Arbitrary Lagrangian-Eulerian (ALE) [91].

During Lagrangian simulations, the mesh nodes are connected to the material and no material passes through the elements during the simulation. The Lagrangian method allows mesh nodes to remain on free boundaries and facilitates the tracking of boundary motion. Furthermore, history dependent variables can be handled in a straightforward way using the Lagrangian method. However, during deformation operations where severe deformation occurs such as extrusion, this results in a distortion of the Lagrangian mesh, and the requirement for frequent remeshing.

In contrast, for the Eulerian method, the mesh is fixed spatially while the material flows through the mesh. Since mesh nodes and the material points are dissociated in the Eulerian description, it is very complicated to capture the free surface's motion and calculate history dependent variables. However, the Eulerian method is much faster computationally and does not need to be re-meshed.

The Arbitrary Lagrangian-Eulerian (ALE) method is a compromise between the Lagrangian and Eulerian methods and was used as a simulation tool to overcome the weaknesses of the Lagrangian and Eulerian simulation approaches. In the ALE simulation, the mesh nodes are neither connected to the material nor fixed in space, but move independently from the material. Unlike the Lagrangian simulation, movement of the mesh nodes with respect to the material domain alleviates the mesh distortion and need for remeshing associated with large plastic strain. Despite the advantages of ALE description, it is unable to simulate the generation of new surfaces. As a result, ALE simulations can only be applied to materials whose geometry is quite predictable during the deformation [92].

### 4.3.2 Material model

Considering aluminum alloys have a relatively high stacking fault energy and hence it is very easy for dislocations to climb and cross slip, dynamic recovery counters strain hardening during deformation. As a result, the flow stress of aluminum alloys typically reaches a steady-state regime after very minor levels of deformation and remains independent of strain at high temperature (>0.5T<sub>m</sub>) [93, 94]. Based on this, the Sellars-Tegart model (Eq. 4-1), which can effectively describe the relationship among stress, strain rate and temperature and is independent of strain, is selected as the material's constitutive model for this research [95, 96]. The material constants used in the Sellars-Tegart model can be easily determined using measured material stress–strain curves at high temperature, and its effectiveness has been verified by many researchers working on simulation of hot forming of aluminum alloys [97-100].

$$A[\sinh(\alpha\sigma)]^n = \dot{\epsilon} \exp\left(\frac{Q_d}{RT}\right) \quad 4-1$$

where  $\sigma$  is the flow stress (MPa),  $\dot{\epsilon}$  is the strain rate ( $s^{-1}$ ) and  $T$  is the temperature (K).  $A$ ,  $\alpha$ ,  $n$  and  $Q_d$  are material constants respectively, and finally  $R$  is the universal gas constant ( $8.314 \text{ J}\cdot\text{mol}^{-1}\text{K}$ ). In this research, these constants (given in Table 4-3) were determined using the DEFORM software

by fitting Eq. 4-1 to flow stress data for AA6082 available in the DEFORM v10.0 database. Fig. 4-8 shows that the stress calculated using the Sellars – Tegart model for a range of strain rates and temperatures fit the material stress–strain curves stored in the DEFORM database very well.

Table 4-3 Material constants used in the Sellars-Tegart constitutive equation for AA6082.

Material parameter	Value
A	$9.04 \times 10^8 \text{ s}^{-1}$
$\alpha$	$0.03 \text{ MPa}^{-1}$
n	5.0
$Q_d$	$145 \text{ kJ}\cdot\text{mol}^{-1}\text{K}^{-1}$
R	$8.314 \text{ J}\cdot\text{mol}^{-1}\text{K}$

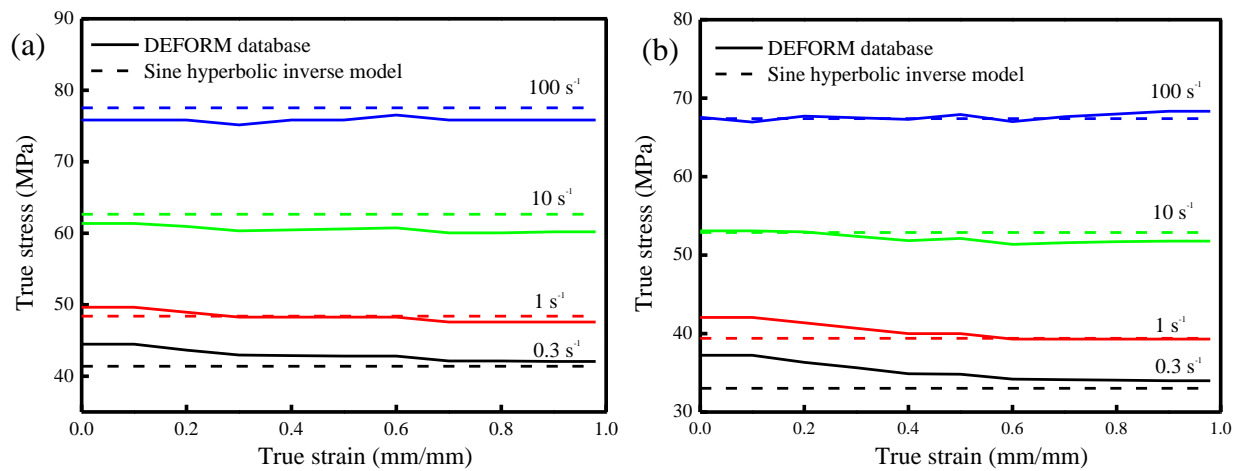


Fig. 4-8 Comparison between the true stress – strain curves in the DEFORM database and those calculated using the Sellars-Tegart (Eq. 4-1) model with constants given Table 4-3: (a) 450 °C and (b) 500 °C.

### 4.3.3 DEFORM 3D simulation

The design environment for forming (DEFORM) is a commercial Finite Element Method (FEM) software package which can be used to solve theoretical and practical problems in metal forming and was used in this research to simulate porthole die extrusion.

#### 4.3.4 Lagrangian simulation

For the asymmetric porthole layout, only half of the billet and porthole dies were modelled in order to reduce the simulation time. As shown in Fig. 4-9a, the symmetrical plane coincides with the welding plane where the two metal streams from the portholes rejoin each, so the model was cut into half along the welding plane. In order to simplify the model, the die mandrel, the die cup and container were merged into one single die in the simulation.

As shown in Fig. 4-9, the billet is 400 mm long and its diameter is slightly smaller than the die's internal diameter in the first step. In order to simulate the heat conduction between tooling and billet accurately, the die and ram were also meshed as well. Since the billet was re-meshed frequently in the Lagrangian simulation, an absolute meshing method was used to keep the element size unchanged during the simulation.

In order to keep the welding interface free of contaminates, no lubricant was used during extrusion. As a result, the billet surface was assumed to stick to the tooling during extrusion and there was assumed to be no relative velocity between the die and the billet except along the die bearing surface [36, 101]. The friction between the billet and the tooling was described as a shear friction model (Eq. 4-2) where the friction factor was set to 1.0, consistent with sticking friction [102]. A shear friction model with a coefficient of 0.7 was applied at the die bearing surface [103]. In addition, the heat transfer coefficient between the billet and the tooling was assumed to be  $25 \text{ kW}\cdot\text{m}^{-2}\text{K}^{-1}$  [104]. According to the extrusion parameters described in the experimental section, the initial billet and die temperature were set to be 480 and 450 °C respectively, and the ram speed was set to be 5 mm/s (or whatever the ram speed was for the trial being simulated). The billet material used was AA6082, and the tooling material was H-13. The simulation parameters used are summarized in Table 4-4.

$$f_s = mk \quad 4-2$$

where  $f_s$  is the friction stress,  $m$  is the friction factor and  $k$  is the material shear stress (using Von Mises definition,  $k = \sigma / \sqrt{3}$ ) [105].

Table 4-4 Simulation parameters and boundary conditions used in the DEFORM model.

Parameter	Value
Friction factor between tooling and billet	1
Friction factor on die bearing	0.7
Heat transfer coefficient	25 kW·m <sup>-2</sup> ·K <sup>-1</sup>
Ram speed	5 mm/s
Billet temperature	480 °C
Die temperature	450 °C
Tooling material	H-13

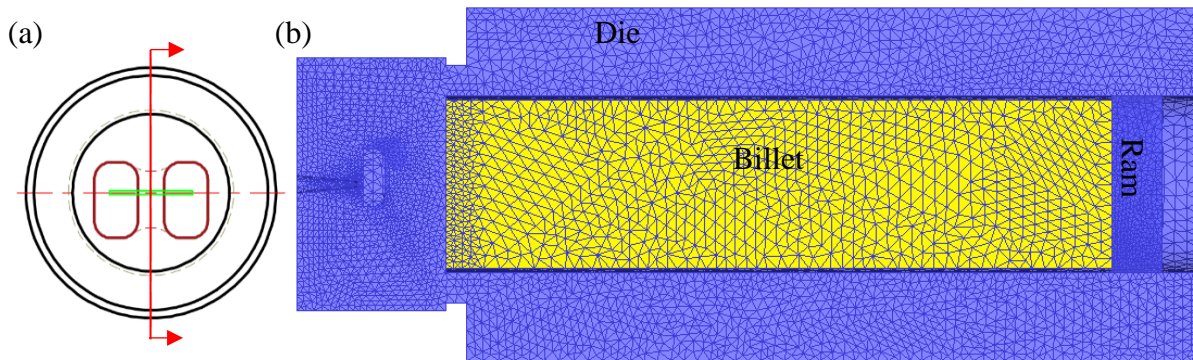


Fig. 4-9 Lagrangian model of porthole die extrusion: (a) the top view of die mandrel and (b) half FEM model.

### 4.3.5 ALE simulation

In this research, the ALE method was used to calculate the state variables at the breakthrough. In the first stage of the extrusion, the billet was upset in the container to make the outer surface of the billet in tight contact with the container. In this research, the billet diameter and the inner diameter of the container were 101.6 and 106 mm respectively. After upsetting, the 400 mm billet should be about  $400 * (101.6 / 106)^2 = 365$  mm, and the 200 mm billet should be about  $200 * (101.6 / 106)^2 = 180$  mm. Consequently, the length of the 400 mm billet and the 200 mm billet in the ALE simulation were set to be 365 and 180 mm respectively. Similar to the Lagrangian model shown in Fig. 4-9, the ALE simulation model of the asymmetric die configurations was also halved along the welding plane (Fig. 4-10). On the other hand, since the symmetric die configuration has

two symmetric planes, the welding plane and middle thickness plane, so only a quarter of the model was needed for the simulation (Fig. 4-11).

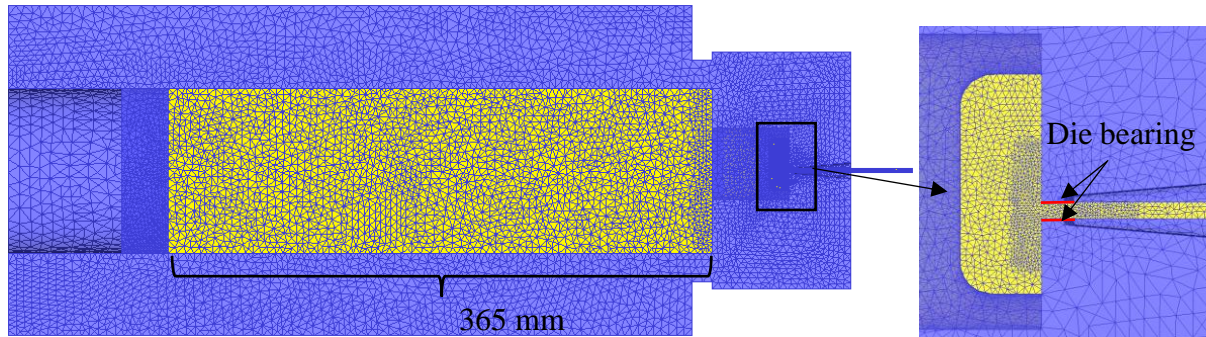


Fig. 4-10 ALE simulation model of asymmetric porthole die extrusion

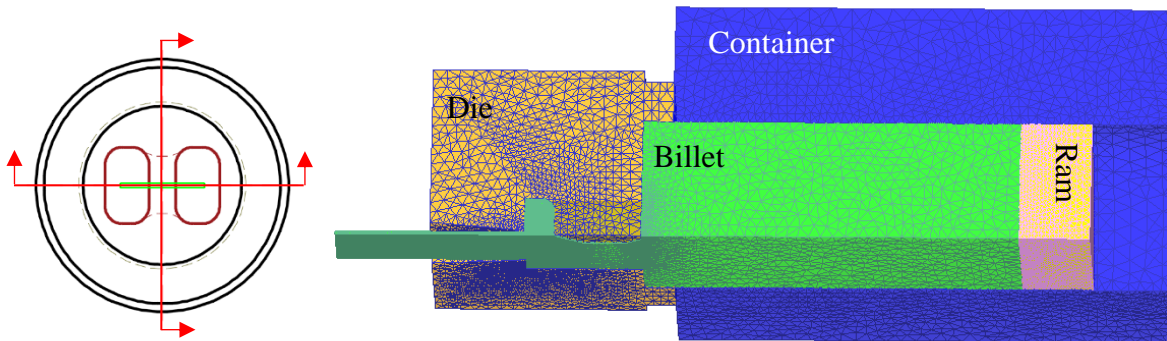


Fig. 4-11 ALE simulation model of symmetric porthole die extrusion

The boundary conditions in the ALE simulation were kept the same as the Lagrangian simulation. Since the ALE simulation does not need frequent remeshing, the computer is able to handle the calculation of more elements in a shorter time. The minimal element size in the ALE simulation was set to be 0.25 mm, which is smaller than the minimal element size in the Lagrangian simulation.

### 4.3.6 Mesh sensitivity

FEM simulation results are always affected by the element size. Small element size gives a more accurate and reliable result than coarse elements, but the simulation time increases exponentially when the element size is refined. In order to balance simulation accuracy and simulation time, it is very important to determine the minimum mesh size needed to ensure accurate simulation predictions. To determine this, several simulation models with different mesh

sizes at the die corner (as Fig. 4-12 and Fig. 4-13) were run to test the mesh size's effect on the simulation predictions. In the Lagrangian simulation, the element size at the corner was reduced from 1.0 mm to 0.4 mm (Fig. 4-12). In the ALE simulation, the element size at the die corner was reduced from 0.6 mm to 0.15 mm (Fig. 4-13), which is much finer than the element size in Lagrangian simulation. Since the ALE simulation does not re-mesh the elements, there is more flexibility to go to a smaller mesh size.

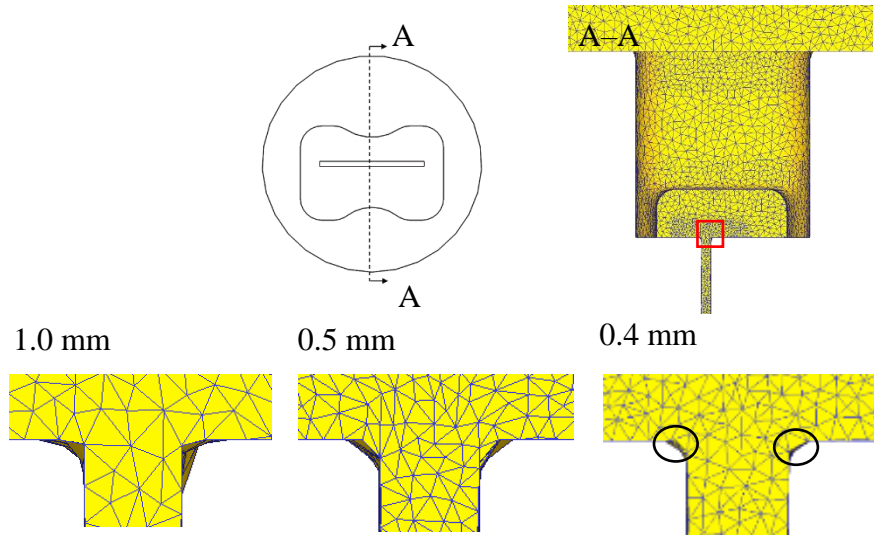


Fig. 4-12 Element size in the Lagrangian simulation (three subfigures in the second row are the blow up of the mesh in the red square).

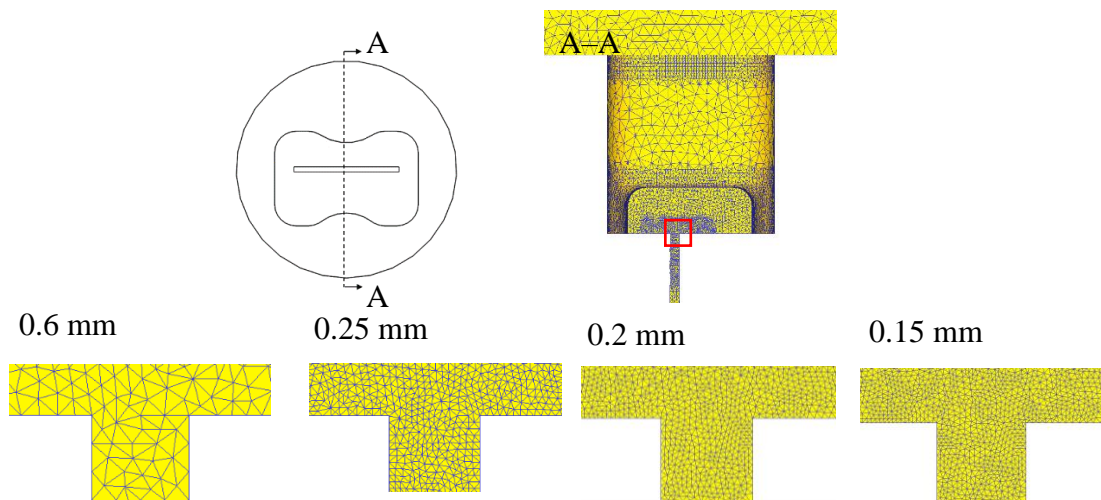


Fig. 4-13 Element size in ALE simulation (four subfigures in the second row are the blow up of the mesh in the red square).

Fig. 4-14 shows the model-predicted strain rate distribution along line 1 mm above the die corner obtained using different element sizes. In Fig. 4-14a, the strain rate obtained from the Lagrangian simulation of 1 mm element size is obviously lower than the strain rate obtained from the Lagrangian simulations of 0.5 mm and 0.4 mm element size. Since the strain rate calculated by the two element sizes of 0.5 mm and 0.4 mm is very close to each other, the 0.5 mm element size was considered to be the optimal element size in Lagrangian simulation. As for the ALE simulation, the 0.5 mm element size gives a higher strain rate, but the strain rate obtained in the simulation of 0.25 mm, 0.2 mm and 0.15 mm element size is almost the same. As a result, the optimal element size for ALE simulation was considered to be 0.25 mm. For our simulations, the mesh size at the die corner is set to be 0.5 mm in Lagrangian simulation, and the mesh size at the die corner is set to be 0.25 mm in ALE simulation. By comparing Fig. 4-14a to Fig. 4-14b, it is clear that the strain rate calculated using the Lagrangian simulation is much lower than that using the ALE simulation. This is because the penetration of the workpiece into the die (encircled by the black ellipse in Fig. 4-12) severely reduces the strain rate at the die corner. On the other hand, the ALE simulation successfully avoids the workpiece penetration into the die, so the ALE simulation gives a more accurate result for the strain rate than Lagrangian simulation.

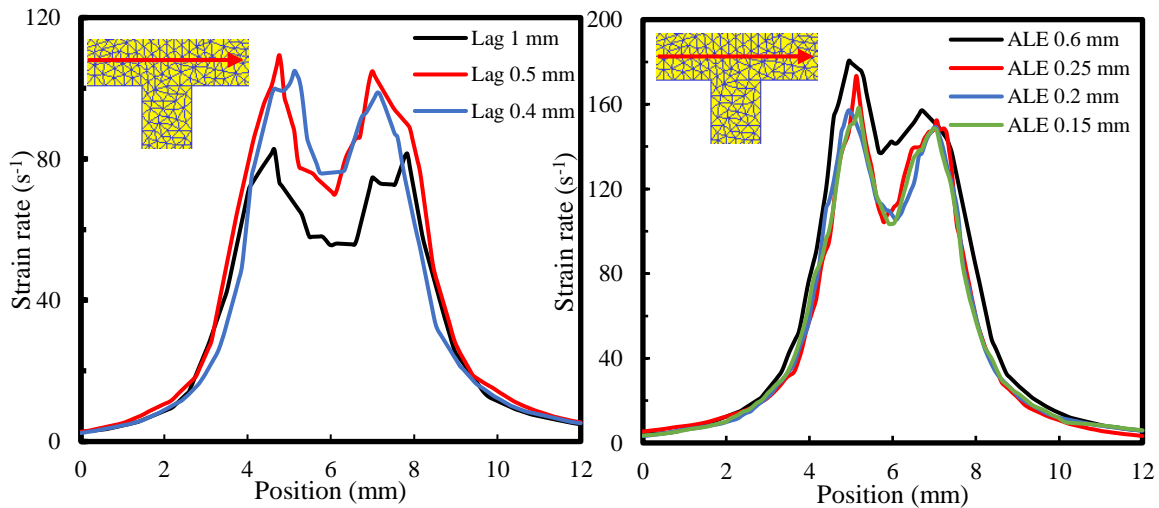


Fig. 4-14 Model-predicted strain rate distribution along line 1 mm above the die corner (red line in the inset figure) calculated by different element sizes: (a) Lagrangian and (b) ALE.

### 4.3.7 Flow path calculation based on ALE simulation

Results from the Lagrangian simulation in DEFORM can provide the flow path of a specific particle during the extrusion process directly. However, due to the high extrusion ratio and complex geometry of this simulation model, re-meshing of the elements happens frequently which can reduce the simulation accuracy and increases simulation time. As indicated earlier, the ALE simulation does not require frequent re-meshing however the DEFORM software does not have a built-in function to calculate the flow path based on the ALE simulation. In order to solve this problem, a MATLAB code to calculate the flow path for a specified location in the extrudate was developed based on the ALE simulation results.

Fig. 4-15 shows a schematic of the flow path calculation based on the ALE simulation results. The DEFORM ALE simulation can provide the velocity field of the workpiece directly, and the flow path is then calculated based on the velocity field. In this research, the flow paths are tracked backwards from the final extrudate through to the original billet. This means the flow paths are tracked back against the velocity direction. As shown in Fig. 4-15, the velocity between the  $i$ th and  $i+1$ th point is assumed to be constant at the velocity of  $i$ th point,  $v_i$ , so the coordinate of  $i+1$ th point ( $a_{i+1}$ ) is determined using Eq. 4-3, where  $dl$  is the displacement between two consecutive points. The time of the  $i+1$ th point is determined by Eq. 4-4, which means it takes  $t_{i+1}$  for the back tracked point to flow from the position of the  $i+1$ th point to the original point. If the displacement increment  $dl$  is small enough, the flow path can be obtained using the MATLAB code very precisely. Mahmoodkhani used and verified this calculation method to model the formation of the transverse seam formation during billet on billet extrusion, and a comparison between the experimental results and model predictions verified that the calculation was accurate [106].

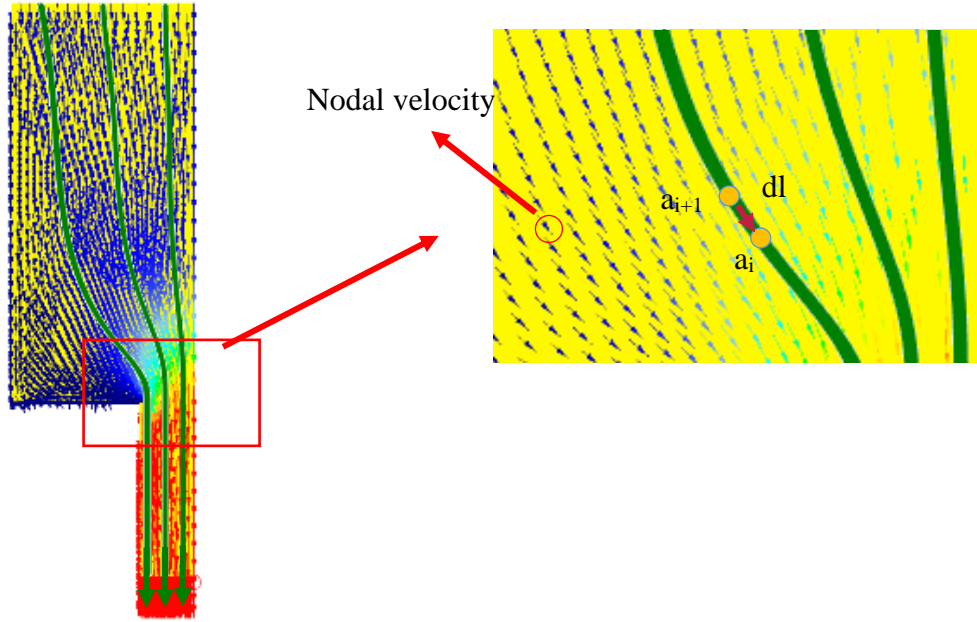


Fig. 4-15 Schematic drawing of point tracking based on ALE simulation.

$$a_{i+1} = a_i - \frac{\vec{v}_i}{|v_i|} \times dl \quad 4-3$$

$$t_{i+1} = t_i - \frac{dl}{(|v_i| + |v_{i+1}|)/2} \quad 4-4$$

## 4.4 Material characterization

### 4.4.1 Metallography

Samples from the extrusion trials were cut and mounted so they could be visualized optically. The metallographic samples were cold mounted using resin epoxy and ground using silicon carbide grinding paper (240 / 480 / 600 / 1200 / 2400 grade). After grinding, the samples were cleansed using ultrasound cleaners to remove debris left on sample surfaces. Then, the samples were polished using 3 and 1  $\mu\text{m}$  diamond spray until no scratches were visible under the microscope.

In order to reveal the grains under optical microscopy, metallographic samples were anodized before observation. The specimen was connected to an anode, while a piece of pure aluminum was used as the cathode. Barker's reagent, which is a mixture of 6 ml (48%)  $\text{HBF}_4$  and 200 ml distilled water, was used to anodize the samples at room temperature. The voltage of the power supply was

set to be 30V. The sample was immersed into the reagent and anodized for about 60 s. After anodization, specimens were observed using an Olympus BH2-UMA microscope.

#### **4.4.2 Electron backscattered diffraction (EBSD)**

EBSD was used to characterize the microstructure and micro-texture of the samples. The specimens were first ground and polished in the same way for metallography observation as noted above. Then, these specimens were given a final polish using colloidal silica, and cleansed using ethanol in an ultrasonic bath for five minutes. All of the EBSD measurements were conducted at the University of British Columbia using a Zeiss-Sigma SEM equipped with a Nikon high speed camera. The EBSD tests were done using the following parameters: accelerating voltage is 20 kV, working distance is 13 mm and the step size is 200 nm. EDAX / TSL-OIM Analysis (6th edition) software was used to process the data obtained from the SEM, and only the FCC phased matrix was indexed.

#### **4.4.3 Tensile test**

Tensile tests were done using an Instron servo-electric mechanical testing machine at room temperature with a strain rate of  $0.001 \text{ s}^{-1}$ . The tensile test samples were cut in a direction vertical to the extrusion direction such that the welding seam was in the middle of the tensile sample gauge length. Since the width of the strips was too small to cut standard tensile tests, miniature dog bone shaped tensile test samples were used in this research, whose dimensions are shown in Fig. 4-16. According to the research by Rahmaan et al [107], the miniature specimen can serve as a good alternative for ASTM (E 8M-04) specimen, for their strain – stress curve coincide with each other before the UTS.

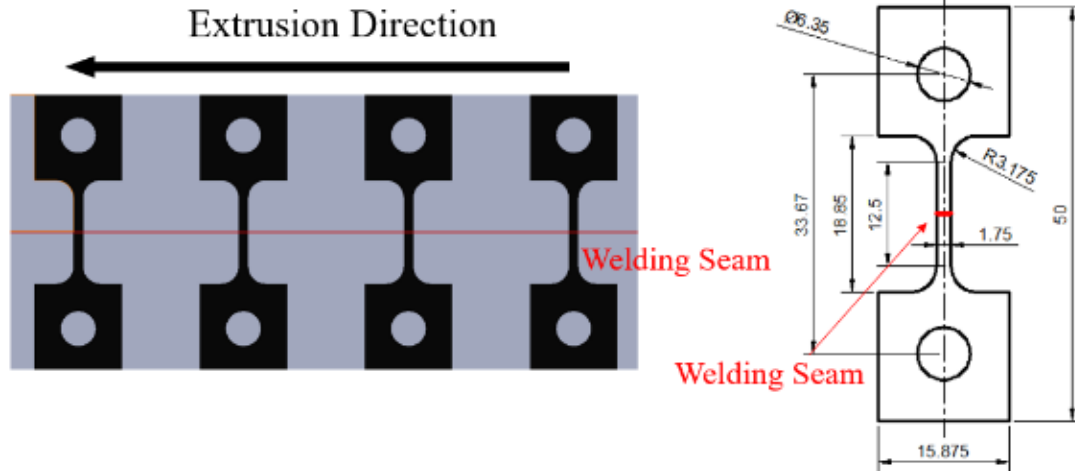


Fig. 4-16 Tensile test samples.

Extensometers used in common tensile test are only able to measure the average deformation in the gauge length, while unable to determine the non-uniform deformation that can occur along the gauge length in a tensile test. In order to examine the different deformation behaviors between the weld seam and matrix, digital image correlation (DIC) aided tensile tests were conducted. DIC aided tensile test consists of three parts: tensile test machine, high speed camera and a computer with the DIC software. Before the tensile test, the test specimens were painted with a base of white and then very fine black spots (a speckle pattern) were sprayed on the white color. During the tensile test, numerous photos (400 per min) of the deforming specimens were taken by the Titanar 2 8/50 high speed camera. Finally, the DIC software Aramis v6 gave the strain distribution in the interested area by comparing the reference image and deformed image based on a series of correlation algorithms [108].

# Chapter 5 Results and discussion

## 5.1 Extrusion trials

### 5.1.1 Typical microstructure

As stated earlier, six consecutive billets were extruded using the porthole dies during each extrusion trial. A typical microstructure cross-section for the extruded strip is shown in Fig. 5-1 for a sample extruded from Trial 1 (Die C / 12.7 mm / Asym). Referring to Fig. 5-1, all of the extruded samples show evidence of PCG at the surfaces of the sample and this PCG layer becomes “piled up” at the weld seam in the form of a triangle, and the thickness of the PCG keeps relatively stable among the samples extruded from the different billets during each trial. As shown in Fig. 5-1, the thickness of the PCG at the weld region of the profiles extruded from different billets in Trial 1 is about 500  $\mu\text{m}$ . The PCG thickness of the profile extruded from the fourth billet (Fig. 5-1d) seems to be slightly thinner than the profiles extruded from the other five billets. That may be due to the unexpected ram speed fluctuation when extruding the fourth billet, and the ram speed’s effects on the PCG thickness will be further discussed in Section 5.4.

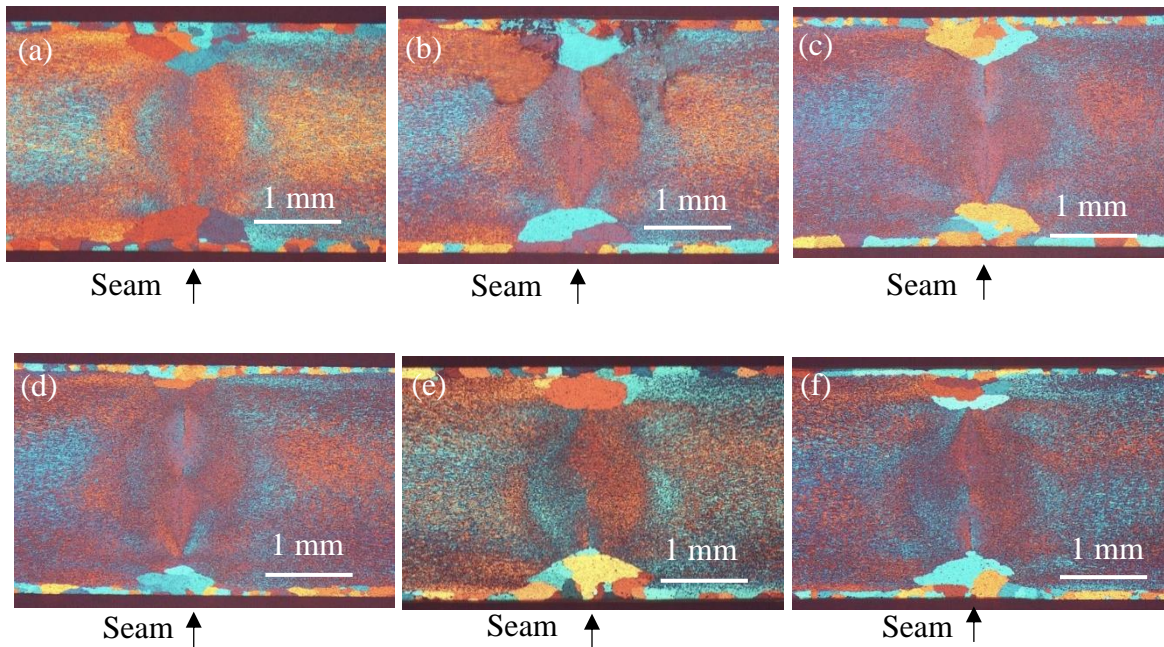


Fig. 5-1 Metallography of extruded profile cross section for samples (T5) taken from six consecutive billets during Trial 1: (a) first billet, (b) second billet, (c) third billet, (d) fourth billet, (e) fifth billet and (f) sixth billet.

Further characterization of the material was done using material from the sixth billet that was extruded. In order to understand the changes in the microstructure and texture from the weld seam to the adjacent material and then further away into the matrix material, EBSD analysis was done both at the weld seam but also a quarter width position in the matrix. This provided an opportunity to understand how changes to the die geometry were influencing the thermomechanical history and the microstructures and textures that formed along the weld line. Tensile tests of the extruded material were also conducted so that these could be compared to the material that was extruded with no weld seam.

### **5.1.2 As-deformed microstructure (low temperature extrusion)**

#### **5.1.2.1 Absence of PCG at the weld seam**

Low temperature extrusion trials were conducted at 400 °C to try and inhibit recrystallization and maintain the as-deformed microstructure. As shown in Fig. 5-2, the PCG layer of material extruded at 400 °C was not thick compared to material which had been extruded at 480 °C. The absence of PCG layer along the weld seam region during low temperature extruded samples indicates that the formation of the PCG layer may be related to the high surface temperature. Referring to Fig. 5-2, samples extruded using Die C and Die E had very different colour contrasts along the weld seam region, and the unique colour contrasts observed under polarized light microscopy are believed to be closely related to the different textures that form in the weld seam region. The inhibition of recrystallization at low temperature provides an opportunity to study the effect of the extrusion conditions on the as-deformed microstructure and texture as well as the mechanical properties of the extruded samples in the absence of recrystallization.

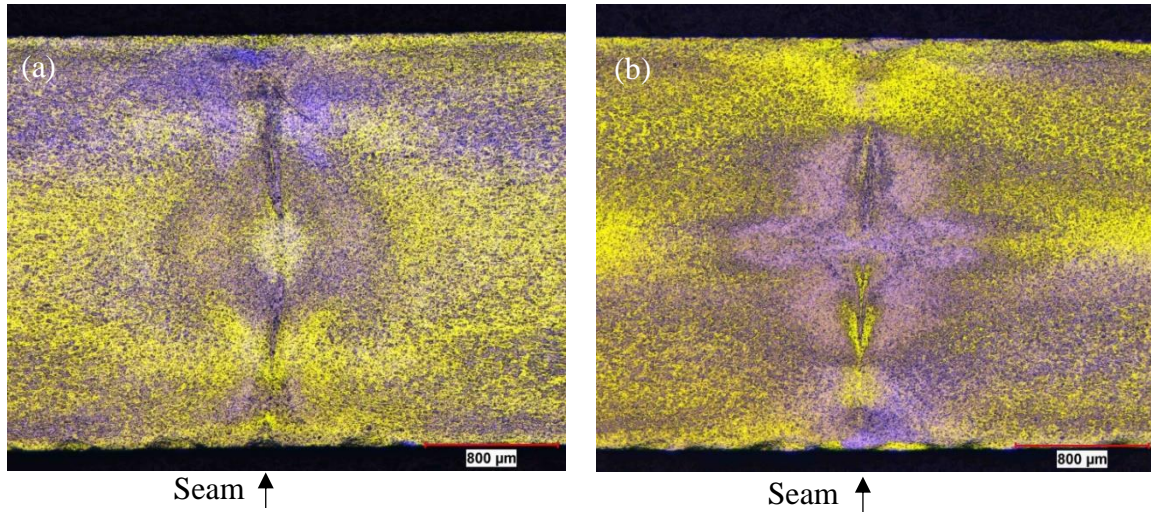


Fig. 5-2 Metallography of the seam (T4) extruded at 400 °C using (a) Die C / 12.7 mm / Sym (Trial 16) and (b) Die E / 12.7 mm / Sym (Trial 17).

### 5.1.2.2 Microstructure away from the seam

Fig. 5-3 is an assembly of images showing the microstructure of the strip cross section through its thickness from the weld seam to the strip edge. Referring to Fig. 5-3, we can see evidence of PCG around the periphery of the strip with a slightly higher thickness at the strip edge relative to its top and bottom. We also see an enhanced level of PCG along the top and bottom of the weld seam region. In the case of material extruded at 400 °C (Fig. 5-3c and d), the PCG along the top and bottom including the weld seam area has been suppressed but is still evident along the strip edges.

Despite the microstructure feature differences at the weld seam region between Die C and Die E samples, most parts of the material away from the seam exhibited very similar microstructure feature regardless of differences in die geometries and extrusion temperatures. The microstructure changes from the weld seam to the strip edge reveal that the bridge geometry's effects on the porthole die extrusion were limited to the weld seam region and the material adjacent to this. Farther away from the weld seam, the microstructure was similar regardless of the die configuration used.

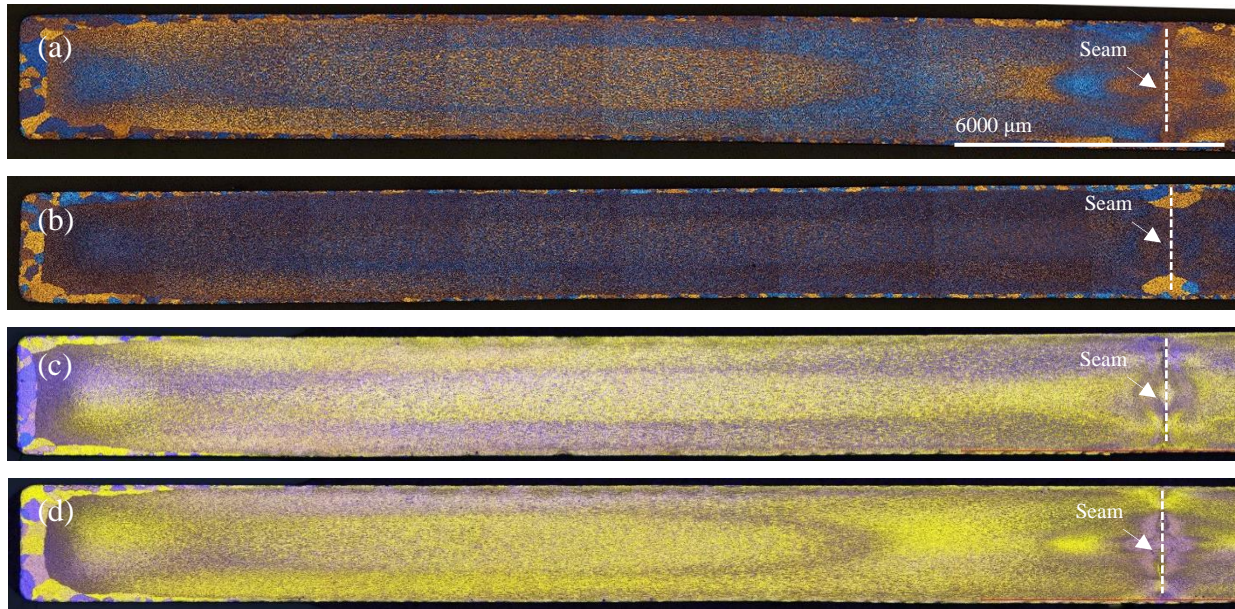


Fig. 5-3 Microstructure variation from the seam to the edge (T4): (a) Die C / 25.4 mm / Sym (480 °C) (Trial 14), (b) Die E / 25.4 mm / Sym (480 °C) (Trial 15), (c) Die C / 12.7 mm / Sym (400 °C) (Trial 16) and (d) Die E / 12.7 mm / Sym (400 °C) (Trial 17).

### 5.1.3 Typical texture

The optical metallography was only able to show the coarse grains at the surface clearly, but it was unable to reveal the grain morphology and texture due to its low resolution. In this research, EBSD tests were also conducted to study the detailed changes in the microstructure and texture of the extruded sample at a range of locations both along the weld seam and away from it at a quarter width region (Fig. 5-4).



Fig. 5-4 Regions studied by EBSD: Weld (seam) region and quarter width region.

#### 5.1.3.1 Texture at the weld seam

Fig. 5-5 shows the EBSD results along the weld seam region for a sample (0.4 mm on either side) extruded in Trial 1 at 5 mm/s and 480 °C. The weld seam region of this sample consists of three parts: the seam (highlighted with a dashed line), the purplish red texture (close to the seam) and the green texture. As shown in this figure, the grains along the seam are coarser and have a

different orientation compared to the neighboring grains. The inverse pole figure also shows the texture along the weld seam.

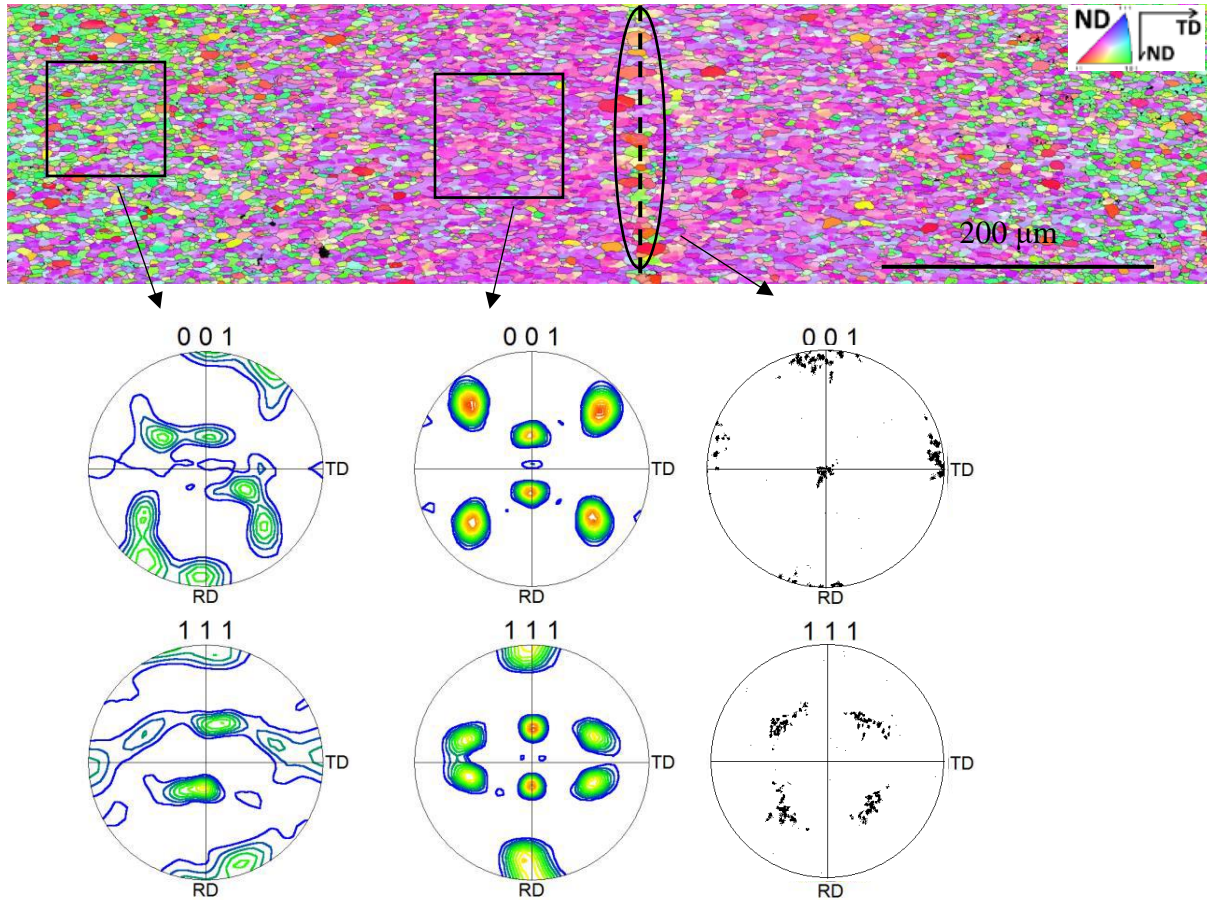


Fig. 5-5 EBSD image (inverse polar figure) and pole figure of weld seam region of samples (T5) extruded by Die C / 12.7 mm / Asym at 5 mm/s and 480 °C (Trial 1).

### 5.1.3.2 Quarter width texture

The EBSD images (Fig. 5-6) show the grains at the quarter width region are pancaked in the thickness direction, which is due to much higher compression strain in the thickness direction compared to the width direction. Referring to Fig. 5-7, the polar figure of the quarter width region is very different from the polar figure of the seam region (Fig. 5-5), which indicates the texture at the matrix is very different from the seam region. To further study the texture of the porthole die extruded samples, an area within a deviation angle of  $15^\circ$  from the idea texture component is used to quantify each texture's fraction and its results are summarized in Table 5-3. In the quarter width region of the extruded samples, the major texture components are deformation texture, S, brass

and copper. On the other hand, the recrystallization texture, cube and goss, only account for a negligible fraction.

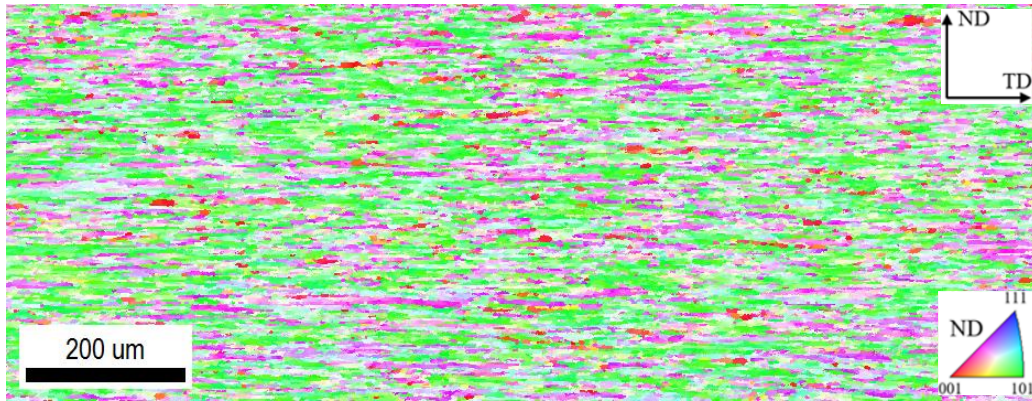


Fig. 5-6 EBSD images (inverse polar figure) of quarter width region of strips (T5) extruded by Die C / 12.7 mm / Asym (Trial 1).

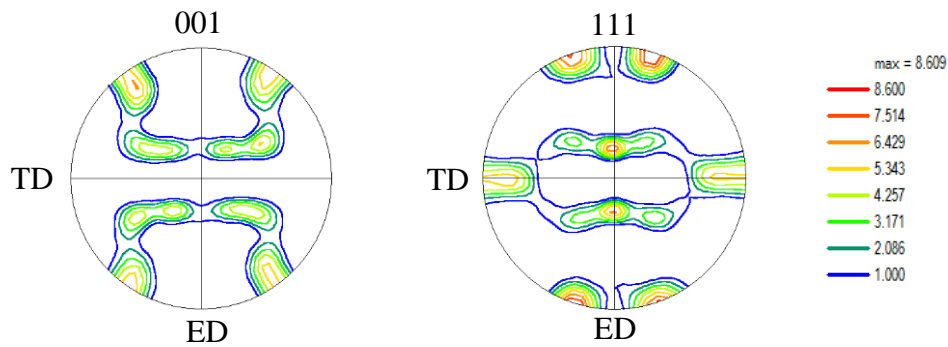


Fig. 5-7 Pole figures of quarter width region of strips (T5) extruded using Die C / 12.7 mm / Asym (Trial 1).

Table 5-1 Identified area fraction of texture components at the quarter width region of samples extruded using Die C / 12.7 mm / Asym (Trial 1).

Die Configurations	copper (%)	brass (%)	S (%)	cube (%)	Goss (%)
Die C / 12.7 mm / Asym	10.7	30.4	52.7	2.2	0.2

## **5.1.4 Mechanical properties of profiles**

### **5.1.4.1 Stress-strain curves**

Before elaborating on the details of the porthole die extruded sample's mechanical properties, the reliability and repeatability of the tensile tests will be discussed. In this thesis, four tensile samples were cut from each extruded profile to measure the reliability and repeatability of the testing results. Referring to Fig. 4-16, the specimens were cut in the direction transverse to extrusion direction and the gauge length is 12.5 mm. Fig. 5-8 shows the measured results of the stress-strain curve from four T5 treated samples taken from the Die C / 12.7 mm extruded sample at a ram speed of 5 mm/s (Trial 1). Before reaching the ultimate strength at the strain about 6%, the four stress strain curves are almost identical with only some small differences. After the peak strength, the stress-strain curves begin to diverge but the differences still remain small. The ultimate strength differences among samples cut from the same extruded profile are within 5 MPa. For example, the ultimate strength of Sample #4 is 341 MPa, and the ultimate strength of Sample #3 is about 345 MPa. At the final fracture stage, there are some differences between the four curves. For instance, Sample #1 fractures at a strain of 9.6%, but Sample #3 fractures at the strain of 10.6%. Based on the above discussion, the strength of tensile samples is very consistent, but the fracture elongation varies more and based on the test results is on the order of ~1%.

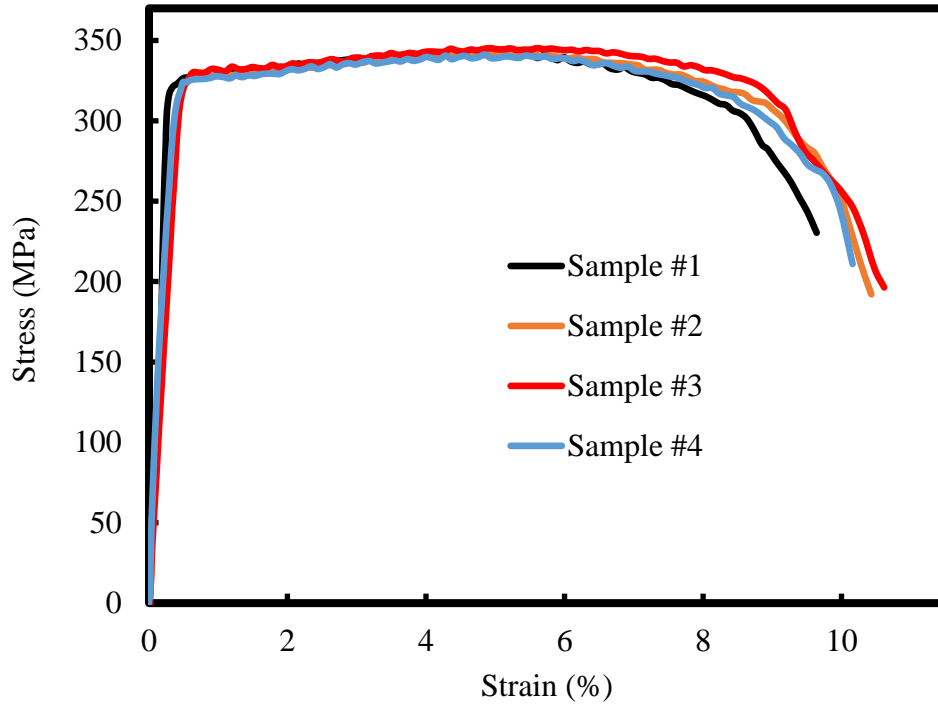


Fig. 5-8 Measured stress-strain curve showing the repeatability of the tensile tests (T5 treated Trial 1 extruded samples).

Table 5-2 Tensile properties of each tensile specimen taken from T5 treated Trial 1 extruded profile.

Sample No.	Yield Strength (MPa)	Ultimate Strength (MPa)	Strain to failure (%)
#1	326.5	342.6	9.6
#2	325.7	342.6	10.4
#3	324.5	345.3	10.6
#4	324.5	341.2	10.1

Fig. 5-9 shows a comparison between the measured engineering stress–strain curve of an extruded profile with a weld seam and an extruded profile without a weld seam that were both extruded under the same conditions. All of these samples were extruded, and artificial aged at 175 °C for 8 hours to get a T5 condition. As shown in Fig. 5-9, the ultimate strength of the porthole die extruded specimens is 345 MPa, and the failure elongation is about 9 - 10%. The seamless sample's strength is almost the same as the porthole die extruded samples, while the elongation is

significantly higher than the porthole die extruded samples. Therefore, the existence of a weld seam in the extruded samples does not affect the strength, but severely deteriorates the ductility.

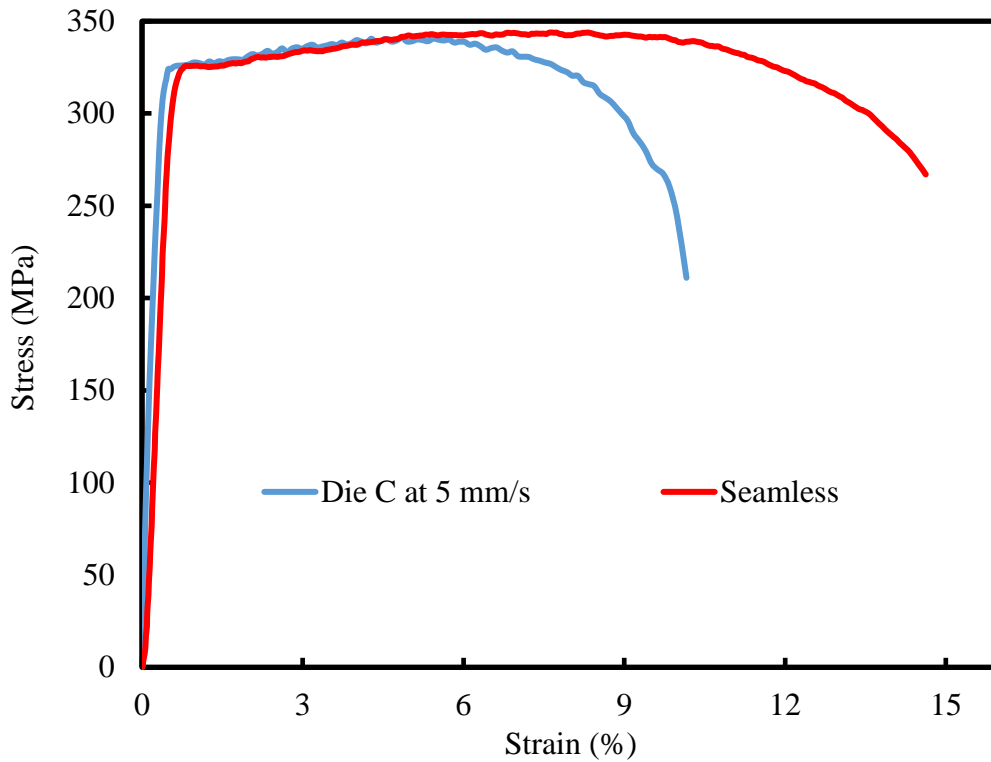


Fig. 5-9 Tensile properties of T5 treated porthole die extruded samples.

Fig. 5-10 shows the geometry and size of fracture surface of tensile specimens. All of porthole die extruded specimens fractured at the seam as Fig. 5-10c, which proves that the seam is the weakest part of the profile. On the other hand, the seamless sample fractured at a random location of the gauge length. Area reduction is defined as Eq. 5-1 in this thesis. The fracture surface area of each sample was measured using Image J software. As shown in Table 5-3, the seamless specimen has the highest reduction in an area of 0.56, which means the seam reduces the material's ductility significantly.

$$\text{Area reduction} = 1 - \frac{\text{fracture surface area}}{\text{undeformed cross section area}} \quad 5-1$$

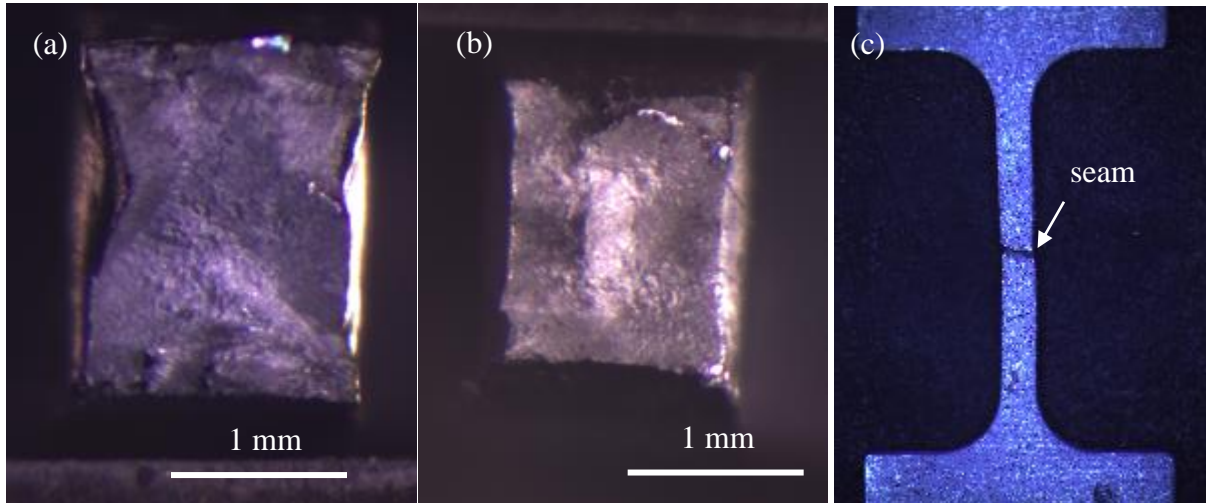


Fig. 5-10 Fracture surface of tensile samples (T5): (a) Die C / 12.7 mm / Asym (Trial 1), (d) seamless (Trial 11) and (e) front view of fractured porthole die extruded specimen.

Table 5-3 Area reduction of tensile specimens

	Die C	Seamless
Area reduction	0.35	0.56

The reduction of area is often reported as additional information (to the percent elongation) to quantify the deformation characterises of a material. These two parameters are often used as indicators of ductility, the ability of the material to be elongated in tension. Because the elongation is not uniform over the entire gauge length and is greatest at the centre of the neck, the percent strain or elongation is not an absolute measure of ductility.

Fig. 5-11 shows the fracture surfaces of extruded samples under SEM observation. The porthole die extruded specimens exhibit a dimpled fracture surface, with the dimple size ranging from approximately 5 to 20  $\mu\text{m}$ . The dimpled fracture surface indicates the porthole die extruded specimens fractured in a ductile manner during tensile testing [109].

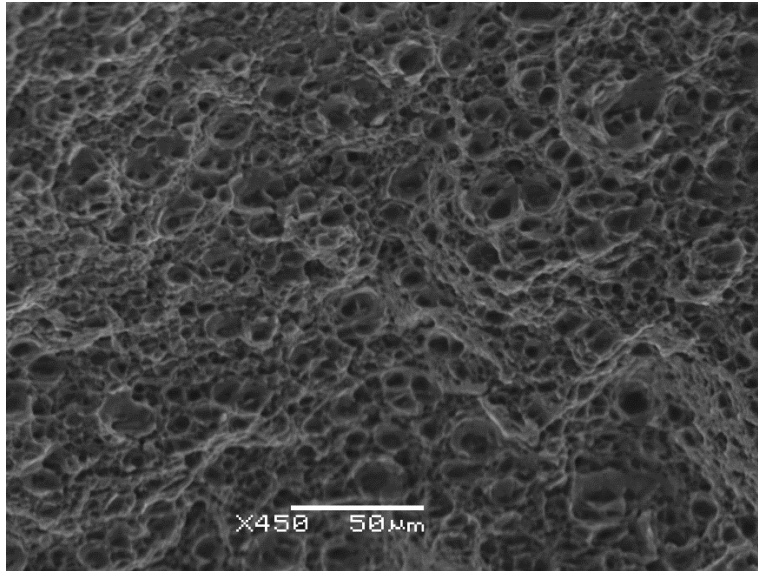


Fig. 5-11 Fractography of porthole die extruded samples (T5) in Trial 1.

#### 5.1.4.2 Tensile test using DIC

The conventional tensile tests can only measure the average strain of the gauge length, but cannot measure the strain distribution. On the other hand, it is very reasonable to assume the strain distribution is not uniform due to the existence of the weld seam in the middle of the test specimen. In order to study how the weld seam can affect the mechanical property of the specimen, tensile tests done using DIC were conducted to measure the evolution in the strain distribution along the gauge length of the tensile specimens during the tensile test. In addition to the test specimens with a weld seam in the middle, a seamless specimen's strain distribution was also measured for comparison.

Fig. 5-12 shows an image of a speckled DIC specimen with white paint and black dots. The seam is in the middle of the specimen, and the strain distribution along the 8 mm white line was measured using the DIC system. As shown in Fig. 5-12a, the strain becomes localized at the seam region of the porthole die extruded specimens when the elongation is only 1%, but the test specimen without a weld seam has a uniform strain distribution (Fig. 5-12a). During the tensile test, the strain of the porthole die extruded specimens continues to localize at the seam. When the elongation is 7%, the strain at the middle of Die C specimen is about 0.16, while the strain is only 0.05 at the location of 3 mm away from the seam (Fig. 5-12c). The test specimen without a seam has a much more uniform strain distribution, even when the elongation reaches 7%. It indicates

that the non-uniform distribution of strain in the test specimens with weld seams is due to the location of the strain at the weld seam in the middle of the specimen. The EBSD results clearly show that the texture and microstructure at the weld seam are quite different from the texture of the adjacent matrix, so this may be one reason the material exhibits different mechanical properties spatially and leads to a concentration of the strain at the weld seam during tensile deformation.

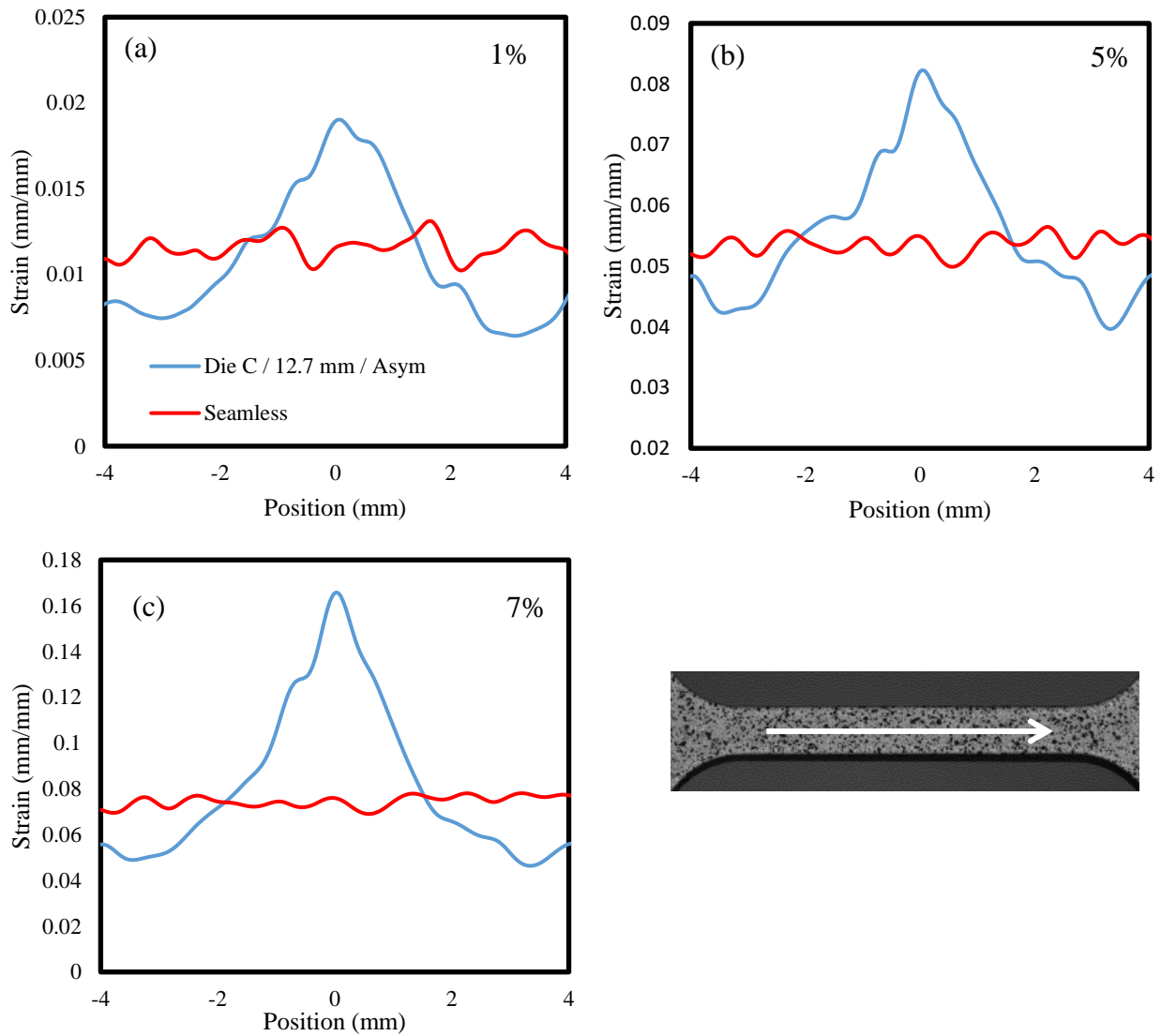


Fig. 5-12 The strain distribution along the white line in the gauge length of T5 heat treated samples (Trial 1): (a) elongation of 1%, (b) elongation of 5% and (c) elongation of 7%.

### 5.1.4.3 PCG influence

According to Chen's research on the extrudate's surface texture mechanical properties, the existence of a PCG layer can alter the mechanical properties of the sample during a tensile test [110]. This is one possible explanation for the strain concentration along the weld seam due to the triangle PCG layer at the weld line, as shown in Fig. 5-13. The triangle PCG layer at the weld line makes the proportion of the PCG versus internal material different from the other parts of the extrudate, which may result in a different mechanical response between the weld seam and the matrix during a tensile test. In order to test this assumption, several samples with the PCG layer removed were prepared for tensile testing. As shown in Fig. 5-13, the PCG layer thickness at the seam is less than 600  $\mu\text{m}$ , so 600  $\mu\text{m}$  of the surface material was removed by machining on each surface to get rid of the PCG completely. After the removal of the PCG layer, the thickness of the tensile specimen was reduced from 2.5 mm to 1.3 mm.

Fig. 5-14 shows the strain distribution along the white line in the gauge length of the sample with and without the PCG layer. In the specimen of full thickness, the strain of the porthole die extruded samples concentrates at the centre, and the maximum strain of the porthole die extruded sample is 3.8% when the elongation is 2.5% (Fig. 5-14a). After the PCG was removed, the strain concentration in the porthole die extruded samples became worse (Fig. 5-14b). When the elongation is 2.5%, the maximum strain in the porthole die extruded sample without the PCG layer is as high as 5.9%. Since the strain concentration did not disappear without the PCG layer, it is very plausible to assume that the triangle PCG layer does not play a role in causing the strain concentration at the weld seam.

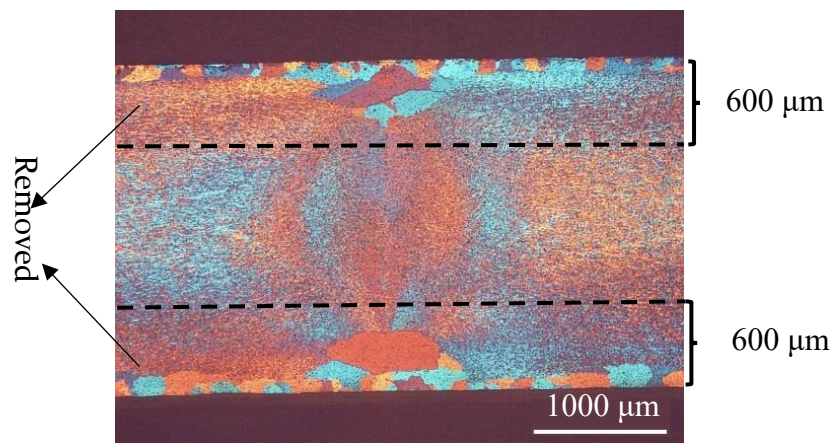


Fig. 5-13 The removal of PCG layer.

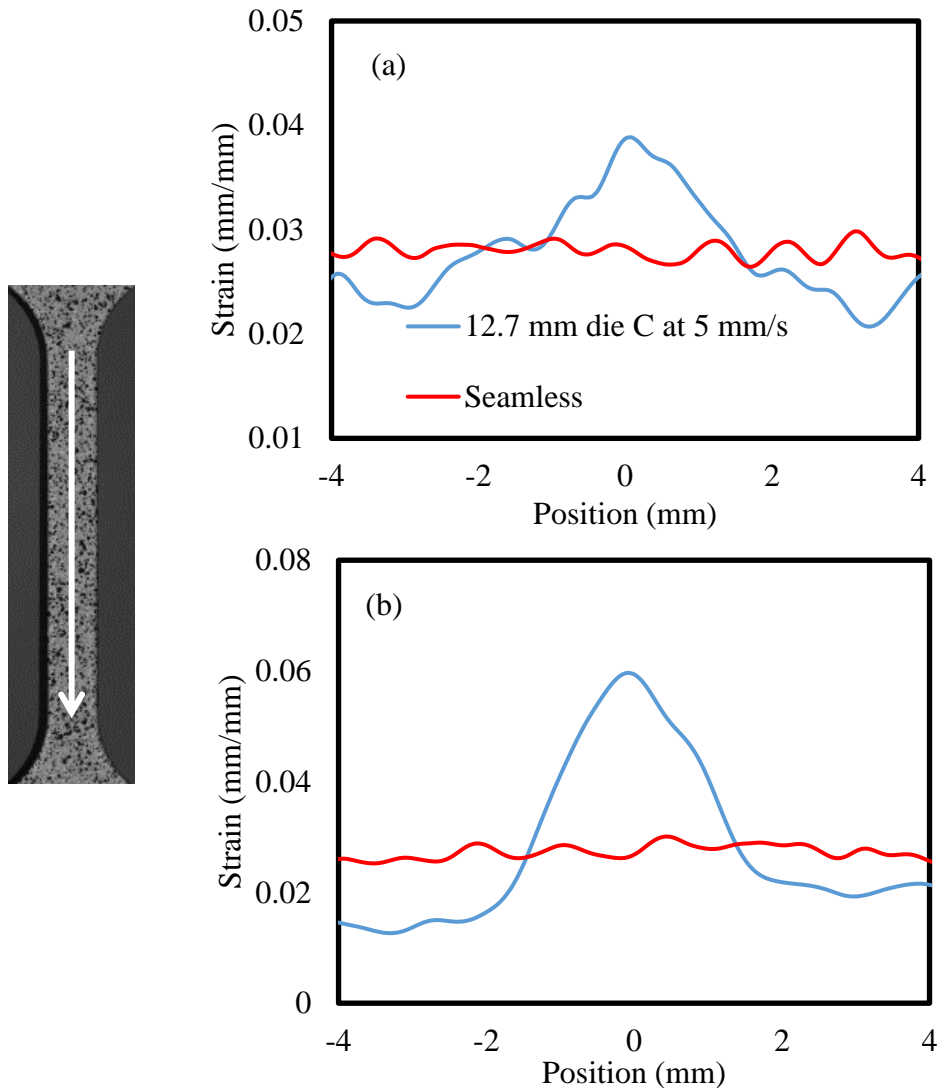


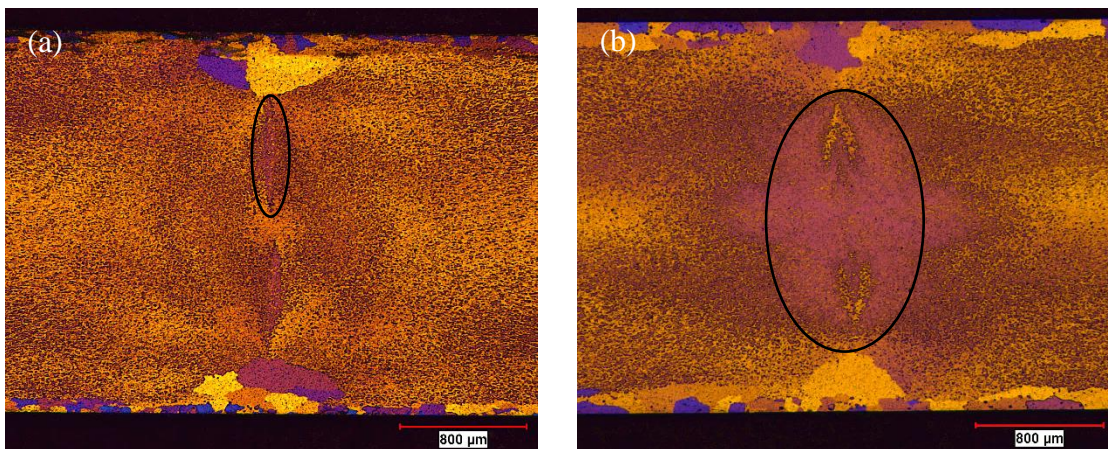
Fig. 5-14 The strain distribution along the gauge length of the T5 heat treated sample (Trial 1) with PCG removed (a) with PCG layer and (b) without PCG layer when the elongation is 2.5%.

## 5.2 Effect of bridge geometry

In this section, the effect of the bridge shape and welding chamber height on porthole die extruded microstructure, texture and mechanical property are outlined. In addition, simulations run using DEFORM were done to help elucidate the experimental results seen in terms of the thermal mechanical history experienced by the material. The information provided in this section can be used as a guideline in terms of the influence on die design on the resulting weld seam microstructure, texture and mechanical properties.

### 5.2.1 Microstructure at the weld seam

Fig. 5-15 shows the metallography of the weld seam region for samples extruded at the ram speed of 4 mm/s using different symmetric die geometries (Die E: flat versus Die C: streamlined) as well as different weld chamber heights (12.7 mm versus 25.4 mm). Referring to Fig. 5-15, all of the weld lines exhibited a triangular PCG surface layer at the weld line. The PCG layer thickness at the weld line does not appear to differ between the different die geometries or welding chamber heights and maintains a thickness of about 400  $\mu\text{m}$ . However, the microstructure features along the weld line do appear to be affected by the die geometries. In the samples extruded using Die C / 12.7 mm, there exists two bi-convex structures along the weld line, and one of them is encircled by the black eclipse as shown in Fig. 5-15a. On the other hand, the bi-convex structures disappear in the sample extruded using Die C / 25.4 mm (Fig. 5-15c). The sample extruded using Die E / 12.7 mm appears to have an oval shaped structure at the weld line (encircled by back eclipse in Fig. 5-15b), which has a different colouring compared to the surrounding material. When the welding chamber height increased from 12.7 mm to 25.4 mm, the Die E / 25.4 mm extruded sample has bi-convex structures (encircled by back eclipse in Fig. 5-15d) similar to the biconvex structures observed in the sample extruded using Die C / 12.7 mm. Since the metallography was prepared by anodizing with Barker reagent and observed under polarized light, the color contrast reflects the grain orientation namely texture of the sample [111].



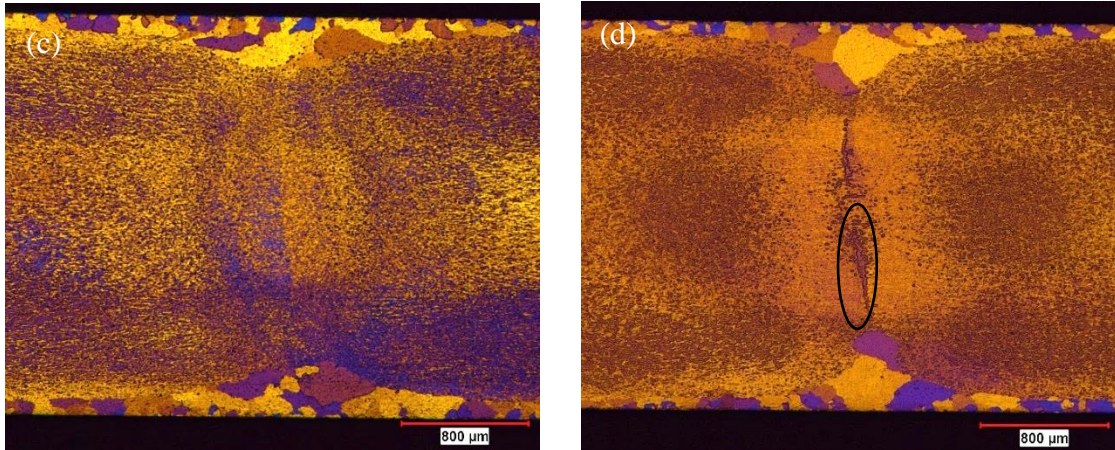


Fig. 5-15 Metallography at the weld seam of samples (T4) extruded using different die configurations: (a) Die C / 12.7 mm / Sym (Trial 12), (b) Die E / 12.7 mm / Sym (Trial 13), (c) Die C / 25.4 mm / Sym (Trial 14) and (d) Die E / 25.4 mm / Sym (Trial 15).

## 5.2.2 Texture analysis

### 5.2.2.1 Weld seam and adjacent area

The transition from the weld seam texture to the matrix texture was thoroughly studied to understand the spatial range of the bridge's influence on the porthole die extruded sample. As shown in Fig. 5-16, the area examined using EBSD covers the weld line and 3 mm away and the full thickness of the profile (except the PCG layer). Due to the extremely large area, the EBSD sensor was unable to scan the whole area at one time. Instead, nine consecutive EBSD images were scanned and stitched together to cover the whole area as shown in Fig. 5-16. In this way, it is possible to study the texture transition from the weld seam region into the adjacent material.

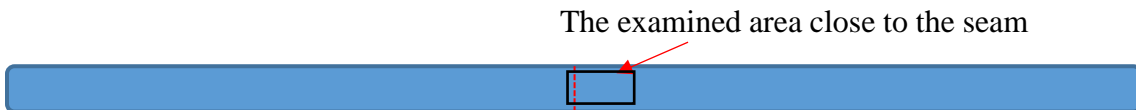


Fig. 5-16 The examined are by EBSD close to the seam.

Fig. 5-17 shows the inverse pole figure of the region close to the seam of the sample extruded using Die C / 12.7 mm / Sym. The grains along the weld seam are mainly made up of a copper texture (purplish colour), and minor goss and cube texture (green and red colour respectively). By comparison between the EBSD image and the metallography (Fig. 5-15a), the biconvex structure

of different colour contrast along the weld seam from the optical metallography image is identified to be goss and cube texture. At a region 1.5 mm away from the weld seam, the texture is mainly brass plus a very small fraction of cube (Fig. 5-17c) at the mid-thickness location. The texture at a further region which is 3 mm away from the weld line (Fig. 5-17d) has almost the same texture at the region 1.5 mm way form the weld line. The EBSD characterization shows Die C bridge's influence is very prominent up to 1.5 mm away from the weld seam in terms of the texture, and the texture changes sharply from the weld line to the neighbouring region. However, the texture become relatively stable and does not change significantly at the region more than 1.5 mm away from the weld line.

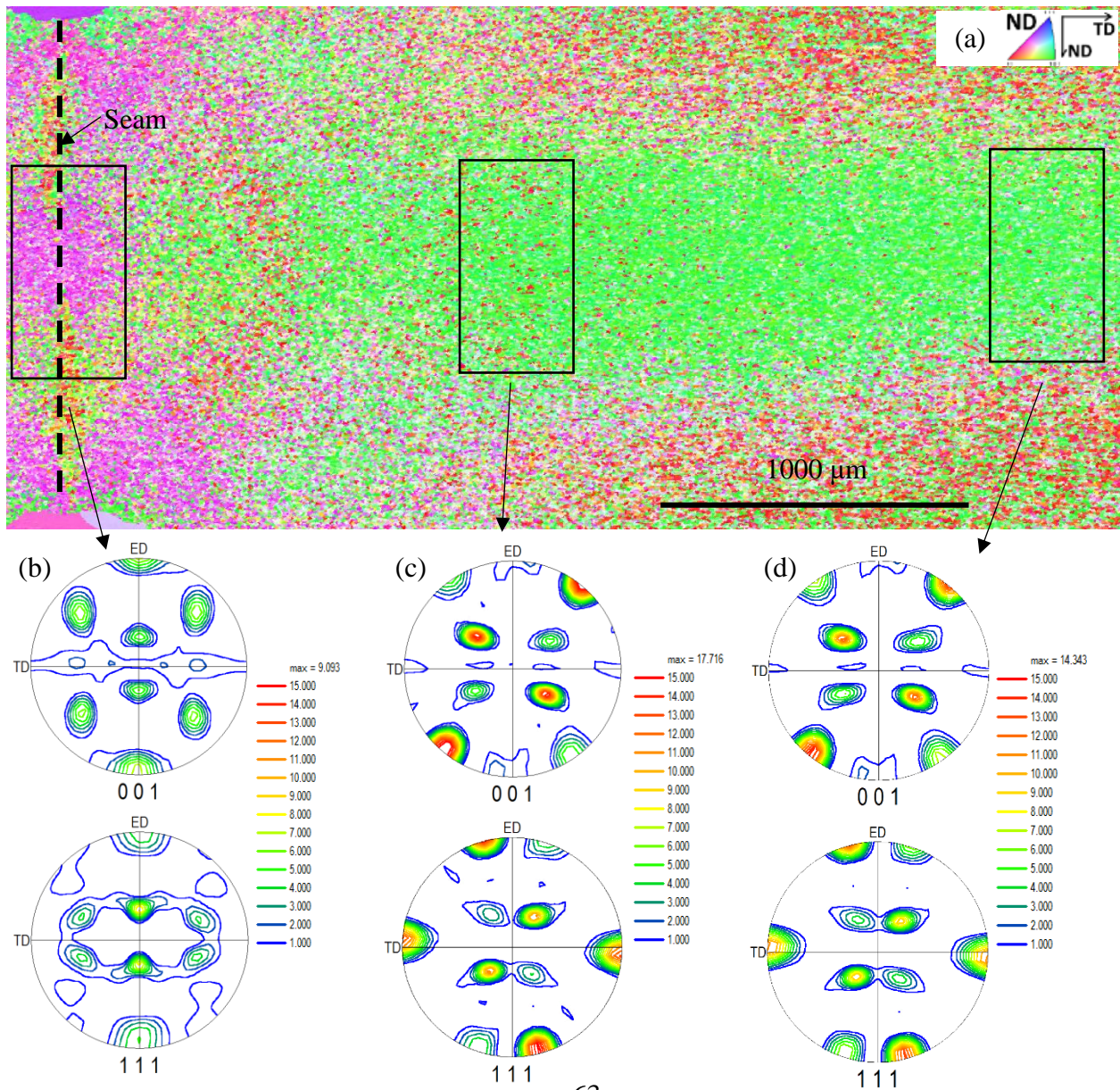


Fig. 5-17 (a) EBSD image (inverse pole figure) of a region close to the weld seam for the sample (T4) extruded using Die C / 12.7 mm / Sym (Trial 12), b) associated pole figure for the weld seam , (c) 1.5 mm away from the weld line and (d) 3 mm away from the weld line.

Fig. 5-18 shows the inverse pole figure of the region close to the weld seam of the sample extruded using Die E / 12.7 mm / Sym. As can be seen, a very different texture is observed for this case where a flat die is used and the material at the weld line is made up of mainly goss and cube texture (green and red colour respectively) plus a small fraction of brass texture (purplish colour). At a region about 1.5 mm away from the weld line, the texture is also made up mainly of the brass texture with some minor goss and cube texture. Moreover, the pole figure of the region 1.5 mm away from the weld line (Fig. 5-18c) is not symmetric to the TD and ED axis, which indicates that part of material experienced a strong shear force during porthole die extrusion. At a region 3 mm away from the weld line, the material is almost all brass texture, and the pole figure (Fig. 5-18d) for material extruded using Die E (the flat die) is almost the same as the pole figure (Fig. 5-17d) of the same area in the sample extruded using the streamlined die (Die C). The texture analysis of the strip extruded using Die E shows that the influence of Die E appears to expand to a region ~3 mm away from the weld line. However, at a region 3 mm away from the weld line, samples extruded using Die C and Die E have very similar textures; the bridge shape influence is very small at regions 3 mm or more away from the weld line.

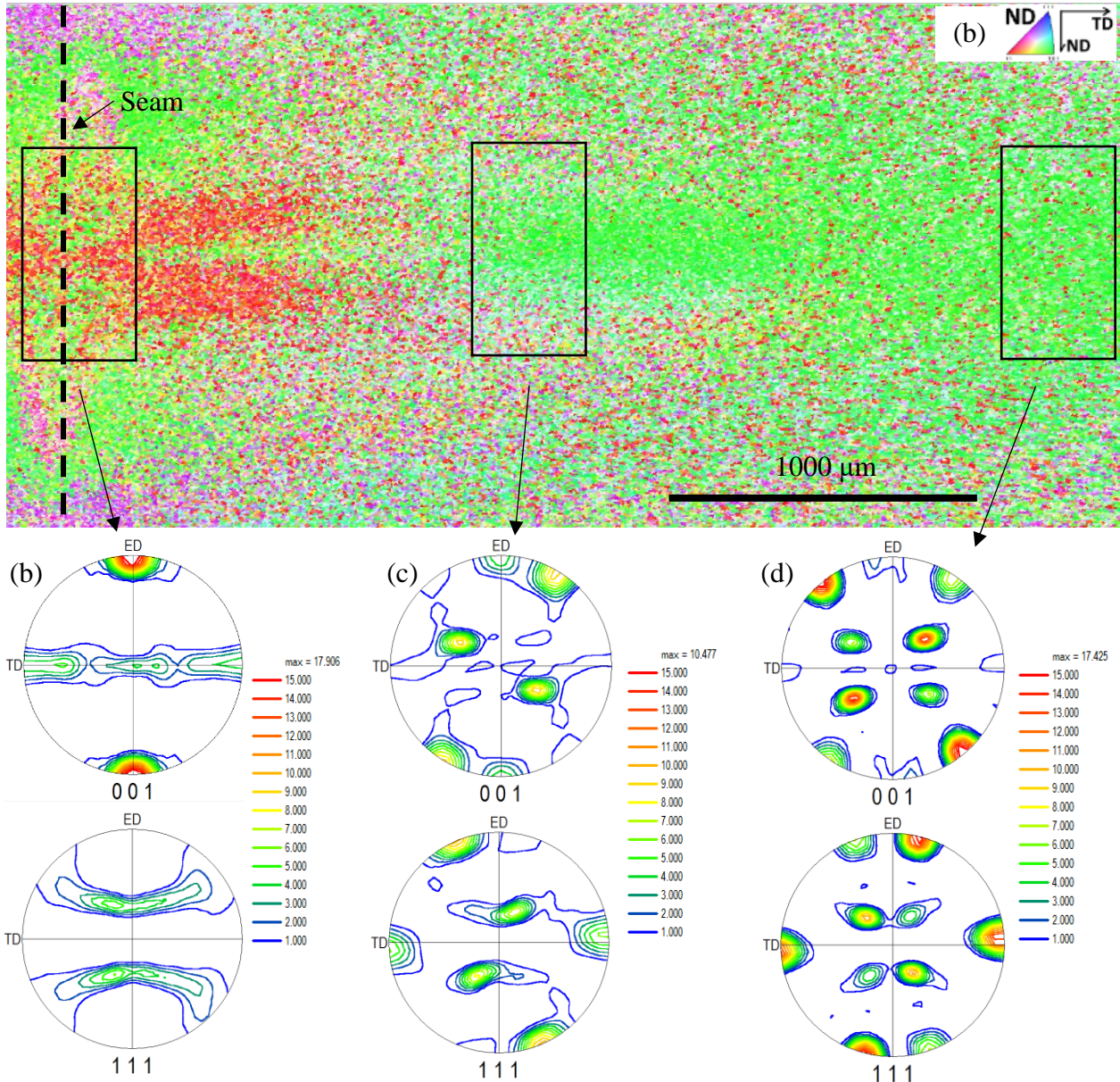


Fig. 5-18 a) EBSD image (inverse pole figure) of the region close to the seam in the sample (T4) extruded by Die E / 12.7 mm / Sym (Trial 13), and the pole figure of region at (b) the weld line, (c) 1.5 mm away from the weld line and (d) 3 mm away from the weld line.

### 5.2.2.2 Matrix

The quarter width region was examined using EBSD to study the microstructure and texture in the matrix far away from the weld seam. As shown in Fig. 5-19, two regions at the quarter width were selected to be characterized using EBSD, one at a mid-thickness location (QC) and the other close to the surface (QE).

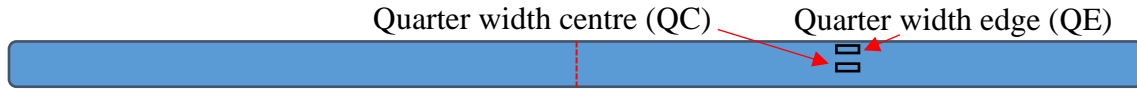
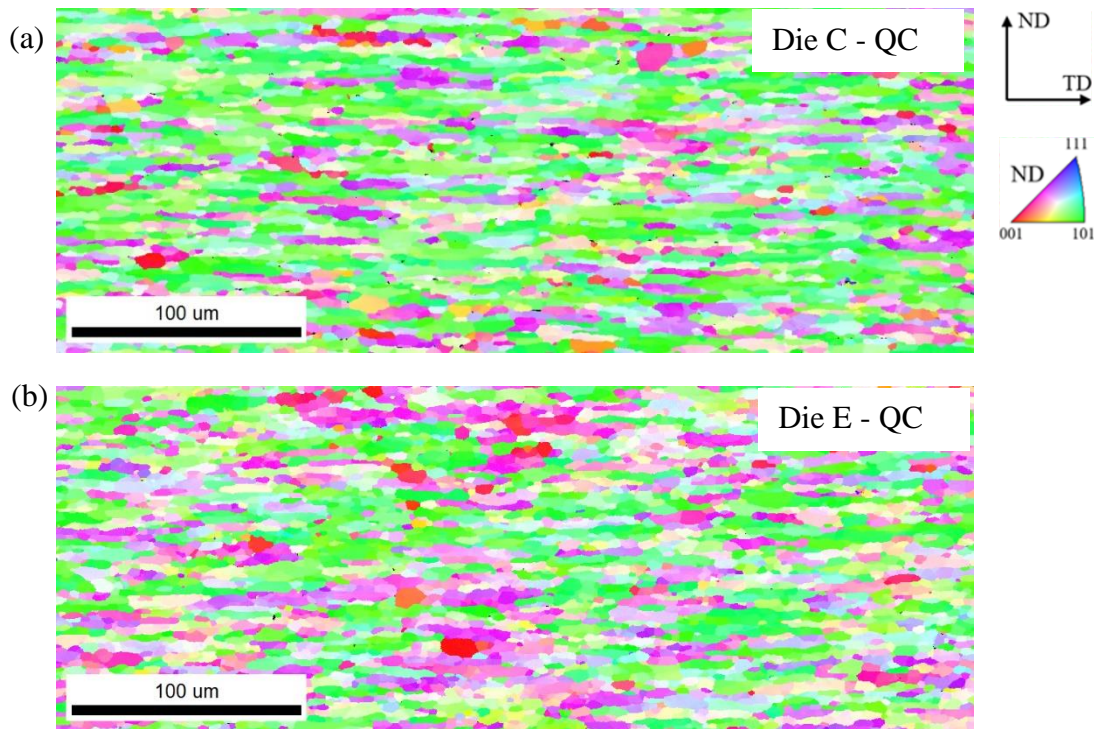


Fig. 5-19 The regions examined by EBSD at the quarter width: quarter width centre (QC) and quarter width edge (QE).

Fig. 5-20 shows the inverse pole figure of the microstructures at the quarter width location of the samples extruded using symmetric dies. Due to a larger reduction in the ND direction compared to the TD direction, the microstructure is compressed in the ND direction to form a fibrous structure (Fig. 5-20). The different coloured microstructures in the inverse pole figures indicates that there exist multiple textures in the quarter width region. Further analysis of the different texture component fraction's shows the quarter width region is mainly made by brass and S texture in material extruded using both Die C and Die E. The texture similarity between the Die C and Die E extruded samples at the quarter location provides evidence that the bridge effect is very small on the material far away from the seam. Different from the QC region's pole figures (Fig. 5-21a and b), the pole figures of the QE region (Fig. 5-21c and d) are not symmetric to the RD and TD axis due to the strong shear force at the surface. In summary, the quarter width region's texture is not affected by the bridge geometry.



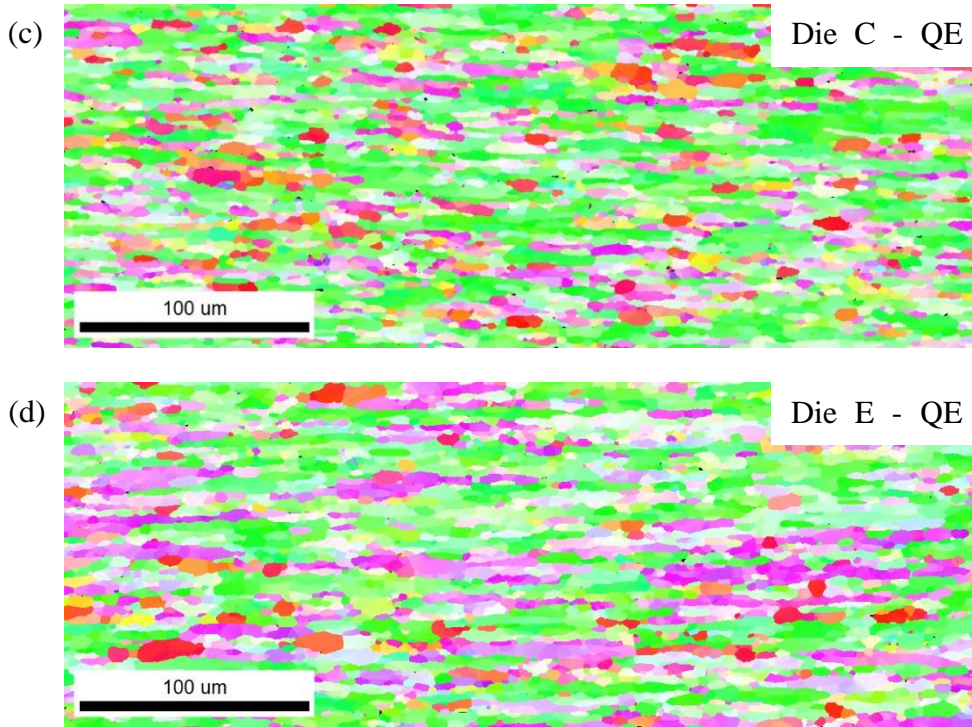
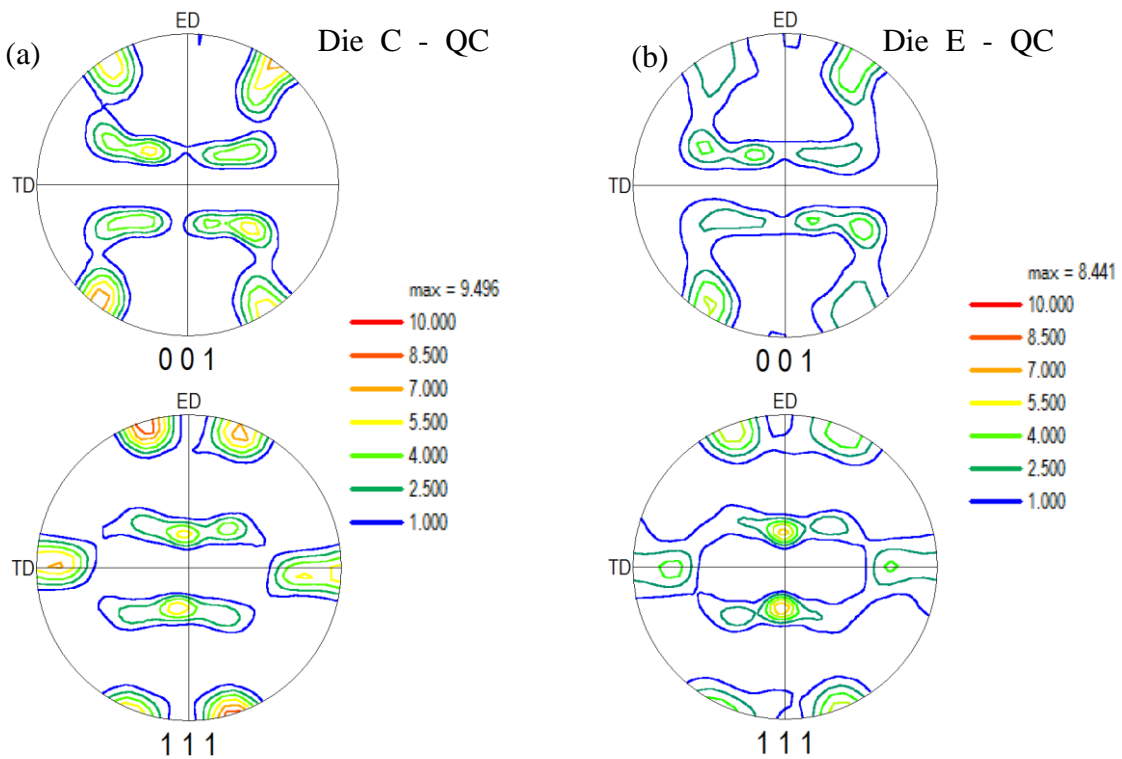


Fig. 5-20 Inverse pole figure of the symmetric dies extruded samples (T4) at the quarter width location: (a) Die C / 12.7 mm / Sym (Trial 12) – QC, (b) Die E / 12.7 mm / Sym (Trial 12) – QC, (c) Die C / 12.7 mm / Sym (Trial 13) – QE, and (d) Die E / 12.7 mm / Sym (Trial 13) – QE.



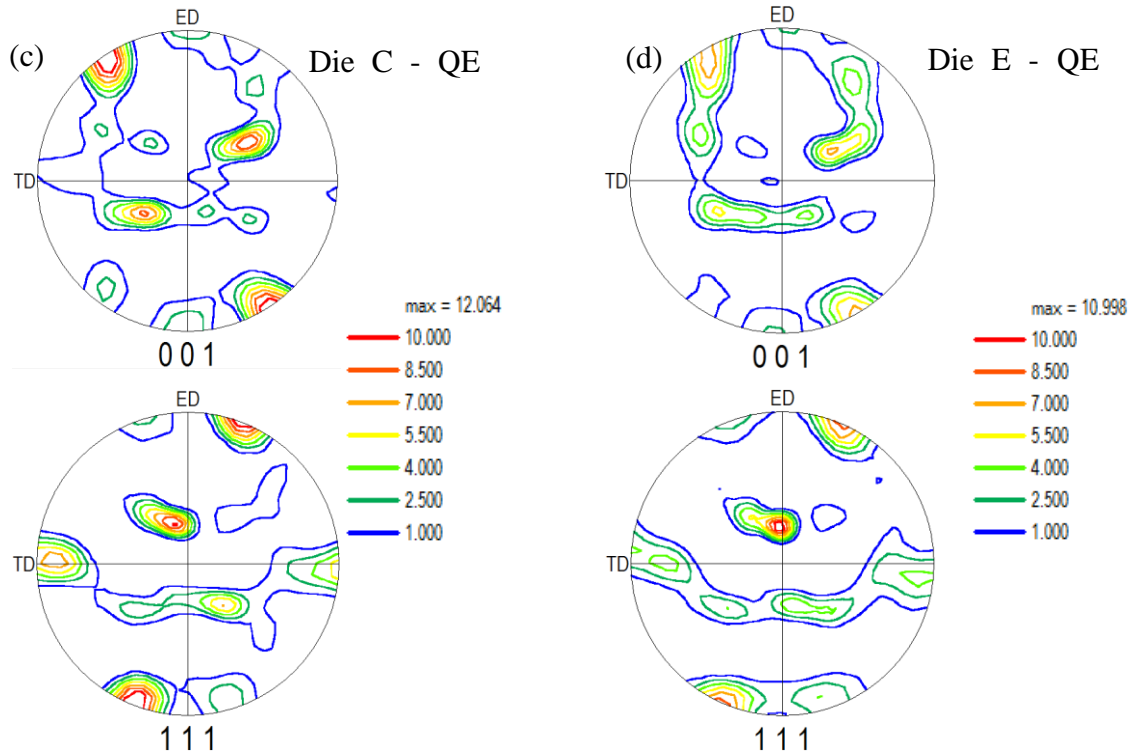


Fig. 5-21 The polar figures of the symmetric dies extruded samples at the quarter width location: (a) Die C / 12.7 mm / Sym (Trial 12) – QC, (b) Die E / 12.7 mm / Sym (Trial 12) – QC, (c) Die C / 12.7 mm / Sym (Trial 13) – QE, and (d) Die E / 12.7 mm / Sym (Trial 13) – QE.

### 5.2.2.3 Welding chamber height

In order to examine the welding chamber height's influence's on extrudate's texture, the seam region, referring to Fig. 5-22, of profiles extruded using two welding chamber heights was examined by EBSD. In this part, four different extruded profiles extruded in Trial 1 (Die C / 12.7 mm / Asym), Trial 2 (Die E / 12.7 mm / Asym), Trial 4 (Die C / 25.4 mm / Asym) and Trial 5 (Die E / 25.4 mm / Asym) were examined using EBSD to understand the role of welding chamber in both Die C and Die E extrusion. For these EBSD measurements the region examined with within 0.5 mm of the weld seam and at the centre of the extruded strip,

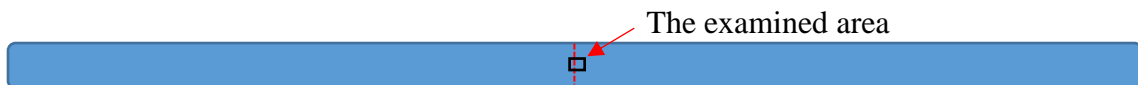
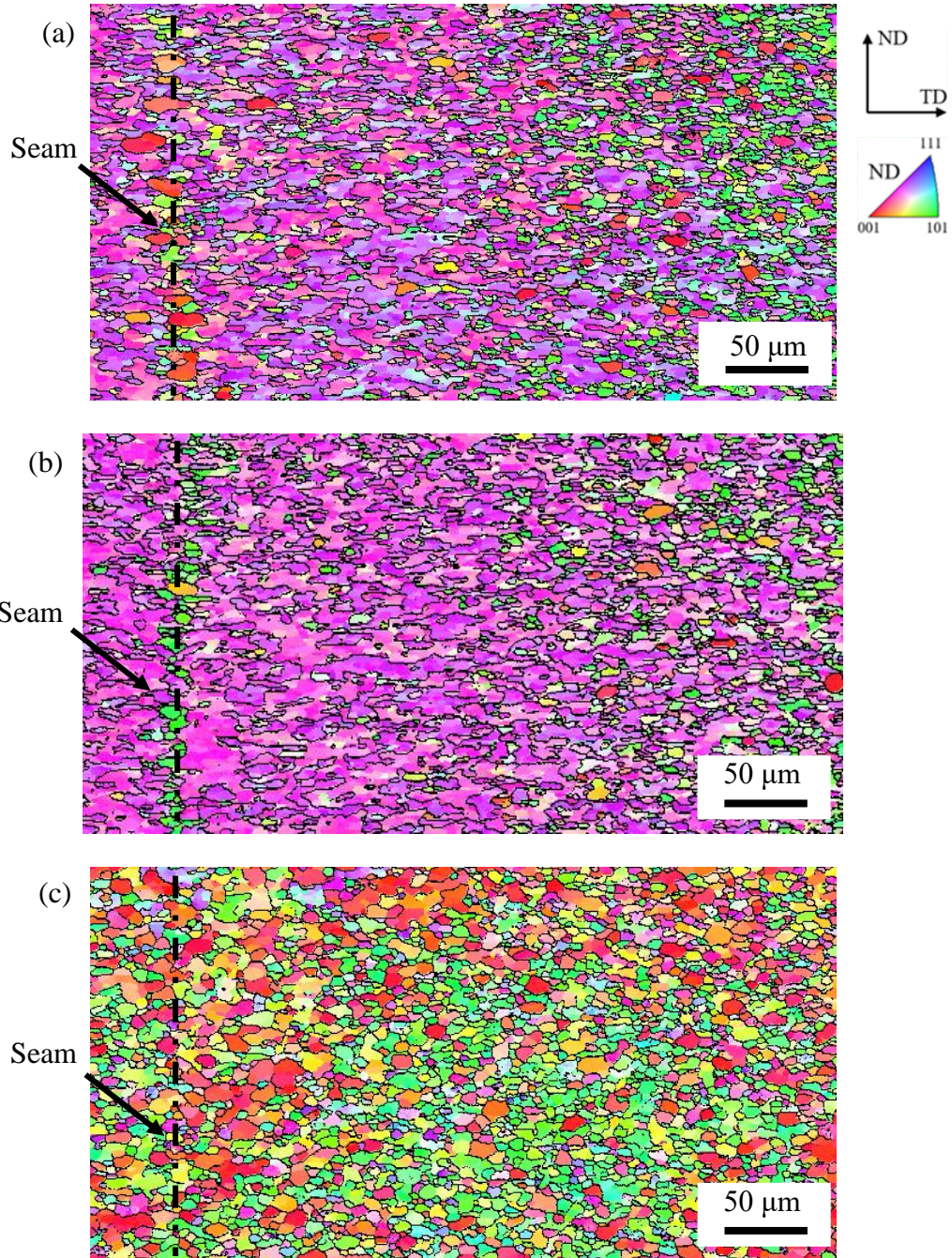


Fig. 5-22 A schematic of the area characterized via EBSD to determine the welding chamber height's effects on texture at the seam region.

By comparing the inverse pole figure's of the seam region at profiles extruded using Die C / 12.7 mm (Fig. 5-23a) and Die C / 25.4 mm (Fig. 5-23b), the seam region in the sample extruded using Die C for different welding chamber heights exhibits similar textures. Both of the seam regions in the two profiles extruded using Die C bridge generally consist of a majority of copper texture (purple colour) and to a lesser extend brass texture (green colour). The texture similarity between the two samples indicates that the welding chamber height's influence on the porthole die extruded sample's microstructure and texture is very small for the streamlined bridge geometry (Die C).

Fig. 5-23c shows an EBSD image of the weld seam region for the sample extruded using Die E / 12.7 mm at 480 °C. The EBSD image shows that the seam region of the sample extruded using Die E / 12.7 mm consists of cube texture (red coloured) and goss texture (green coloured). The texture of the samples extruded using Die E / 25.4 mm at the seam region was also examined via EBSD to study the die geometry's effects on porthole die extrusion. In the region close to the weldline of the sample extruded using Die E / 25.4 mm, the green and red textures are identified to be goss and cube texture respectively (Fig. 5-23d), which are very similar to the texture observed at the seam region of the sample extruded using Die E / 12.7 mm (Fig. 5-23c). However, the goss and cube texture quickly become a copper texture (purple colour) at a position slightly away from the seam. The copper texture close to the weld line is similar to the texture observed in samples extruded using Die C at the weld seam region (Fig. 5-23a and Fig. 5-23b). The EBSD results of the sample extruded by Die E / 25.4 mm indicates that the Die E extruded sample's texture has a tendency to be more similar to the Die C extruded sample, when the welding chamber height increased from 12.7 mm to 25.4 mm. In another word, the bridge shape's influence on the porthole die extrusion diminishes when the welding chamber height increases.



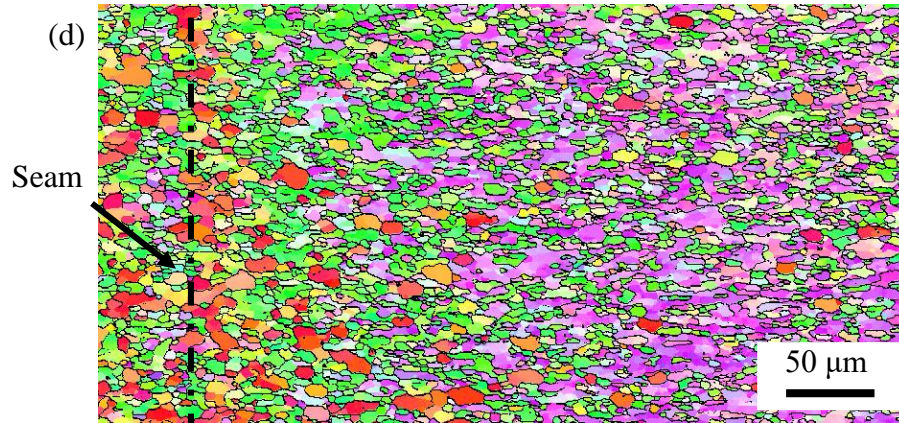


Fig. 5-23 Measured EBSD images (inverse pole figure) of the weld seam region in profiles (T5) extruded for different extrusion trials: (a) Die C / 12.7 mm / Asym (Trial 1), (b) Die C / 25.4 mm / Asym (Trial 2), (c) Die E / 12.7 mm / Asym (Trial 4) and (d) Die E / 25.4 mm / Asym (Trial 5).

#### 5.2.2.4 Porthole layout

In order to check the porthole layout's effects on the porthole die extrusion, the full thickness of the seam region in the sample extruded using the asymmetric dies was also examined using EBSD in this research. As shown in Fig. 5-24a, the texture of the seam region extruded by Die C / 12.7 mm / Asym is not symmetric to the middle thickness due to the asymmetric layout of the portholes. The top half of seam region is goss and cube texture (green and red colour), and the bottom half is brass texture (purplish red colour).

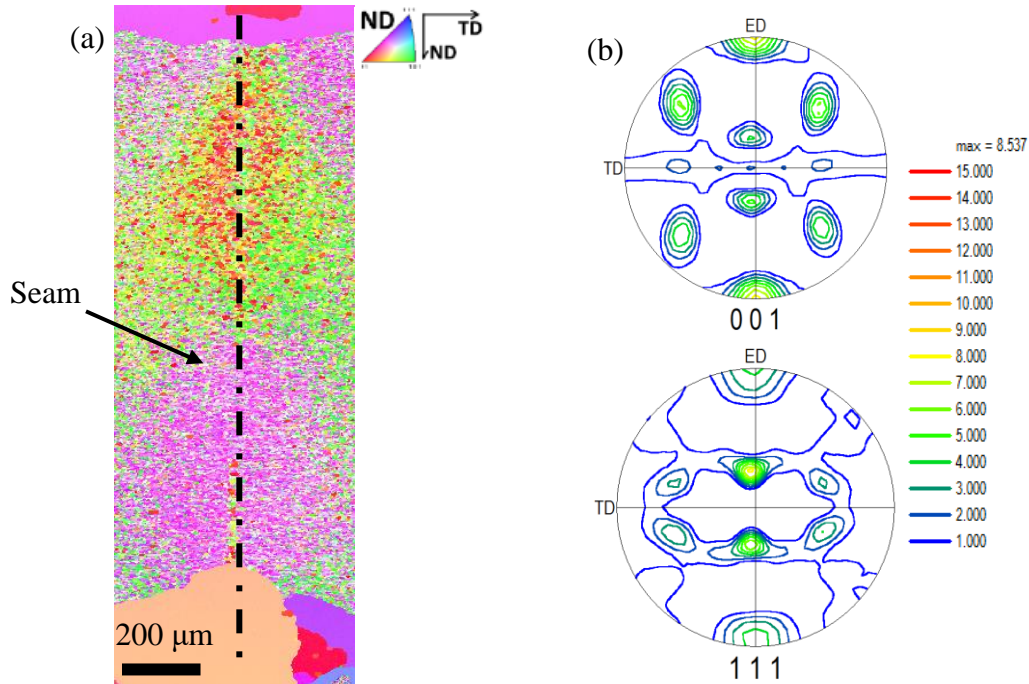


Fig. 5-24 (a) EBSD image (inverse pole figure) and (b) the polar figure of the seam region in the sample (T5) extruded by Die C / 12.7 mm / Asym (Trial 1).

Different from the seam region extruded using Die E / 12.7 mm / Sym (Fig. 5-18a), the seam region in the sample extruded using Die E / 12.7 mm / Asym (Fig. 5-25a) has a high percent of brass texture (purplish red colour) at the bottom half of the extrudate. The rest of the seam region is still made up mainly by goss and cube texture (green and red colours). The EBSD tests on the samples extruded using the asymmetric dies show that the porthole layout has a big effect on the texture through the thickness of the weld seam region, which may be due to the different thermal mechanical history the seam region experienced between the symmetric and asymmetric die extrusion.

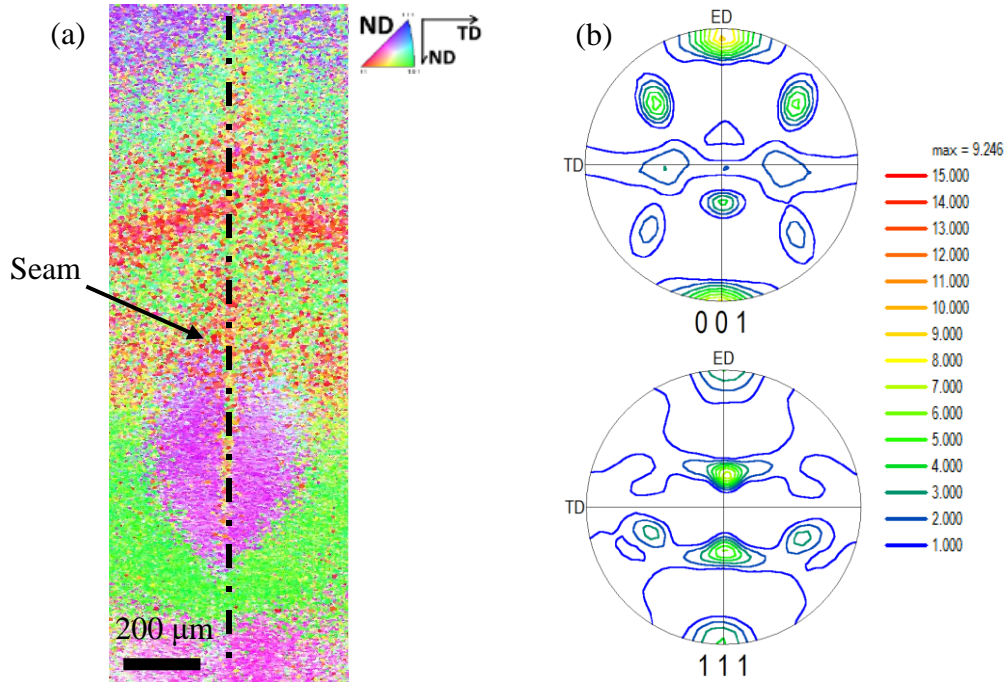


Fig. 5-25 (a) EBSD image (inverse polar figure) and (b) the polar figure of the seam region in the sample (T5) extruded by Die E / 12.7 mm / Asym (Trial 2).

### 5.2.3 Mechanical properties

Before the discussion of die configuration's effects on extruded samples' mechanical properties, the repeatability of the tensile tests of T4 treated sample was examined very carefully. Fig. 5-26 shows the four samples' stress – strain curves cut from the Die E / 12.7 mm extruded sample at the ram speed of 5 mm/s (Trial 12). Before reaching the ultimate strength at the strain about 11%, the four stress – strain curves almost overlap and do not show any differences. After the peak strength, the stress – strain curves begin to diverge but the differences still remain very small. At the final fracture stage, there are some differences between the four curves. The ultimate and yield strength measured from the four tensile specimens are almost same. The fracture elongation amongst the four tensile specimens varies from 14.4% to 16.2%, which is still a very small variation.

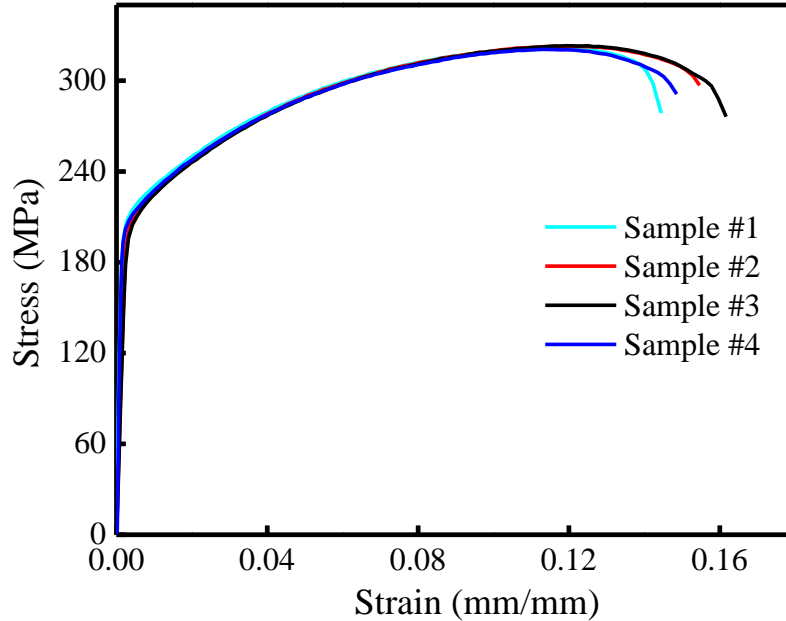


Fig. 5-26 Repeatability of tensile tests of T4 porthole die extruded samples (Trial 12).

In this research, tensile tests in conjunction with DIC were used to measure the stress – strain curve of porthole die extruded samples and the strain evolution during the tensile test. Fig. 5-27 shows the measured stress – strain curves of the four different extruded samples produced using different die geometries in the T4 condition for the 0.5Mn0.15Cr samples. The yield strength and ultimate strength of short welding chamber extruded samples are about 210 and 325 MPa respectively, and the strength of the deep welding chamber extruded samples is about 10 MPa lower. On the other hand, the samples extruded using deep welding chamber has a slightly higher fracture elongation than the sample extruded using short welding chamber. What’s more, the Die C extruded samples have a slightly higher strength and fracture elongation than Die E extruded samples. Another noticeable phenomenon is that the UTS occurs at relatively lower strain in Die E extruded sample than in Die C extruded sample, which implies that the deformation of Die E extruded samples during tensile test is not as uniform as the deformation of Die C extruded samples. Through the comparison between the seamed samples and seamless samples’ mechanical properties, the strength of extruded samples is not affected by the existence of the seam significantly, but the ductility is much lower than the seamless samples.

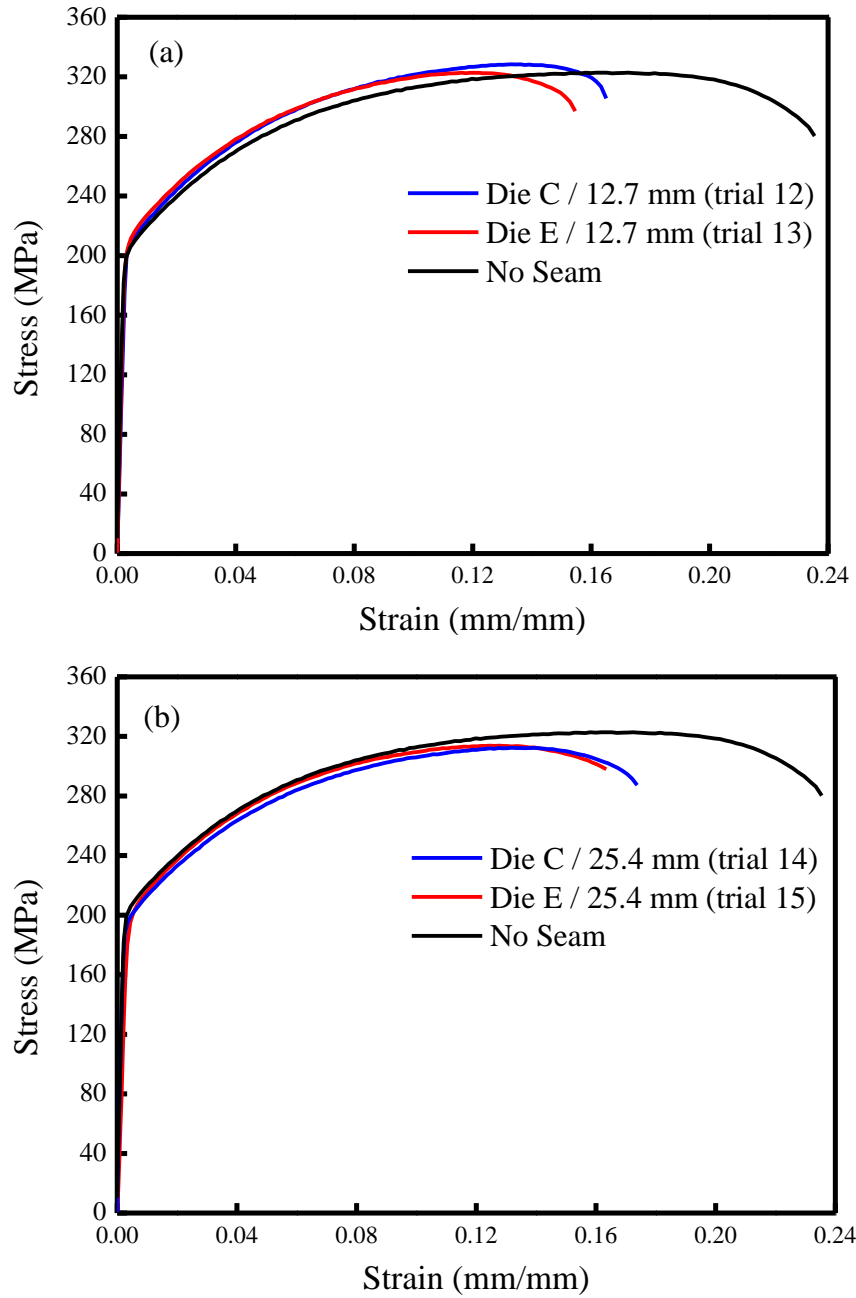


Fig. 5-27 Measured stress–strain curves of T4 samples extruded using different die geometries at ram speed of 5 mm/s: (a) 12.7 mm welding chamber and (b) 25.4 mm welding chamber height.

Table 5-4 Tensile properties of porthole die extruded samples using different die configurations.

	Yield strength (MPa)	Ultimate strength (MPa)	Fracture strain (%)	Strain when UTS occurs (mm/mm)
Die C / 12.7 mm	211.8	328.4	0.162	0.132
Die E / 12.7 mm	209.0	322.0	0.152	0.116
Die C / 25.4 mm	201.0	314.7	0.173	0.134
Die E / 25.4 mm	200.6	311.5	0.158	0.123
No Seam	202.5	321.7	0.235	0.172

Fig. 5-28 shows the measured strain distribution along the gauge length of different samples during tensile test. When the elongation is only 1%, the strain in Die E / 12.7 mm began to concentrate at the weld seam, and the peak strain is as high as 2.3%. The other three porthole die extruded samples' strain concentration is not as obvious as the Die E / 12.7 mm extruded sample, but the peak strain at the center can also reach 1.5%. When the elongation comes to 8%, it's very obvious that the two Die E extruded samples have a higher strain concentration than the two samples extruded using Die C at the centre. When the elongation is 12%, the peak strain of the samples extruded using Die E / 12.7 mm and Die E / 25.4 mm are about 22% and 19% respectively, but the peak strain of Die C extruded sample is only about 16%. On the other hand, the strain distribution for the seamless sample is very uniform even when the strain reaches 12%. From the analysis of the strain distribution during the tensile test, it is clear that material extruded using Die E have a greater tendency for the strain to concentrate along the weld seam at an earlier stage than samples extruded using Die C. It appears that an increase in the weld chamber height can help to alleviate the strain concentration material extruded using Die E a little bit but its influence in Die C extruded sample is negligible.

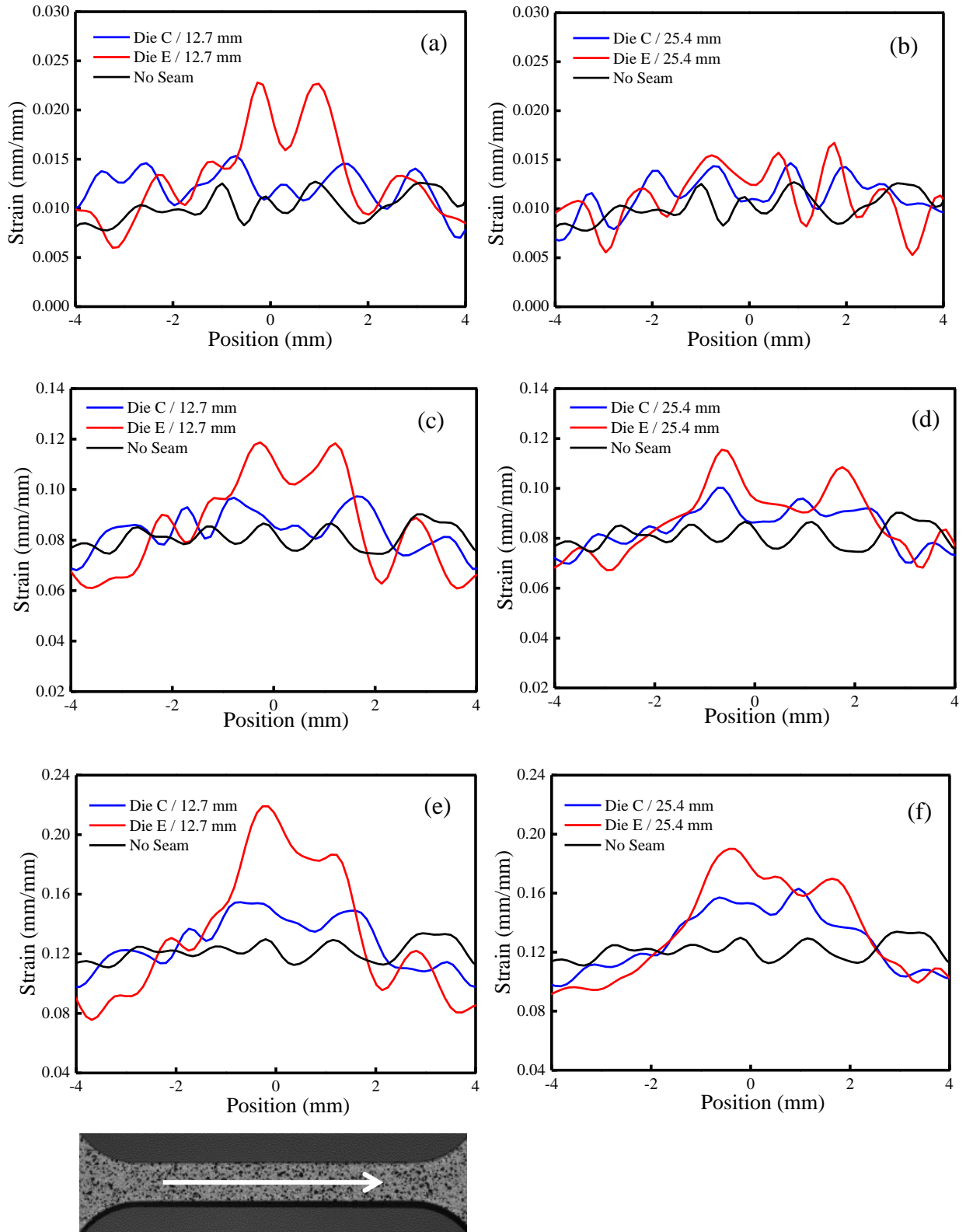


Fig. 5-28 Strain distribution along the white line in the gauge length during tensile test, when (a) elongation is 1% and welding chamber is 12.7 mm, (b) elongation is 1% and welding chamber

height is 25.4 mm, (c) elongation is 8% and welding chamber is 12.7 mm, (d) elongation is 8% and welding chamber is 25.4 mm, (e) elongation is 12% and welding chamber is 12.7 mm and (d) elongation is 12% and welding chamber is 25.4 mm.

### **5.2.3.1 Heat treatment**

Some as-received samples were solutionized at 550 °C for 10 min, then artificial aged at 175 °C for 8 hours to produce a T6 heat treatment condition. As shown in Fig. 5-29, after the T6 heat treatment, the yield strength of the porthole die extruded sample increased from 205 to 365 MPa, but the fracture elongation dropped from 16% to 7%. Besides the change of the strength and ductility, the strain hardening rate of the T6 samples is very low, because the high number of shearable precipitates obstruct the dislocation movement and propagation [112]. Moreover, the T6 heat treated Die C and Die E extruded samples have almost the same stress – strain curve, similar to the T4 condition.

Strain distribution along the gauge length was also measured during the tensile test, as shown in Fig. 5-30. When the elongation is only 1%, the T6 treated samples have already exhibited a strain concentration, but the T4 Die C sample does not show obvious strain concentration at the same time. When the elongation comes to 3%, the strain concentration is very severe in the T6 samples, and the peak strains of T6 Die C and Die E samples are 7% and 6% respectively. In contrast, the peak strain of T4 Die E sample is only 5%, and the strain distribution of T4 Die C sample is still uniform. The T6 heat treatment of the material extruded using the porthole die process appears to make the strain concentration occur earlier during a tensile test.

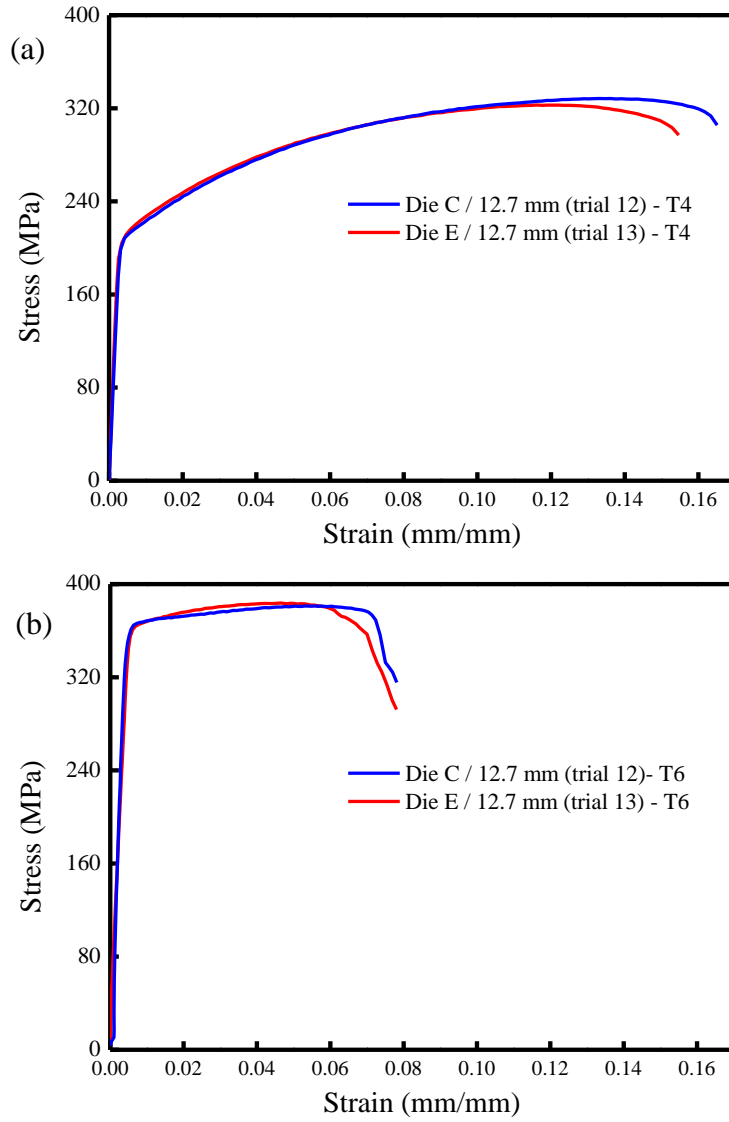


Fig. 5-29 Heat treatment's effect on porthole die extruded samples' mechanical property: (a) T4 and (b) T6.

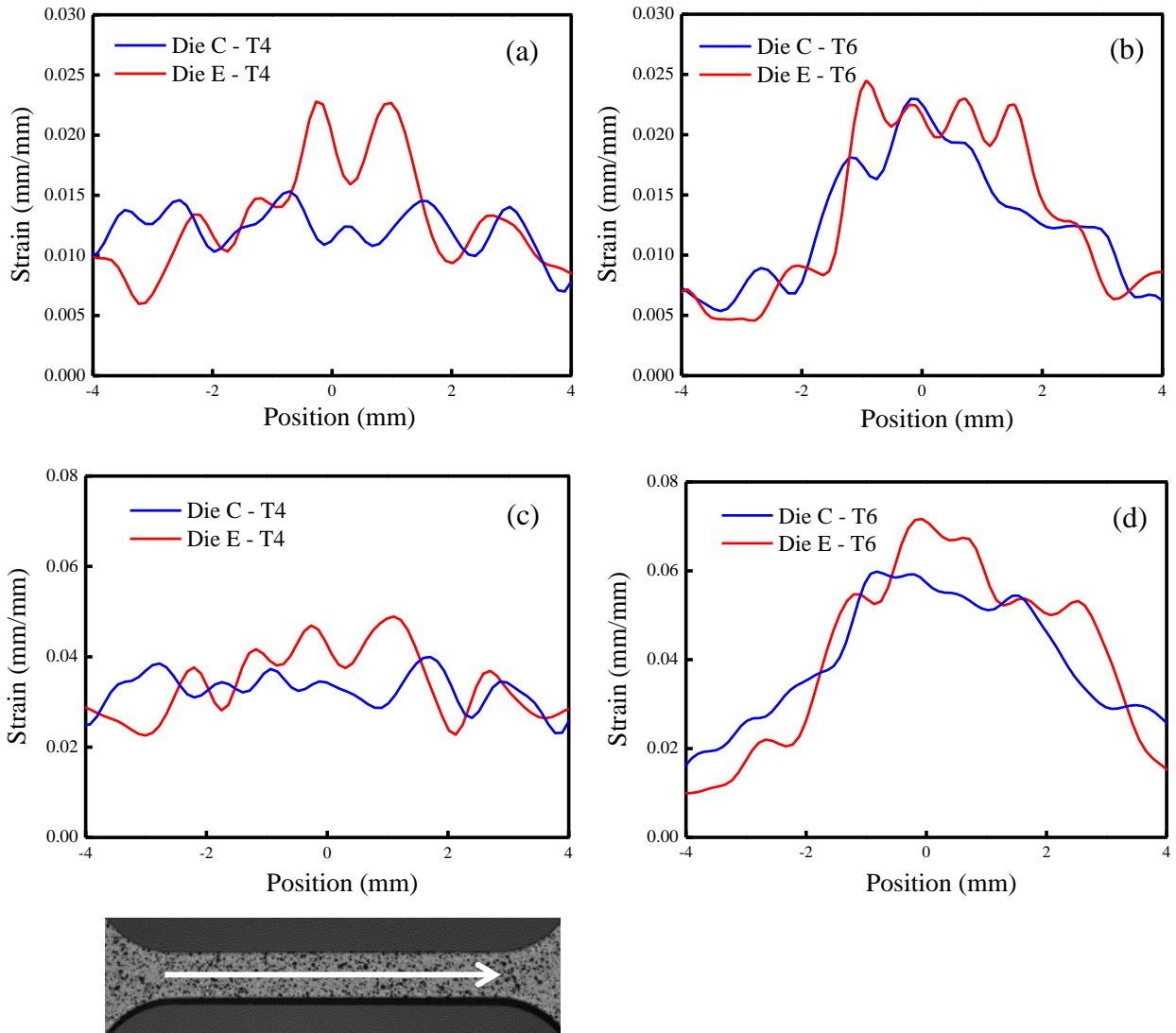


Fig. 5-30 Measured strain distribution along the white line of the gauge length for the extruded samples, when (a) the elongation is 1% and T4 heat treated, (b) the elongation is 1% and T6 heat treated, (c) the elongation is 3% and T4 heat treated and (d) the elongation is 3% and T6 heat treated.

## 5.3 Model

### 5.3.1 Model verification

In order to verify the accuracy of the simulation models, a number of different model-predictions were compared to the experimental measurements. These included the measured load but also macrostructures of the material in the welding chamber that provides information on

material flow and the location of dead metal zones. Referring to Fig. 5-31, the model predictions of the load were compared to the experimental measurements during the extrusion experiments. As shown in this figure, the load predicted using both the Lagrangian and ALE simulation (of just the peak load) simulations agree with the measured experimental data well. The break-through load measured during extrusion Trial 1 and 2 using Die C and Die E is 706 and 702 tonnes respectively, and the break through load predicted from the ALE simulation is 702 and 691 tonnes respectively. As noted earlier, the extrusion load is largely determined by the volume of bridge rather than the shape of the bridge [65]. In this these, the volume of Die C bridge and Die E bridge are about  $1.7 \times 10^4$  and  $2.0 \times 10^4 \text{ mm}^3$  respectively. Since the flat bridge in Die E has a larger volume than the streamlined bridge in Die C, the extrusion load measured for the extrusion trial using Die E is higher than Die C. The measured extrusion load for the same strip extrusion without a bridge is only 425 tonnes.

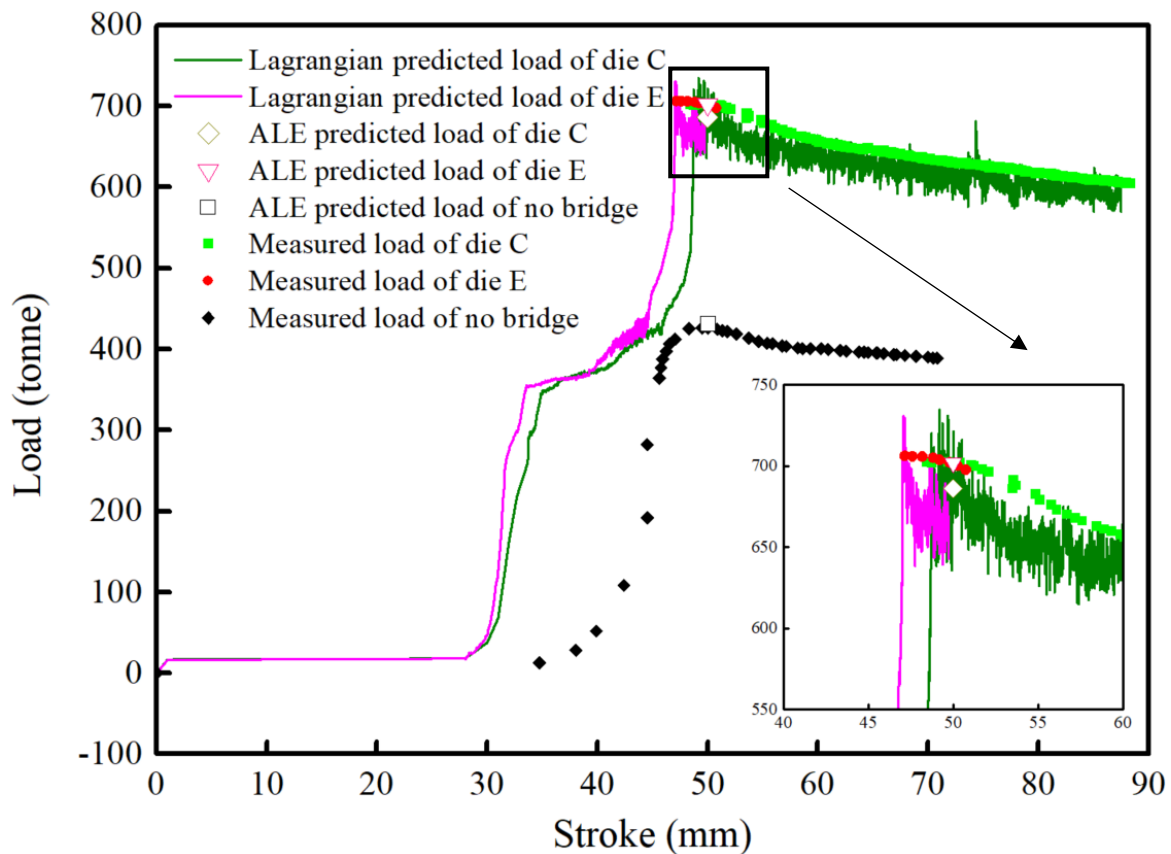


Fig. 5-31 Comparison between model-predicted and measured load-stroke behaviour during extrusion using Die C (trial 1) and Die E (Trial 2) as well as a no-bridge die (Trial 11).

Table 5-5 Measured and model predicted load at the breakthrough.

	Die C (Trial 1)	Die E (Trial 2)	No bridge (Trial 11)
Measured load (tonne)	702	706	425
ALE predicted load (tonne)	691	702	432
Lagrangian predicted load (tonne)	697	713	
Difference between measured and ALE predicted load (%)	1.6	0.6	1.6

The effectiveness of the simulation was also verified by comparing the model-predicted Dead Metal Zone (DMZ) during porthole die extrusion to what we see experimentally along a sliced plane in the welding chamber (Fig. 5-32). The sliced plane is 6.35mm away from the tip of the pointed bridge, and the die configuration is Die C / 12.7 mm / Asym (Trial 1). As shown in Fig. 5-32b, the sliced residual material had four DMZs at the four corners, and the area of the DMZ closer to the die orifice was smaller than the DMZ farther away due to the asymmetric layout of the portholes. In the model simulation, the DMZ was defined as the region whose velocity was below 0.3 mm/s, and was labeled using light blue in Fig. 5-32c; the model-predicted DMZ was very similar to the DMZ shown in the sliced plane which provides confidence that that model is able to simulate the material flow quite well.

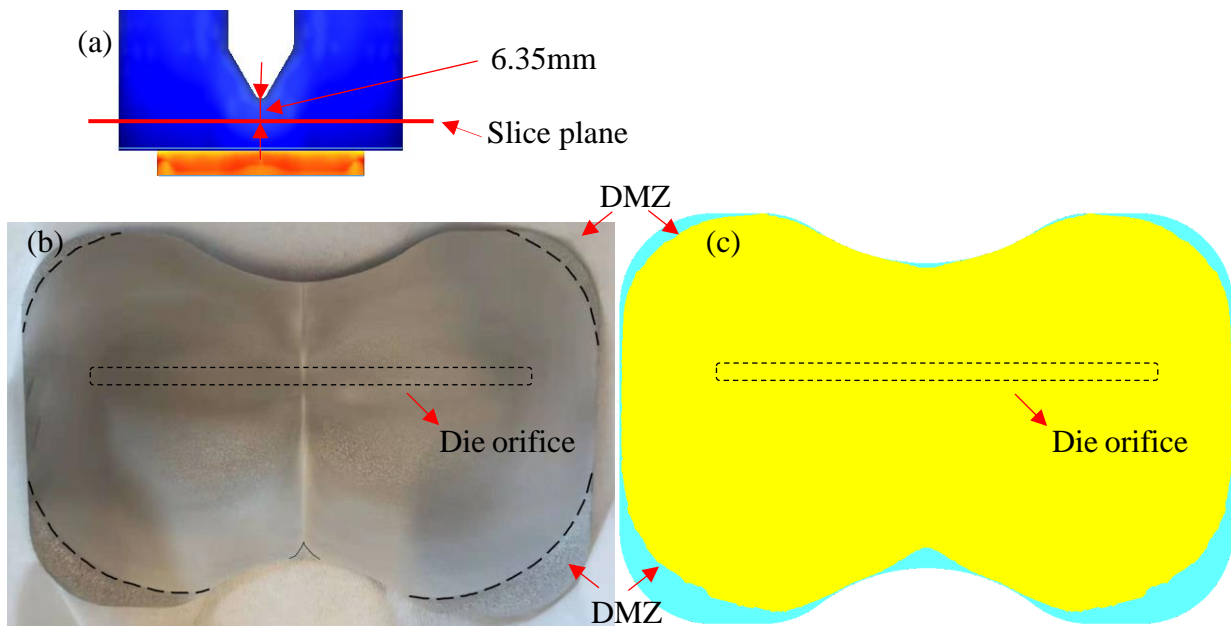


Fig. 5-32 Comparison between the experimental and model-predicted DMZ a slice plane shown in (a): (b) experimental result and (c) model-prediction.

### **5.3.2 Simulation of the porthole die extrusion trials**

In this section, the four symmetric porthole die extrusions used in the extrusion trials, Die C / 12.7 mm / Sym (Trial 12), Die E / 12.7 mm / Sym (Trial 13), Die C / 25.4 mm / Sym (Trial 14) and Die E / 25.4 mm / Sym (Trial 15), were simulated using DEFORM 3D to help understand and explain the unique texture and mechanical properties produced in the samples after extrusion. The extrusion temperature was set to be 480 °C, and the ram speed was set to be 5 mm/s.

#### **5.3.2.1 Velocity distribution**

Fig. 5-33 shows the model-predicted velocity distribution in the welding chamber of the four symmetric porthole die extrusions used in the extrusion trials. It is noticeable that the bridge shape makes a very significant difference on the velocity distribution in the porthole die extrusion. Under the Die E bridge there exists a region of very low velocity, which is probably a dead metal zone (DMZ) (encircled in Fig. 5-33b and d). Meanwhile, under Die C bridge, the material velocity is relatively high, except for the very thin layer of material stuck to the bridge surface. A dead metal zone is considered to be rigid and impenetrable by the flowing material during porthole die extrusion. The welding chamber height's effect on the Die C extrusion's velocity distribution is very small, but the size of DMZ in Die E extrusion increases a bit when the welding chamber height increases.

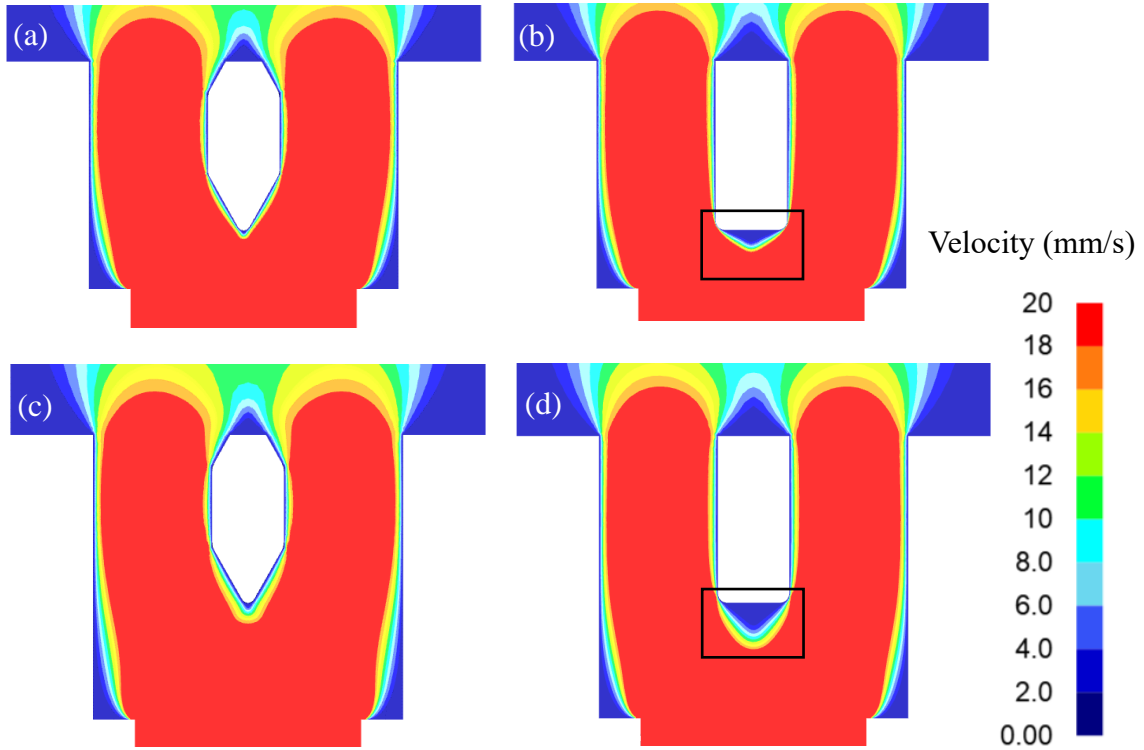


Fig. 5-33 Model-predicted velocity distribution during porthole die extrusions for different bridge geometries and welding chambers: (a) Die C / 12.7 mm / Sym (Trial 12), (b) Die E / 12.7 mm / Sym (Trial 13), (c) Die C / 25.4 mm / Sym (Trial 14) and (d) Die E / 25.4 mm / Sym (Trial 15).

As shown in Fig. 5-34b, there exists a dead metal zone at the end of the Die E bridge, which all of the material flow paths have to pass around (highlighted in the black rectangle). The existence of the dead metal zone at the exit of the bridge can severely disrupt the flow smoothness of the material and may affect the thermal mechanical history of the material during porthole die extrusion. However, during extrusion using Die C, the material flow paths are much smoother without being disrupted by a dead metal zone.

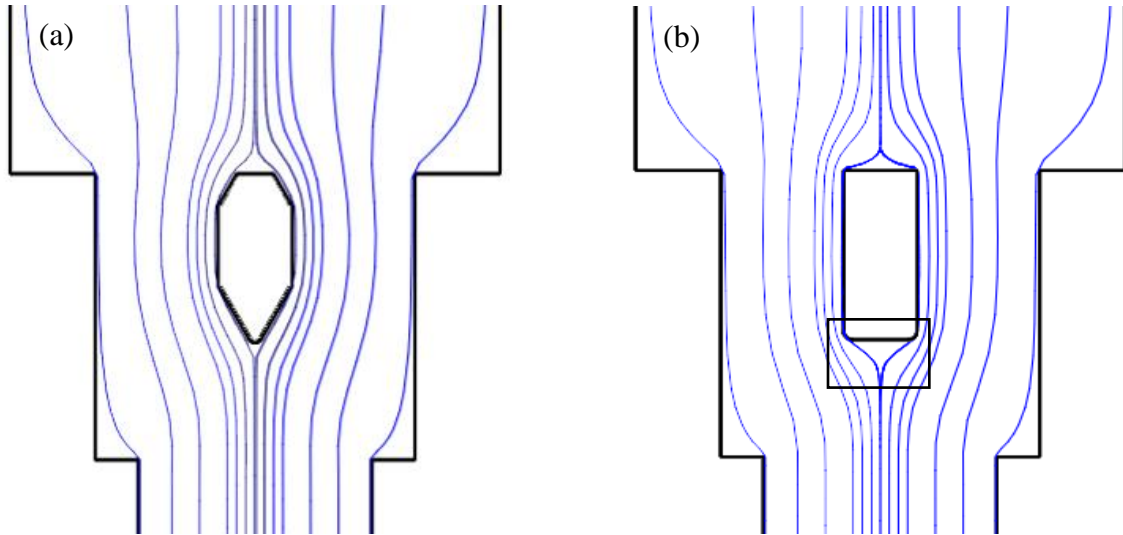


Fig. 5-34 Model-predicted flowlines in porthole die extrusions: (a) Die C / 25.4 mm / Sym (Trial 14) and (b) Die E / 25.4 mm / Sym (Trial 15).

### 5.3.2.2 Thermal mechanical history

Fig. 5-35 shows the model-predicted temperature distribution through the cross section of the extruded profile at the die exit. Referring to Fig. 5-35, the Die E / 12.7 mm extruded sample has the highest exit temperature. The flat bridge and short welding chamber lead to the most disruption to the material flow (least smooth) over the shortest period of time and cause more heat to be created due to the plastic deformation which occurs and thereby increases the exit temperature. The exit temperature of the other three die configurations are very similar. The higher exit temperature of Die E / 12.7 mm extruded sample can also be seen based on the very rough surface quality close to the seam, which is believed to be caused by local melting of the surface (Fig. 5-45). It is also interesting to note that the highest exit temperature does not always happens at the weld line (see the temperature distribution of Die C / 25.4 mm). As shown in Fig. 5-35, the die bearing length is not constant but varied along the perimeter of the extruded strip. These variations spatially in the die bearing length are done to try and even out the flow of the material when it is being extruded. At the centre, the bearing length is shorter than other areas and this is used as a way to even out the material flow and its velocity, and is the reason the temperature along the weld line is slightly lower than the neighbouring material.

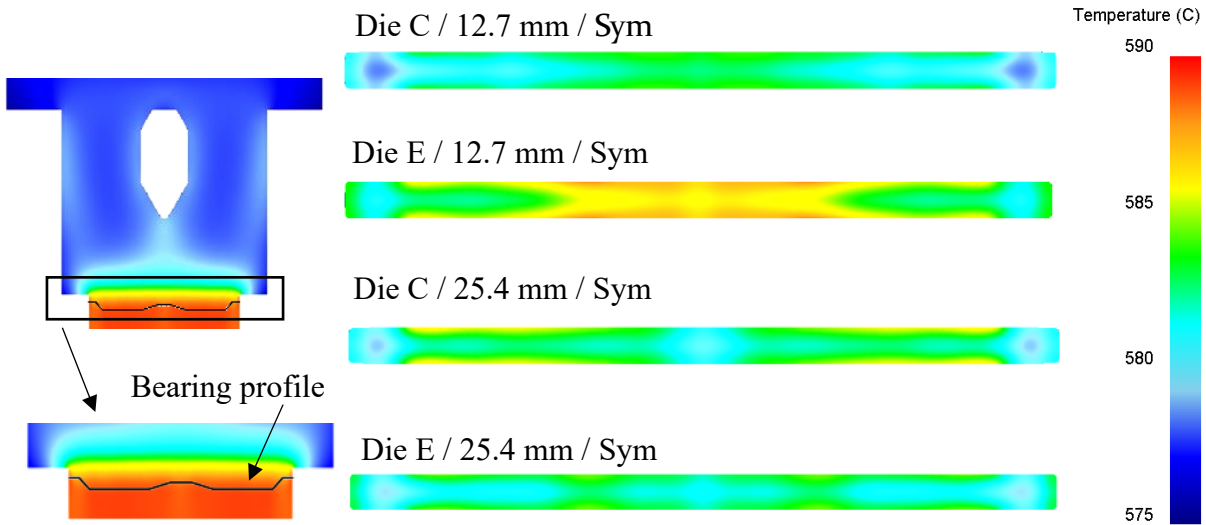


Fig. 5-35 Temperature distribution at the die exit.

In this section, two points in each die configuration are selected, and their thermal mechanical history was calculated, as shown in Fig. 5-36. The centre point at the seam was selected to represent the thermal mechanical history of the centre point along the weld line, and the quarter width point, which is 12 mm away from the seam, was selected to represent the material away from the seam.

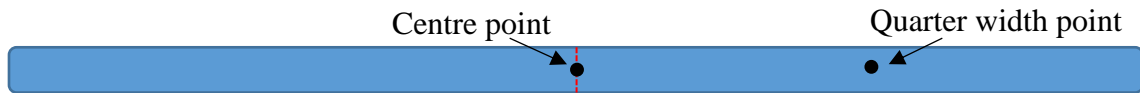


Fig. 5-36 The two selected points for thermal mechanical history calculation.

Fig. 5-37 shows the model-predicted flow paths of the centre point and the quarter width point in each die configuration extrusion. Due to symmetry, only half of the model is shown in Fig. 5-37 to save space. The black line is the model-predicted flow path of the centre point, and the green line is the model-predicted flow path of the quarter width point. Every point's coordinate on the flow paths and its corresponding time were calculated based on Eq. 4-3 and Eq. 4-4. Moreover, the time needed for each tracked point to pass through the porthole plus welding chamber region (shown by the red rectangles) was also calculated and labeled beside the flow path. For instance, the quarter width point's flow path in Die C / 12.7 mm extrusion (the green line in Fig. 5-37a) is labeled by the number "1.5", which means it takes 1.5 s for the quarter width point to pass through the porthole and welding chamber region in Die C / 12.7 mm.

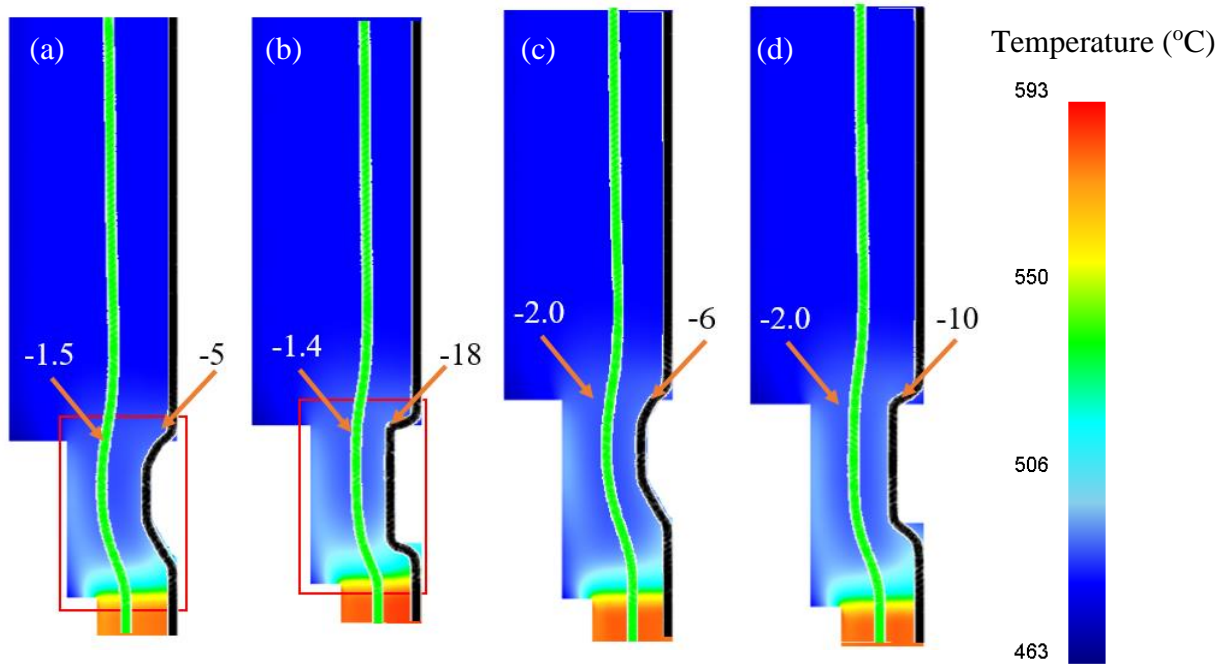


Fig. 5-37 Model-predicted flow paths in different porthole die extrusion dies of different bridges and welding chambers: (a) Die C / 12.7 mm / Sym (Trial 12), (b) Die E / 12.7 mm / Sym (Trial 13), (c) Die C / 25.4 mm / Sym (Trial 14) and (d) Die E / 25.4 mm / Sym (Trial 15).

Each point's temperature along the flow path can be calculated by doing an interpolation of the temperature field obtained using the DEFORM simulation. By correlating each point's temperature and time, the temperature history of each tracked point can be obtained (Fig. 5-38). As expected, the centre point in Die E / 12.7 mm has the highest exit temperature, and the other three die configurations have almost the same exit temperature, as shown in the inset figure in Fig. 5-38a. Although the exit temperatures are fairly similar, the difference in temperature history are much more prominent for the centre points extruded using the different dies. As shown in Fig. 5-37, the material within and close to the porthole and welding chamber (encircled by the red rectangle) has a higher temperature than the rest of the material outside. As a result, the temperature history is highly dependent on the time needed to pass through the hot region (the porthole plus welding chamber). For instance, the centre points in Die E / 12.7 mm has the lowest flow speed, and was in the porthole plus welding chamber region for the longest time. Therefore, compared by the other three die configurations, the centre point in Die E / 12.7 mm has a higher temperature for a longer time. As discussed in the previous paragraph, the welding chamber height does not make a difference on the centre point's flow behavior in Die C extrusion, so the centre points in Die C /

12.7 mm and Die C / 25.4 mm have the almost the same temperature history. Since increasing the welding chamber height in Die E extrusion reduces the obstruction effects on material flow, the centre point in Die E / 25.4 mm passes through the porthole plus welding chamber region faster than the centre point in Die E / 12.7 mm. As a result, the welding chamber height can have a significant effect on the centre point's temperature history for material extruded using Die E. By increasing the welding chamber height, the temperature history of material extruded using Die E is more similar to material extruded using Die C. Since the quarter width point's flow paths are not affected by the bridge geometry, the quarter width points in the four die configurations exhibit very similar temperature history (Fig. 5-45b).

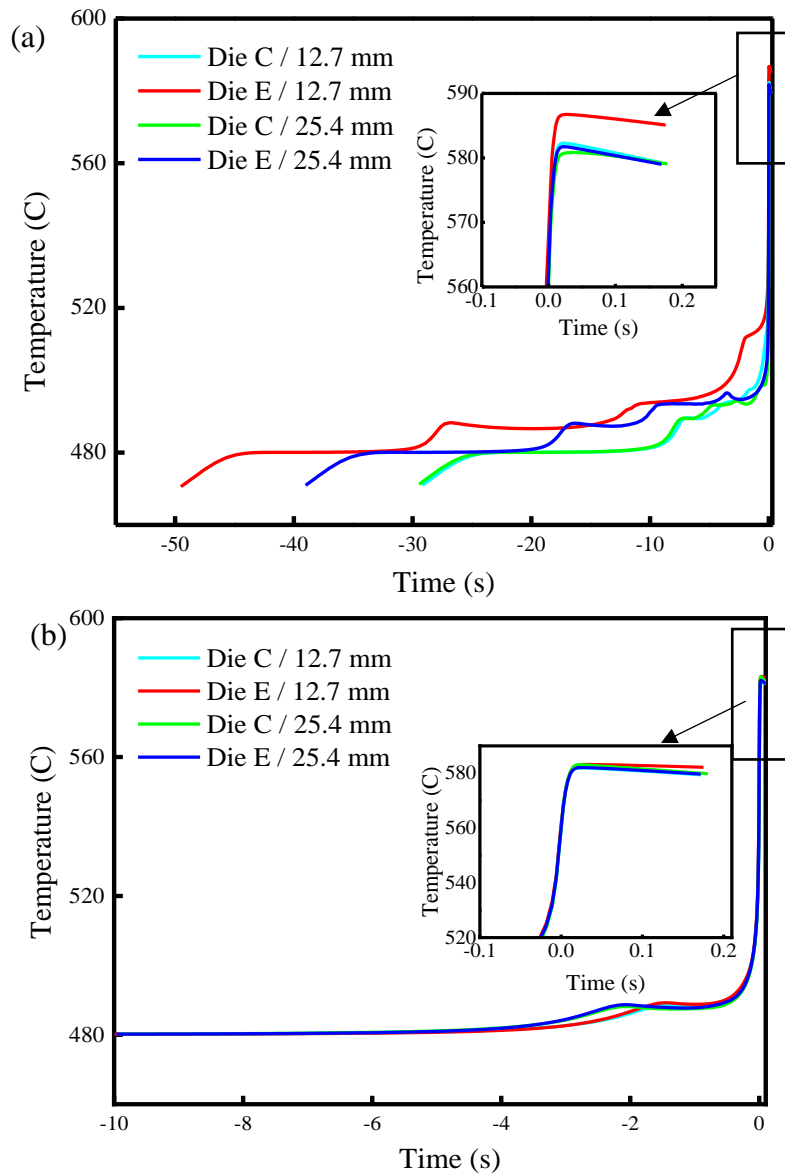


Fig. 5-38 Model-predicted temperature history of tracked points during porthole die extrusion: (a) centre point and (b) quarter width point.

### 5.3.2.3 Strain distribution

Fig. 5-17 shows the model-predicted strain distribution throughout the cross section of the extruded profiles using the different die configurations. The strain is exceptionally high at the edge and the seam, but in the rest of the cross-section the strain remains relatively low. It also appears that the strain distribution at the weld seam is significantly affected by the details of the die geometry. In the material extruded using Die C, the high strain region at the seam is lenticular shaped and not affected by the welding chamber height (Fig. 5-39a and c). On the other hand, the weld seam region of material extruded using Die E, has a bulge in the middle, which extends further into the matrix, especially at the centre (Fig. 5-39b and d). This result is confirmed with the measured EBSD results close to the weld seam for these two cases (Fig. 5-17 and Fig. 5-18). Increasing the weld chamber height from 12.7 mm to 25.4 mm for material extruded using Die E, caused the high strain region at the weld seam to shrink a little and not extend out as much (Fig. 5-39d).

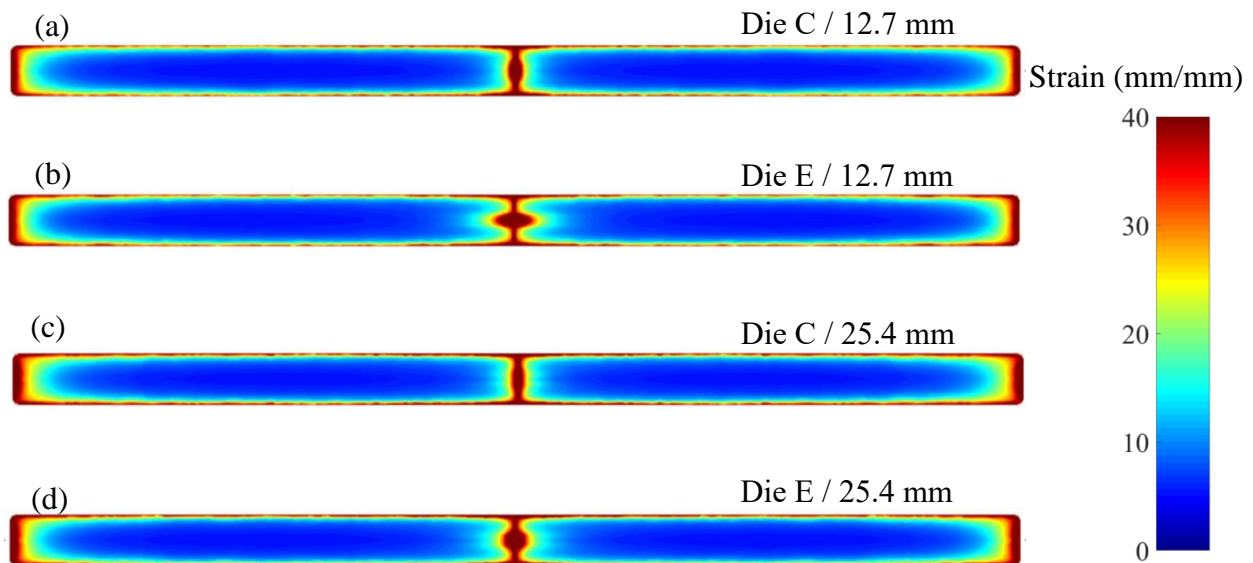


Fig. 5-39 Strain distribution through the cross section of the extruded profile: (a) Die C / 12.7 mm / Sym (Trial 12), (b) Die E / 12.7 mm / Sym (Trial 13), (c) Die C / 25.4 mm / Sym (Trial 14) and (d) Die E / 25.4 mm / Sym (Trial 15).

Fig. 5-40 shows the strain history of the centre point in the extrusions made using different die configurations. Referring to Fig. 5-40 shows that that material made using Die E / 12.7 mm extrusion has the highest strain value among the four die configurations and reaches 120 at the die exit. The extremely high strain value of the weld seam centre point is due to the extremely high shear strain experienced when flowing against the bridge surface. When the welding chamber height for Die E is increased to 25.4 mm, the strain value of the centre point (Die E / 25.4 mm) drops to 68 at the die exit. The strain of the weld seam centre for material extruded using Die C is much lower than Die E because flow paths in Die C extrusions are smoother and less obstructed by the bridge, and the strain value does not change significantly when the welding chamber height changes from 12.7 to 25.4 mm.

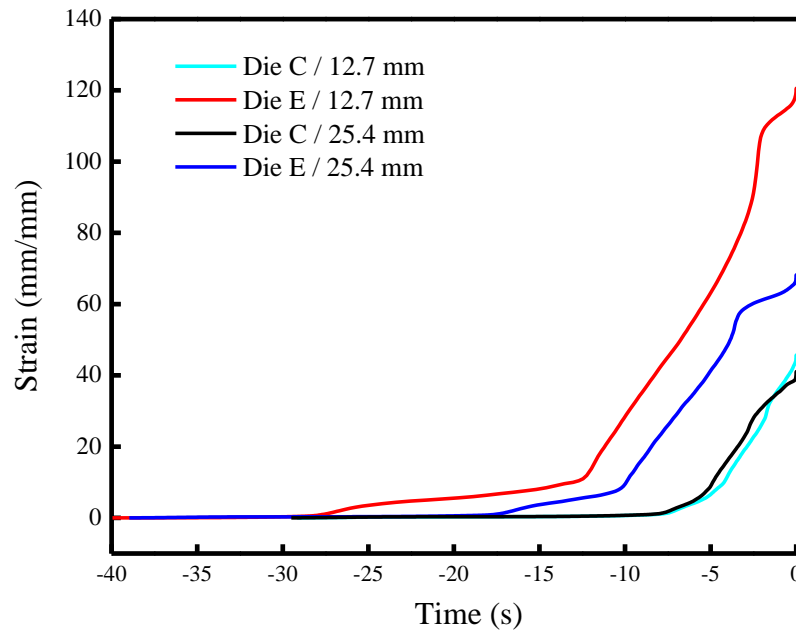


Fig. 5-40 Model-predicted strain history at the centre of the weld seam for different dies and different weld chamber heights.

Fig. 5-41 shows the comparison between the EBSD image and the model-calculated strain distribution. Referring to Fig. 5-41a and c, the texture at seam is different from the neighbouring area's texture, and the boundary of the seam texture (marked by white dash line) roughly matches the high strain region ( $\epsilon > 40$ , red coloured) at the seam calculated from simulation. The result implies that the texture distribution through the cross section of the profile is influenced by the strain distribution.

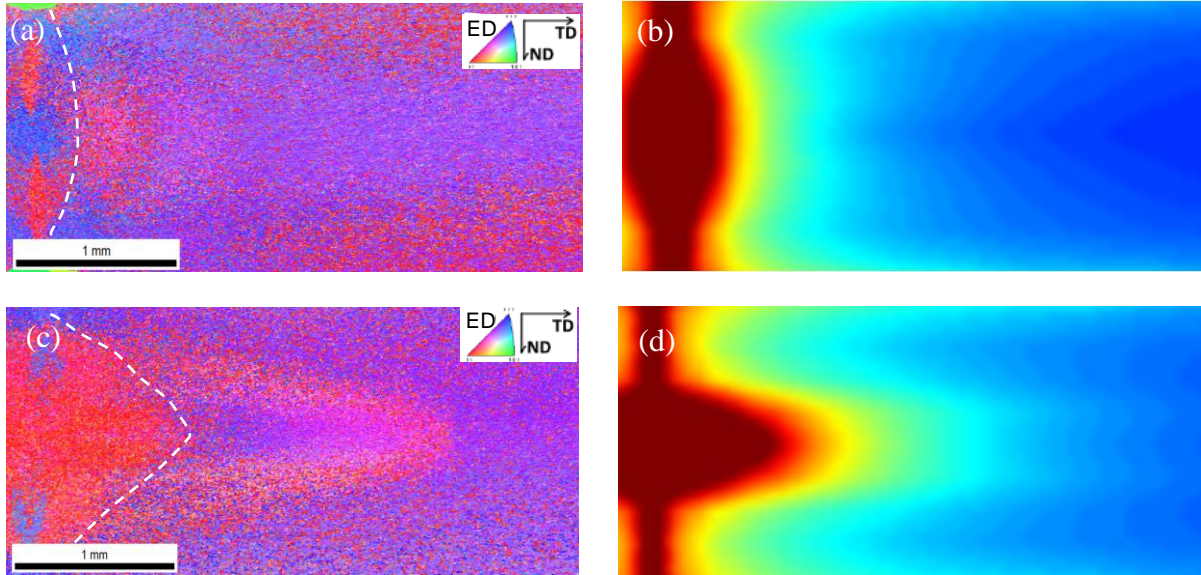


Fig. 5-41 (a) EBSD image (inverse polar figure) of Die C / 12.7 mm / Sym, (b) model-calculated strain of Die C / 12.7 mm / Sym, (c) EBSD image (inverse polar figure) of Die E / 12.7 mm / Sym and (d) model-calculated strain of Die E / 12.7 mm / Sym.

### 5.3.2.4 Welding quality prediction

As discussed in Section 2.3.3, there are several parameters used to predict the weld quality of the seam in porthole die extruded samples. In this section, weld quality parameters described earlier (Q, K and J) were calculated based on the integration of the mean stress over effective stress along the flow path of the centre point (see Eq. 2-2, 2-3 and 2-4). As shown in Table 5-6, each die configuration has a different predicted welding quality parameter, which may indicate that each die configuration will have a different weld quality. Due to the longer contact time in the deep welding chamber, the 25.4 mm welding chamber dies have a higher Q, K and J values than the 12.7 mm welding chamber dies. Material extruded using Die C also have a higher Q, K and J value than material extruded using Die E due to the smoother material flow. However, the stress – strain curves of the samples extruded using these different dies are very similar to each other and do not indicate a significant welding quality difference. What's more, the metallography and EBSD images also do not show any cracks or obvious welding defects at the seam region. It seems that for these extrusion trials, the minimum conditions have been met to produce a robust weld and hence difference in the welding quality parameters do not give a precise prediction about welding quality of porthole die extrusions used this research.

One explanation for why different die configurations extruded samples have almost the same strength and fracture elongation despite their different welding quality parameters (Q, K and J value) could be all of them have reached a sound welding quality. Donati et al [29] compared a series of criteria for seam quality prediction, and it was found out that K value is better than Q value in predicting the welding quality of 6082 alloy porthole die extrusion. In the temperature range from 430 to 513 °C, the critical K value for a sound welding quality is 23 [113]. As shown in Table 5-6, all of die configurations' K value is above 23, and all of them should be considered to be sound welding quality. In the recent research by Yu et al. [30], the critical J value for 6084 alloy to achieve a sound welding quality is 10.83, which is below all of the J values of the four die configurations used in this thesis. Therefore, the relative lower fracture elongation of the porthole die extruded samples compared by seamless sample should be the non-uniform texture and microstructure throughout the cross section rather than the poor bonding at the weld seam.

Table 5-6 Welding quality prediction of porthole die extrusions of different bridges and welding chambers.

	Die C / 12.7 mm	Die E / 12.7 mm	Die C / 25.4 mm	Die E / 25.4 mm
Q	1.0	0.69	4.2	2.9
K	45.4	28.9	131.5	86.2
J	14.9	13.3	20.3	18.5

## 5.4 Effect of ram speed

### 5.4.1 Breakthrough load

Breakthrough load increases with ram speed due to the intrinsic material behaviour of the aluminum alloy [62]. As indicated by Eq. 4-1, the material's flow strength increases with a higher strain rate. Since the average strain rate increases with ram speed, the material flow strength is expected to increase at a higher ram speed and the breakthrough load will also increase [8]. Fig. 5-42 shows the experimental and model-predicted breakthrough load for various porthole die extrusions performed at different ram speeds. As shown in Fig. 5-42, the breakthrough load predicted by the model matches the measured experimental result well, and the difference between experimental and simulated extrusion load is within 15 tonne (about 2.5% of the measured load). This provides additional evidence that the model predictions are accurate. Second, the

breakthrough load increases with ram speed as expected. However, the temperature increase that occurs at high ram speed has a tendency to compensate for the material's strengthening effect due to the high strain rate, and the breakthrough load increase was limited to 15 ~ 25 tonnes when the ram speed varies from 4 mm/s to 7 mm/s. Third, as noted before, Die E extrusion has a slightly higher breakthrough load than Die C, and 25.4mm welding chamber also has a higher breakthrough load than the 12.7 mm welding chamber due to the higher volume of material.

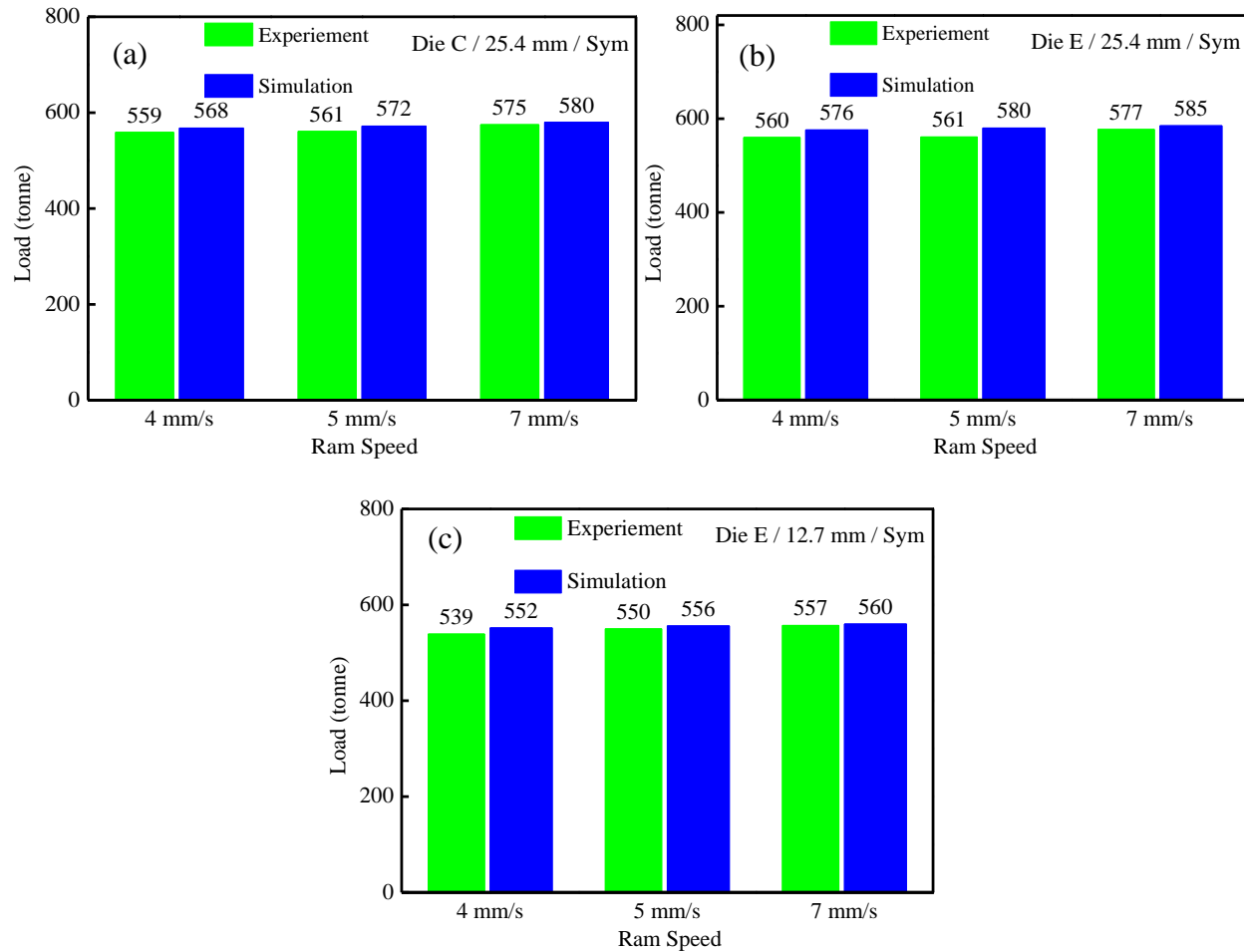
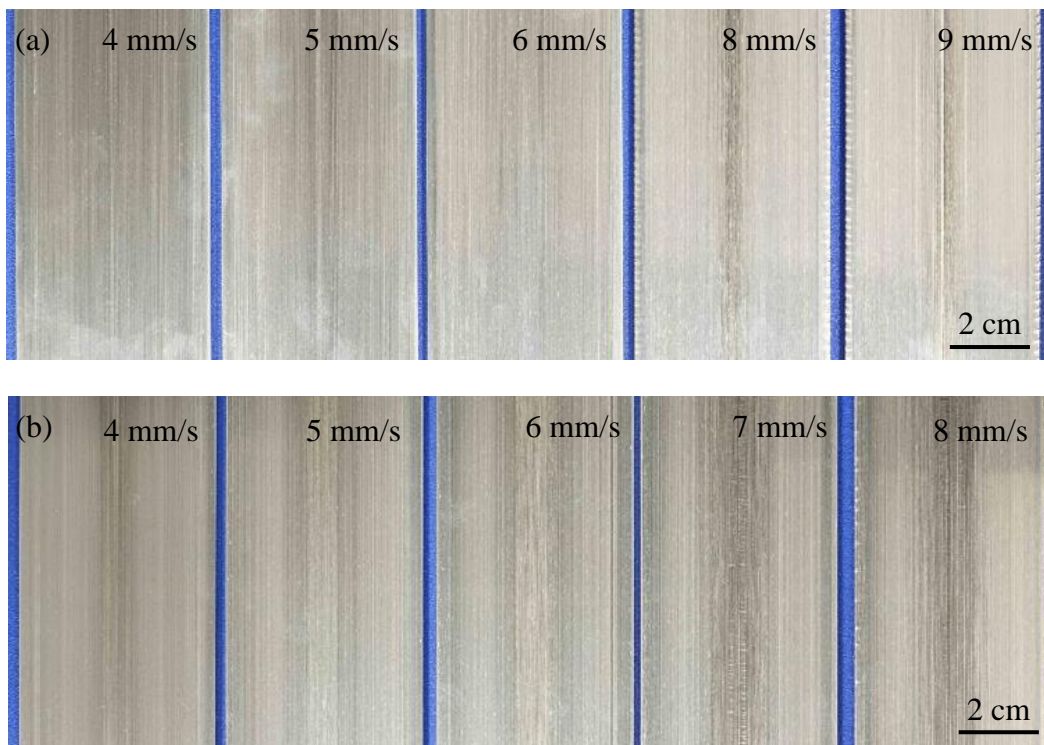


Fig. 5-42 Breakthrough load at different ram speeds: (a) Die C / 12.7 mm / Sym (Trial 12), (b) Die E / 12.7 mm / Sym (Trial 13), (c) Die C / 25.4 mm / Sym (Trial 14) and (d) Die E / 25.4 mm / Sym (Trial 15).

### 5.4.2 Surface quality

In this research, the ram speed's effects on the porthole die extrusion were studied by extruding five consecutive billets of varying ram speeds from 4 to 8 mm/s. The extruded samples' surface

did not show any deterioration irrespective of which die configuration was used, when the extrusion ram speed increased from 4 mm/s to 6 mm/s, as shown in Fig. 5-43. However, the surface defects on the extrudate began to appear at a ram speed of 7 mm/s. Surface defects of porthole die extruded samples can be categorized into three types. The first type of surface defect is speed crack on the extrudates' edge. Speed cracks are thought to occur when the friction between the extrudate and the die bearing is beyond the strength of the extra hot extrudate caused by a high ram speed [62]. What's more, the severity of speed cracking is not constant along the profile length, as shown in Fig. 5-44. At the front of the profile, the speed crack is not very severe, and the cracks are relatively short (Fig. 5-44a). However, at the back of the profile, more speed cracks appear on the edge of the profiles and the cracks propagate deeply into the material (Fig. 5-44b). The reason for this is that the exit temperature of the extrudate can keep increasing during the whole process of the extrusion, so it is reasonable to assume the back of profile's temperature is higher than the front part [8].



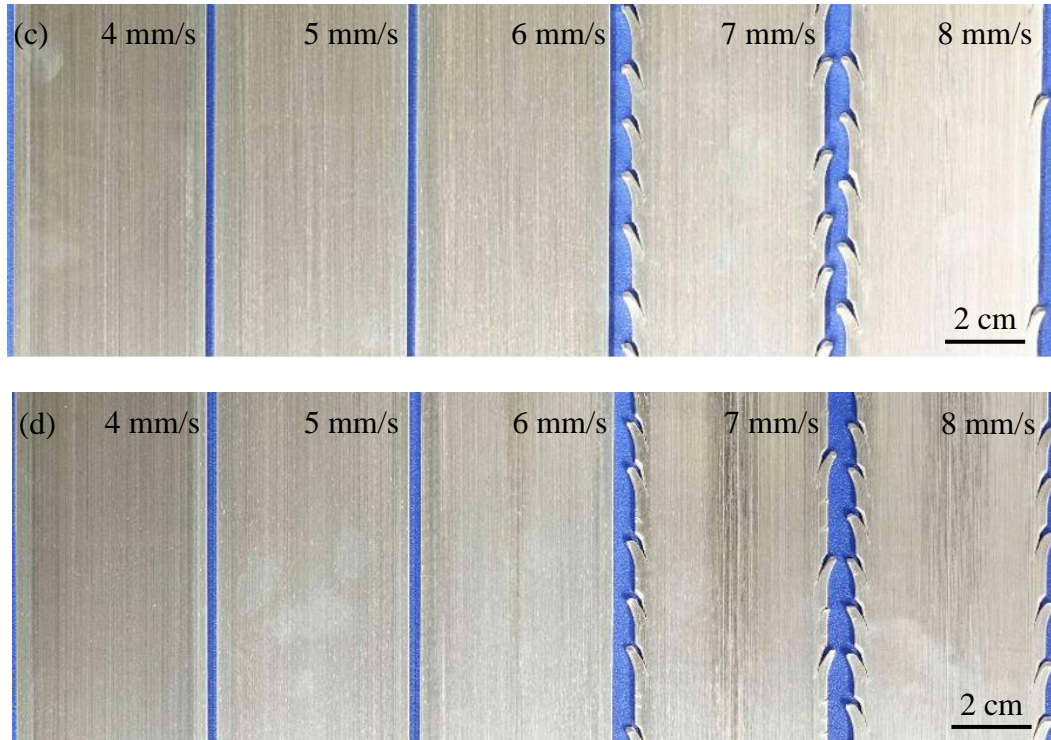


Fig. 5-43 Outer appearance of the extruded samples at different ram speeds through different die configurations: (a) Die C / 12.7 mm / Sym (Trial 12), (b) Die E / 12.7 mm / Sym (Trial 13), (c) Die C / 25.4 mm / Sym (Trial 14) and (d) Die E / 25.4 mm / Sym (Trial 15).

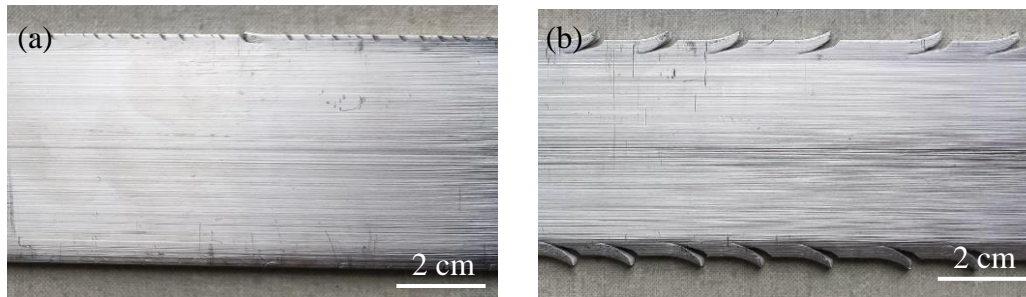


Fig. 5-44 (a) The front and (b) back part of the extruded profile by Die C / 25.4 mm / Sym (Trial 14) at 7 mm/s.

Besides the speed cracking, another surface defect related to the ram speed is the groove or striations of cracks along the weld seam. When the ram speed reached 8 mm/s, material extruded using Die C / 12.7 mm exhibited a noticeable groove along the weld line (Fig. 5-45a). The appearance of this groove at the weld line could be due to the lack of enough contact time of the metal streams to fully deform the material at the seam. However, the surface defects along the

weld seam for samples extruded using Die E / 12.7 mm appear different from the other three die configurations. There are striations of cracks near the weld seam together with a groove along the weld line for samples extruded using Die E / 12.7 mm at 8 mm/s. The formation of small cracks near the weld seam in the sample extruded using Die E / 12.7 mm could be due to its relatively higher exit temperature compared to the other die configurations, which is also verified through the simulation result (Fig. 5-35). Increasing the welding chamber height seems to alleviate the surface defects along the weld seam to some extent. Even through the groove still exists at the weld line in the sample extruded using Die C / 25.4 mm at 8 mm/s (Fig. 5-45c), the groove is not as deep as the groove that developed in the sample extruded using Die C / 12.7 mm. The relatively shallow groove in the sample extruded using Die C / 25.4 mm could be due to the longer contact time of the metal streams in the deep welding chamber. The small cracks close to the seam disappeared in the sample extruded using Die E / 25.4 mm at 8 mm/s, but the groove at the weld line still exists (Fig. 5-45d). Besides the groove, the region close to the weld line in the sample extruded using Die E / 25.4 mm at 8 mm/s appears to be slightly rougher than the rest of the material. Based on these observations and discussion, the surface quality of samples extruded under different ram speeds is summarized in Table 5-7.

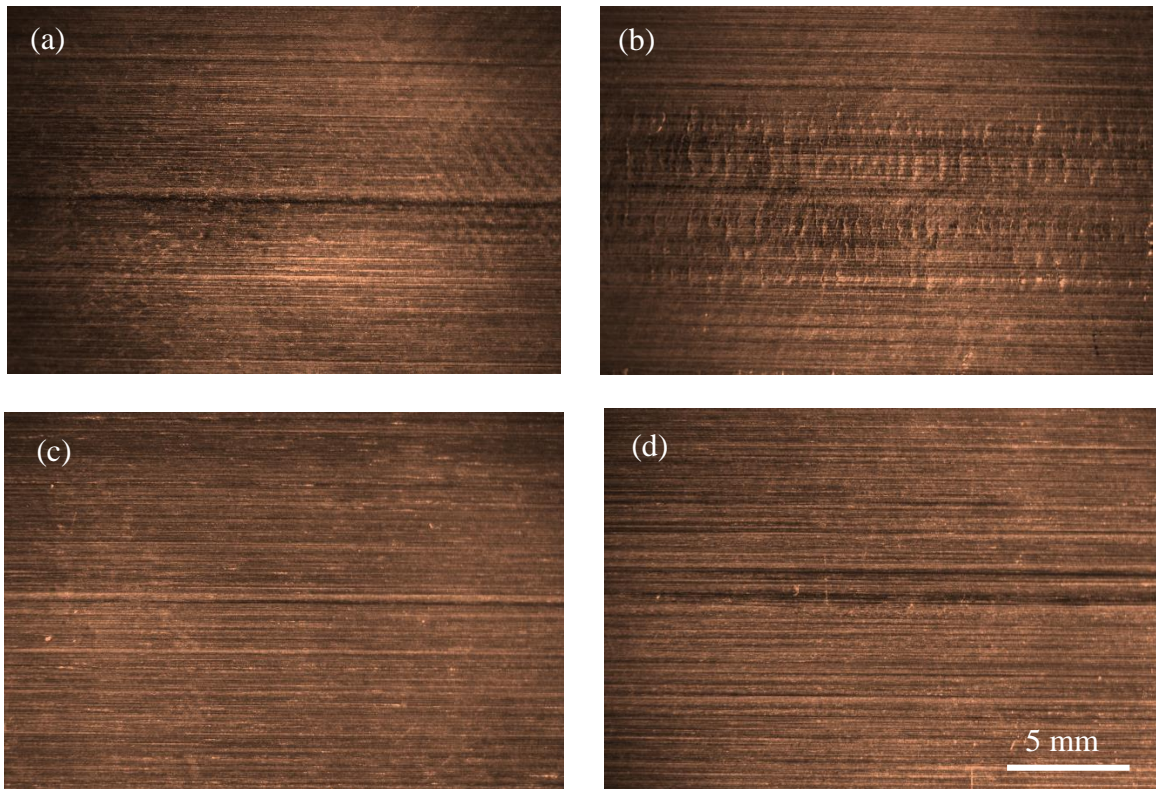


Fig. 5-45 The surface quality at the seam: (a) Die C / 12.7 mm / Sym (Trial 12), (b) Die E / 12.7 mm / Sym (Trial 13), (c) Die C / 25.4 mm / Sym (Trial 14) and (d) Die E / 25.4 mm / Sym (Trial 15).

Table 5-7 Summary of the surface quality at different ram speeds.

Extrusion condition	Surface quality at the weld seam	Surface quality at the edge
Die C / 12.4 mm at 4 mm/s	Good	Good
Die C / 12.4 mm at 5 mm/s	Good	Good
Die C / 12.4 mm at 6 mm/s	Good	Good
Die C / 12.4 mm at 8 mm/s	Groove	Speed crack
Die C / 12.4 mm at 9 mm/s	Deep groove	Speed crack
Die E / 12.4 mm at 4 mm/s	Good	Good
Die E / 12.4 mm at 5 mm/s	Good	Good
Die E / 12.4 mm at 6 mm/s	Rough surface	Good
Die E / 12.4 mm at 7 mm/s	Striations of cracks	Good
Die E / 12.4 mm at 8 mm/s	Striations of cracks	Speed crack
Die C / 25.4 mm at 4 mm/s	Good	Good
Die C / 25.4 mm at 5 mm/s	Good	Good
Die C / 25.4 mm at 6 mm/s	Good	Good
Die C / 25.4 mm at 7 mm/s	Good	Severe speed crack
Die C / 25.4 mm at 8 mm/s	Shallow groove	Severe speed crack
Die E / 25.4 mm at 4 mm/s	Good	Good
Die E / 25.4 mm at 5 mm/s	Good	Good
Die E / 25.4 mm at 6 mm/s	Good	Good
Die E / 25.4 mm at 7 mm/s	Very shallow groove	Severe speed crack
Die E / 25.4 mm at 8 mm/s	Groove and slightly rough surface	Severe speed crack

### 5.4.3 Microstructure

The ram speed effect on the extruded samples' microstructure were examined using optical metallography. Fig. 5-46 shows the changes in the microstructure for samples extruded using the Die C / 25.4 mm die configuration with increasing ram speed. All of the samples have a triangle

shaped PCG at the welding line, and the thickness of PCG layer increased with increasing ram speed. As shown in Fig. 5-46a, the thickness of the PCG layer at the weld seam was 330  $\mu\text{m}$  at a ram speed of 4 mm/s, while the thickness of PCG layer increased to 945  $\mu\text{m}$  when the ram speed was 8 mm/s. According to other researches, the exit temperature and stored energy play an important role in the PCG thickness during porthole die extrusion [114-116]. The high exit temperature due to the high ram speed can cause the fine dispersoids to dissolve in the matrix and allow abnormal grain growth to occur [114]. Stored energy also increased with the ram speed, which promoted the PCG layer to penetrate into the interior part of the sample [116]. Fig. 5-47 shows the relationship between the PCG thickness and ram speed for the Die C / 25.4 mm extrusion. It is very interesting to see the PCG thickness increased in a linear trend relative to the ram speed.

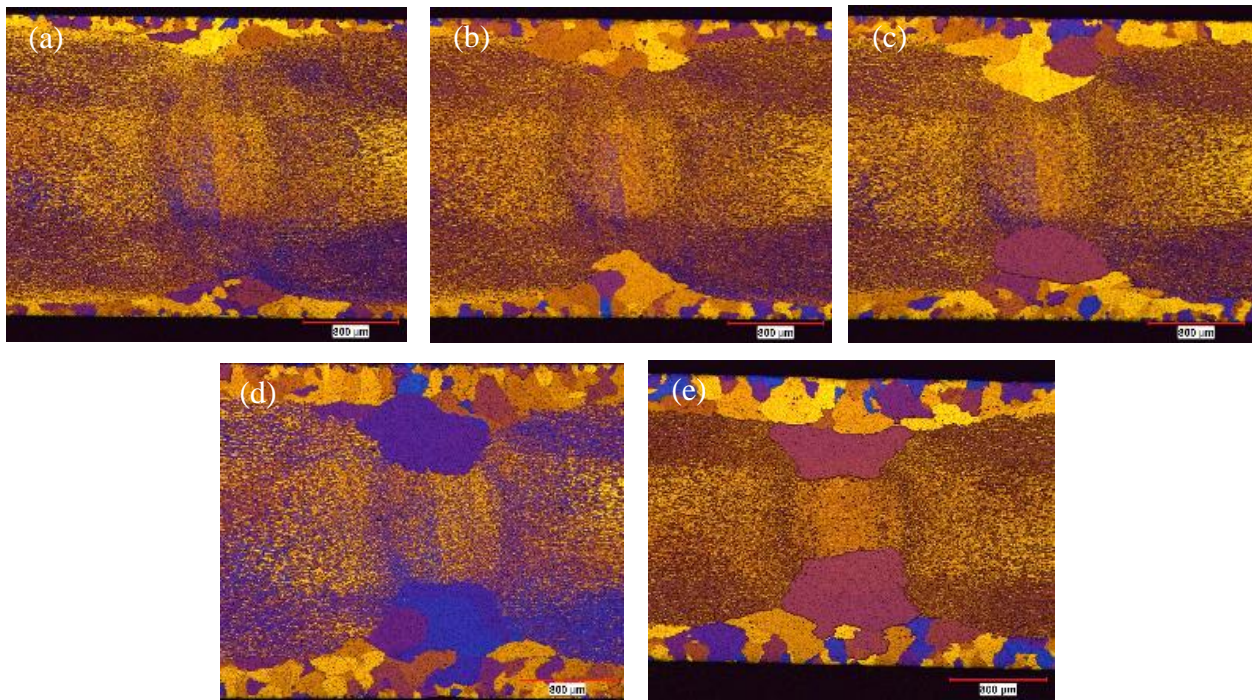


Fig. 5-46 Optical metallography of samples (T4) extruded using Die C / 25.4 mm / Sym (Trial 14) at different ram speeds: (a) 4 mm/s, (b) 5 mm/s, (c) 6 mm/s, (d) 7 mm/s and (e) 8 mm/s.

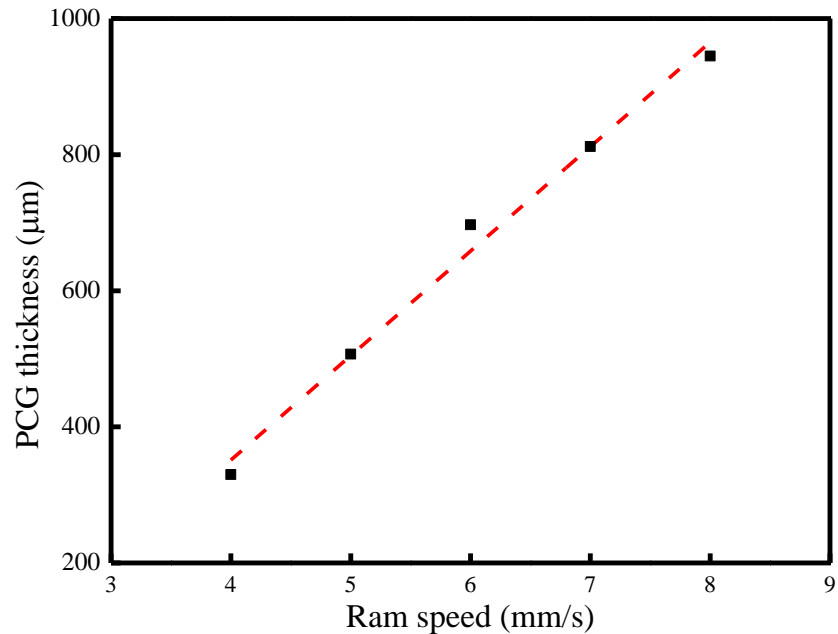
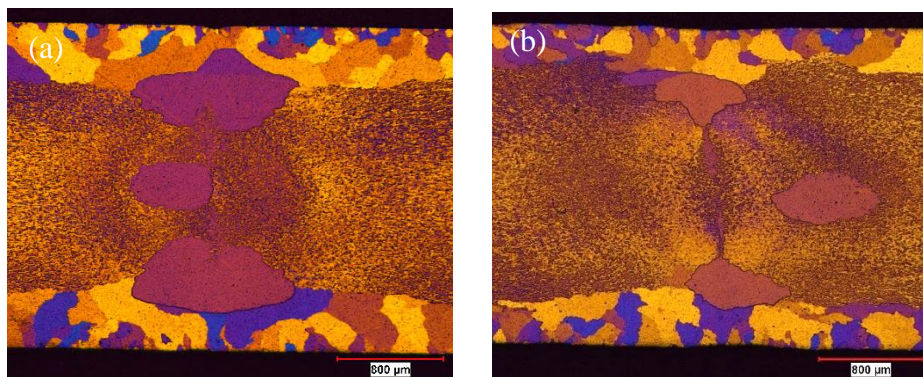


Fig. 5-47 The relationship between the PCG thickness and ram speed.

Another interesting phenomenon of the microstructure for samples extruded at a high ram speed is the occasional abnormal grain growth that occurred in the middle thickness of the strip. As shown in Fig. 5-48a and b, there is a coarse grain of about 600 μm detached from the PCG layer in the middle thickness close to the weld seam. The abnormal grain growth in the middle thickness might be because of the high temperature and high stored energy due to the high ram speed. On the other hand, these abnormal coarse grains were not observed in the middle thickness of every high ram speed extruded sample, as shown in Fig. 5-48c. The absence of coarse grain in some high ram speed extruded samples' middle thickness indicates the abnormal grain growth in the interior part of the material was random and not consistent throughout the extrudate.



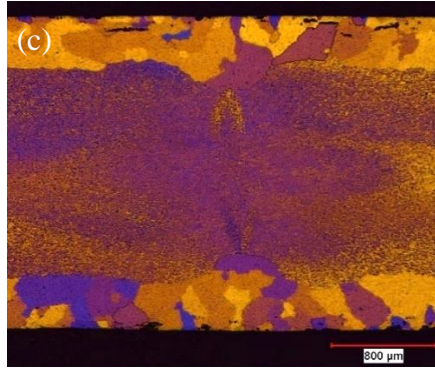
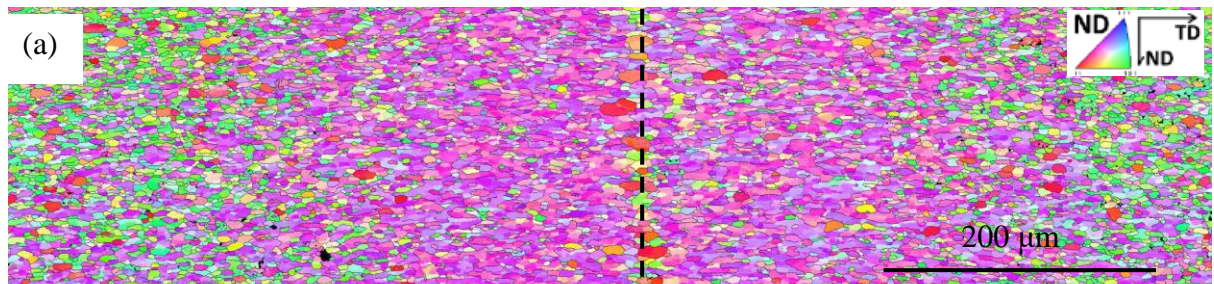


Fig. 5-48 abnormal grain growth in high ram speed extruded samples (T4): (a) Die C / 12.7 mm at 8 mm/s (Trial 12), (b) Die E / 25.4 mm at 7 mm/s (Trial 15) and (c) Die E / 12.7 mm at 8 mm/s (Trial 13).

#### 5.4.4 Texture analysis

Ram speed's influence on texture is examined by EBSD tests on the welding region (Fig. 5-4). Fig. 5-49 shows the EBSD images of the seam region of the sample extruded through Die C / 12.7 mm / Asym at the ram speed of 5 mm/s (trial 1) and 7 mm/s (Trial 3). The microstructures between the two samples at the seam region are almost the same. The pole figures show that the strips extruded through Die C at 8 mm/s and 440 °C (Fig. 5-49b) have the almost same texture as the samples extruded at 5 mm/s and 480 °C (Fig. 5-5). This result shows that the ram speed's effect on the profile's texture is very small.



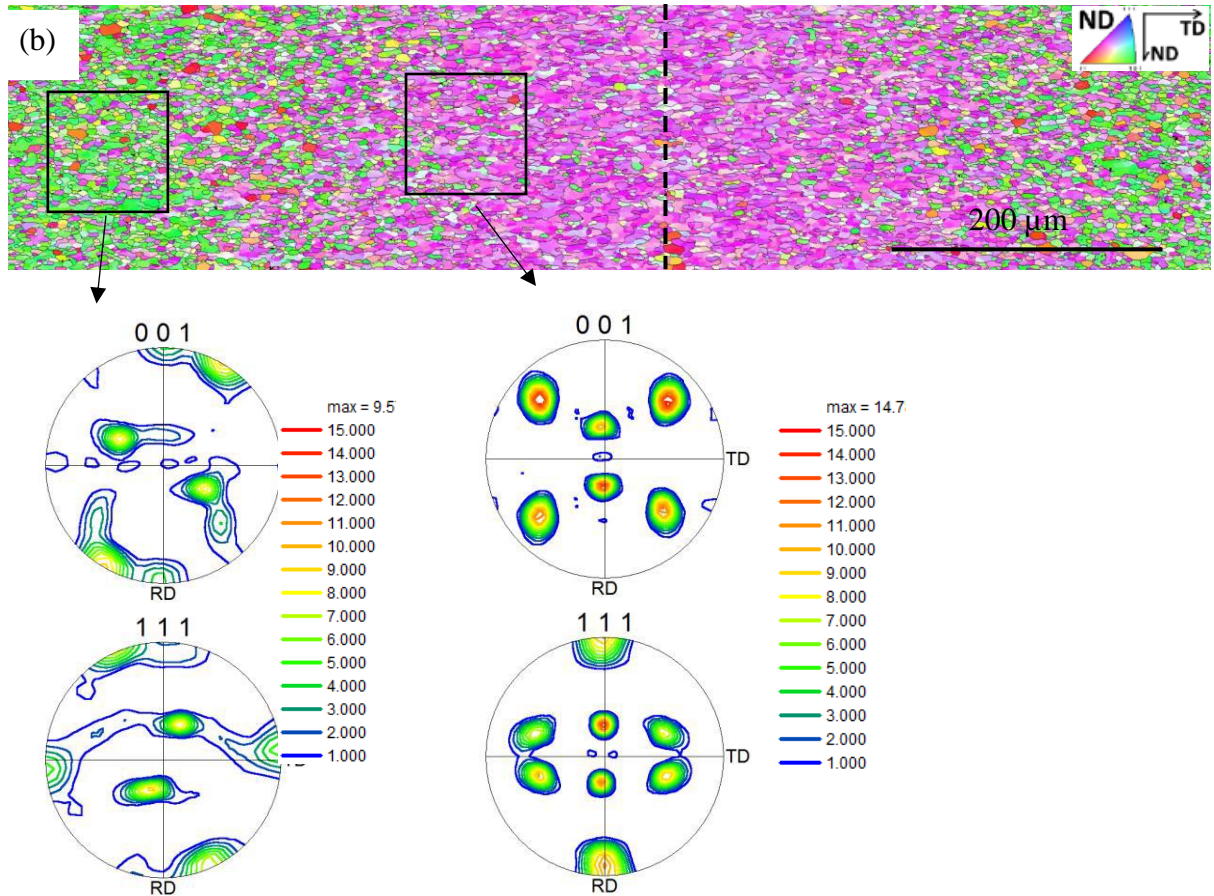


Fig. 5-49 EBSD image (inverse polar figure) of welding region of samples (T5) extruded by Die C / 12.7 mm at ram speed of (a) 5 mm/s (Trial 1) and (b) 7 mm/s (Trial 3).

### 5.4.5 Mechanical properties

The measured stress–strain curves of samples extruded using different dies at different ram speeds are plotted in Fig. 5-50, together with the no seam sample. As shown in Fig. 5-50, all of the samples have a yield and ultimate strength of ~210 and ~330 MPa regardless of the ram speed or extrusion die geometry. On the other hand, the fracture elongation results vary significantly between the no seam sample and porthole die extruded samples. The sample with no weld seam had a fracture elongation of 23.5% due to its relatively homogeneous microstructure throughout the profile’s cross section, but the fracture elongation of porthole die extruded samples with a weld seam varied between 14% to 18%. The fracture elongation did not change noticeably when the ram speed was varied between 4 to 6 mm/s, but the fracture elongation of the sample began to drop when the ram speed was 8 mm/s, which indicated that 8 mm/s is the maximum ram speed to obtain

a sound weld seam. Compared to the other three die configurations, the sample extruded using Die C / 25.4 mm had a slightly higher fracture elongation, and it may be due to the smoother material flow and longer contact time in the welding chamber.

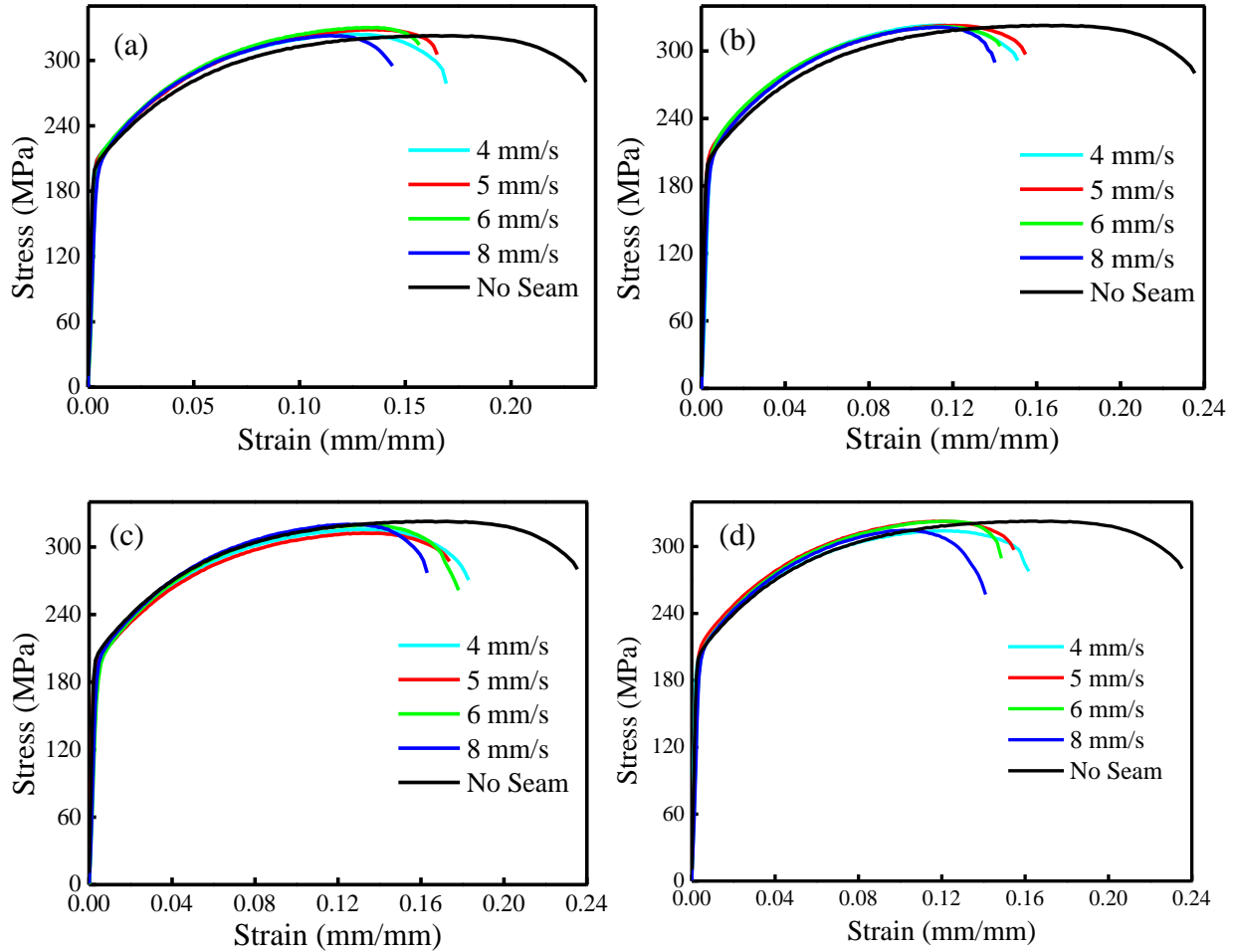


Fig. 5-50 Stress – strain curve of samples extruded at different ram speed (T4): (a) Die C / 12.7 mm / Sym (Trial 12), (b) Die E / 12.7 mm / Sym (Trial 13), (c) Die C / 25.4 mm / Sym (Trial 14) and (d) Die E / 25.4 mm / Sym (Trial 15).

### 5.4.6 Model predictions

DEFORM simulations were conducted to help understand and explain the ram speeds' effects on the porthole die extrusion. Fig. 5-51 shows the temperature distribution of the samples extruded by Die C / 25.4 mm at the die exit. The surface temperature of the extruded strip increased significantly when the ram speed increased from 4 mm/s to 7 mm/s. When the ram speed was 4 mm/s, the surface temperature was about 575 °C. However, the surface temperature was over 593

°C, which is very close to the melting point, when the ram speed was 7 mm/s. The simulation results offered further evidence that the surface cracking at high ram speed was due to the high exit temperature.

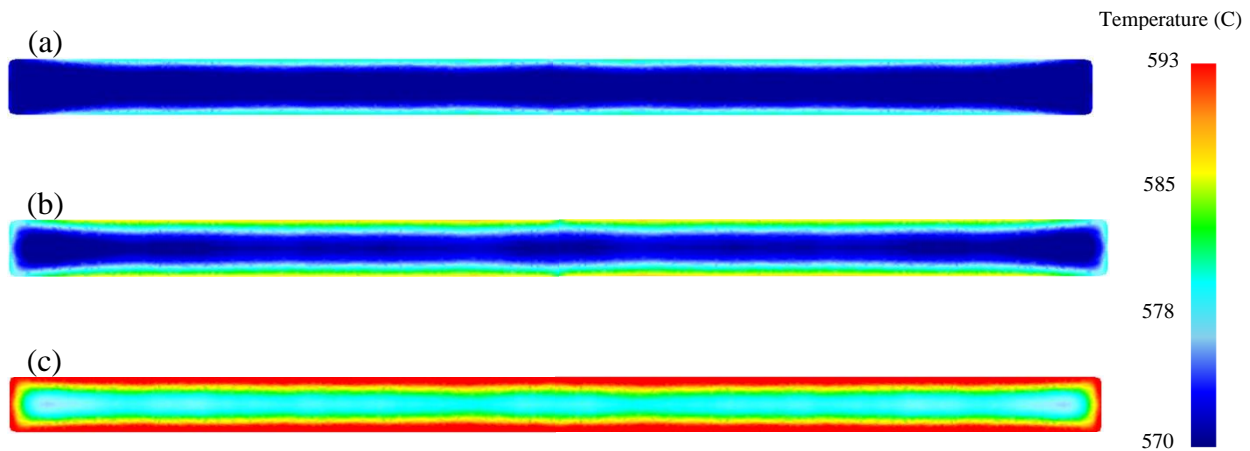


Fig. 5-51 The temperature distribution throughout the cross section of the profile extruded by Die C / 25.4 mm (Trial 14) at the die exit: (a) 4 mm/s, (b) 5 mm/s and (c) 7 mm/s.

## 5.5 Effect of composition

### 5.5.1 Microstructure

Fig. 5-52 shows the microstructures of the extruded profiles for the three different compositions (0Mn, 05Mn and 0.5Mn0.15Cr) extruded through Die C at 480 °C using a ram speed of 5 mm/s. Referring to Fig. 5-52, the microstructure of the 0Mn alloy shows an equiaxed structure with grains of about 50  $\mu\text{m}$  in size, which indicated that the profile was fully recrystallized during extrusion due to the lack of dispersoids (Fig. 5-52a). What's more, the weld line is not distinguishable from the matrix, and the surface grain size is quite similar to the interior grains. In contrast, the Mn and Mn / Cr containing profiles showed a very fine interior microstructure and PCG layer on the surface (Fig. 5-52b and c). Unlike the 0Mn case, the weld line is easily visible in these microstructures and is revealed by the change of colour across the weld line under the optical microscope.

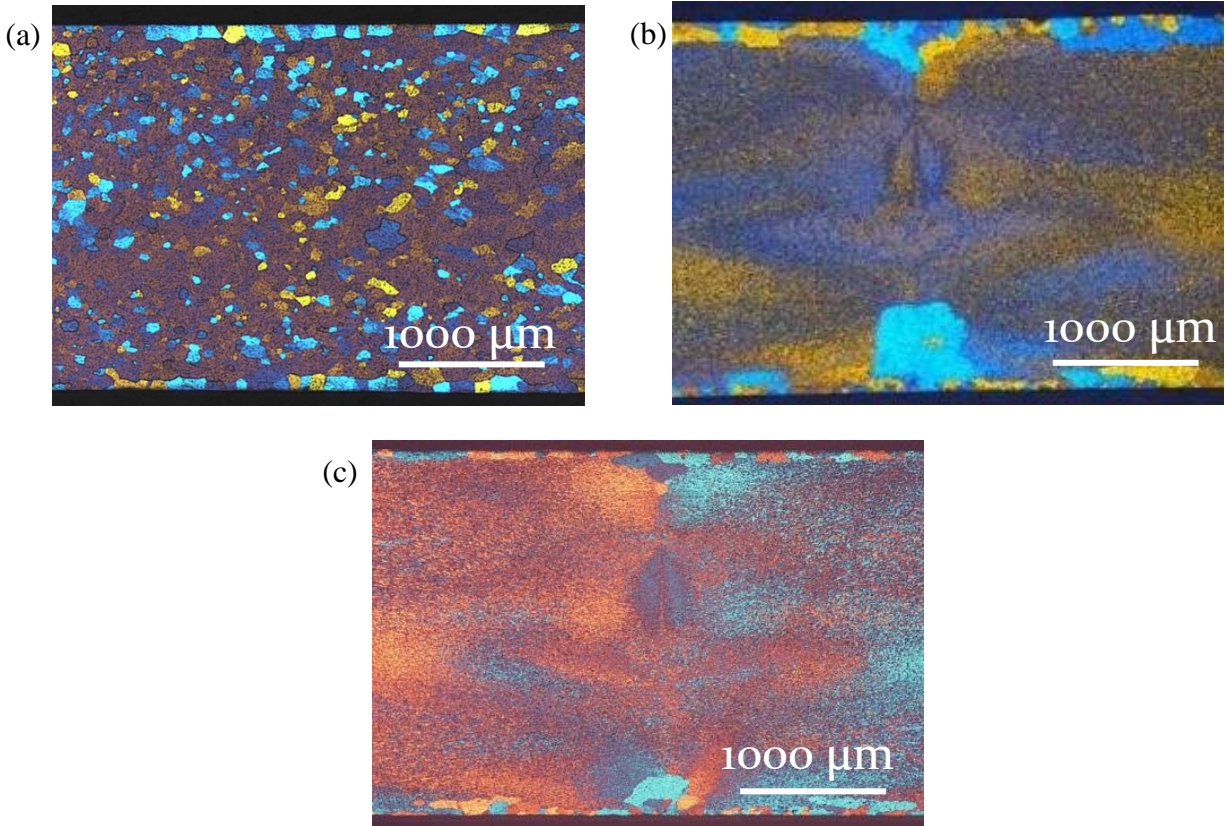


Fig. 5-52 Optical metallography of welding region in the extrudates of different compositions (T4): (a) 0Mn (Trial 9), (b) 0.5Mn (Trial 7) and (c) 0.5Mn0.15Cr (Trial 2).

To examine the microstructure variation from the welding zone to the other parts of material along the strip, the entire microstructure cross-section was examined via optical microscopy, as shown in Fig. 5-53 for the 0Mn case. Referring to Fig. 5-53, the microstructure across the entire profile was recrystallized and the materials extruded using Die E and Die C look very similar.

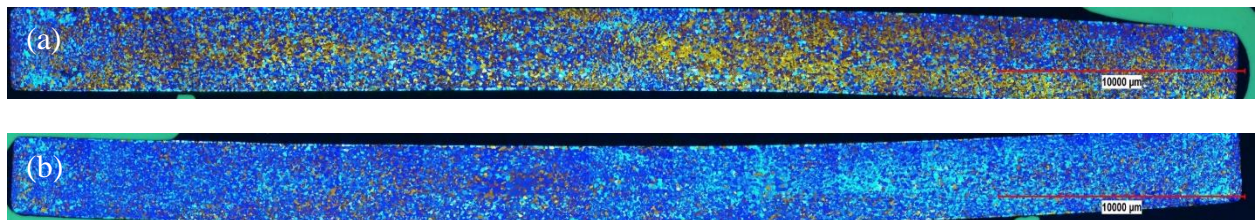


Fig. 5-53 Optical metallography of the 0Mn profiles' cross section extruded by different die configurations (T4): (a) Die C (Trial 8) and (b) Die E (trail 9).

The Mn / Cr effects on the extruded profiles were also examined by the extrusion without bridge. As shown in Fig. 5-54a, the microstructure was fully recrystallized and it does not show

an obvious difference from the microstructure extruded using Die C and Die E. As a result, it is safe to say that the complex porthole die extrusion process, such as metal separation and then rejoining, does not affect visibly the fully recrystallized sample's final microstructure. However, the 0.5Mn0.15Cr samples exhibit a very fine and deformed interior microstructure and a PCG layer on the surface (Fig. 5-54b). By comparing the metallography of the 0.5Mn0.15Cr materials extruded using Die C and Die E as well as a no bridge case, the microstructure of the no bridge sample did not show any microstructure variation from the centre to the edge. From this perspective, the recrystallization that occurs during porthole die extrusion of the 0Mn sample seems to have a unique function to allow for the creation of a microstructure that is more uniform through the cross section than the un-recrystallized samples.

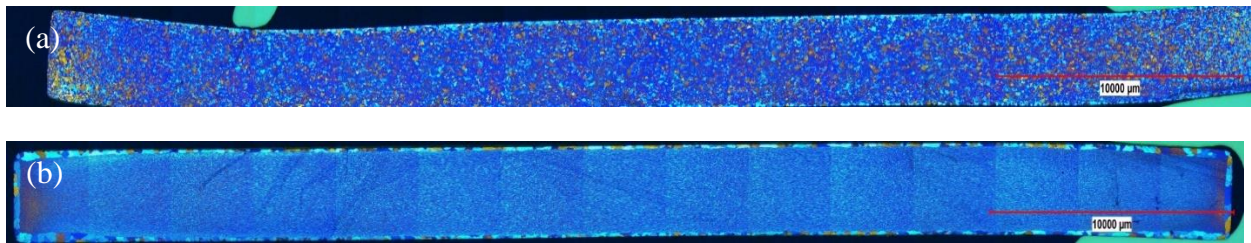


Fig. 5-54 Optical metallography of the profiles' cross section of different compositions extruded using no bridge die (T4): (a) 0Mn (Trial 10) and (b) 0.5Mn0.15Cr (Trial 11).

## 5.5.2 EBSD

### 5.5.2.1 0Mn sample texture

EBSD characterization was used to study the subtle microstructure differences between the weld seam and the other parts of the extruded material, and also to determine local texture characteristics of the porthole die extruded 0Mn samples. The two locations selected to be examined using EBSD were at the centre and the quarter width of the profile, as shown in Fig. 5-4.

Fig. 5-55 shows the EBSD image of the 0Mn samples extruded by Die C / 12.7 mm (Trial 8) die at both the centre and the quarter width location. The microstructure at both of the centre and the quarter width locations show equiaxed grains (Fig. 5-55), whose results were consistent with the optical microscopy (Fig. 5-53). Even though the EBSD images of the two locations were very similar to each other, there were still some small noticeable differences between the two in terms of grain orientation. The orientation of grains was mapped using different colours in the inverse

pole figure (Fig. 5-55), and the two major components – red and green coloured grains – corresponded to the orientation with {100} and {110} parallel to the normal direction respectively. Further grain orientation analysis done using the TSL-OIM software showed that the red and green grains took up about 37.8% and 31.0% of the volume fraction at the centre region, but in the quarter width region the red and green corresponded to 53.7% and 12.8% of the volume fraction.

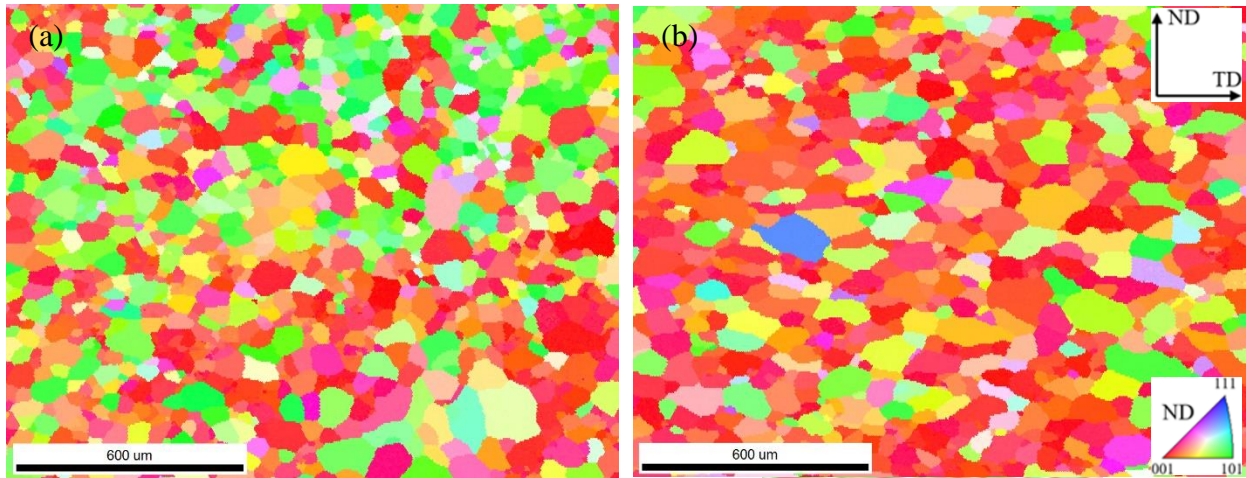


Fig. 5-55 Measured EBSD image (inverse pole figure) of 0Mn sample extruded by Die C / 12.7 mm (Trial 8, T4) at (a) centre and (b) quarter width.

The pole figures also show the grain orientation differences between the centre and the quarter width region (Fig. 5-55). Although the pattern of the pole figures seems to be very similar between the two, the maximum intensity of the pole figure of the centre region and the quarter width are 19 and 23. The higher maximum intensity of the pole figure of the quarter width indicated that the grain orientation is more aligned in the quarter width region than in the centre. The reason why the centre region exhibits a less consistent grain orientation may lie in the complex thermal mechanical history of the welding region during porthole die extrusion. On the other hand, the quarter width region was not affected by the existence of the bridge and only experienced plane strain deformation during extrusion, so the texture after recrystallization was predominantly  $\langle 100 \rangle \{001\}$ , which is a typical recrystallized texture in plane strain [31].

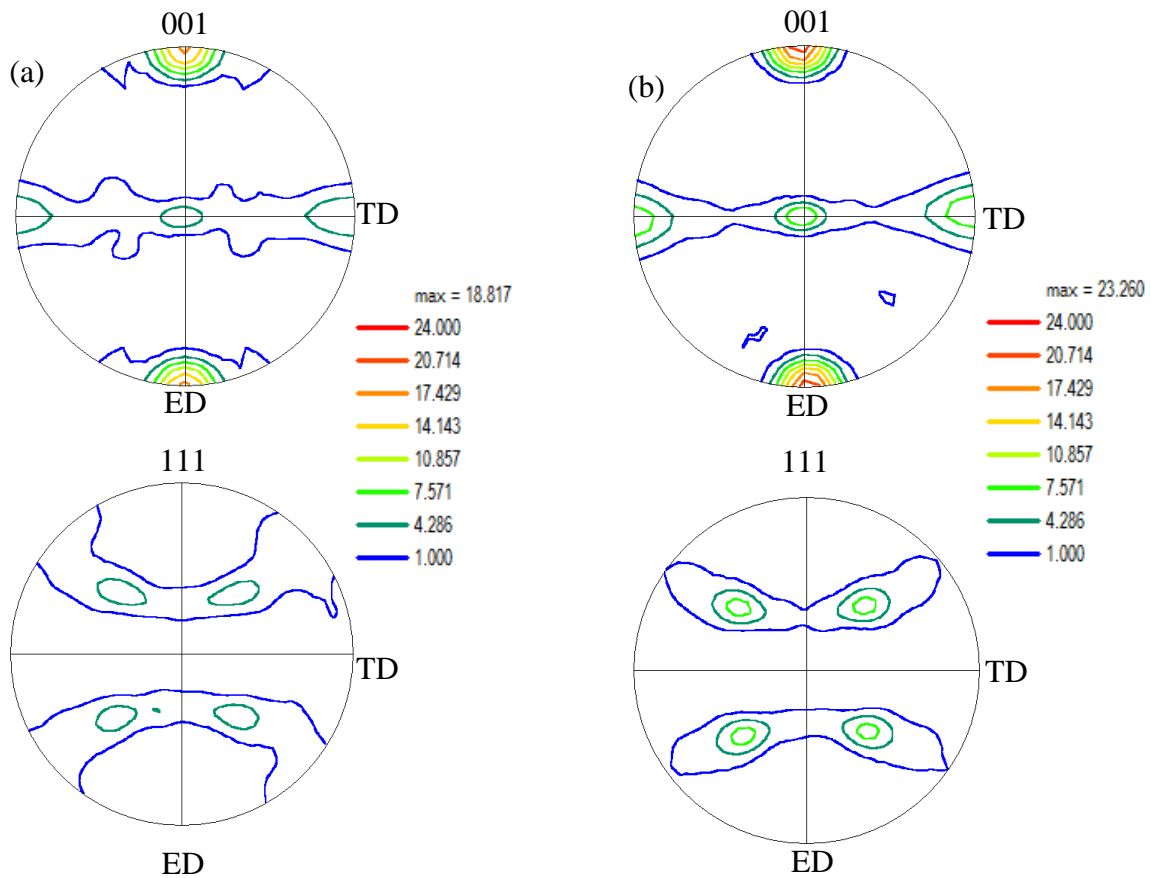


Fig. 5-56 Polar figure of 0Mn sample extruded by Die C /12.7 mm (Trial 8, T4) at (a) centre and (b) quarter width.

### 5.5.2.2 0.5Mn samples

Unlike the 0Mn alloy, 0.5Mn alloy has some  $\alpha$ -Al(MnFe)Si dispersoids at a high temperature to inhibit the recrystallization and grain growth during extrusion. As shown in Fig. 5-57, the microstructure and texture along the weld seam of the 0.5Mn extruded using Die C / 12.7 mm (Trial 6) was almost the same as the 0.5Mn0.15Cr material extruded using the same die configuration. On the other hand, the material along the weld seam in the 0.5Mn sample did not show enough stability to keep the original microstructure during solution treatment at 550 °C for 10 min. As shown in Fig. 5-58a, the centre region was dominated by several huge grains due to abnormal grain growth during solution heat treatment. However, the quarter width still maintained the original microstructure after solution heat treatment (Fig. 5-58b). The difference between the centre region and the quarter width's microstructure after solution heat treatment lies in the higher

strain and stored energy accumulated along the weld seam, which promoted abnormal grain growth. The 0.5Mn sample exhibited an intermediate recrystallization behaviour at a high temperature between 0.5Mn0.15 sample and 0Mn sample. Its microstructure remained un-recrystallized during porthole die extrusion, but the seam region experienced severe abnormal grain growth during solution heat treatment.

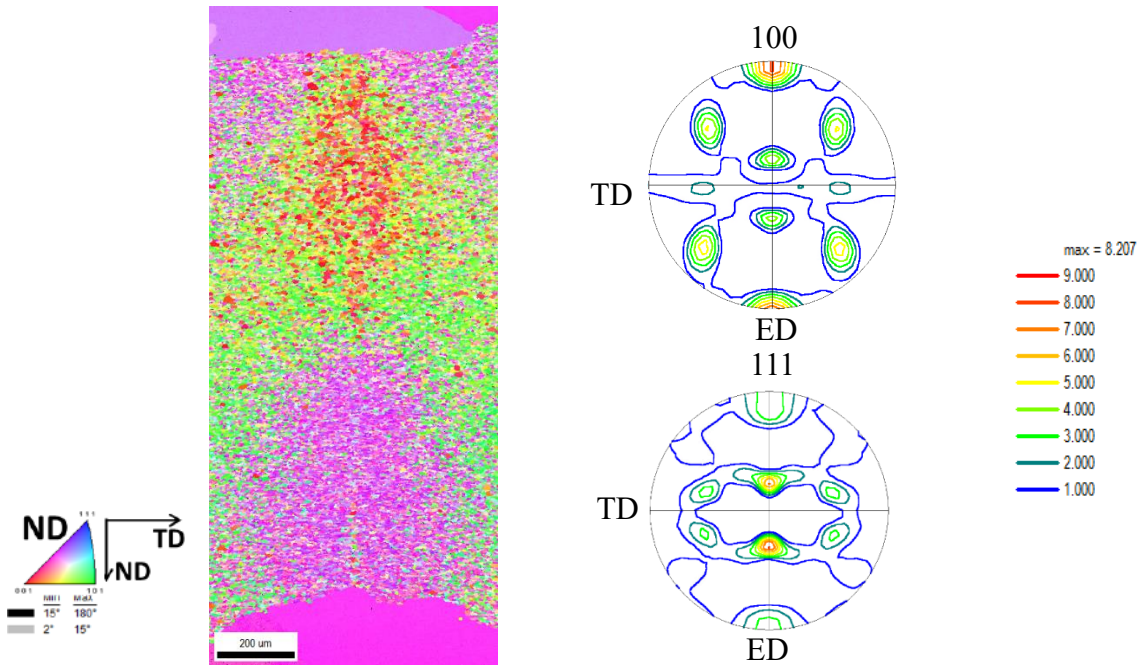


Fig. 5-57 EBSD image (inverse pole figure) and polar figures at the seam of the 0.5Mn sample (Trial 6, T4).

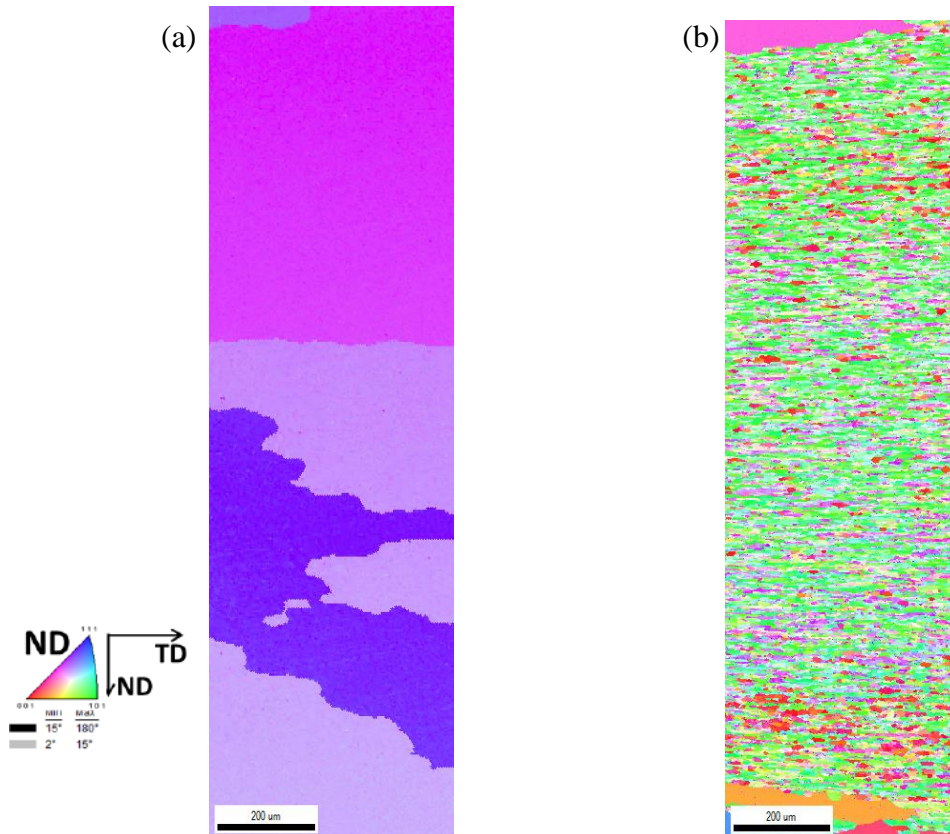


Fig. 5-58 EBSD image (inverse pole figure) and polar figures at the seam of the 0.5Mn sample after solution treatment: (a) the centre region and (b) the quarter width.

## 5.5.3 Mechanical properties

### 5.5.3.1 0Mn samples

Fig. 5-59 shows the measured engineering stress – strain curve of the 0Mn profiles extruded through Die C, Die E and the no bridge die configurations. Referring to Fig. 5-59, the three samples extruded using different porthole die configurations have almost the same yield and ultimate strength, and even the fracture elongations of the three samples are very similar. The fracture elongation of Die C and the no seam sample is about 14%, and the fracture elongation of Die E is about 12%. On the other hand, the fracture elongation of T6 heat treated 0.5Mn0.15Cr sample is only about 8% (Fig. 5-29). Compared to the stress – strain curve of the 0.5Mn0.15Cr samples, the difference between the seamless and porthole die extruded 0Mn samples' fracture elongation was much smaller. As shown in Fig. 5-53 and Fig. 5-54, the small difference between porthole die extruded and the samples extruded without a weld seam indicate that they both exhibit similar

properties. Another noticeable difference between the 0Mn and 0.5Mn0.15 samples was the relatively lower ultimate and yield strength of the 0Mn samples. The yield and ultimate strength of the 0Mn extruded samples were ~260 and ~300 MPa, but the yield and ultimate strength of 0.5Mn0.15Cr samples were ~320 and ~350 MPa respectively. The reason lies in that Mn / Cr rich aluminum alloys contain high content of dispersoids to impede the dislocation movement. In the research by den Bakker et al. [57], they also found that porthole die extruded profiles made up by deformed and fibrous microstructure exhibit a higher strength than the profiles made up by a recrystallized microstructure. What's more, the extruded 0Mn samples did not fracture at the seam as 0.5Mn0.15 samples, but fractured at the location about 3 to 4 mm away from the seam, as shown in Fig. 5-60.

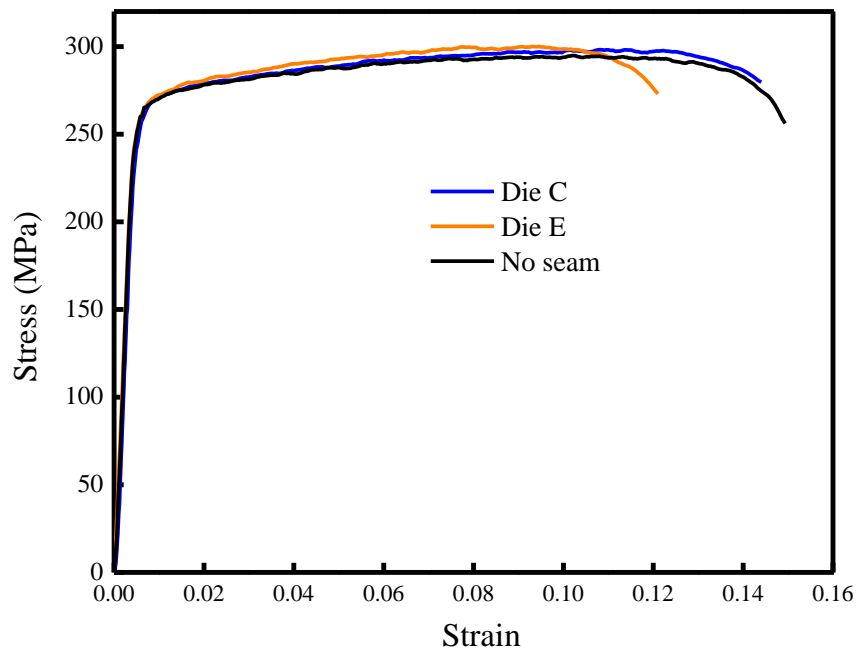


Fig. 5-59 Measured stress–strain curve of 0Mn sample in the T6 condition.

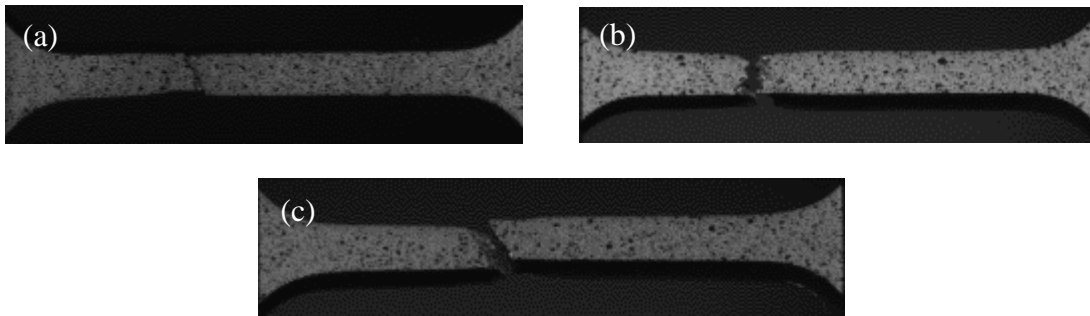
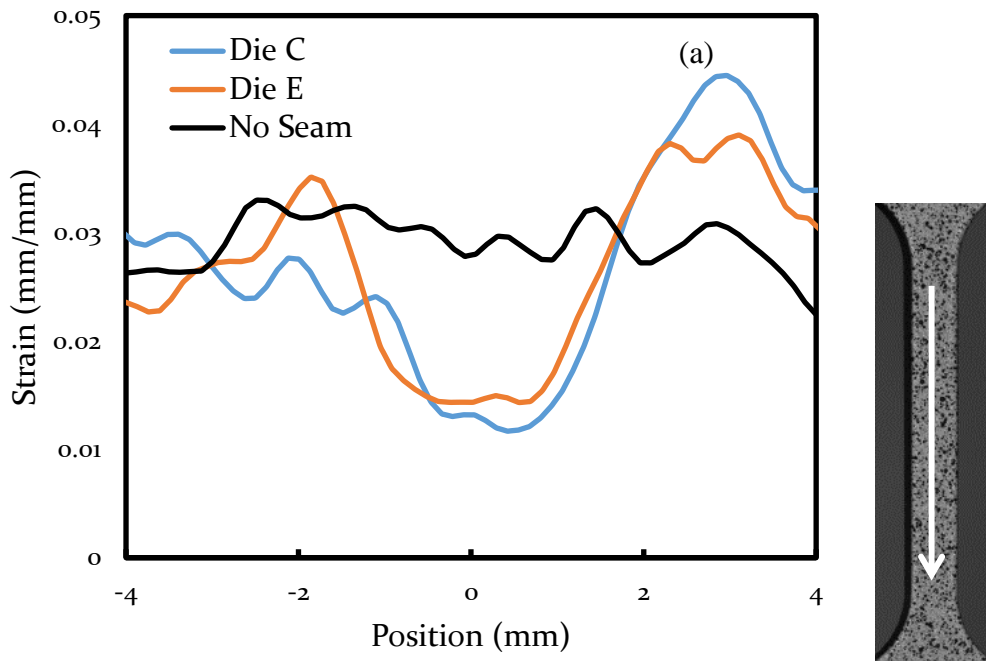


Fig. 5-60 Fracture position of T6 treated 0Mn samples extruded by different dies: (a) Die C / 12.7 mm (Trial 8), (b) Die E / 12.7 mm (Trial 9) and (c) no bridge (Trial 10).

In order to further investigate the weld seam and the matrix mechanical property differences, the strain distribution along the gauge length during a tensile test was measured using DIC, as shown in Fig. 5-61. The measured strain distribution of the 0Mn sample with a weld seam had two peaks about 2~3 mm away from the seam; the strain was relatively lower at the seam. Samples extruded using Die C and Die E had very similar strain levels along the gauge length, which is different from the 0.5Mn0.15Cr samples where the samples extruded using Die E had a higher strain concentration. It seems the material at the seam was slightly stronger than the quarter width material, which may account for the lower measured strain level at the weld seam. This is a very different from other researchers' studies on porthole die extrusion and indicates that it is possible for the seam to have a higher strength than the matrix under some unique circumstances.



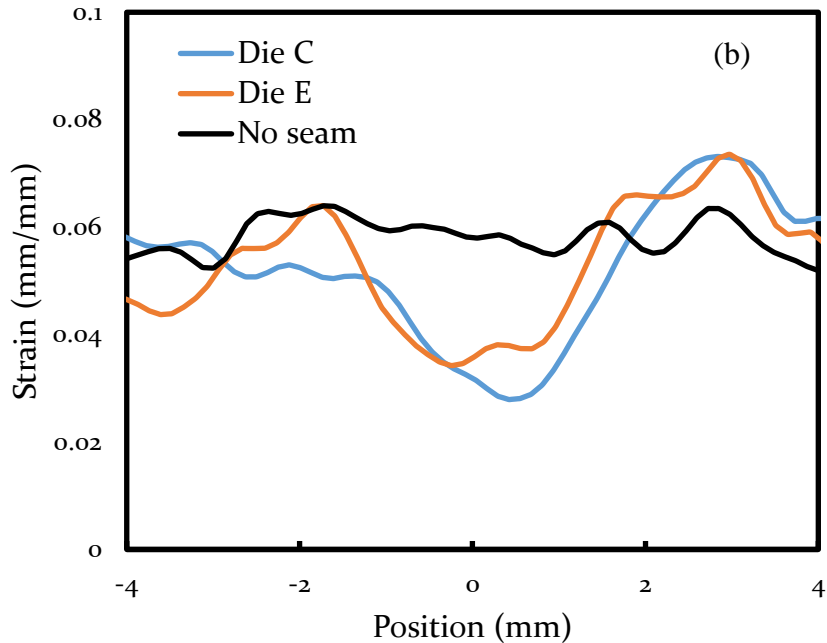


Fig. 5-61 Strain distribution along the white line during the tensile test of the 0Mn samples when the elongation is (T6): (a) 0.025 and (b) 0.05.

### 5.5.4 Texture influence on mechanical properties

Since the PCG layer is not the cause for the strain concentration as discussed in the previous section (see Section 5.1.4.3), another possible reason that may contribute to the strain concentration could be the texture difference between the weld seam and the matrix. The non-recrystallized extruded samples have very different texture from recrystallized extruded samples, and the strain distribution along the gauge length are also very different. Based on this, it is very reasonable to postulate that the texture plays an important rule in non-uniform strain distribution along the gauge length during tensile test.

#### 5.5.4.1 0.5Mn0.15Cr sample

In this research, the true stress – true strain of the weld seam (centre) texture and matrix (quarter) texture were simulated using the VPSC model developed by Tomé and based on the measured pole figures of the brass texture at the weld seam region (Fig. 5-5) and matrix quarter width texture (Fig. 5-7a) respectively. The VPSC calculation of the different mechanical properties for the different textures found along the weld seam (centre) and matrix (quarter) width locations was done by UBC. Fig. 5-62 shows the VPSC model results of the true stress-true strain weld seam

texture and quarter width texture for the sample extruded using Die C / 12.7 mm / Asym (Trial 1) in the TD direction. It is noticeable that the quarter width texture has a higher strength and also a higher strain hardening rate in the TD direction compared to the centre (weld seam) texture.

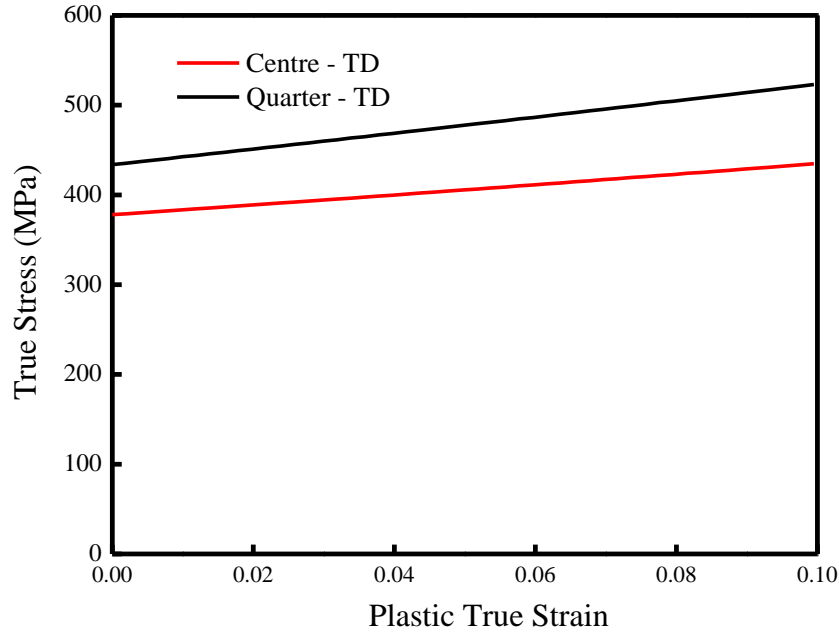


Fig. 5-62 VPSC model-predicted true stress–true strain curves in the TD direction for the weld seam (centre) and matrix (quarter width) textures for material extruded using Die C / 12.7 mm/ Asym (Trial 1).

In order to examine the different texture’s influence on the strain distribution along the gauge length, a very simple model was constructed in DEFORM to simulate the tensile test of the porthole die extruded sample. The simulated tensile specimen was created using two types of material in the simulation that reflected the properties of the weld seam and matrix. Most of the sample except the weld seam region was assumed to have mechanical properties made up by the matrix texture, whose mechanical property was assumed to be those shown for the Quarter – TD curve (black curve) in Fig. 5-62. On the other hand, the material at the weld seam region was assumed to have the mechanical properties shown for the weld seam as the Centre – TD curve (red curve) in Fig. 5-62. As shown in Fig. 5-5, the seam region is approximately 600  $\mu\text{m}$  wide, so the seam region width was also assumed to be 600  $\mu\text{m}$  wide for the simulation. In this simple simulation model, the transition texture between the seam and matrix and its mechanical property

were not taken into consideration. Fig. 5-63 shows a schematic of the tensile test and indicates spatially which parts of the material were assumed to have which mechanical properties.

Fig. 5-64a shows the model-predicted strain distribution along the gauge length of the tensile specimen when the elongation reaches 2.5%. The model-predictions shows the strain tends to concentrate at the centre of the tensile specimen and then gradually decreases towards edge. Fig. 5-64b shows a comparison between the measured (without the PCG layer) and model-predicted strain distribution. Referring to Fig. 5-64b, a comparison between the model-predicted results and measured results shows they are qualitatively similar, however the strain at the centre in the model predictions is a little higher the model-predicted strain is a little higher than the experimental result at the centre and also shows a small dip in the peak which was not seen in the measurements. This may be due to a lack of transitional texture in the simulation model and other factors related to assuming a similar texture throughout the weld seam and matrix. Considering the simplicity of this model, the simulated result provides strong evidence that the difference in texture and hence mechanical properties of the weld seam and matrix is the reason we see a concentration of the strain along the weld seam during tensile testing. In future work, a more detailed simulation model considering the transitional texture should be constructed to study the texture's influence on the samples spatial strain distribution.

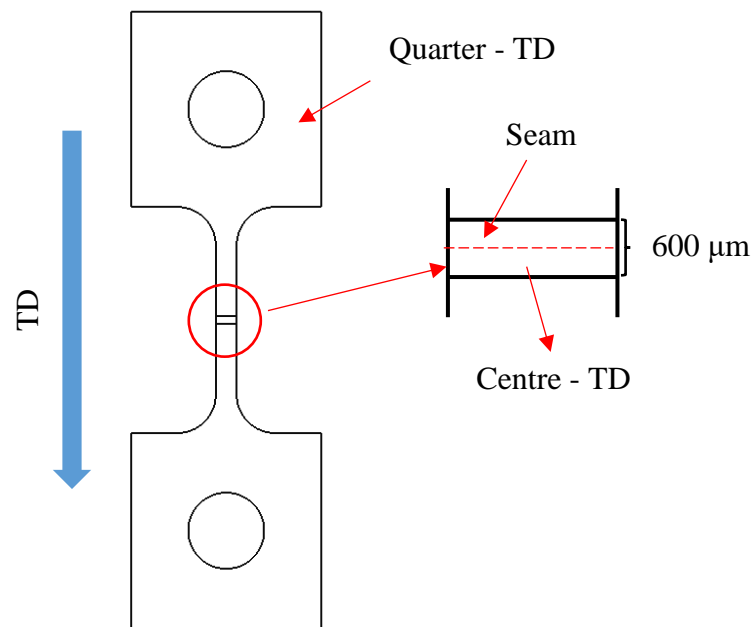


Fig. 5-63 Schematic showing how the simulation of the tensile test for the porthole die extruded sample.

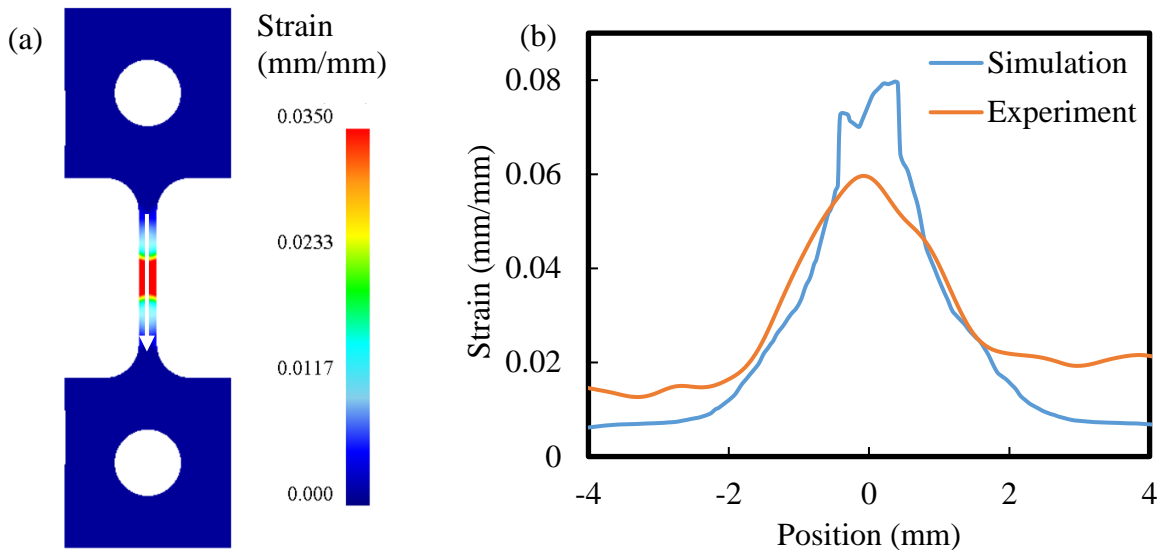


Fig. 5-64 Comparison between the measured and simulated strain distribution in the tensile specimen extruded using Die C / 12.7 mm / Asym (Trial 1) when the elongation is 2.5%: (a) model-predicted strain distribution map and (b) model-predicted and measured strain distribution profile along the white line.

#### 5.5.4.2 0Mn sample

A same method was also used to simulate the strain distribution along the gauge length of the 0Mn samples. VPSC simulation of the seam texture and quarter width texture were also conducted at UBC to understand the unique measured strain distribution of the 0Mn samples extruded using a porthole die as it appeared in this case the weld seam was stronger and showed lower strains along the weld seam relative to the adjacent material. As shown in Fig. 5-65, VPSC simulations indicated that the centre texture along the weld seam was stronger than the quarter width texture in the TD direction.

As shown in Fig. 5-63, the material at the weld seam region of 600  $\mu\text{m}$  wide in the middle was assumed to have the mechanical properties shown for the weld seam as the Centre Rex curve (red curve) in Fig. 5-65. On the other hand, Most of the sample except the weld seam region was assumed to have mechanical properties made up by the matrix texture, whose mechanical property was assumed to be those shown for the Quarter Rex curve (black curve) in Fig. 5-65. The simulated

strain distribution at the gauge length during the tensile test when the elongation is 5% is shown in Fig. 5-66. Comparing to the DIC measured strain distribution, the simulation result also shows the strain is concentrated at the location about 3 mm away from the strain and the strain value remains relatively low at the seam. The model predicted result matches the experimental result very well, and it indicates the non-uniform texture distribution between the seam and the matrix can result in non-uniform strain distribution at tensile test.

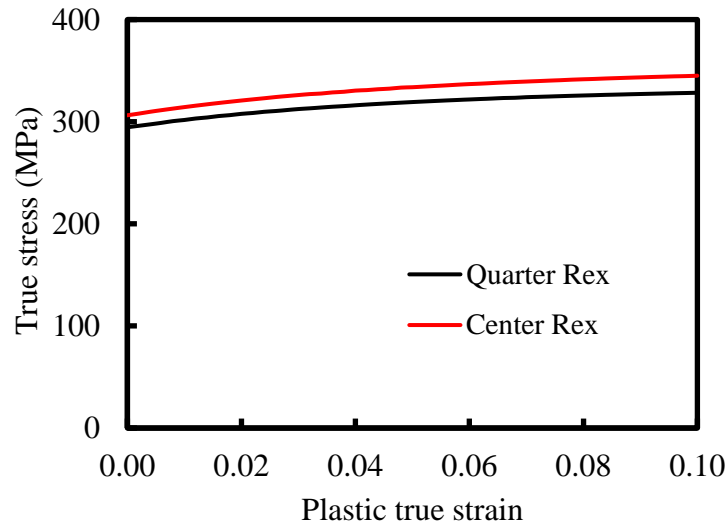


Fig. 5-65 VPSC simulation results of the center and quarter texture in 0Mn samples.

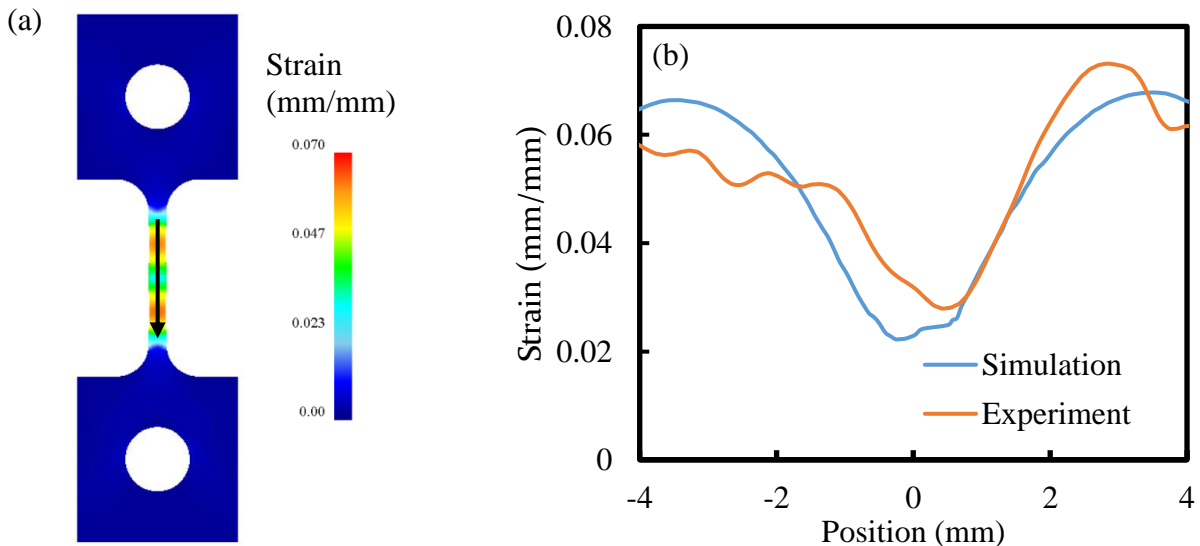


Fig. 5-66 Comparison between the measured and simulated strain distribution in the tensile specimen extruded using Die C / 12.7 mm / Asym (Trial 8) when the elongation is 5%: (a) model-

predicted strain distribution map and (b) (b) model-predicted and measured strain distribution profile along the black line.

### 5.5.4.3 0.5Mn samples

The samples shown in Fig. 5-67 were extruded using Die C and Die E with a welding chamber height of 12.7 mm at the ram speed of 5 mm/s. Due to the presence of a higher number of dispersoids created by the addition of Mn, the 0.5Mn samples exhibited slightly higher strength but lower elongation than 0.5Mn samples. The ultimate strength of 0.5Mn0.15Cr samples in T1 state was about 325 MPa, but the ultimate strength of 0.5Mn samples was about 300 MPa.

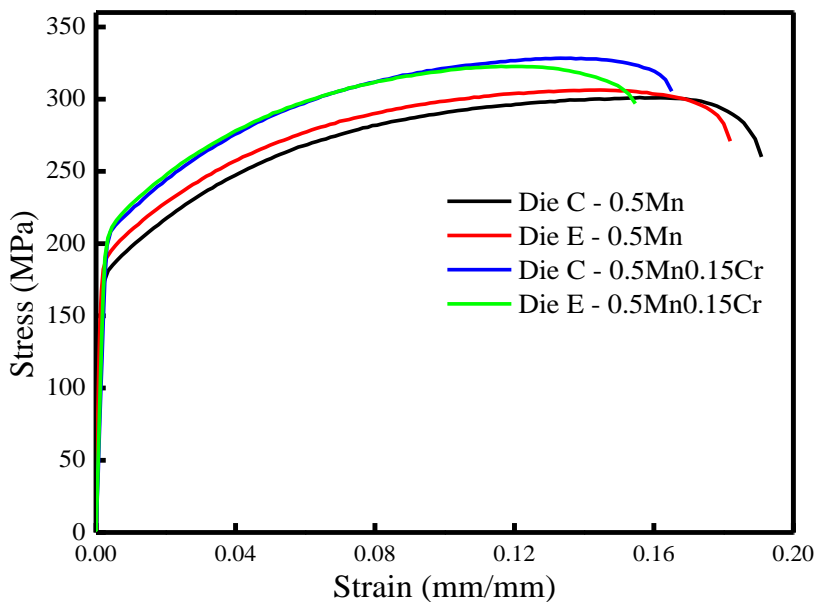


Fig. 5-67 Measured stress – strain curves of 0.5Mn0.15Cr and 0.5Mn samples in T4 state.

Fig. 5-68 shows the T6 heat treatment's effects on the 0.5Mn samples extruded by Die C / 12.7 mm die configuration. The T6 samples were obtained by solutionizing T4 samples at 550 °C for ten minutes and followed by artificial aging at 175 °C for eight hours. After T6 heat treatment, the 0.5Mn samples' strength increased significantly, while the fracture elongation and work hardening rate decreased. The T6's effects on the stress – strain curve did not seem to be different from the typical T6's effects on 6xxx aluminum alloys. However, the most unexpected result is the fracture position of the seamed samples changed after T6 heat treatment. As shown in Fig. 5-69, the T4 sample fractured in the middle of the gauge length corresponding to the seam, on the other hand, the T6 sample fractured away from the seam. According to EBSD results of 0.5Mn

samples (Fig. 5-57 and Fig. 5-58), the seam region of 0.5Mn extruded sample experienced abnormal grain growth at solution temperature of 550 °C, and the texture at the seam region was replaced by several huge grains. The change of fracture position of 0.5Mn after T6 heat treatment provided additional proof that texture plays an extremely important role on the porthole die extruded sample's mechanical properties.

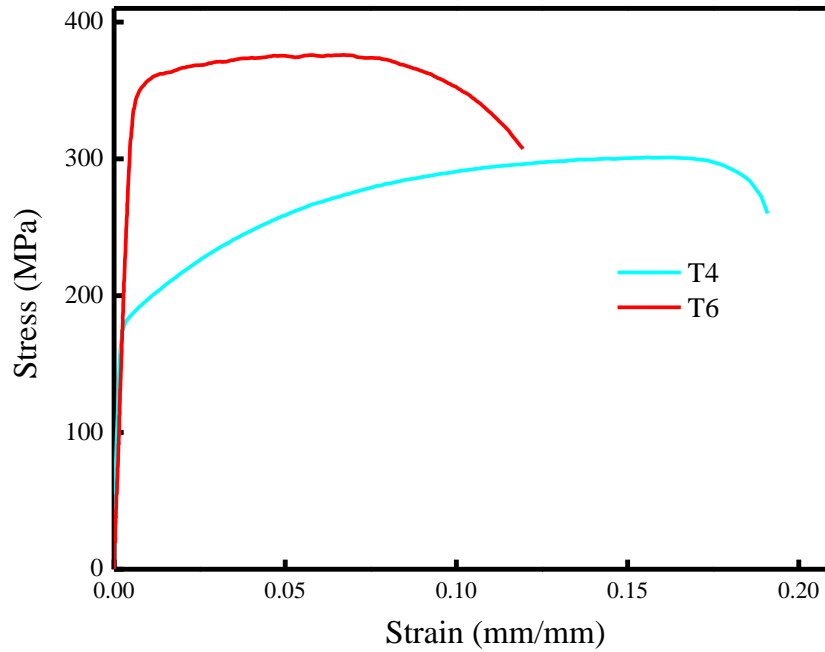


Fig. 5-68 Stress – strain curve of 0.5Mn samples extruded by Die C / 12.7 mm (Trial 6): (a) T4 and (b) T6.

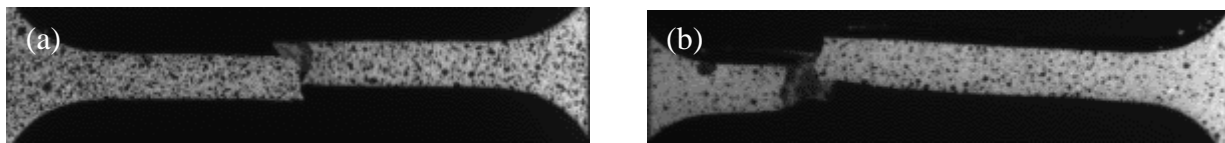


Fig. 5-69 Fracture location of 0.5Mn samples extruded by Die C / 12.7 mm (Trial 6): (a) T4 and (b) T6.

## Chapter 6 Application of the extrusion model

### 6.1.1 Bridge angle

To further understand the quantitative effect of the welding chamber bridge geometry on the extrusion process, the bridge angle was varied from  $15^\circ$  to  $90^\circ$  in increments of  $15^\circ$  to study the bridge angle effects on porthole die extrusion as shown in Fig. 6-1. The welding chamber height is set to be 12.7 mm, ram speed is 5 mm/s and the extrusion temperature is  $480^\circ\text{C}$ .

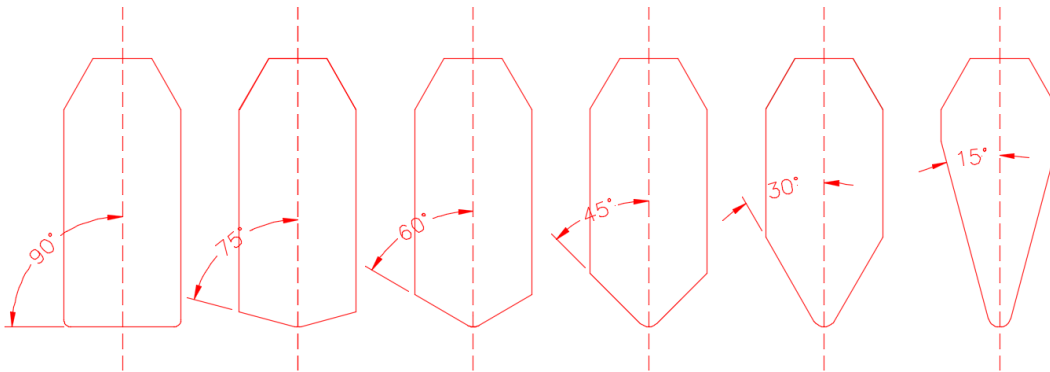


Fig. 6-1 Bridges of varying angles.

Fig. 6-2 shows the effect of the bridge angle on the velocity distribution in the welding chamber during porthole die extrusion. When the bridge angle varies from  $15^\circ$  to  $45^\circ$ , the velocity beneath the bridge maintains a high value over 30 mm/s, except for a very thin layer of the material stuck on the surface of the bridge (Fig. 6-2a, b and c). When the bridge angle is  $60^\circ$ , there exists a small part of the material under the bridge which has a flow speed less than 3 mm/s. As the bridge angle increases, the region that has a lower velocity expands significantly under the bridge. When the bridge angle reaches  $75^\circ$  and  $90^\circ$ , the region of low velocity is so large it cannot be neglected (encircled in Fig. 6-2e and f). The region of low velocity under the bridge can disrupt the material's flow smoothness and affect the material's flow path. In summary, the increasing bridge angle reduces the material's flow smoothness.

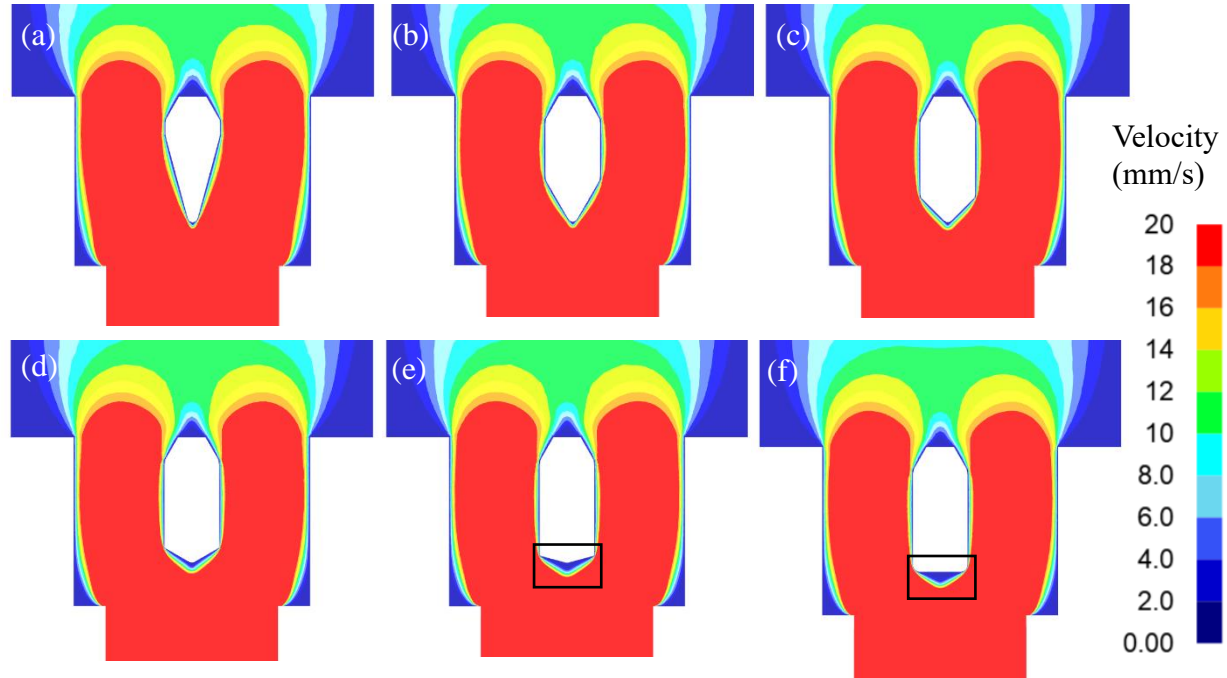


Fig. 6-2 Model-predicted velocity distribution in the welding chamber for different bridge angles: (a) 15°, (b) 30°, (c) 45°, (d) 60°, (e) 75° and (f) 90°.

Fig. 6-3 shows the model-predicted normalized temperature distribution at the die corner (the black line) when the bridge angle is varied from 15° to 90°. The normalized temperature is calculated based on Eq. 6-1. At the weld seam, the temperature increases as the bridge angle increases. For instance, the seam temperature is about 6 °C higher for the die with 90° than the die with 15°. The lower weld seam temperature for the bridges with the smaller angle's could be because of the smoother material flow and absence of the dead metal zone. On the other hand, at the region more than 7 mm away from the seam, the temperature differences in dies of different bridge angles are very small, which provides further evidence that the bridge's influence diminishes on the material far away from the seam.

$$T_N = T - T_{15^\circ} \quad 6-1$$

where  $T_N$  is normalized temperature (°C),  $T$  is the temperature of each die configuration's extrusion (°C) and  $T_{15^\circ}$  is the temperature of die 15° extrusion.

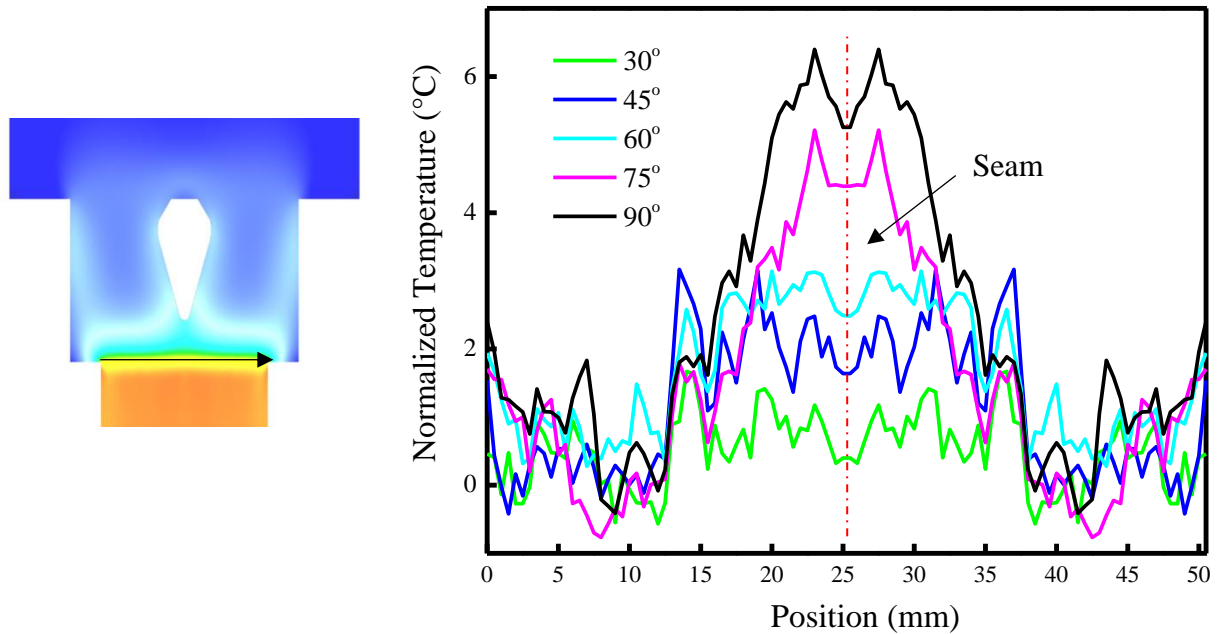


Fig. 6-3 Bridge angle's influence on temperature distribution at the die corner.

Fig. 6-4 shows the model-predicted evolution of strain throughout the cross section of the extruded profiles as the welding bridge angle varies from  $15^\circ$  to  $90^\circ$ . When the bridge angle is  $15^\circ$  (Fig. 6-4a), the high strain region at the seam is lenticular shaped with a very slight bulge at the middle thickness. With the angle increased to  $45^\circ$ , the bulge of the high strain region grows slightly bigger into the neighbouring material (Fig. 6-4b and c). When the bridge angle is  $60^\circ$ , the bulge of the high strain region at the middle thickness is very obvious and has a tendency to continue growing as the bridge angle increases. When the bridge angle is  $75^\circ$ , the high strain region is already cross shaped. When the bridge is  $90^\circ$ , the influence of the bridge is most prominent among the six dies and the high strain region also extended farthest into the neighbouring material. The velocity distribution (Fig. 6-2) shows the material flow becomes less smooth and even obstructed by the dead metal zone in the welding chamber when the bridge angle increases. As a result, a higher strain is accumulated at the seam region and more material close to the seam is affected in a bigger angle bridge die extrusion. Fig. 6-5 shows the strain distribution along the middle thickness of the profile from the seam to the edge. At the seam, the higher bridge angle exhibits higher strain, but the strain decreases very dramatically when getting away from the seam. At the location about 4 mm away from the seam, the strains in all of extrusions with different bridge angles comes to very close to each other.

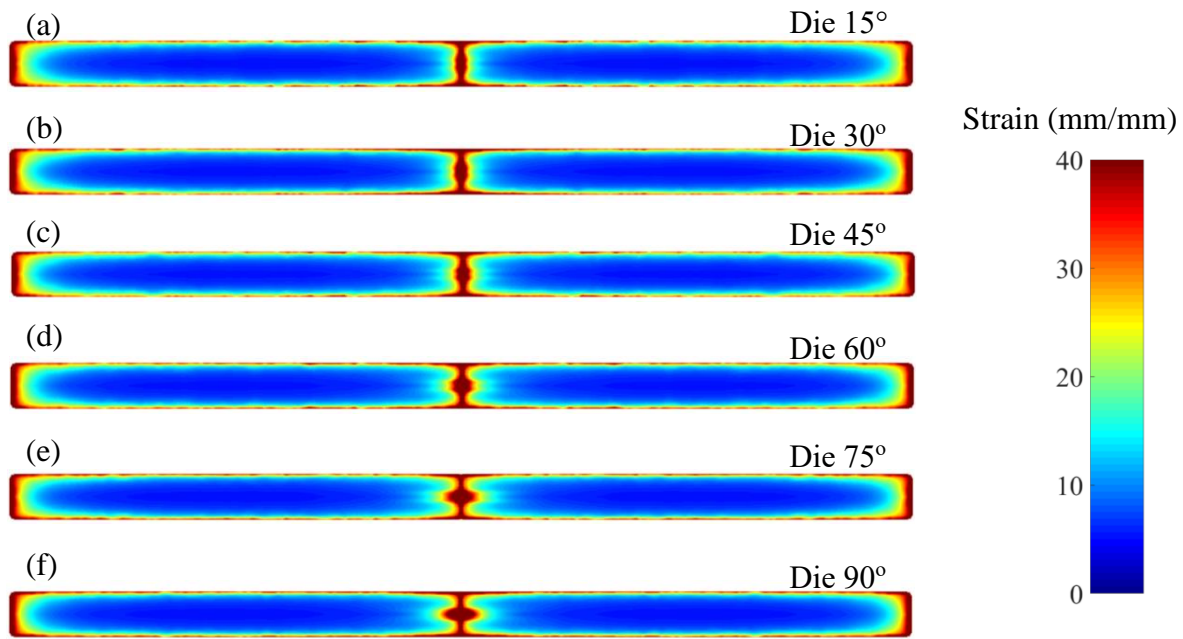


Fig. 6-4 Bridge angle's effects on the strain distribution: (a) die 15°, (b) die 30°, (c) die 45°, (d) die 60°. (e) die 75° and (f) die 90°.

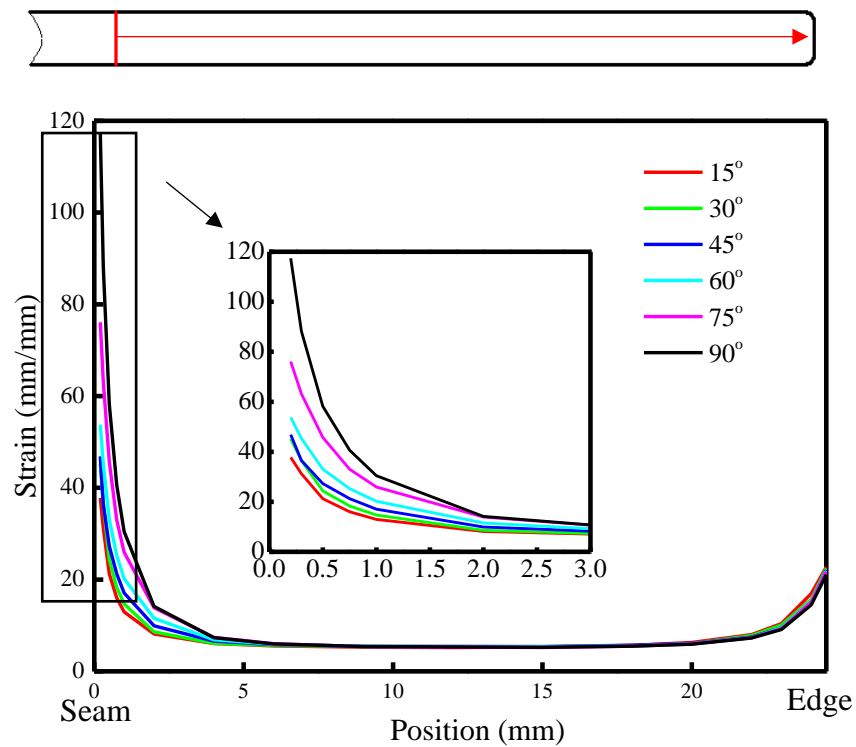


Fig. 6-5 Strain distribution from the seam edge in the middle thickness (the red line) of the profiles extruded using bridges of different angles.

### 6.1.2 Upper part of bridge

Earlier, the bottom part of the bridge geometry influence on porthole die extrusion have been thoroughly examined, but the upper part of bridge geometry influences are still unknown. In this section, both Die C and Die E have three variations in terms of the shape of their upper part where the material will enter into the welding chamber, as shown in Fig. 6-6. The three variations of Die C are labeled as C1, C2 and C2, and the three variations of Die E are labeled as E1, E2 and E3. The upper part of the bridge is changed in order to study the upper part of bridge's influences on porthole die extrusion. In this section, the welding chamber height is set to be 12.7 mm.

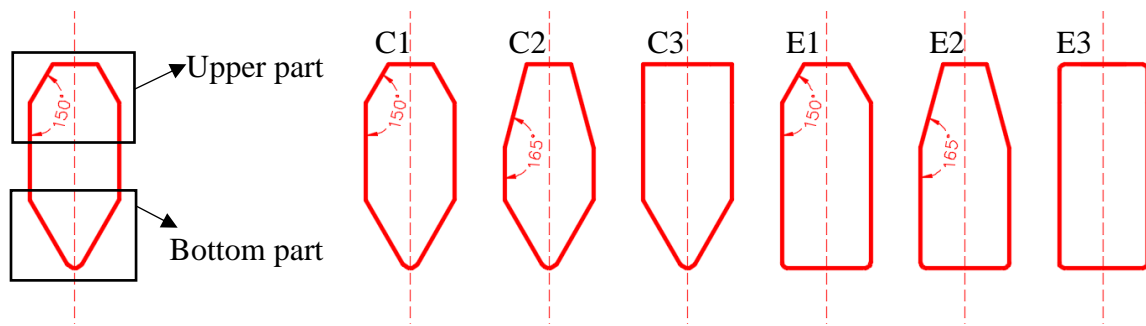


Fig. 6-6 Bridge geometries proposed to examine the upper part of bridge's effects on porthole die extrusion.

Fig. 6-7 shows the model-predicted normalized temperature distribution at the die corner (the black line) when the upper part of the bridge is varied for Die C and Die E extrusion. The normalized temperature distribution is calculated based on Eq. 6-2. It is very interesting to see the change of the upper part of the bridge does not have a significant effect on the temperature distribution. For instance, normalized temperature of Die C2 and Die C3 are very close to zero, which indicate the temperature distribution of the three variations of Die C is almost the same. On the other hand, the temperature distribution is affected by the bottom part of bridge significantly, and Die C and Die E extrusion exhibit very different temperature distribution along the black line.

$$T_N = T - T_{C1} \quad 6-2$$

where  $T_N$  is normalized temperature ( $^{\circ}\text{C}$ ),  $T$  is the temperature of each die configuration's extrusion ( $^{\circ}\text{C}$ ) and  $T_{C1}$  is the temperature of Die C1 extrusion.

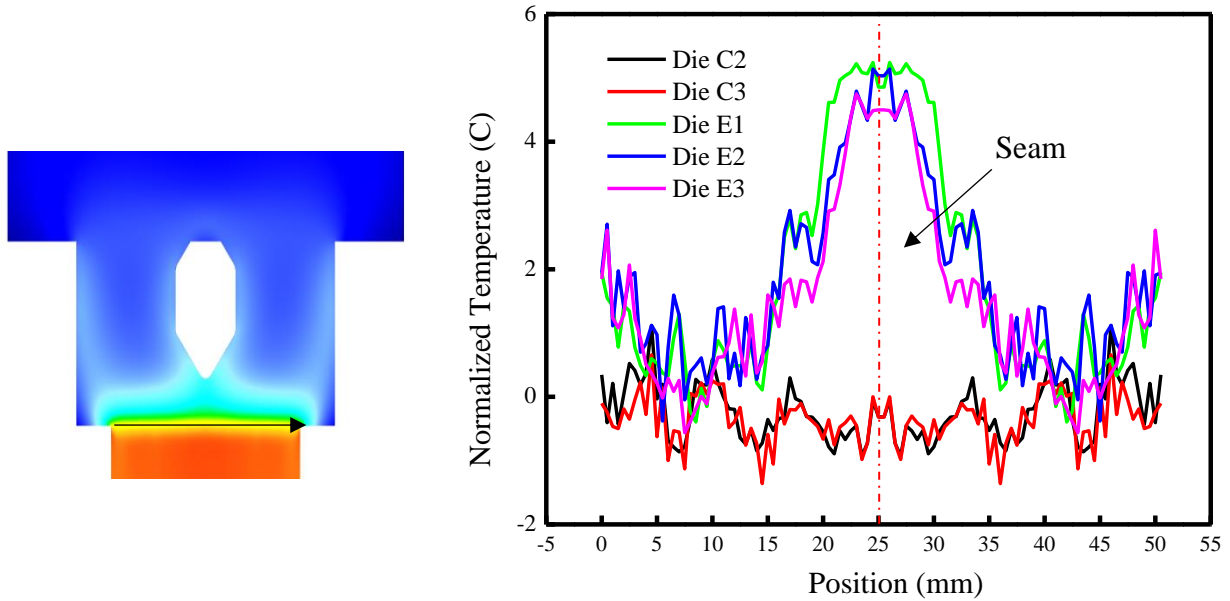


Fig. 6-7 Model-predicted temperature distribution along the mid-width of the strip for a range of die geometries which include changes to the upper part of the die.

Fig. 6-8 shows the strain distribution through the cross section of the profiles extruded by Die C and Die E bridges of different upper parts. Very similar to upper part of bridge's influence on temperature distribution, the strain distribution is almost same among the profiles extruded by the bridge of the same bottom part but different upper parts. On the other hand, the strain distribution differences between Die C bridges and Die E bridges are very prominent. Fig. 6-9 shows the strain distribution along the middle thickness of the extruded profile. It also shows that only the bottom part determines the strain distribution.

Based on the above discussion, it is very safe to say the shape of upper part of bridge's influence on porthole die extrusion is almost negligible compared to the bottom part of bridge. Therefore, only the shape of the bottom part of bridge should be taken into consideration in porthole die extrusion die design.

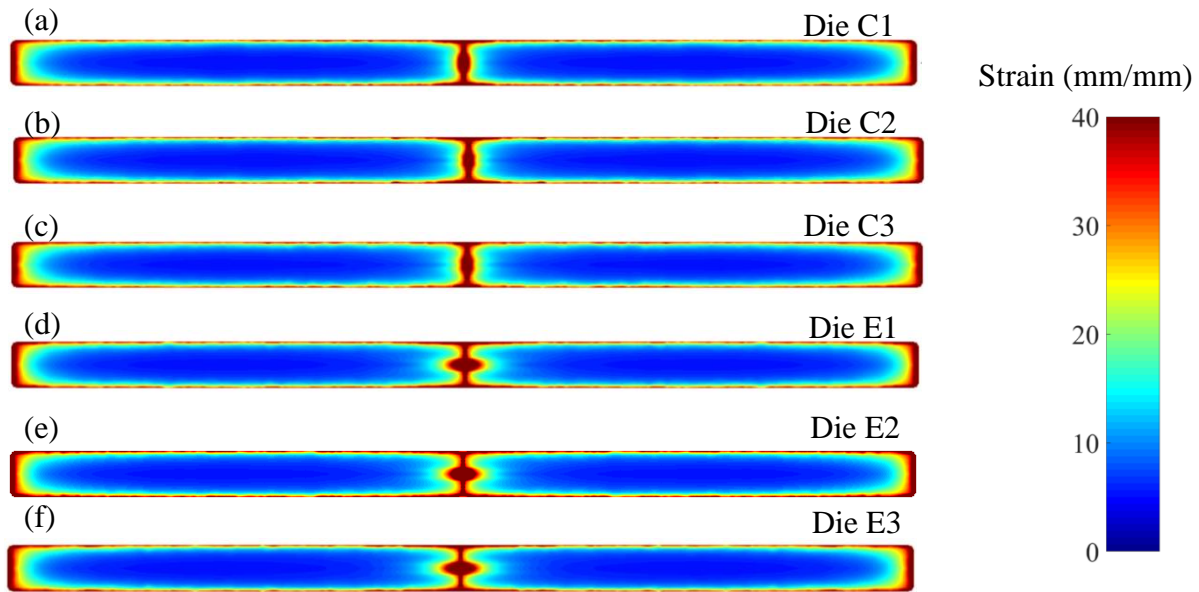


Fig. 6-8 Strain distribution from the seam edge in the middle thickness (the red line) of the profiles extruded using bridges of different angles.

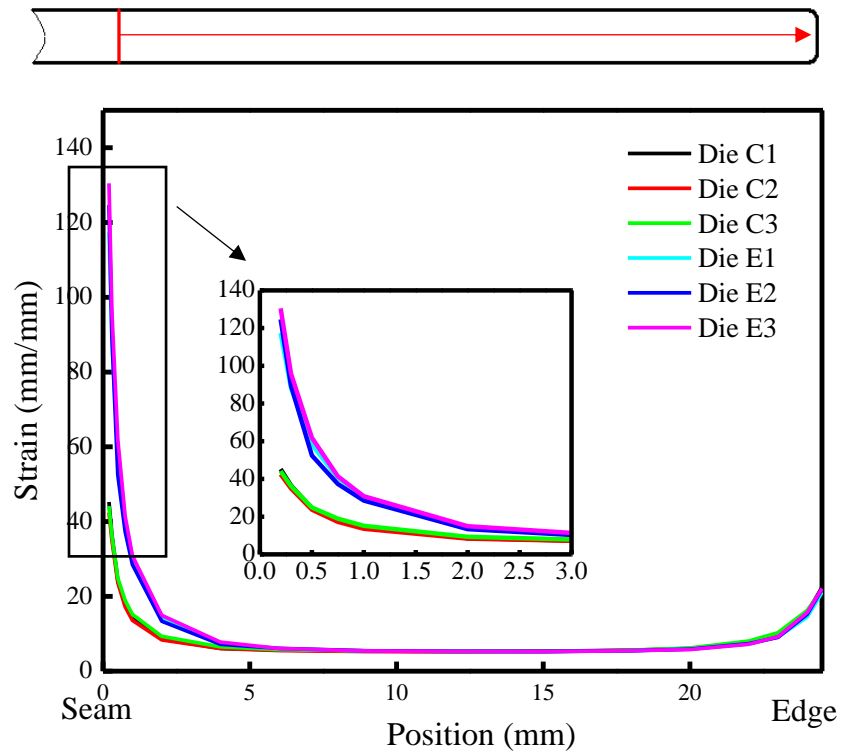


Fig. 6-9 Model-predicted strain distribution from the weld seam in the middle thickness (the red line) of the profiles extruded using bridges with different upper geometries.

## 6.2 Charge seam

### 6.2.1 Charge seam simulation - effect of die geometry

In order to examine the bridge geometry's effects on the charge seam formation in porthole die extrusion, four different bridges with different angles of sharpness were examined, as shown in Fig. 6-10. What's more, four different welding chamber heights, ranging from an extremely shallow welding chamber of 6.35 mm to very deep welding chamber of 38.1 mm were also examined, as shown in Fig. 6-11. Through the combination of the four different bridge geometries and four different welding chamber heights, a total of sixteen die configurations were examined. In this chapter, each kind of the die configuration is designated by its bridge shape and welding chamber height. For instance, the die made by bridge 30° and 12.7 mm welding chamber is designated by 30° / 12.7 mm.

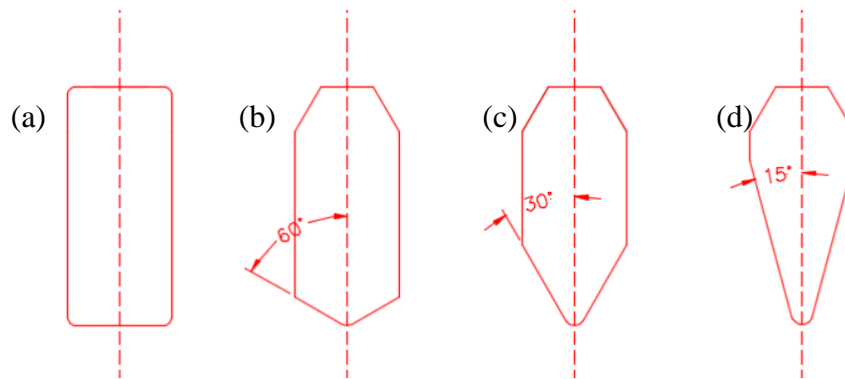


Fig. 6-10 Schematic showing the different geometries used to examine the bridge geometry's effects on the charge seam formation in porthole die extrusion: (a) bridge 90° (Die E), (b) bridge 60°, (c) bridge 30° (Die C) and (d) bridge 15°

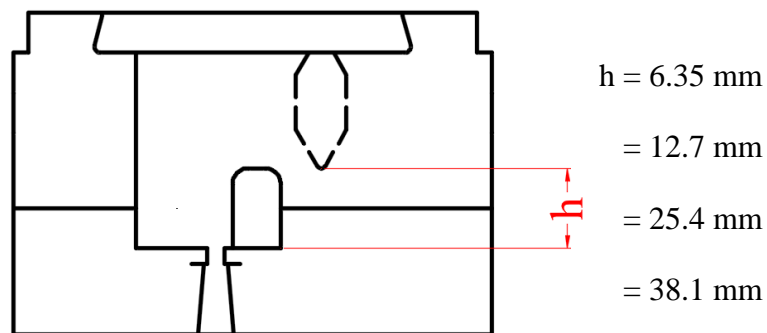


Fig. 6-11 Schematic showing the four different welding chamber heights used to examine the welding chamber height's effects on the charge seam formation in porthole die extrusion.

### **6.2.2 Model configuration**

Even though the DEFORM software has a very strong ability to simulate both the transient and steady state aspects of porthole die extrusion, it does not have a module to calculate and visualize the charge seam evolution. Due to its simple use and exceptional strong ability to solve practical extrusion problems, such as bearing optimization, profile distortion and multi extrusion cycle simulation, HyperXtrude is another widely used software package in both the extrusion industry and research. Compared to the endless remeshing in the DEFORM lagrangian simulation, the transient moving boundary analysis in HyperXtrude is based on an ALE method and able to simulate the extrusion process efficiently without the need for remeshing. For instance, in this thesis, it took about half month for DEFORM 3D lagrangian method to simulate the extrusion from the ram stroke of 0 mm to the ram stroke of 90 mm, while HyperXtrude was able to simulate the whole ram stroke (0 ~ 180 mm) in only 20 hours. Despite its huge advantage over DEFORM lagrangian in terms of efficiency, HyperXtrude can not simulate the filling stage of the extrusion and is unable to predict the possible incomplete filling of the welding chamber in porthole die extrusion as all of other simulation methods based on ALE. In this thesis, HyperXtrude is chosen as a supplementary alternative to simulate the charge seam and billet skin tracking, which cannot be simulated by DEFORM 3D.

Due to the symmetry of the porthole die extrusion die, only one quarter of the workpiece was modeled to save simulation time, as shown in Fig. 6-12. For the convenience of controlling elements at different locations, the workpiece was divided into four components – profile, bearing, porthole + welding chamber and billet. The bearing and profile component were meshed by prism elements. Since the bearing component experienced the most severe deformation, the bearing was meshed by the finest element size of 0.2 mm. The other two components were meshed by tetrahedron elements. The element size of the billet ranged from 2 to 5 mm, and the element size of the porthole +welding chamber ranged from 0.5 to 1 mm.

The material used in HyperXtrude simulation is AA6082, and its constitutive equation is Eq. 4-1. The ram speed is 5 mm/s, and the billet and tooling temperature are 480 °C and 450 °C

respectively. The details of extrusion parameters and boundary condition used for HyperXtrude is shown in Table 4-4.

Since HyperXtrude can not simulate the upset process at the very beginning of the extrusion, the initial state ( $t = 0$  s) is the time when the new billet was upsetted to be in full contact with the container.

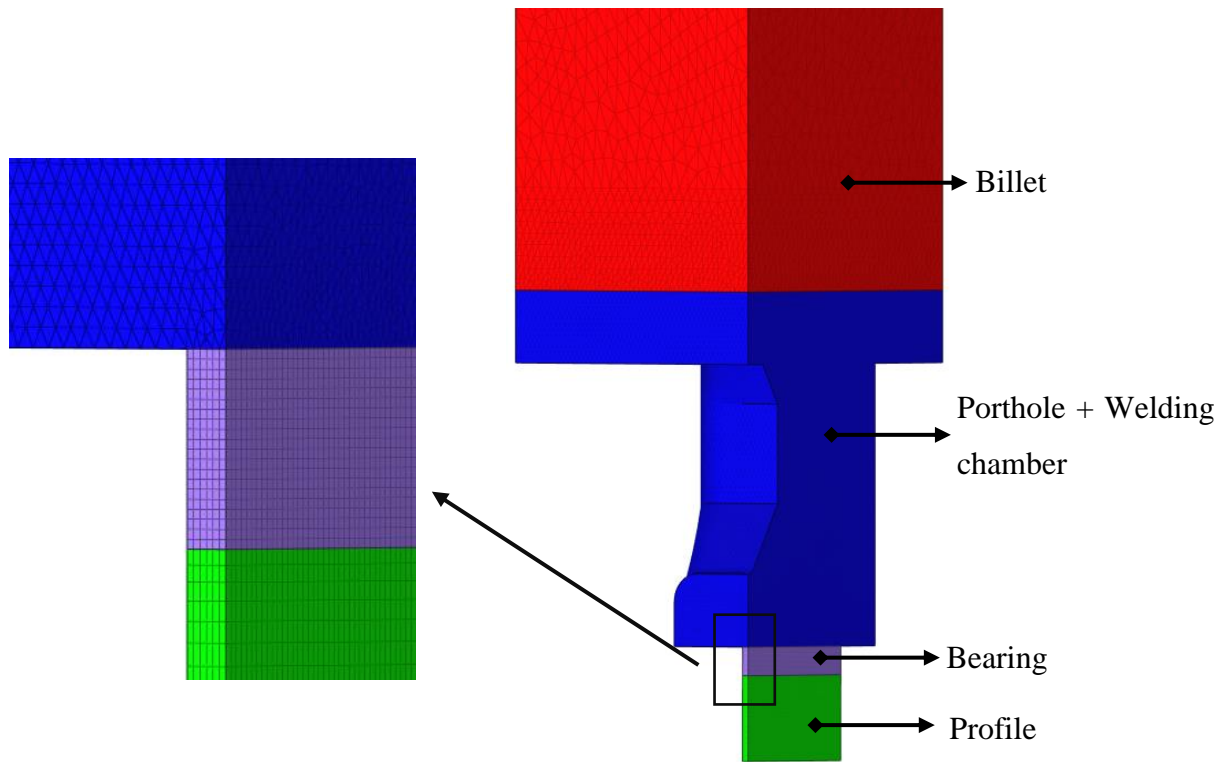


Fig. 6-12 Mesh generation scheme for the simulation of charge seam.

### 6.2.3 Charge seam formation

Fig. 6-13 shows the model-predicted flow behaviour of the new billet in the  $30^\circ / 12.7$  mm die configuration during billet on billet extrusion. In Fig. 6-13, the new billet material and old billet material are labeled by red and blue colour respectively, and the interface between the red domain and blue domain is the charge seam. In the initial state ( $t = 0$  s), the billet was upsetted to fully contact the container and the interface between the new and old material is a straight line (Fig. 6-13a). The velocity distribution along the interface between the new and old material is not uniform, and the material at the porthole opening flows faster than the other material, which makes the interface elongated and curved into the portholes (Fig. 6-13b). The new billet material in the

portholes will finally break out the die opening and replace parts of the old billet material in the profile's cross section when the ram keeps on moving, as shown in Fig. 6-13c. Due to the obstruction of the bridge, the quarter width part of the profile will be replaced by the new billet material earlier than the middle part. As shown in Fig. 6-13c, there exists two new billet material domains in the profile's cross section, and the charge seam is oval shaped. Fig. 6-13d shows the end of the extrusion cycle when only 20 mm billet butt remains in the container. Due to the extremely slow velocity of the DMZ, old material resides in the DMZ even when the new extrusion cycle is completed.

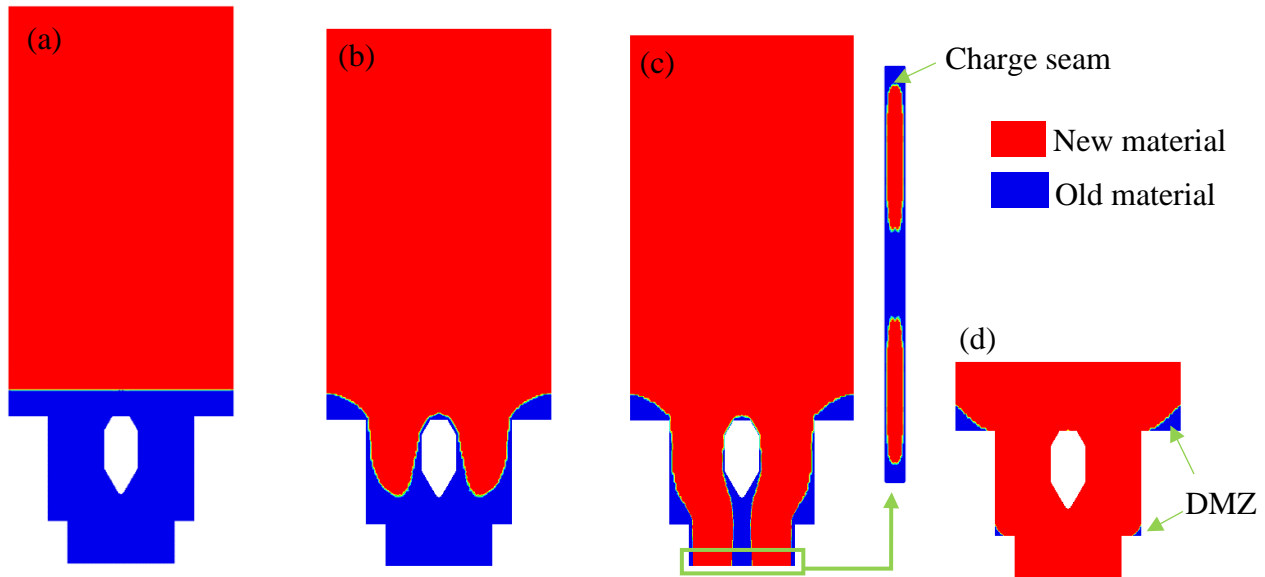


Fig. 6-13 X-section view of the extrusion process showing the model-predicted flow behaviour of new material (red) into the die cavity: (a)  $t = 0$  s, (b)  $t = 1.5$  s, (c)  $t = 1.8$  s and (d)  $t = 32$  s.

### 6.2.3.1 Bridge angle

The charge seam evolution for the two extreme bridge geometries' ( $15^\circ / 12.7$  mm and  $90^\circ / 12.7$  mm), were compared to examine the effect of bridge geometry on the formation of the charge seam, as shown in Fig. 6-14. The old billet material (blue) and new billet material (red) show the evolution of the charge seam during the extrusion process and the green colour indicates the transition zone between old and new material, namely the charge seam. At the time  $t = 0$  s, both of the profiles are made by entirely of old billet material. When  $t = 1.64$  s, the new billet material begins to show up in the profile extruded by the bridge at  $90^\circ$ , while at the same time, the profile extruded by the bridge at  $15^\circ$  is still completely made up by old billet material. Only 0.02 s later,

the new material appeared in the profile extruded by the bridge 15°, and the new billet material domain in the profile extruded by the bridge 90° expands very sharply in a short period of time. This result indicates that the bridge geometry does not affect the start time of the charge seam very much, and the new billet material replaces the old billet material in the extruded profile section area very quickly as soon as the charge seam appears in the extruded profile. When  $t = 1.75$  s, the charge seams in the two die configurations are almost the same. However, the charge seams began to show differences between the two dies at the time  $t = 2.25$  s. As can be seen in Fig. 6-14, there is more old billet material in the centre part of the profile extruded by the 90° bridge. At the time  $t = 2.63$  s, the two charge seams in the profile extruded by the 15° bridge converge at the centre of the profile, while this is not the case for the 90° bridge geometry. In contrast, the two charge seams converge at the time  $t = 3.45$  s for the 90° bridge profile. At the time  $t = 4.74$  s, the old billet material finally disappeared in both profiles.

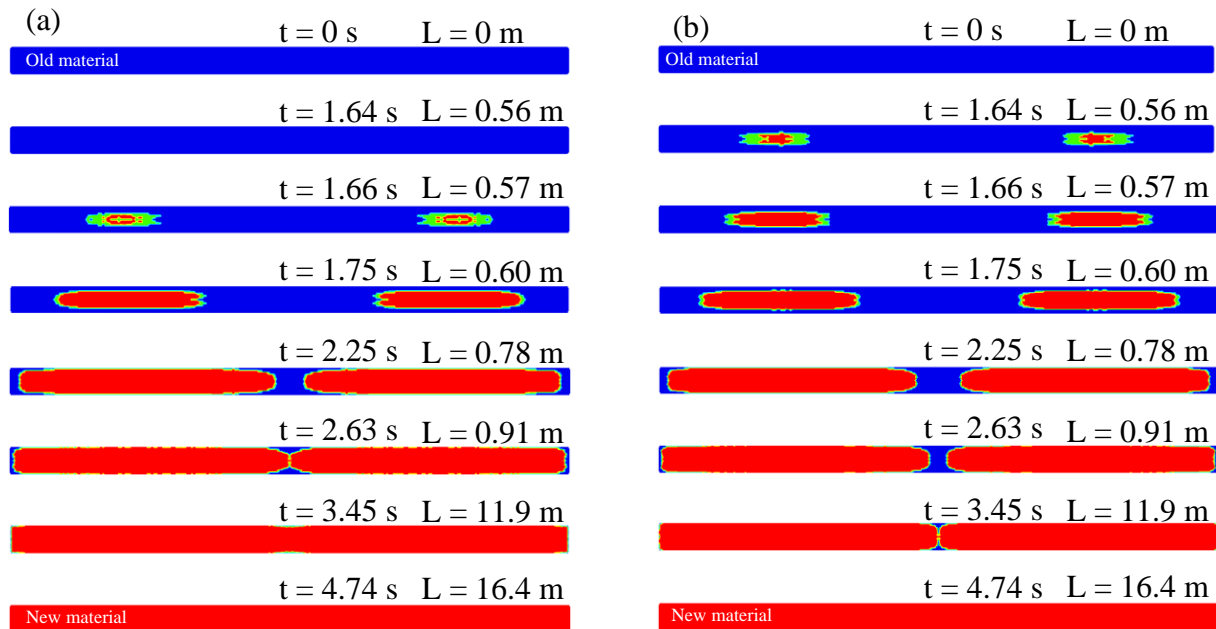


Fig. 6-14 Front view of the extruded strip showing model predictions of the charge seam evolution for two different dies with different bridge angles: (a) 15° / 12.7 mm and (b) 90° / 12.7 mm.

### 6.2.3.2 Welding chamber height

Two die configurations, 90° / 6.35 mm and 90° / 38.1 mm, were taken as an example to examine the welding chamber height's effects on the charge seam evolution during billet on billet extrusion.

The charge seam begins to show up in the profile extruded by the short welding chamber,  $90^\circ / 6.35$  mm, at the time  $t = 1.45$  s. On the other hand, the charge seam appears in the profile extruded at the time  $t = 2.22$  s, meanwhile very large fraction of the profile has already been replaced by new material in the die configuration  $90^\circ / 6.35$  mm. At the time  $t = 2.57$  s, there is more old material remained in the centre than in the edge in the profile extrude by  $90^\circ / 6.35$  mm, which indicates the old material is more easily replaced by the new material in the edge than in the centre in short welding chamber die. At the time  $t = 3.24$  s, the two charge seams begin to converge at the middle of the profile by  $90^\circ / 38.1$  mm, while the two charge seams in the profile by  $90^\circ / 6.35$  mm are still separated by the remaining material in the centre. The two charge seams in the profile by the short weld chamber finally converge at the time  $t = 3.51$  s, while at the same time the charge seams at the centre almost disappear but some old material still remains in the profile edge. The deep welding chamber die contains more old material than the short welding chamber die, which delays the appearance of the charge seam in the profile. On the other hand, the deep welding chamber increases the distance between the bridge and die opening, and reduces the bridge obstruction effects on the material flow. Therefore, the old material in the centre can be replaced by old material much more easily in deep welding chamber than in short welding chamber.

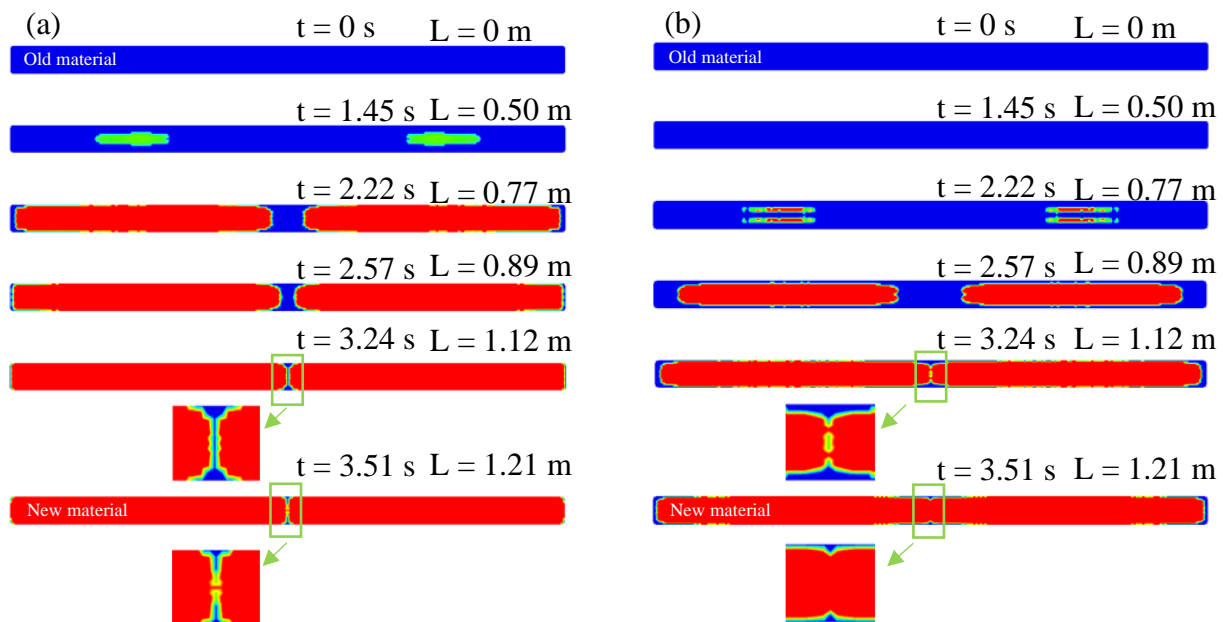


Fig. 6-15 Front view of the extruded strip showing model predictions of the charge seam evolution for different welding chamber heights: (a)  $90^\circ / 6.35$  mm and (b)  $90^\circ / 38.1$  mm.

### 6.2.4 Charge seam length calculation

Fig. 6-16 shows the new material fraction's evolution along the profile length extruded by the sixteen die configurations of different bridge geometries and welding chamber heights. The stopping mark, which indicates the start of a new extrusion cycle, is referred as the origin point in Fig. 6-16. At the very beginning of a new extrusion cycle, the new material fraction of the profile keeps at zero for a short time, and this is because the profile was completely made by the residual material in the die cavity. At a certain length after the stop mark, the value of new material fraction is no longer zero, which indicates that the charge seam starts to formed. As discussed in the previous section, the new material fraction increases at a very fast rate at the beginning, while the increase of the new material fraction almost staggers when it comes to nearly 100 %. Take the die 30° / 25.4 mm as an example, the charges seam first appears at the length of 0.66 m, and the new material fraction rapidly increases to 50% at the length of 0.73 m. However, the new material fraction is 99.5% at the length of 1.01 m, and finally reaches 100% at the length of 1.46 m. The bridge geometry does not make a significant effect on the new material fraction evolution, but the welding chamber height determines the start position of the charges seam. Since the deep welding chamber die contains more old material, it takes more time for the new material to be pushed out of the die.

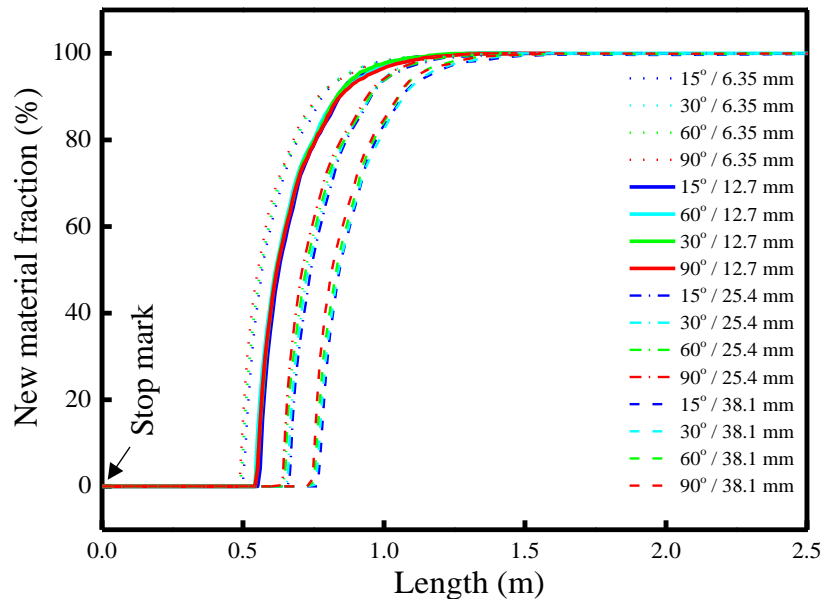


Fig. 6-16 Model-prediction of the new material fraction in the profile's cross section versus extrude length.

## 6.3 Back end defect

### 6.3.1 The model setup of billet skin tracking

In this thesis, back end defect is simulated and examined by HyperXtrude. The material used in this section is AA6082, and its constitutive equation is Eq. 4-1. The ram speed is 5 mm/s, and the billet and tooling temperature are 480 °C and 450 °C respectively. The details of extrusion parameters and boundary condition used for HyperXtrude is shown in Table 4-4.

Five die configurations, 30° / 6.35 mm, 30° / 12.7 mm, 30° / 25.4 mm, 30° / 38.1 mm and 90° / 25.4 mm, were examined to study the welding chamber height and bridge geometry's effects on the billet skin flow. The mathematical model used for billet skin tracking analysis was divided into five components: profile, bearing, porthole + welding chamber, billet and billet skin. The four components –profile, bearing, porthole + welding chamber and billet were meshed in the same way as in the charge seam analysis simulation (Section 6.2.2). The extra component billet skin was set to be 1 mm thick, and has three layers of elements through its thickness.

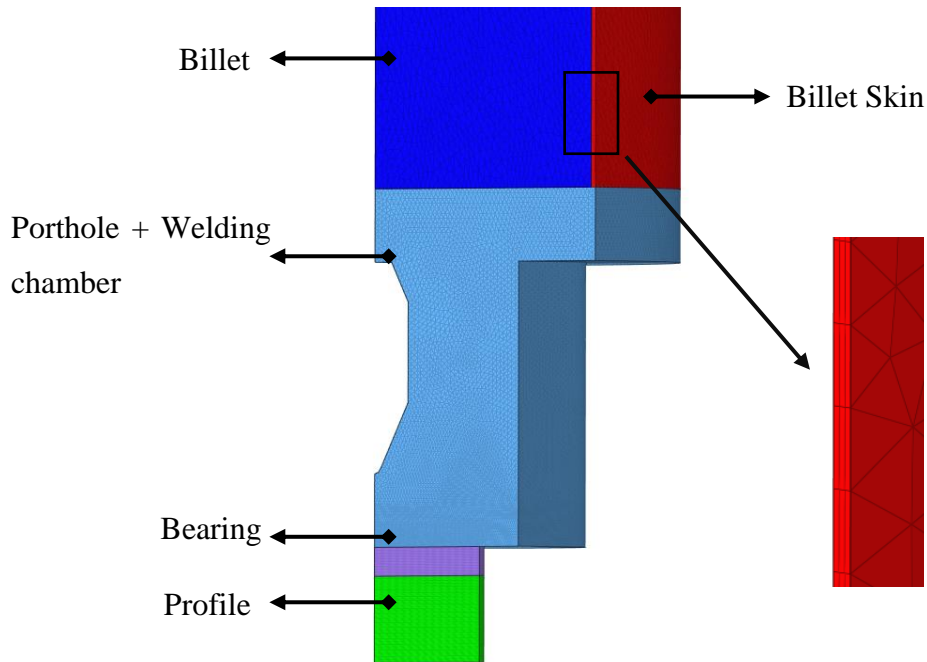


Fig. 6-17 Mesh generation scheme for the billet skin tracking.

### 6.3.2 Billet skin flow behaviour

Fig. 6-18 shows the billet skin flow behaviour in the die configuration of  $30^\circ / 12.7$  mm. The billet skin was set as the one millimeter of the billet surface and labeled as red colour, while the other parts of the material, including billet, portholes, welding chamber and profile, were considered to be internal material and labeled as blue colour. Due to the high friction on the billet surface, the billet skin flows slower than the internal material and progressively accumulated in front of the ram (Fig. 6-18b). Since the front tip of the billet skin is closer to the billet centre, the velocity of the front tip can be faster than the rest part of the billet skin which is stuck on the container surface (Fig. 6-18c). At the time  $t = 27.5$  s when 85.9% of the extrusion is completed (Fig. 6-18c), the front tip of the billet skin enters into the portholes and will be pushed out of the die cavity very soon. At the time  $t = 28.5$  s when 88.4% of the extrusion is completed (Fig. 6-18d), the billet skin first appears in the profile and the length of profile after that should be scrapped due to the quality concern. Considering the total length of profile extruded from one billet is about 11 m, so at least  $11 \times (100\% - 88.4\%) = 1.28$  m of profile at the back end should be scrapped.

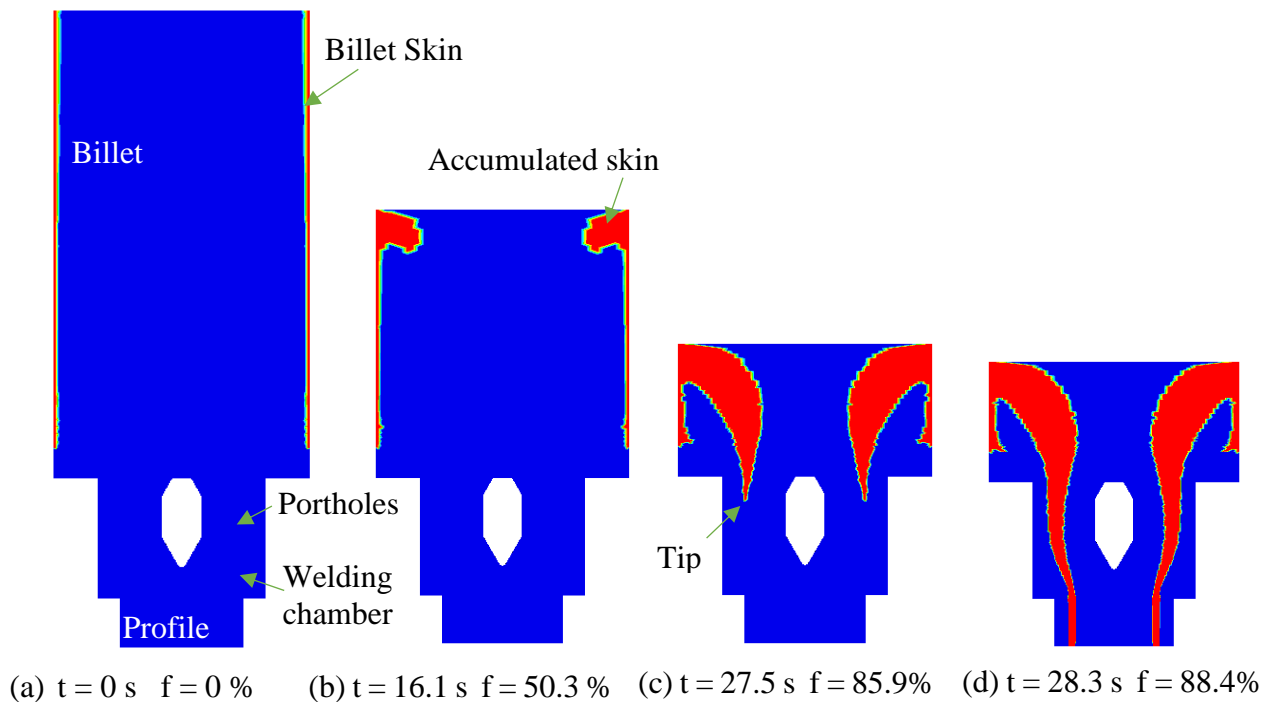


Fig. 6-18 X-sectional view of the extrusion process showing the model-predicted flow behaviour of the billet skin in red: (a)  $t = 0$  s, (b)  $t = 16.1$  s, (c)  $t = 27.5$  s and (d)  $t = 28.3$  s.

### 6.3.3 Die geometry influence

#### 6.3.3.1 Bridge angle

In this scheme, the welding chamber height is kept as 12.7 mm, and a series of porthole die extrusions of varying bridge angles are simulated by HyperXtrude. As shown in Fig. 6-19, length of profile containing back end defects almost keeps at the same value of 1.28 m without a change, even when the bridge angle changes from 15° to 90°. The model predicted result shows that the bridge angle's effect on back end defects is negligible.

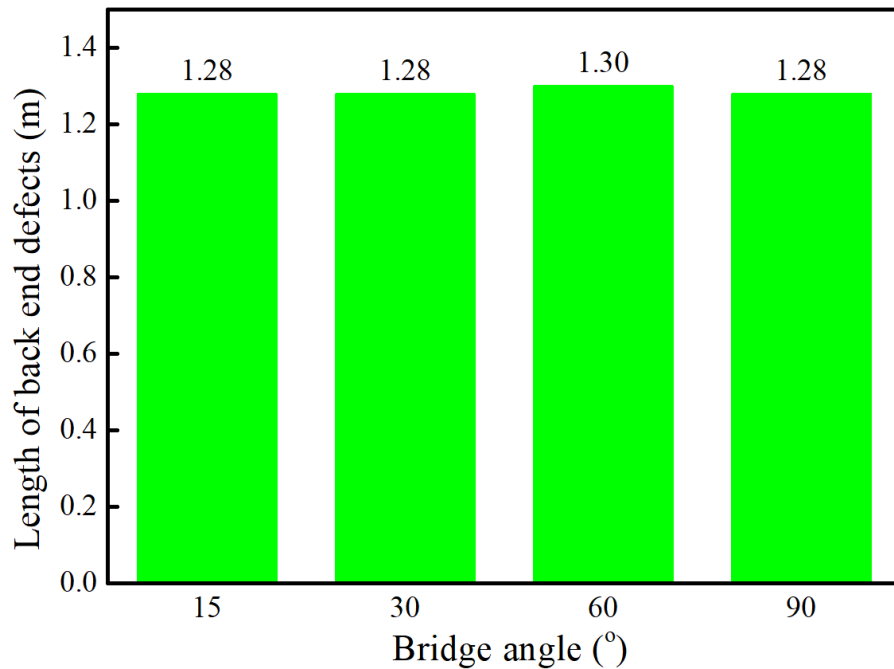


Fig. 6-19 Model predictions of the length of profile containing a back end defects as a function of the bridge angle.

#### 6.3.3.2 Welding chamber height

The welding chamber height's influence on back end defects is studied through a series of stimulations of extrusions of different welding chamber heights but of the same bridge geometry. In this paragraph, the bridge geometry examined is bridge 30°, and the welding chamber height varies from 6.35 to 38.1 mm. As shown in Fig. 6-20, the length of profile containing back end defects decreases from 1.28 to 1.00 m when the welding chamber height increases from 6.35 mm to 38.1 mm. It takes a slightly longer time for the front tip of billet skin (Fig. 6-18c) to pass through

a deeper welding chamber. Therefore, back end defects appear later in a deeper welding chamber extruded profile, and a shorter length of profile needed to scrapped at the end of the profile.

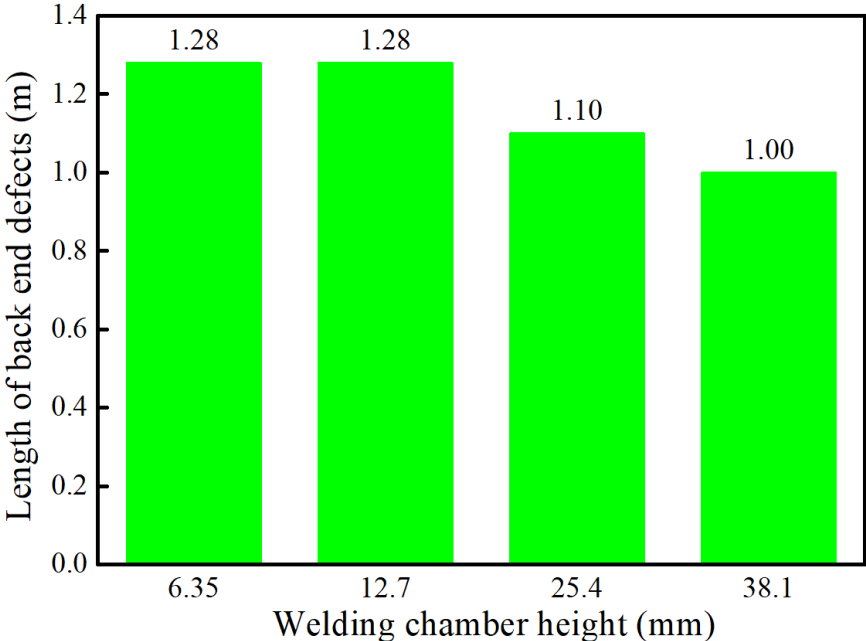


Fig. 6-20 Model predictions of the length of profile containing a back end defect as a function of the welding chamber height.

## **Chapter 7 Summary, conclusions and future work**

### **7.1 Summary**

Porthole die extrusion is the most widely used technology to produce complex hollow aluminum cross sections using a bridge, mandrel and welding chamber as part of the extrusion die. In these porthole die extrusions, weld seams are formed in the extruded product due to the separation of the metal into streams and then rejoining of it in the welding chamber during the extrusion process. It is often along these weld seams that failure occurs in service, hence, there was a need to more fully understand how these weld seams form and the factors that influence the microstructure that is created along the weld seams during the extrusion process. Inherently, there is an interdependency between the final microstructure that forms along the weld seam and its final mechanical properties, the details of the die geometry, the extrusion process parameters and the composition of the aluminum alloy that is being extruded.

In this research, porthole die extrusion of aluminum alloys was studied in terms of die design (bridge shape and welding chamber height), material composition and extrusion parameters (ram speed). In total, seventeen extrusion trials were conducted, and the extruded sample microstructures and mechanical properties were characterized. The extrudate was a simple strip with a weld seam that ran along its length and made it relatively easy to do tensile tests with the weld seam in the middle of the gauge length of the tensile specimen.

The research has shown that the FE simulation results of the porthole die extrusion process are in good agreement with the experimental results and has provided quantitative information on the thermal mechanical history experiences at different spatial points in the extrudate, which was used to help understand the microstructure and texture evolution at the weld seam and matrix and why these are different for different die geometries. For example, the thermal mechanical history calculated based on the ALE simulation was able to explain the texture difference between material extruded using Die C and Die E.

The research focussed on AA6xxx alloys with varying levels of Mn and Cr that create dispersoids in the material and inhibit recrystallization behaviour after extrusion; microstructures ranged from fully recrystallized to fully fibrous (unrecrystallized) in the matrix of the extrudate.

The validated model was also used to understand and quantitatively predict the effect of the die geometry on the formation of the charge weld seam and back end defect during porthole die extrusion using billet-on-billet extrusion.

## 7.2 Conclusions

In this research, a series of experiments alongside a well validated thermal mechanical model of the porthole die extrusion process were undertaken to understand the role the die geometry, extrusion process and alloy composition play on the microstructure evolution at the weld seam and in the matrix during the extrusion of AA6xxx aluminum alloy. The main conclusions that can be drawn from this research on the weld seam formation during porthole die extrusion of AA6xxx alloys are listed below and have been separated into the three main areas, namely: effect of die geometry, effect of ram speed and effect of alloy composition. Conclusions drawn from the impact of the die geometry on the charge weld formation and back end defect, which is more useful for practitioners and represents the applied knowledge that was developed are listed at the end.

### **Die Geometry:**

1. The presence effect of a bridge and the formation of a weld seam perturbs material within 3 mm of it. Outside this area, the microstructure and texture that form are independent to the details of the bridge geometry.
2. The bridge shape determines the texture that forms along the weld seam of the porthole die extruded samples because of its influence on the thermal mechanical history during extrusion. The weld seam region for material extruded using the streamlined die (Die C) exhibits a copper texture, while the weld seam region for material extruded using the flat die (Die E) exhibits a cube and goss texture. This is because the materials extruded using Die E experienced higher temperatures and strains at the weld line compared to materials extruded using Die C.
3. An increase of the weld chamber height did not affect the weld seam texture for material extruded using the streamline die (Die C), but did cause material extruded using the flat die (Die E) to become more similar to material extruded using the streamlined die.
4. Tensile properties of material that was unrecrystallized after extrusion clearly showed that the material would fail along the weld seam due to it being softer than the matrix material.

This resulted in a concentration of the strain at the weld seam early on and a lower failure strain compared to material without a weld seam. Qualitatively the concentration of the strain along the weld seam for materials extruded using Die E appeared to be higher than for materials extruded using Die C. This can be understood when we consider the different textures found at the weld seam for Die E and Die C.

**Ram speed:**

1. The increase of the ram speed can severely deteriorate the extrudate's surface quality, especially at the edge and the seam. What's more, the high exit temperature resulting from increasing ram speed prompts the grain growth at the surface and increases the thickness of PCG layer. Despite the prominent influence on the surface quality and microstructure, the mechanical properties of porthole die extruded samples are not affected by ram speed noticeably.

**Alloy composition:**

1. The presence of Mn / Cr containing dispersoids at a high exit temperature effectively inhibit the recrystallization and maintain a deformation texture. On the other hand, in dispersoid free material, the extrudate is recrystallized after extrusion. Recrystallization of the matrix appears to alleviate the microstructure differences between the matrix and the weld seam in porthole die extruded AA6xxx samples, and ensures the samples with a weld in them have similar tensile properties to samples without a weld.

Besides the aforementioned fundamental scientific contributions, this research also provides useful guidance for practical extrusion industry:

1. The sharpness of the bridge determines the temperature and strain distribution along the cross section of porthole die extruded profiles. A sharper bridge results in a lower exit temperature and strain along the weld seam.
2. The upper part of bridge's influence on porthole die extrusion is very small compared to the bottom part of bridge. Only the shape of bottom part of bridge needs to be carefully designed in porthole die extrusion.

3. The charge seam length is mainly determined by the welding chamber height. A deep welding chamber can result in a longer charge seam, which means a longer length of the front part of the extruded profile should be scrapped.
4. The length of back end defects is mostly affected by the welding chamber. A deeper welding chamber helps reduce the length of profile to be scrapped at the back end. On the other hand, the effect of the bridge shape angle on back end defects is negligible.

### **7.3 Future work**

1. *Texture evolution analysis.* Even though the final textures in the extruded profiles have already been thoroughly studied in this research, the texture evolution in porthole die extrusion still remains largely unknown. Partial extrusion trials have been conducted, and the remaining billets will be separated from the die and cut into half. The section plane of the billet will be macroetched to reveal the dead zone and flow paths in extrusion. The micro-texture along some specific flow paths should be observed by EBSD to study the texture evolution during porthole die extrusion.
2. *Tensile test simulation.* In this research, the strain concentration at the seam is believed to be related to the texture variation between the seam and the matrix. A very rough tensile test model only considering the weld seam texture and the matrix texture has been built as part of this research. In the future, a more comprehensive tensile test model considering spatial variations in texture in the sample, especially the transition texture between the weld seam and the matrix, could be constructed to further analysis the relationship between sample mechanical properties and texture distribution.

## References

- [1] P.K. Mallick, *Materials, design and manufacturing for lightweight vehicles*, 2010, Elsevier.
- [2] *2015 North American light vehicle aluminum content study*, 2014, Available from: <http://docplayer.net/24541103-2015-north-american-light-vehicle-aluminum-content-study-executive-summary-june-2014.html>.
- [3] J. Hirsch, *Aluminium in innovative light-weight car design*, *Materials Transactions*, 2011, 52(5): p. 818-824.
- [4] G. Gaustad, E. Olivetti, and R. Kirchain, *Improving aluminum recycling: A survey of sorting and impurity removal technologies*, *Resources Conservation and Recycling*, 2012, 58: p. 79-87.
- [5] *Ford's aluminum-body F-150 SSV*, 2016, Available from: <http://search.proquest.com.proxy.lib.uwaterloo.ca/docview/1809030292?accountid=14906>.
- [6] *From the Ford GT to the F-150: Aluminum extrusion aids auto lightweighting*, 2014, Available from: [https://www.designnews.com/materials-assembly/ford-gt-f-150-aluminum-extrusion-aids-auto-lightweighting/21014447343681?doc\\_id=276054](https://www.designnews.com/materials-assembly/ford-gt-f-150-aluminum-extrusion-aids-auto-lightweighting/21014447343681?doc_id=276054).
- [7] M. Bauser, G. Sauer, and K. Siegert, *Extrusion (2nd Edition)*, 2006, ASM International, Materials Park, OH.
- [8] P.K. Saha, *Aluminum extrusion technology*, 2000, ASM International, Materilas Park, OH.
- [9] R. Vissers, M.v. van Huis, J. Jansen, H. Zandbergen, C. Marioara, and S. Andersen, *The crystal structure of the  $\beta'$  phase in Al–Mg–Si alloys*, *Acta Materialia*, 2007, 55(11): p. 3815-3823.
- [10] O. Myhr, Ø. Grong, H. Fjaer, and C. Marioara, *Modelling of the microstructure and strength evolution in Al–Mg–Si alloys during multistage thermal processing*, *Acta Materialia*, 2004, 52(17): p. 4997-5008.
- [11] A.K. Gupta, D.J. Lloyd, and S.A. Court, *Precipitation hardening processes in an Al-0.40%Mg-1.3%Si-0.25%Fe aluminum alloy*, *Materials Science and Engineering a-Structural Materials Properties Microstructure and Processing*, 2001, 301(2): p. 140-146.
- [12] O. Reiso, *Extrusion of AlMgSi Alloys*, *Materials Forum*, 2004, 28: p. 32-46.
- [13] H. Chen, G.Q. Zhao, C.S. Zhang, Y.J. Guan, H. Liu, and F.J. Kou, *Numerical simulation of extrusion process and die structure optimization for a complex aluminum multicavity wallboard of high-speed train*, *Materials and Manufacturing Processes*, 2012, 26(12): p. 1530-8.
- [14] *Transporation - Auto*, 2016, Available from: [http://www.aec.org/?page=ea\\_auto](http://www.aec.org/?page=ea_auto).
- [15] H. Zhu, M.J. Couper, and A.K. Dahle, *Effect of process variables on Mg-Si particles and extrudability of 6xxx series aluminum extrusions*, *JOM*, 2011, 63(11): p. 66-71.
- [16] J.G. Kaufman, *Introduction to aluminum alloys and tempers*, 2000, ASM International, Materials Park, OH.
- [17] *Building the 2015 Ford F-150 safe and strong*, 2015, Available from: <http://www.trucktrend.com/features/1504-building-the-2015-ford-f-150-safe-and-strong/>.
- [18] S.Y. Lee, D.C. Ko, S.K. Lee, I.K. Lee, M.S. Joeng, D.H. Kim, and Y.J. Cho, *Porthole extrusion process design for magnesium-alloy bumper back beam by using FE analysis and extrusion limit diagram*, *Advances in Mechanical Engineering*, 2015, 6(0): p. 120745-120745.

- [19] G. Liu, J. Zhou, and J. Duszczuk, *FE analysis of metal flow and weld seam formation in a porthole die during the extrusion of a magnesium alloy into a square tube and the effect of ram speed on weld strength*, Journal of Materials Processing Technology, 2008, 200(1-3): p. 185-198.
- [20] J. Yu, G. Zhao, and L. Chen, *Investigation of interface evolution, microstructure and mechanical properties of solid-state bonding seams in hot extrusion process of aluminum alloy profiles*, Journal of Materials Processing Technology, 2016, 230: p. 153-166.
- [21] H. Valberg, *Extrusion welding in aluminium extrusion*, International Journal of Materials and Product Technology, 2002, 17(7): p. 497-556.
- [22] J.Q. Yu, G.Q. Zhao, and L. Chen, *Analysis of longitudinal weld seam defects and investigation of solid-state bonding criteria in porthole die extrusion process of aluminum alloy profiles*, Journal of Materials Processing Technology, 2016, 237: p. 31-47.
- [23] L. Donati and L. Tomesani, *Seam welds in hollow profile extrusion: Process mechanics and product properties*, Materials Science Forum, 2009, Trans Tech Publ.
- [24] D.R. Cooper and J.M. Allwood, *The influence of deformation conditions in solid-state aluminium welding processes on the resulting weld strength*, Journal of Materials Processing Technology, 2014, 214(11): p. 2576-2592.
- [25] J. Yu and G. Zhao, *Interfacial structure and bonding mechanism of weld seams during porthole die extrusion of aluminum alloy profiles*, Materials Characterization, 2018, 138: p. 56-66.
- [26] M. Plata and J. Piwnik, *Theoretical and experimental analysis of seam weld formation in hot extrusion of aluminum alloys*, Proceedings of seventh international aluminum extrusion technology seminar, 2000, Chicago, USA.
- [27] E. Ceretti, L. Fratini, F. Gagliardi, and C. Giardini, *A new approach to study material bonding in extrusion porthole dies*, CIRP Annals - Manufacturing Technology, 2009, 58(1): p. 259-262.
- [28] R. Akeret, *Properties of pressure welds in extruded aluminum-alloy sections*, Journal of the Institute of Metals, 1972, 100(NJUL): p. 202-207.
- [29] L. Donati and L. Tomesani, *The prediction of seam welds quality in aluminum extrusion*, Journal of Materials Processing Technology, 2004, 153-154: p. 366-373.
- [30] J. Yu, G. Zhao, W. Cui, L. Chen, and X. Chen, *Evaluating the welding quality of longitudinal welds in a hollow profile manufactured by porthole die extrusion: Experiments and simulation*, Journal of Manufacturing Processes, 2019, 38: p. 502-515.
- [31] A. Rollett, F. Humphreys, G.S. Rohrer, and M. Hatherly, *Recrystallization and related annealing phenomena*, 2004, Elsevier, Oxford, UK.
- [32] T. Kayser, B. Klusemann, H.G. Lambers, H.J. Maier, and B. Svendsen, *Characterization of grain microstructure development in the aluminum alloy EN AW-6060 during extrusion*, Materials Science and Engineering: A, 2010, 527(24-25): p. 6568-6573.
- [33] A. Güzel, A. Jäger, F. Parvizian, H.G. Lambers, A.E. Tekkaya, B. Svendsen, and H.J. Maier, *A new method for determining dynamic grain structure evolution during hot aluminum extrusion*, Journal of Materials Processing Technology, 2012, 212(1): p. 323-330.
- [34] S. Gourdet and F. Montheillet, *A model of continuous dynamic recrystallization*, Acta Materialia, 2003, 51(9): p. 2685-2699.

- [35] A. Foydl, A. Segatori, N.B. Khalifa, L. Donati, A. Brosius, L. Tomesani, and A.E. Tekkaya, *Grain size evolution simulation in aluminium alloys AA 6082 and AA 7020 during hot forward extrusion process*, *Materials Science and Technology*, 2013, 29(1): p. 100-110.
- [36] M. Schikorra, L. Donati, L. Tomesani, and A.E. Tekkaya, *Microstructure analysis of aluminum extrusion: Prediction of microstructure on AA6060 alloy*, *Journal of Materials Processing Technology*, 2008, 201(1-3): p. 156-162.
- [37] K. Huang and R.E. Loge, *A review of dynamic recrystallization phenomena in metallic materials*, *Materials & Design*, 2016, 111: p. 548-574.
- [38] A.R. Eivani, *Modeling of microstructural evolution during homogenization and simulation of transient state recrystallization leading to peripheral coarse grain structure in extruded Al-4.5Zn-1Mg alloy*, Doctoral dissertation, 2010, Delft University of Technology, Delft, Netherlands.
- [39] A.R. Eivani, J. Zhou, and J. Duszczuk, *Mechanism of the formation of peripheral coarse grain structure in hot extrusion of Al-4.5Zn-1Mg*, *Philosophical Magazine*, 2016, 96(12): p. 1188-1196.
- [40] N. Nanninga, C. White, T. Furu, O. Anderson, and R. Dickson, *Effect of orientation and extrusion welds on the fatigue life of an Al-Mg-Si-Mn alloy*, *International Journal of Fatigue*, 2008, 30(9): p. 1569-1578.
- [41] J. Yu, G. Zhao, C. Zhang, and L. Chen, *Dynamic evolution of grain structure and microtexture along a welding path of aluminum alloy profiles extruded by porthole dies*, *Materials Science and Engineering: A*, 2017, 682: p. 679-690.
- [42] X.H. Fan, D. Tang, W.L. Fang, D.Y. Li, and Y.H. Peng, *Microstructure development and texture evolution of aluminum multi-port extrusion tube during the porthole die extrusion*, *Materials Characterization*, 2016, 118: p. 468-480.
- [43] P.D. Wu, S.R. MacEwen, D.J. Lloyd, and K.W. Neale, *Effect of cube texture on sheet metal formability*, *Materials Science and Engineering: A*, 2004, 364(1): p. 182-187.
- [44] T. Furu and K. Pedersen, *The influence of grain structure and texture on formability and toughness of extruded aluminium alloys*, *Materials science forum*, 2006, Trans Tech Publ.
- [45] K. Zhang, K. Marthinsen, B. Holmedal, T. Aukrust, and A. Segatori, *Through thickness variations of deformation texture in round profile extrusions of 6063-type aluminium alloy: Experiments, FEM and crystal plasticity modelling*, *Materials Science and Engineering: A*, 2018, 722: p. 20-29.
- [46] D. Tang, W. Fang, X. Fan, T. Zou, Z. Li, H. Wang, D. Li, Y. Peng, and P. Wu, *Evolution of the Material Microstructures and Mechanical Properties of AA1100 Aluminum Alloy within a Complex Porthole Die during Extrusion*, *Materials*, 2018, 12(1): p. 16.
- [47] R. Hu, T. Ogura, H. Tezuka, T. Sato, and Q. Liu, *Dispersoid formation and recrystallization behavior in an Al-Mg-Si-Mn alloy*, *Journal of Materials Science & Technology*, 2010, 26(3): p. 237-243.
- [48] S. Esmaili, X. Wang, D.J. Lloyd, and W.J. Poole, *On the precipitation-hardening behavior of the Al-Mg-Si-Cu alloy AA6111*, *Metallurgical and Materials Transactions A*, 2003, 34(3): p. 751-763.
- [49] M. Murayama and K. Hono, *Pre-precipitate clusters and precipitation processes in Al-Mg-Si alloys*, *Acta Materialia*, 1999, 47(5): p. 1537-1548.
- [50] S.J. Andersen, H.W. Zandbergen, J. Jansen, C. Traeholt, U. Tundal, and O. Reiso, *The crystal structure of the  $\beta''$  phase in Al-Mg-Si alloys*, *Acta Materialia*, 1998, 46(9): p. 3283-3298.

- [51] M. Kenyon, J. Robson, J. Fellowes, and Z. Liang, *Effect of Dispersoids on the Microstructure Evolution in Al–Mg–Si Alloys*, *Advanced Engineering Materials*, 2019, 21(4): p. 1800494.
- [52] K. Strobel, E. Sweet, M. Easton, J.F. Nie, and M. Couper, *Dispersoid Phases in 6xxx Series Aluminium Alloys*, *Materials Science Forum*, 2010, 654-656: p. 926-929.
- [53] L. Lodgaard and N. Ryum, *Precipitation of dispersoids containing Mn and/or Cr in Al-Mg-Si alloys*, *Materials Science and Engineering a-Structural Materials Properties Microstructure and Processing*, 2000, 283(1-2): p. 144-152.
- [54] L. Lodgaard and N. Ryum, *Precipitation of chromium containing dispersoids in Al-Mg-Si alloys*, *Materials Science and Technology*, 2000, 16(6): p. 599-604.
- [55] W.-W. Zhang, B. Lin, P. Cheng, D.-T. Zhang, and Y.-Y. Li, *Effects of Mn content on microstructures and mechanical properties of Al-5.0Cu-0.5Fe alloys prepared by squeeze casting*, *Transactions of Nonferrous Metals Society of China*, 2013, 23: p. 1525-1531.
- [56] N. Nanninga, C. White, O. Mills, and J. Lukowski, *Effect of specimen orientation and extrusion welds on the fatigue life of an AA6063 alloy*, *International Journal of Fatigue*, 2010, 32(2): p. 238-246.
- [57] A.J. den Bakker, X. Wu, L. Katgerman, and S. van der Zwaag, *Microstructural and X-ray tomographic analysis of damage in extruded aluminium weld seams*, *Materials Science and Technology*, 2015, 31(1): p. 94-104.
- [58] H. Valberg, T. Loeken, M. Hval, B. Nyhus, and C. Thaulow, *The extrusion of hollow profiles with a gas pocket behind the bridge*, *International Journal of Materials & Product Technology*, 1995, 10(3-6): p. 222-267.
- [59] K.J. Kim, C.H. Lee, and D.Y. Yang, *Investigation into the improvement of welding strength in three-dimensional extrusion of tubes using porthole dies*, *Journal of Materials Processing Technology*, 2002, 130: p. 426-431.
- [60] A.J. den Bakker, R.J. Werkhoven, W.H. Sillekens, and L. Katgerman, *The origin of weld seam defects related to metal flow in the hot extrusion of aluminium alloys EN AW-6060 and EN AW-6082*, *Journal of Materials Processing Technology*, 2014, 214(11): p. 2349-2358.
- [61] L. Donati, L. Tomesani, and G. Minak, *Characterization of seam weld quality in AA6082 extruded profiles*, *Journal of Materials Processing Technology*, 2007, 191(1-3): p. 127-131.
- [62] L. Donati and L. Tomesani, *The effect of die design on the production and seam weld quality of extruded aluminum profiles*, *Journal of Materials Processing Technology*, 2005, 164-165: p. 1025-1031.
- [63] F. Gagliardi, G. Ambrogio, and L. Filice, *On the die design in AA6082 porthole extrusion*, *Cirp Annals-Manufacturing Technology*, 2012, 61(1): p. 231-234.
- [64] Y.A. Khan, H. Valberg, and I. Irgens, *Joining of metal streams in extrusion welding*, *International Journal of Material Forming*, 2009, 2(S1): p. 109-112.
- [65] F. Gagliardi, M. Schwane, T. Citrea, M. Haase, N.B. Khalifa, and A.E. Tekkaya, *Bridge design influences on the pressure conditions in the welding chamber for porthole die extrusion*, *Key Engineering Materials*, 2014, 622-623: p. 87-94.
- [66] M. Schwane, F. Gagliardi, A. Jager, N. Ben Khalifa, and A.E. Tekkaya, *Modeling approach for the determination of material flow and welding conditions in porthole die extrusion with gas pocket formation*, *Key Engineering Materials*, 2013, 554-557(1): p. 797-803.

- [67] J. Liu, G.Y. Lin, D. Feng, Y.M. Zou, and L.P. Sun, *Effects of process parameters and die geometry on longitudinal welds quality in aluminum porthole die extrusion process*, Journal of Central South University of Technology, 2010, 17(4): p. 688-696.
- [68] F. Kolpak, A. Schulze, C. Dahnke, and A.E. Tekkaya, *Predicting weld-quality in direct hot extrusion of aluminium chips*, Journal of Materials Processing Technology, 2019, 274.
- [69] J.Q. Yu, G.Q. Zhao, W.C. Cui, C.S. Zhang, and L. Chen, *Microstructural evolution and mechanical properties of welding seams in aluminum alloy profiles extruded by a porthole die under different billet heating temperatures and extrusion speeds*, Journal of Materials Processing Technology, 2017, 247: p. 214-222.
- [70] S. Bingöl and M.S. Keskin, *Effect of different extrusion temperature and speed on extrusion welds*, Journal of achievements in materials and manufacturing engineering, 2007, 23(2): p. 39-42.
- [71] H.H. Jo, C.S. Jeong, S.K. Lee, and B.M. Kim, *Determination of welding pressure in the non-steady-state porthole die extrusion of improved Al7003 hollow section tubes*, Journal of Materials Processing Technology, 2003, 139(1-3): p. 428-433.
- [72] K.E. Nilsen, *Numerical modelling of the aluminium extrusion process and comparison with results obtained from industrially extruded complex sections*, Doctor of Philosophy, 2014, Bournemouth University.
- [73] F. Gagliardi, T. Citrea, G. Ambrogio, and L. Filice, *Influence of the process setup on the microstructure and mechanical properties evolution in porthole die extrusion*, Materials & Design, 2014, 60: p. 274-281.
- [74] S. Bingöl and A. Bozacı, *Experimental and numerical study on the strength of aluminum extrusion welding*, Materials, 2015, 8(7): p. 4389-4399.
- [75] G.E. Totten and D.S. MacKenzie, *Handbook of aluminum*, 2003, Marcel Dekker Inc., New York, US.
- [76] J. Yu, G. Zhao, X. Zhao, L. Chen, and M. Chen, *Microstructures of longitudinal/transverse welds and back-end defects and their influences on the corrosion resistance and mechanical properties of aluminum alloy extrusion profiles*, Journal of Materials Processing Technology, 2019, 267: p. 1-16.
- [77] A.J. den Bakker, L. Katgerman, and S. van der Zwaag, *Analysis of the structure and resulting mechanical properties of aluminium extrusions containing a charge weld interface*, Journal of Materials Processing Technology, 2016, 229: p. 9-21.
- [78] N. Nanninga, C. White, R. Dickson, and Performance, *Charge Weld Effects on High Cycle Fatigue Behavior of a Hollow Extruded AA6082 Profile*, Journal of Materials Engineering and Performance, 2011, 20(7): p. 1235-1241.
- [79] S. Lou, A. Wang, S. Lu, G. Guo, C. Qu, and C. Su, *Tensile property and micro-texture evolution of the charge weld in a billet-to-billet extrusion of AA6061 aluminum profile*, The International Journal of Advanced Manufacturing Technology, 2019.
- [80] X. Ren, J.L. Zhang, J.P. Li, J. Liu, H.H. Zhang, and X.R. Wang, *Microstructural characterization of extrusion welds in 6xxx aluminum alloys*, in *Proceedings of the 3rd International Conference on Material, Mechanical and Manufacturing Engineering*, P. Yarlagadda, Editor. 2015. p. 1857-1863.
- [81] B. Reggiani and L. Donati, *Experimental, numerical, and analytical investigations on the charge weld evolution in extruded profiles*, International Journal of Advanced Manufacturing Technology, 2018, 99(5-8): p. 1379-1387.

- [82] B. Reggiani, A. Segatori, L. Donati, and L. Tomesani, *Prediction of charge welds in hollow profiles extrusion by FEM simulations and experimental validation*, The International Journal of Advanced Manufacturing Technology, 2013, 69(5-8): p. 1855-1872.
- [83] Y. Mahmoodkhani, M. Wells, N. Parson, C. Jowett, and W. Poole, *Modeling the Formation of Transverse Weld during Billet-on-Billet Extrusion*, Materials, 2014, 7(5): p. 3470-3480.
- [84] L. Chen, G. Zhao, and J. Yu, *Effects of ram velocity on pyramid die extrusion of hollow aluminum profile*, The International Journal of Advanced Manufacturing Technology, 2015, 79(9-12): p. 2117-2125.
- [85] C.S. Zhang, Y.Y. Dong, C.X. Wang, G.Q. Zhao, L. Chen, and W.C. Sun, *Evolution of transverse weld during porthole extrusion of AA7N01 hollow profile*, Journal of Materials Processing Technology, 2017, 248: p. 103-114.
- [86] T. Sheppard, *Extrusion of Aluminium Alloys*, 1999, Springer US.
- [87] Y.T. Kim and K. Ikeda, *Flow behavior of the billet surface layer in porthole die extrusion of aluminum*, Metallurgical and Materials Transactions A, 2000, 31(6): p. 1635-1643.
- [88] P. Robbins, K. Chien, C. Jowett, and W. Dixon, *The design and benefits of a thermally stable container*, Proceedings of the Eleventh International Aluminum Extrusion Technology Seminar, 2016.
- [89] X. Lu, C. Zhang, G. Zhao, Y. Guan, L. Chen, and A. Gao, *State-of-the-art of extrusion welding and proposal of a method to evaluate quantitatively welding quality during three-dimensional extrusion process*, Materials & Design, 2016, 89: p. 737-748.
- [90] C. Liu, *Microstructure evolution during homogenization and its effect on the high temperature deformation behaviour in AA6082 based alloys*, Doctoral dissertation, 2017, The University of British Columbia, Vancouver, Canada.
- [91] E. Stein, R. De Borst, and T.J.R. Hughes, *Encyclopedia of computational mechanics, 3 volume set*, 2004, Wiley.
- [92] M.N.A. Nasr, E.G. Ng, and M.A. Elbestawi, *A modified time-efficient FE approach for predicting machining-induced residual stresses*, Finite Elements in Analysis and Design, 2008, 44(4): p. 149-161.
- [93] M. Pietrzyk, L. Madej, L. Rauch, and D. Szeliga, *Computational Materials Engineering: Achieving High Accuracy and Efficiency in Metals Processing Simulations*, 2015, Elsevier Science.
- [94] J.G. Lenard, *Primer on Flat Rolling* 2014, Elsevier.
- [95] C. Sellars and W.M. Tegart, *Hot workability*, International Metallurgical Reviews, 1972, 17(1): p. 1-24.
- [96] T. Sheppard and D. Wright, *Determination of flow stress: Part I constitutive equation for aluminium alloys at elevated temperatures*, Metals Technology, 1979, 6(1): p. 215-223.
- [97] S.M. Lou, Y.X. Wang, C.X. Liu, S. Lu, S.J. Liu, and C.J. Su, *Analysis and prediction of the billet butt and transverse weld in the continuous extrusion process of a hollow aluminum profile*, Journal of Materials Engineering and Performance, 2017, 26(8): p. 4121-4130.
- [98] C. Zhang, M. Wen, G. Zhao, L. Chen, W. Sun, and K. Bai, *One-time determination of 20 material parameters in a strain-compensated constitutive model and its application in extrusion for an Al-Zn-Mg thin-walled profile*, Thin-Walled Structures, 2019, 135: p. 65-77.

- [99] T. Sheppard and A. Jackson, *Constitutive equations for use in prediction of flow stress during extrusion of aluminium alloys*, *Materials Science and Technology*, 1997, 13(3): p. 203-209.
- [100] Y. Liu, C. Geng, Q. Lin, Y. Xiao, J. Xu, and W. Kang, *Study on hot deformation behavior and intrinsic workability of 6063 aluminum alloys using 3D processing map*, *Journal of Alloys and Compounds*, 2017, 713: p. 212-221.
- [101] C.S. Zhang, G.Q. Zhao, Y.J. Guan, A.J. Gao, L.J. Wang, and P. Li, *Virtual tryout and optimization of the extrusion die for an aluminum profile with complex cross-sections*, *International Journal of Advanced Manufacturing Technology*, 2015, 78(5-8): p. 927-937.
- [102] M. Schikorra, L. Donati, L. Tomesani, and A.E. Tekkaya, *Microstructure analysis of aluminum extrusion: grain size distribution in AA6060, AA6082 and AA7075 alloys*, *Journal of Mechanical Science and Technology*, 2007, 21(10): p. 1445-1451.
- [103] C. Jowett, Y. Mahmoodkhani, N.C. Parson, and G. Garza, *What Does Exit Temperature Measurement Tell Us*, in *Eleventh International Aluminum Extrusion Technology Seminar and Exposition*. 2016: Chicago, USA. p. 641-659.
- [104] X. Duan and T. Sheppard, *Simulation and control of microstructure evolution during hot extrusion of hard aluminium alloys*, *Materials Science and Engineering A*, 2003, 351(1-2): p. 282-292.
- [105] L. Donati, L. Tomesani, M. Schikorra, N. Ben Khalifa, and A. Tekkaya, *Friction model selection in FEM simulations of aluminium extrusion*, 2010. 27-41.
- [106] Y. Mahmoodkhani, M.A. Wells, N. Parson, and W.J. Poole, *Numerical modelling of the material flow during extrusion of aluminium alloys and transverse weld formation*, *Journal of Materials Processing Technology*, 2014, 214(3): p. 688-700.
- [107] T. Rahman, A. Bardelcik, J. Imbert, C. Butcher, and M.J. Worswick, *Effect of strain rate on flow stress and anisotropy of DP600, TRIP780, and AA5182-O sheet metal alloys*, *International Journal of Impact Engineering*, 2016, 88: p. 72-90.
- [108] B. Pan, H. Xie, Z. Guo, and T. Hua, *Full-field strain measurement using a two-dimensional Savitzky-Golay digital differentiator in digital image correlation*, *Optical Engineering*, 2007, 46(3): p. 033601-10.
- [109] W.D. Callister and D.G. Rethwisch, *Materials Science and Engineering: An Introduction, 9th Edition*, 2013, John Wiley and Sons, Incorporated, Hoboken, NJ.
- [110] J. Chen, W.J. Poole, and N.C. Parson, *The effect of through thickness texture variation on the anisotropic mechanical response of an extruded Al-Mn-Fe-Si alloy*, *Materials Science and Engineering A*, 2018, 730: p. 24-35.
- [111] G.F. Vander Voort, *Color Metallography*, in *Metallography and Microstructures*, G.F. Vander Voort, Editor. 2004, ASM International. p. 0.
- [112] R. Lumley, *Fundamentals of Aluminium Metallurgy: Production, Processing, and Applications*, 2010, Taylor & Francis Group.
- [113] L. Donati and L. Tomesani, *Seam welds in hollow profile extrusion: Process mechanics and product properties*, *Materials Science Forum*, 2009, 604: p. 121-131.
- [114] F.J. Humphreys, *A unified theory of recovery, recrystallization and grain growth, based on the stability and growth of cellular microstructures—II. The effect of second-phase particles*, *Acta Materialia*, 1997, 45(12): p. 5031-5039.
- [115] W.Z. Misiolak and W.R. Van Geertruyden, *Combined numerical simulation and microstructure characterization for prediction of physical properties in extruded aluminum alloys*, *Key Engineering Materials*, 2010, Trans Tech Publ.

- [116] Y. Mahmoodkhani, J. Chen, M.A. Wells, W.J. Poole, and N.C. Parson, *The Effect of Die Bearing Geometry on Surface Recrystallization During Extrusion of an Al-Mg-Si-Mn Alloy*, Metallurgical and Materials Transactions A, 2019, 50(11): p. 5324-5335.